Topological Mechanical Systems Beyond the Limit of Linear Ideal Springs

by

Harold Yuanhui Liu

A dissertation submitted in partial fulfillment
of the requirements for the degree of
Doctor of Philosophy
(Physics)
in the University of Michigan
2022

Doctoral Committee:

Associate Professor Xiaoming Mao, Chair
Professor Ellen Arruda
Professor David Lubensky
Professor Kai Sun
Associate Professor Qiong Yang

Harold Yuanhui Liu
lharold@umich.edu
ORCID iD: 0000-0002-3358-7931

To my family, companion, friends, and everyone who entered my life.

ACKNOWLEDGMENTS

During the 6-year span of my graduate study, numerous people have generously offered their help to me. Therefore I'd like to take this opportunity to present my deepest gratitude toward all the wonderful people that have entered my life and made my journey through graduate school spectacular.

The person I would like to show the most of my gratitude for is my advisor Professor Xiaoming Mao. This thesis would not be able to come together without her tremendous help. She is always kind and considerate to offer suggestions on my questions and concerns. She has always been able to address key research topics and give clear guidance for me to complete research projects smoothly. I've learned a great deal from her on scientific research methods, scientific presentation skills, and even team and collaboration building skills.

I'd also like to thank my wonderful collaborators, including Professors David Lubensky, Kai Sun, Ellen Arruda, Zi Chen, and Nicholas Boechler, and their staffs, postdocs, and students Andrea Poli, Xuedong Zhai, Haning Xiu, Kai Qian, Ian Frankel, and Nathaly Villacis. It has always been pleasant to work together with them, and to exchange and reflect ideas with. Beside the wonderful co-workers, I'd like to show my gratitude for the National Sciecne Foundation (NSF) and Multidisciplinary University Research Initiatives (MURI) from the Department of Defense (DOD) for their funding that helped me through the Ph.D. career.

Through my years in Professor Mao's research group, I've come across many wonderful groupmates and friends, though many of them have already left UM. Di Zhou, being the first postdoc I've worked with, and Leyou, being the most senior graduate student when I joined, taught and guided me immensely when accumulating the background of the research topics of the group. Shang Zhang, who was not only a senior graduate student, but also a close friend, helped me with both research and career search. Francesco Serafin, who also became my close friend, offered his brilliant insights on many subjects in both research and life. It was an extraordinary experience for me to see the rapid expansion of the research group after the MURI collaboration has started, many new bloods have joined including Ethan Stanifer, James McInerney, Siddartha Sarkar, who I worked closely with on multiple projects with. Nan Cheng, Aric Moilanen, Jose Ortiz, and Jiadong Liu, who I all talked to extensively about research ideas. I enjoyed working with these great physicists to the most extent.

Besides the friends I've made within the research group, there are also numerous others who gave me support during the doctoral years. Owen Puls, Siwen Li, Heqiu Li, Yongyi Wu, Xiong Xiao, along with many other wonderful physics friends in my cohort, have been great supports to me as we go through tough courses and share memorable times. Andrei Klishin, and my first academic advisor Greg van Anders, have taught me the first steps of going into scientific research. My old time friends Xiaotian Tan and Zhewen Hu, have made my journey in graduate school as joyful as possible.

I'd like to show my appreciation to my family. My parents Huazhen Zhang and Hanjie Liu have shaped my world since the very first step I took and became role models for me ever since, I would never become who I am now if without their prodigious support. My sister Alice Liu, by bring joy to the family, has lightened up my spirit from time to time.

Last but not least, I'd like to express my gratefulness to my dearest, Min Yuan. Her love and company aided me with endless amount of energy to go through the most stressful times, as well as enabled me to find the momentum to pursue the best version of myself beyond my own expectation.

TABLE OF CONTENTS

LIST OF FIGURES

FIGURE

LIST OF ABBREVIATIONS

TMM Topological Mechanical Metamaterials

ZM Zero Modes

FM Floppy Modes

SSS State of Self Stress

VM Vertex Model

ATN Active Tension Network

PBC Periodic Boundary Condition

AS Angular Spring

NN Nearest Neighbor

NNN Next Nearest Neighbor

PBC Periodic Boundary Condition

DOF Degree of Freedom

PDE Partial Differential Equation

ABSTRACT

In recent years, *topological mechanical metamaterials* (TMM) have gradually attracted attention across different disciplines including physics, mechanical engineering, and materials science. It has achieved great success in analyzing mechanical rigidity and programming mechanical responses in Maxwell lattices. The engineering of TMMs opened up numerous opportunities for achieving particular mechanical functionalities in engineering applications such as mechanical impact buffers, waveguides, phonon diodes, etc. Besides the achievements in the theoretical aspect, there have been also numerous progress made in the manufacturing of TMMs. However, issues such as finite hinge and material composition takes the realization of TMMs away from the limit of ideal springs. The focus of this thesis is to examine systems beyond the limit of ideal spring models and study both the novel physical phenomena and engineering advantage by these considerations.

The first project presented in this dissertation expands on a lattice model in which the elastic energy is related to rings of springs. This so-called Vertex Model (VM) is presented as an attempt to understand the geometric effect on epithelial tissues. In a slight variation of the VM, the Active Tension Network model (ATN), topologically polarized zero modes (ZMs) were discovered. This work may provide useful insights into tissue morphogenesis.

The second project presents a numerical study on the effect of bending rigidity in Maxwell lattices. Specifically, the study focuses on the stress-focusing effect on a domain wall that carries *states of self-stress* (SSS) formed by connecting two opposite topologically polarized domains. By including the bending stiffness of the hinges, a masking effect on the stress focusing was observed as the bending stiffness increased, and by designing the lattice geometry, lowering and homogenization of the bending stress were achieved. Furthermore, stress focusing was able to be achieved for shear strain as well. This geometric manipulation could help prevent fracturing at the hinges in response to different strains.

The third project shows an engineering effort of designing bistable unit cells in Maxwell lattices. Such a design makes the entire lattice to be multi-stable, and the topological transitions more easily achievable. The multi-stable lattice also shows interesting interface profiles during the transition due to the incompatibility of the lattice spacing in the two topologically distinguished lattice regions. Furthermore, structural assembly and 3D-printing techniques were employed to realize the multi-stable lattices to test the numerically predicted edge stiffness difference between the op-

posite lattice boundaries. Such an engineering design offers potential application opportunities for impact mitigation, mechenological computation, and flexible robots.

The fourth project is an analytical and numerical study of the non-linear effect on the Maxwell lattices. In this study, exact geometric relations were solved to describe the Maxwell lattice with two boundaries prescribed. Under such a condition, a sinusoidal perturbation was given at one boundary of the lattice to study the nonlinear effect on the topological polarization of the lattice. Under such a condition, local regions of topological polarization switching were observed, along with well-known non-linear effects such as harmonic generations. Furthermore, solitary waves were observed as the perturbation is localized, which allows us to make an analogy to the time domain to create an artificial "non-Hermitian" system. The inclusion of non-linearity promotes further understanding of TMMs beyond the small deformation regime, as well as opens up opportunities for further applications such as adaptive smart materials.

CHAPTER 1

Introduction

1.1 Overview

The study of mechanical stability has been a topic of interest since the ancient times when building architecture and machinery all over the world, and the first systematic study on this matter has been done by Sir James Clerk Maxwell in 1864 in his publication *on the calculation of the equilibrium and stiffness of frames* [6]. In this work, he introduced the mechanical frames as a composition of points (referred to as *sites*)connected by rigid struts (referred to as *bonds*) and argued that a stiff frame would require that

$$N_b \geq dN - \frac{d(d+1)}{2}, \tag{1.1}$$

where N_b is the number of bonds, N is the number of sites, and d is the dimension of the system. Eq. (1.1) is known as the *Maxwell's rule*, which holds an essential role in understanding mechanical stability. The term $\frac{d(d+1)}{2}$ corresponds to the number of rigid translations and rotations under free boundary, sometimes referred to as "trivial" zero modes. In a special case when equality is satisfied in Maxwell's rule, the frame can be *isostatic*. At this point the mechanical frame becomes isostatic, it is on the verge of mechanical instability. And it turns out that isostaticity is directly related to the rigidity criticality of the mechanical frames [7; 8] (more details are provided in 1.2.1).

Furthermore, the study of rigidity has been expanded to other forms of mechanical frames, for example, the epithelial tissue network, with the hope to explain the role mechanics play in guiding the epithelial tissue at the developmental stage. The most widely known epithelial tissue model is the *Vertex Model* (VM), first introduced by Honda [9]. In this model, the epithelial tissue was modeled as a compact quasi-2D polygonal elastic sheet that tightly tiles the entire space with no gap, with the elastic energy associated with the perimeter and area of each polygon. Later research has discovered that the epithelial tissues often are at or near isostaticity [10; 11; 12; 13], which makes them able to both support and accommodate transformations during various biological processes.

In a pioneering work by Kane & Lubensky in 2014, mechanical isostaticity was linked together with topological states of matter. It was discovered that isostaticity provides a particle-hole symmetry in addition to the time-reversal symmetry of classical Hamiltonian mechanical systems, which results in a symmetry-protected topological order class called BDI, which is a well-studied class in electronic systems. This work also provided two examples, namely a 1D mechanical Su-Schrieffer-Heeger chain model, and a 2D deformed kagome lattice. Starting with this, further studies on mechanical topological states have shown that they can intervene with topological defects in crystals [14], buckling of metamaterials [15], and soft strains in isostatic lattices [16]. In addition, the mechanical counterpart of Weyl points [17] in 2D and Weyl lines [18] in 3D was also studied, which complements the map between mechanical and electronic topological states. The works on topological mechanical states have been then expanded to many other different mechanical systems such as random fiber networks [19], quasi-crystals [20], and origami and kirigami structures [21]. Furthermore, the study of mechanical topological states has led to many potential engineering applications such as transformable topological mechanical metamaterials [22], phonon diodes [23], stable geared topological metamaterials [24], protection layers [25], and topological origami metamaterials [26; 27]. On the other hand, multiple efforts have been made to bring these theoretically predicted applications to reality with the current additive manufacturing technology [2; 3; 28; 5], in which it was realized that the non-ideality of the lattice would elevate the energy of the soft modes to be finite, thus disrupting the theoretically predicted topological mechanical states.

From the common ground of isostaticity, it is natural and important to understand how the non-ideal springs in the Vertex Model, which are associated with faces instead of edges, affect the topological states. And from the engineering perspective, it is important to not only understand how the topological states change when bending stiffness makes the springs non-ideal but also to minimize the negative effects it has on the topologically protected mechanical properties.

1.2 Linear Elasticity Theory for Discrete Lattices

As a starting point leading to the investigation of mechanical systems with non-ideal springs, the background discussion of mechanical rigidity and mechanical topological states in ideal spring-mass mechanical frames is provided here.

1.2.1 Rigidity in Maxwell Lattices

Maxwell's rule mentioned in section 1.1 offers a criterion to separate systems from rigid to floppy with the average coordination number $z \equiv 2N_b/N$ as each bond has two sites. And the

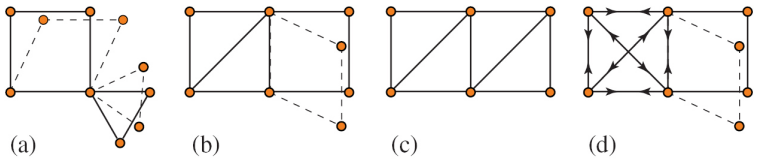

Figure 1.1: Frames of bonds connecting N = 6 sites. (a) has 6 sites, 7 bonds, 5 ZMs, and two floppy modes indicated by the dotted bonds. (b) has 6 sites, 8 bonds, 4 ZMs, and one floppy mode. (c) and (d) are constructed from (b) by adding an additional diagonal bond. (c) satisfies Maxwell's rule with only the three trivial ZMs. (d) has 4 ZMs and one SSS indicated by the arrows on the bonds in the left square.

critical coordination number

$$z_c^N = 2d - \frac{d(d+1)}{N} \tag{1.2}$$

marks the threshold between rigid and floppy systems. A system is rigid when $z > z_c^N$ and becomes floppy when $z < z_c^N$. In the limit of large N, z_c^N reduces to $z_c^\infty = 2d$, and the term *Maxwell Lattice* refers to the lattices that have the average coordination number $z = z_c = 2d$, which is on the verge of mechanical instability.

In the original work by Maxwell, *redundant* constraints were included, which do not contribute to the rigidity of the system. Thus, in a later work by Calladine [29], Maxwell's rule has been generalized t

$$dN - N_b = N_0 - N_s, \tag{1.3}$$

where N_0 is the number of *Zero Modes* (ZM), corresponding to site displacements that cause no change in bond lengths, and N_s is the number of *States of Self-Stress* (SSS), corresponding to bond tensions that produce no net force at any site. This generalized counting is called the *Maxwell-Calladine Index Theorem*

N_0 here also includes the $\frac{d(d+1)}{2}$ trivial rigid translation and rotations of the system, and the other non-trivial ZMs that involve internal displacements of the sites are called *Floppy Modes* (Floppy Modes (FM)), which has a count

$$M = N_0 - \frac{d(d+1)}{2} \tag{1.4}$$

$$= dN - N_b + N_s - \frac{d(d+1)}{2} \tag{1.5}$$

from the Maxwell Calladine index theorem. These floppy modes are also sometimes referred to as *mechanisms* in the engineering literature [29]. A rigid system can then be described as a system that *has no floppy modes* or a system that can carry loads (SSSs), in which description of the redundant constraints are taken care of. In the examples shown in Fig. 1.1 [30], all the frames have

the same number of sites $N = 6$, but they have different rigidity. Figure 1.1(a) is an example of a frame obeying the simple Maxwell's rule, in which there are $N = 6$ sites, $N_b = 7$ bonds, and it has $N_0 = 2 \times 6 - 7 = 5$ ZMs and $M = 5 - 3 = 2$ floppy modes illustrated by the dotted lines after removing the trivial ZMs since there is no SSSs. Figure 1.1(b) has one more bond compared to the frame in figure 1.1(a), and there is no SSS in the frame either, therefore, the number of mechanisms is reduced to $M = 1$. However, comparing figure 1.1(c) and (d), they both have one additional bond added compared to figure 1.1(b), but they can be placed either as a diagonal in the right square or an extra diagonal in the left square. In the first case, there is no mechanism left after placing this additional bond, which still follows Maxwell's rule. In the second case, however, there is still one mechanism that remains in the frame because the additional bond is a redundant constraint in the frame, and provides an SSS, which is illustrated by the arrows.

The Maxwell Calladine index theorem offered a more rigorous definition on *isostaticity*, which is when systems have neither any floppy modes ($M = 0$) nor any SSSs ($N_s = 0$). Maxwell frames ($z = 2d$) with no SSSs are called *isostatic* frames. Such isostatic frames necessarily satisfy the relation $z = z_c$, but for systems with $z = z_c$, SSSs could present to keep the systems away from isostaticity.

The definition of *isostaticity* is unambiguous for a finite lattice under free boundary as it takes the trivial ZMs into account when counting floppy modes. However, in a system under Periodic Boundary Conditions (PBCs), $d(d+1)/2$ SSSs are needed to make the lattice elastically stable [31], thus a new definition of *isostatic lattices* is proposed to be when $N_0 = N_s = d$ [30].

1.2.2 The Dynamical Matrix

In the mechanical frame of N sites modeled as point masses, and N_b bonds modeled as ideal springs that have a finite stretching stiffness but are free to rotate about the point mass, the elastic energy can be written simply as

$$E = E_0 + \frac{1}{2} \sum_{i,j \in bonds} k_{ij} (\mathbf{u}_i - \mathbf{u}_j)^2, \tag{1.6}$$

where $\mathbf{u}$ is the displacement field on the sites, and k_{ij} is the stretching stiffness of the spring connecting sites i and j. In the limit of small displacements, the elastic energy can be expanded in a quadratic form in $\mathbf{u}$ as

$$E = E_0 + \frac{1}{2} u_i \mathbf{D}_{ij} u_j. \tag{1.7}$$

And in this form, $\mathbf{D}_{ij} = \frac{\partial^2 E}{\partial u_i \partial u_j}$ is known as the *dynamical matrix*.

1.2.3 The Equilibrium and Compatibility Matrices

To capture the linear response, the dynamical matrix can be further separated into the *equilibrium matrix* $\mathbf{Q}$ and the *compatibility matrix* $\mathbf{C}$. The equilibrium matrix satisfies

$$\mathbf{Q} \cdot |t\rangle = |f\rangle \,, \tag{1.8}$$

where $|t\rangle$ represents the tensions on bonds, which is an N_b dimensional vector, and $|f\rangle$ are the net forces on sites, which is an $d \cdot N$ dimensional vector. As a result, the equilibrium matrix $\mathbf{Q}$ has dimension $dN \times N_b$.

The compatibility matrix $\mathbf{C}$ takes a complementing relation

$$\mathbf{C} \cdot |u\rangle = |e\rangle \,, \tag{1.9}$$

where $|u\rangle$ represents the displacements on sites, which is a $d \cdot N$ dimensional vector, and $|e\rangle$ represents the extensions of bonds, which is an N_b dimensional vector, thus making $\mathbf{C}$ having a dimension of $N_b \times dN$.

The compatibility matrix $\mathbf{C}$ is determined by the first-order bond elongation relation

$$e_{ij} = (\mathbf{u}_i - \mathbf{u}_j) \cdot \hat{b}_{ij}, \tag{1.10}$$

with $\hat{b}_{ij}$ as the unit vector pointing from site j to i. And the equilibrium matrix $\mathbf{Q}$ is constructed from the site force relation

$$\vec{f}_i = -\sum_{ij}^{j\in\mathcal{N}(i)} \vec{t}_{ij}, \tag{1.11}$$

where $\vec{t}_{ij}$ is the tension to site i from site j that are the neighbors of site i.

By virtual work theorem, it is proven that $\mathbf{C} = \mathbf{Q}^T$ for all ideal spring-mass systems. The dynamical matrix is related to $\mathbf{Q}$ and $\mathbf{C}$ by

$$\mathbf{D} = \mathbf{Q}\mathbf{k}\mathbf{Q}^T = \mathbf{C}^T\mathbf{k}\mathbf{C}, \tag{1.12}$$

where $\mathbf{k}$ is a $N_b \times N_b$ dimensional diagonal matrix of spring stiffness.

This duality between $\mathbf{Q}$ and $\mathbf{C}$ matrices provides a particle-hole symmetry for the mechanical topological states, as we will discuss in Sec. 1.3.1.

1.2.4 States of Self-Stresses (SSS) and Zero Modes (ZM)

In the special case of *state of self-stress*(SSS), no net force is produced on the sites, corresponds to the null space of the equilibrium matrix $\mathbf{Q}$ as

$$\mathbf{Q} \cdot |t_{SSS}\rangle = 0. \tag{1.13}$$

And the *zero modes* (ZM) corresponds to the null space of the compatibility matrix as it is a set of displacements that cause no bond extensions:

$$\mathbf{C} \cdot |u_{ZM}\rangle = 0. \tag{1.14}$$

We will see in Sec. 1.3.1 that they can be topologically protected.

1.3 Topological Mechanical Metamaterial (TMM)

For a free 2D lattice of N sites cut from a periodic Maxwell lattice, there are necessary of order $\sqrt{N}$ *zero modes* due to the order $\sqrt{N}$ bonds being cut, and all sample-spanning *state of self-stress* are lost. In the case when there is no bulk ZMs, this ZMs originated from the cut of the boundary and must be localized at surfaces. It was discovered by Kane & Lubensky in their work in 2014, that these surface modes are intrinsically linked to the topology of the lattice phonon spectrum. The formulation of a topological invariant for the spectrum as well as the interpretation of the invariant in terms of the localization of the ZMs and SSSs are discussed in this section.

1.3.1 Topological Mechanics in Maxwell Lattice

To illustrate the topological nature of the phonon spectrum, we begin by considering a 1D model whose phonon spectrum is identical to that of the Su-Schrieffer-Heeger (SSH) model for polyacetylene [32; 33], schematically shown in Fig. 1.2 (a) - (d).

In this model, rigid bars of length r can rotate freely about fixed positions on a 1D periodic lattice, and the ends of the bars are connected by harmonic springs whose lengths are adjusted so that the equilibrium configuration is one in which alternate rods make an angle $\bar{\theta}$ with the upward or downward normals, creating repeated 2-site unit cells of length a. Bars tilt to the right if $\bar{\theta} > 0$ and to the left if $\bar{\theta} < 0$. Expanding in deviations $\delta\theta_i$ about $\bar{\theta}$, the extension of spring β is $\delta l_\beta = C_{\beta s}\delta\theta_s$, where $C_{\beta s}$ is the compatibility matrix relates the stretch of spring β with rotations of rod s. With further derivation, we have

$$C_{\beta s}(\bar{\theta}) = c_1(\bar{\theta})\delta_{s,\beta} - c_2(\bar{\theta})\delta_{\beta,s+1} \tag{1.15}$$

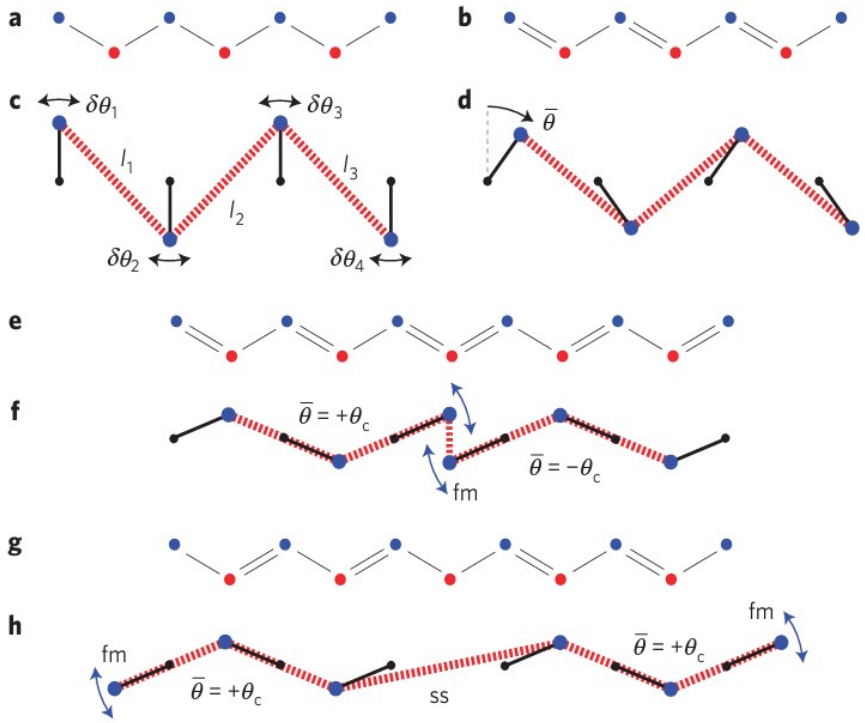

Figure 1.2: (a), (b) The SSH model of polyacetylene, with A and B sublattices indicated by blue circles and red squares, respectively. (c), (d) the mechanical analog of (a) and (b), in which masses, represented by the larger blue dots, are connected by springs in red and are constrained to rotate about fixed pivot points, represented by small black dots. (e) A domain wall in polyacetylene connecting the AB and BA dimerized states. There is a topologically protected zero-energy state associated with the A sublattice at the defect. (f) A mechanical counterpart of (e) with a topologically protected ZM at the domain wall connecting a $\bar{\theta} = +\theta_c$ lattice and a $\bar{\theta} = -\theta_c$ lattice. (g) A domain wall connecting the BA and AB dimerized states, which has a zero-energy state associated with the B sublattice. (h) The equivalent mechanical SSH chain that has a SSS at the domain wall. Adapted from [1].

with

$$c_{1(2)} = \frac{(a \pm 2r\sin\bar{\theta})r\cos\bar{\theta}}{\sqrt{a^2 + 4r^2\cos^2\bar{\theta}}}. \tag{1.16}$$

And the Fourier transform of $C_{\beta s}$ gives

$$C(q) = c_1 - e^{iqa}c_2. \tag{1.17}$$

Under PBC, because each site corresponds to one bond only, we have $N = N_b$, and the Maxwell Calladine index theorem tells us that $N_0 = N_s$. As a bond is cut to free the boundary the number of ZMs becomes $N_0 = N_s + 1$, therefore if there is no SSS in the system, there must be one ZM, which can either be a mode in the bulk or a surface mode on one of the boundaries. Since the compatibility matrix has only diagonal elements $\mathbf{C}_{11} = c_1$ and $\mathbf{C}_{22} = -c_2$, then the ratio $\lambda = c_1/c_2$ determines whether the surface state localizes on the left or the right boundary. In another word, the one zero modes is on the left if $|c_1| > |c_2|$ and on the right if $|c_1| < |c_2|$. Furthermore, the compatibility matrix $C(q) \equiv |C(q)|e^{i\phi}$ (or more generally its determinant) maps points in the Brillouin zone ($-\pi/a < q \leq \pi/a$) to a path in the complex plane, and since it depends on e^{iqa}, the path will be closed and will return to its starting point as q advances between equivalent points in the zone ($q \to q + (2\pi/a)$). These curves are characterized by an integer winding number:

$$n = \frac{1}{2\pi\mathrm{i}}\int_0^{2\pi} d\phi = \frac{1}{2\pi\mathrm{i}}\int_0^{2\pi/a} dq \frac{\mathrm{d}}{\mathrm{d}q}\,\mathrm{Im}\ln\det C(q), \tag{1.18}$$

which for the $C(q)$ in Eq. (1.17) is either $+1$ or 0, corresponding to the two cases of right or left boundary localization of the one surface ZM.

This formulation, although only shown in this 1D example, can be easily generalized to higher dimensions, and the more generic form of the topological winding numbers associated with each $\mathbf{q}_i$ is calculated as

$$n_i = \frac{1}{2\pi}\oint_{C_i} d\mathbf{q}\cdot\nabla_{\mathbf{q}}\phi(\mathbf{q}) = \frac{1}{2\pi\mathrm{i}}\oint_{C_i} d\mathbf{q}\cdot\mathrm{Tr}\left[\mathbf{Q}(\mathbf{q})^{-1}\nabla_{\mathbf{q}}\mathbf{Q}(\mathbf{q})\right], \tag{1.19}$$

where $\phi(\mathbf{q})$ is the phase of $\det\mathbf{Q}(\mathbf{q})$ ($\mathbf{Q}(\mathbf{q}) = |\mathbf{Q}(\mathbf{q})|e^{\mathrm{i}\phi(\mathbf{q})}$). Here C_i is a cycle of the Brillouin zone connecting $\mathbf{q}$ and $\mathbf{q}+\mathbf{B}_i$, where $\mathbf{B}_i$ is a primitive reciprocal vector satisfying $\mathbf{a}_i\cdot\mathbf{B}_j = 2\pi\delta_{ij}$. These winding numbers, combined with the primitive translation vectors $\mathbf{a}_i$, form a topological polarization vector

$$\mathbf{R}_T = \sum_i n_i\mathbf{a}_i, \tag{1.20}$$

which is a generalization of the 1D winding number, indicating the localization of the surface ZMs, and SSSs.

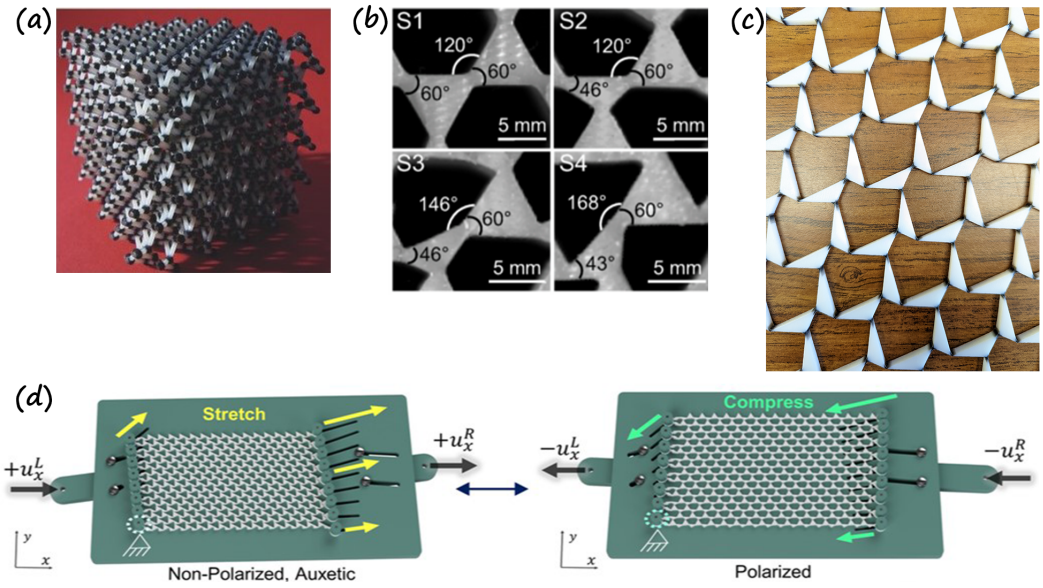

Figure 1.3: Examples of 3D-printed TMMs. (a) 3D-printed 3D topologically polarized specimen from Ref. [2]. (b) 2D kagome lattice TMMs fabricated from Shore 15A durometer silicone rubber in Ref. [3]. (c) A multi-material 3D-printed kagome lattice TMM using Stratasys Polyjet printer, also shown in Ref.[4]. (d) A PCLDA-SMP transformable topological metamaterial in its topologically polarized and unpolarized states from Ref. [5].

1.3.2 Experiments and engineering of TMMs

The investigation on mechanical topological states has started a wave of further research to create *Topological Mechanical Metamaterials* (TMMs), and this opened up opportunities for many potential applications as mentioned in Sec. 1.1, and an immediate step to take is the fabrication and engineering of TMMs. There have been multiple efforts made in the manufacturing of TMMs [3; 2; 28; 34; 5]. Especially, the current 3D printing technology has attracted attention as a potential candidate for a convenient and controllable manufacturing method [2; 3]. Some of the manufactured topological TMMs are shown in Fig. 1.3. It was soon realized that there are multiple factors interfering with the topological properties, such as buckling [15] and bending stiffness at the hinges [2; 3; 28; 34] that keep the TMMs away from the ideal spring limit. In the theoretical prediction of topological mechanics, due to the topologically protected polarization of boundary modes, a contrast in the boundary stiffness between the two boundaries on the opposite sides of the topological polarization with 3 orders of magnitude has been predicted [22], which has not been observed in the past experiments due to the non-ideality.

1.3.3 The Approximations in Ideal Spring-Mass Models

To see why we need to go beyond the limit of ideal springs even in the discrete model, we need to first see why the discrete model with ideal springs is needed and what limitations are in the ideal springs model. When modeling continuum elastic materials, the standard theory of elasticity is usually used [35]. It considers a continuous elastic body composed of infinitesimal points with positions $\vec{r}$. A displacement field $\vec{u} = \vec{r'} - \vec{r}$ is formed when deformation happens and the points $\vec{r}$ are moved to new positions $\vec{r'}$. And a strain tensor

$$u_{ik} = \frac{1}{2}\left(\frac{\partial u_i}{\partial x_k} + \frac{\partial u_k}{\partial x_i}\right) \tag{1.21}$$

can be written with the displacement field (to the linear order), representing the deformation between two neighboring points in the original and the deformed bodies, as the square of length change between two points before and after the deformation can be written as

$$dl'^2 - dl^2 = 2u_{ik}dx_i dx_k. \tag{1.22}$$

Furthermore, with the consideration of elastic energy, one can write a stress tensor $\sigma_{ik} = \frac{\partial E}{\partial u_{ik}}$ to break down the forces experienced by the infinitesimal elements due to the deformation. By assuming the elastic body to follow *Hooke's law*, which states that the deformation is proportional to the applied force when it's small, one can write down the stress tensor as

$$\sigma_{ik} = \frac{\partial E}{\partial u_{ik}} = C_{ijkl}u_{jl}, \tag{1.23}$$

where C_{ijkl} is the stiffness tensor representing the elastic moduli of the elastic body.

This continuum treatment for elastic solid bodies has been a great success in describing elastic deformations and their related mechanical properties, as well as the dynamics [36; 37]. However, the homogenization of the solid body ignores the microscopic structures, which are then captured by a discrete treatment of lattice formulations described in Sec. 1.2. Comparing between the continuous and discrete treatments of elastic media, the discrete treatment can only capture deformation larger than the scale of the springs connecting the sites, and it only concerns the length change of the springs. Thus, attention needs to be paid beyond this simplification, and I'll explore the physics it leads to. Specifically, the studies presented in this thesis include I). springs that take a different energy functional form, II). inclusion of rotational energy for the springs, III). a geometric design that makes the unit cells to be bistable, and IV). the regime where the deformation on the lattice is no longer small.

1.4 Outline of Chapters

With the introductions listed above on mechanical rigidity, mechanical topological states, and the current state of the art in the experiments and engineering of TMMs, I'll give an outline in the following chapters of this thesis.

In Chapter II, I take a closer look at the *Vertex Model* (VM), and a modified case of it named the *Active Tension Network* (ATN) model, for epithelial tissues. In these models, we discovered the unlikelihood of topologically polarized surface ZMs in the VM, and demonstrated the possibility of topological polarization showing up in the ATN model. In this model of "ring" springs, the cellular mechanical network is under an unusual geometry while the surface modes are topologically polarized. It could shed light on some of the edge phenomena during biological processes. This chapter is based on the work published in Soft Matter by Liu *et. al.* [38].

In Chapter III, I take a dive into the issue of bending stiffness, to see to what degree they interfere with the topological modes of the lattice, with a simple approach of using *angular springs* (AS), and a first-order approximation of the AS using the *next nearest neighbor* (NNN) springs. Furthermore, we relate and utilize the polarization of both the *nearest neighbor* (NN) lattice, to design a lattice that both lower the overall magnitude of both NN and NNN stresses, and homogenize the distribution of the NNN stresses. This reduces the bending stresses focused on the hinges, and thus is helpful for preventing hinge fracturing. On the other hand, by engineering the geometry, we demonstrate the ability to focus stress at domain walls against shearing as well, thus showing the opportunity to create metamaterials that respond to different given strains. This chapter is based on a manuscript in preparation by Liu *et. al.*

Chapter IV demonstrates an engineering approach to control the transformation of the Maxwell lattice between topological regimes by incorporating bi-stability into the unit cells. By making the unit cells have two energy-minimized configurations, one in the topologically polarized phase, while another in the topologically unpolarized phase, it is convenient to utilize the bi-stability to transform the Maxwell lattice between the two topologically distinct states. Furthermore, the Maxwell lattice formed by bi-stable unit cells has multiple stable configurations, thus it is possible to study the static interface formed between two topologically distinguished states, which is served as a first step toward the understanding of the interface that can form dynamically. The work shown in this chapter is based on the manuscript to PNAS by Xiu *et. al.* [39]. In which I have contributed on theoretical calculation, numerical simulation, and the additive manufacturing and experimental testing of the assembled continuum TMM as a second author. The finalized version in the publication may appear with more contexts than this Chapter.

In Chapter V, we take the deformation in the Maxwell lattice to a non-linear level and investigate the quasi-statically effect of non-linearity on the topological states. First, for topologically

polarized Maxwell lattices, an asymmetric response is observed depending on the boundary in which a sinusoidal wave is prescribed. When the input wave is at the hard boundary, it does not travel far before the amplitude exponentially grows to the extent that the lattice breaks, but when it is at the soft boundary, the well-known effects from non-linearity such as harmonic generation, and amplification enhanced frequency conversion. Furthermore, we observe that, under a strongly non-linear situation, a solitary wave appears in the system, thus by mapping one of the spatial components as a temporal component, we map the system as a non-Hermitian realized using only spatial elements, which in the future may facilitate the experimental realization of non-Hermitian systems. This chapter is based on the work submitted to PNAS by Xiu *et. al.* [4]. In which I have contributed on the theoretical derivation and numerical simulation as a co-first author.

Finally, in Chapter VI, I give a summary of the works I present in the thesis, and to conclude, I discuss the future directions that one can do to extend the topics mentioned, as well as other forms of non-ideality of the springs one that may be important.

CHAPTER 2

Epithelial Tissue Network Model as a Maxwell System

This chapter summarizes the published work *"Topological Floppy Modes in Models of Epithelial Tissues" Soft Matter, 2021,17, 8624-8641* co-authored by Harry Liu, Di Zhou, Leyou Zhang, David Lubensky, and Xiaoming Mao.

2.1 Introduction

The mechanics of epithelial tissues, where living cells closely pack a surface and mechanically interact with one another, is crucial for many morphogenetic processes, such as gastrulation, wound healing, embryogenesis, etc. [40; 41; 42; 43; 44; 45]. These processes can require particular cellular arrangements that are associated with specific mechanical properties, which have been studied intensely through analyses of the stresses and strains on the epithelial network [46; 47; 48; 49; 50; 51; 52]. The relation between structure and mechanics in epithelial tissues not only offers a gateway for a deeper understanding of many of these natural processes but also opens possible paths to engineer potentially beneficial synthetic processes. In particular, boundaries and interfaces often play crucial roles in the mechanics of epithelial tissues, because they offer a platform where the dynamics of cells are most rich. A thorough understanding of the mechanics on the boundaries and interfaces would be very helpful to characterize these phenomena.

Recent advances in theories of topological mechanics provide a fundamental framework for understanding mechanics on boundaries and interfaces of *marginally stable* (i.e.,"Maxwell") networks and how these mechanical properties are robustly controlled by topological features in the bulk [1; 30; 53]. Many designs have been proposed utilizing topologically protected mechanical properties to produce novel cellular topological mechanical metamaterials with unusual properties such as reconfigurable surface stiffness, stress distribution, and localized modes [14; 15; 16; 54].

Interestingly, epithelial tissues often operate at or near the verge of mechanical instability [10; 11; 12; 13], as they are then able both to support stress and to accommodate transformations during various biological processes. Moreover, it has recently been shown that topological floppy boundary modes can show up in disordered biopolymer networks when excited by active driving [19]. It is thus interesting to ask whether topological mechanical properties on boundaries and interfaces can also arise in epithelial tissues.

In this paper, we study topological mechanics in epithelial tissue sheets based on two models, namely a simple (passive) VM and an active tension network (ATN) model [55; 56]. We adapt these models so as to put them at the Maxwell condition where the number of degrees of freedom is equal to the number of constraints. This condition is crucial for topological polarization to appear. We observe that in the ATN topologically polarized phases exist and that these phases only arise when cells become concave. This is based on the observation that topological phase transitions in these models can only occur when edges of cells form straight lines, which leads to gap closing and only happens at the onset of convexity change. We cannot, though, exclude the possibility of topological polarization via the creation and annhilation of Weyl points in the convex configuration.

This topological polarization indicates exponentially localized floppy modes and states of self-stress on boundaries and interfaces of the system. Mechanically, boundaries and interfaces with exponentially localized floppy modes are much softer in comparison to other parts of the tissue. In contrast, if a boundary does not have exponentially localized floppy modes, it would appear as rigid as the interior of the tissue. On the other hand, interfaces in the tissue with exponentially localized states of self-stress tend to accumulate both external stress and internal stress from cell activity. These properties are solely owing to the cell geometry of the *bulk* of the tissue, instead of to special cell activities at the boundary or interface. This is a manifestation of the "topological protection" of these floppy modes and states of self-stress, which endows the aforementioned phenomena with remarkable robustness: any weak interactions or slight changes in the geometry, as long as they do not change the topological phase of the bulk of the tissue, will not destroy the boundary and interface mechanical response.

These topological mechanical properties may lead to interesting behaviors such as robust localization of dynamics or stress. It would be of interest to study how these topological properties relate to phenomena involving tissue boundary/interface dynamics, such as dorsal closure [57; 58] and invasion of larval tissue by histoblast nests [59; 60] in *Drosophila*, epiboly in teleost fish [61], and collective migration and wound healing in a variety of *in vitro* and *in vivo* systems [62; 63].

2.2 The Models

In their simplest form, epithelial tissues comprise a monolayer of adjacent cells, which can often be approximated by polygons. Thus, the mechanics of an epithelial tissue can be analyzed by studying a two-dimensional sheet of edge-sharing polygons. A variety of variants on the basic theme of a vertex model, in which the degrees of freedom are the positions of the polygon vertices, have been proposed and can explain many observations of mechanical phenomena in epithelial tissues [9; 64; 65; 10; 66; 67; 68; 69; 70]. These include both passive models in which cell shapes are assumed to be governed by an (effective) energy and extensions that explicitly account for various active processes in living tissues. Here, we reserve the term vertex model (VM) for a particular, common choice of a passive energy described below in Sec. 2.2.1. We also consider an interesting example of an active model, the active tension network (ATN) model, where mechanical equilibrium is attained when both force balance at each vertex and the "stall tension" on each edge are reached, with the result that the tension on each edge can effectively be specified independently (subject to force balance constraints).

In this section, we first briefly introduce the VM and the ATN to analyze the counting of the degrees of freedom and constraints in them. We then discuss the conditions under which these models become "Maxwell networks", meaning that they have balanced degrees of freedom and constraints, providing the right condition for topological floppy modes to arise. We also determine the force-balance conditions for these models, the equilibrium states of which are both stressed.

2.2.1 Models of epithelial cell sheets

In the remainder of this paper, we consider tissue sheets parameterized by a set of vertex coordinates $\{\vec{R}_i\}$. We use the term VM specifically to refer to a model where the dynamics of these coordinates is assumed to be governed by a mechanical energy with the form [9]

$$E = \frac{1}{2}\sum_f \left[K_P(P_f - P_0)^2 + K_A(A_f - A_0)^2\right], \tag{2.1}$$

where K_P is the elastic constant of cortical tension that constrains the perimeter of cells, and K_A is an area elastic constant that could arise, for example, from an interplay between cell incompressibility in 3D and resistance to cell height differences across the tissue. The sum is over all cells in the tissue, which are labeled by f and have perimeter P_f and area A_f.

Tissues governed by the energy of Eq. (2.1) have been shown to exhibit a jammed phase, where any displacements of vertices cost elastic energy and the system develops a shear modulus, when the ratio $P_0/\sqrt{A_0}$ drops below a critical value [10]. In this jammed phase, the tissue is stabilized

by an equilibrium tension, as we discuss below in the constraint counting.

In the ATN, instead of a passive tension that attempts to restore a preferred perimeter in each cell, the edges are active and try to reach a preferred "stall tension", determined by the local activity of the actomyosin bundle along the edge and cadherin clusters between the cells. Mechanical equilibrium of the tissue is reached when forces balance at each vertex and each edge is at its stall tension. Ref. [56] introduced a relaxational dynamics that specifies how the myosin concentration and the tension on each edge evolve towards this equilibrium state. To study topological modes, however, we are only interested in small displacements from mechanical equilibrium. In this case, we may treat the edge tensions as constants, corresponding to the long-time, elastic-like behavior of the tissue. A similar limit was taken in Ref. [56] in the discussion of the "isogonal" soft modes.

Thus, for the purposes of this paper an ATN is simply a model in which each edge is endowed with a fixed tension T_{ij} (where i and j denote the two vertices joined by the edge) and each cell has a pressure $\Pi_f = 2K_A(A_f - A_0)$ conjugate to its area. The T_{ij}'s and Π_f's must be chosen so that the net force on each vertex vanishes when the vertices are at their equilibrium positions but are otherwise arbitrary. The model can then be viewed as having an effective energy whose differential for small vertex displacements from mechanical equilibrium is given by

$$dE[\{\mathbf{r}_i\}] = \sum_{\langle i,j \rangle} T_{ij} dR_{ij} + \sum_f \Pi_f dA_f \tag{2.2}$$

where $R_{ij} = |\vec{R}_i - \vec{R}_j|$ is the distance between these two vertices.

2.2.2 Mechanical stability and Maxwell's counting

In order to analyze topological mechanics in the VM and the ATN, we need to first count the degrees of freedom and constraints in these models and identify the "Maxwell condition" where the balance of degrees of freedom and constraints is met. This condition puts the system at the verge of mechanical instability, allowing unusual topologically protected modes to arise [1; 53].

For both models, deviations from a mechanically balanced state can be described by the displacement field of the vertices $\{\vec{u}_i\} = (u_1^x, u_1^y, \cdots, u_V^x, u_V^y)$ for all V vertices. Thus, each vertex i displaces from its mechanical equilibrium state $\vec{r}_i$ to a new position $\vec{r}_i \to \vec{R}_i = \vec{r}_i + \vec{u}_i$.

We now consider what constraints a displacement field in each model must satisfy to be a zero mode (ZM) that costs no elastic energy ($dE = 0$). In both the VM and the ATN, the mechanical equilibrium states we expand around are *stressed*, which means edges bear nonzero tension. As we derive in more detail in App. 2.5.1, this results in an "irrotational" constraint from each stressed edge,

$$(\vec{u}_i - \vec{u}_j) \times \hat{l}_{ij} = 0, \tag{2.3}$$

where i, j denote the two vertices connected by this edge, and $\hat{l}_{ij} = (\vec{r}_j - \vec{r}_i)/|\vec{r}_j - \vec{r}_i|$ is the unit vector pointing from vertex i to j in the equilibrium state.

The area term of each cell contributes a constraint that the cell area needs to be preserved by any ZM (for details see App. 2.5.1). To set up the notation, we consider a cell with V_f vertices labeled as $i = 1, \ldots, V_f$, and $\vec{\mathcal{U}}_i = \vec{u}_{i+1} - \vec{u}_i$ being the relative displacement between the neighboring sites. We use $\vec{\mathcal{L}}_i = \vec{r}_{i+1} - \vec{r}_i$ to denote the vector connecting the two vertices in the equilibrium state we expand around. The constraint that the area is preserved can then be written as

$$\sum_{i=1}^{V_f-1} \sum_{j>i}^{V_f-1} \left(\vec{\mathcal{U}}_{i+1} \times \vec{\mathcal{L}}_i - \vec{\mathcal{U}}_i \times \vec{\mathcal{L}}_{i+1} \right) = 0. \tag{2.4}$$

These two constraints [Eqs. (2.3, 2.4)] are the same between the VM and the ATN. The VM has an additional term which preserves the perimeter of each cell,

$$\sum_{i}^{V_f} \vec{\mathcal{U}}_i \cdot \hat{l}_{i,i+1} = 0. \tag{2.5}$$

Therefore, the number of constraints in the VM is $N_C = 2F + E$, where F is the number of cells and E is the number of edges in the network. This follows from the fact that each cell provides a constant perimeter and a constant area constraint, and each edge provides a no-rotation constraint because it's stressed. In contrast, in the ATN the number of constraints is $N_C = F + E$, as the cell perimeter does not need to be conserved for ZMs.

The number of degrees of freedom is $N_{DOF} = 2V$ in both models, because two coordinates are required to specify the position of each vertex in two dimensions. Assuming that all vertices have coordination number $z = 3$ (3 edges meet at each vertex, which is natural for polygonal tilings), we have $E = zV/2 = 3V/2$. Using Euler's characteristics [71] we have $F = E - V = V/2$. Therefore, the total number of constraints on the VM including the area constraint is $N_C = 5V/2 > N_{DOF}$ and the model is over-constrained in the presence of stress. The numbers of constraints and of degrees of freedom become equal when the area constraint is neglected, leading to $N_C = 2V = N_{DOF}$, making the system a Maxwell network.

On the other hand, the ATN is a Maxwell network with the area constraint included, as in this case, $N_C = F + E = 2V = N_{DOF}$.

As we mentioned above, our choice of the elastic energy terms for these models is guided by the requirement of placing the models at the Maxwell point, so that topological modes are permitted. Thus, for the VM we henceforth consider only the limit that the cortical tension of the cells is the dominant contribution to the energy, i.e. $K_A \to 0$. That is, we drop the area elasticity contribution, or, equivalently, assume that pressure differences between cells are negligible. This limit has been

considered in several previous studies on this model [10; 11; 12; 56]. In contrast, for the ATN, we consider the generic case where pressure differences between cells may be significant and the area contribution cannot be ignored.

We emphasize that all of these choices are made solely in order to place the two models at the Maxwell point, where topologically protected zero modes are possible. In particular, we do not claim that these particular limits have any special biophysical importance *a priori*; rather, under these necessary criteria for Maxwell lattices, we are interested in whether or not the VM and ATN have unusual topological properties that might be of biological interest. Importantly, Refs. [72; 73; 74] show that small deviations from these ideal limits through the inclusion of weak additional terms in the energy (e.g., adding back the area term in the VM or introducing deviations from fixed tensions in the ATN) preserve the topological polarization, and only weakly lift the energy of the ZMs. Thus, we expect that our qualitative conclusions will continue to hold in the vicinity of the Maxwell point.

The counting argument we give here for the VM is consistent with that provided by Bi and Yan [12]. Their count $N_C = (E - E_0) + F$, where E_0 is the number of edges without tension, includes contributions from each tensioned edge and from each face. In our case, the energy expansion is done around a pre-stressed network where every edge carries a tension, so that $E_0 = 0$, our constraint count $N_C = E + F$ then matches that in [12].

The Maxwell-Calladine index theorem asserts that in a mechanical network, the difference between the number of ZMs and the number of states of self-stress (SSSs, i.e., eigenmodes of the stress distribution leaving all components of a network in force balance) is given by the difference between the numbers of degrees of freedom and of constraints [29; 1; 30],

$$N_{ZM} - N_{SSS} = N_{DOF} - N_C. \tag{2.6}$$

Thus, if a network is Maxwell (defined as $N_{DOF} = N_C$ in the bulk, i.e. neglecting any boundary effects), it must have equal numbers of ZMs and SSSs in the bulk. This condition means that an infinite Maxwell lattice has no ZMs unless there are SSSs. For a finite sized system under open boundary conditions, however, a subextensive number of ZMs arise due to the removed constraints on the boundary. Whether these ZMs are localized or extensive, and where they localize, is a topologically protected property, characterized by a topological winding number [1]. The topological state, in turn, is determined by the architecture of the tissue network, i.e., by the angles and lengths of the edges.

It is worth emphasizing that these counting arguments are done in a stressed equilibrium state in both models. This is different from most current models of topological mechanics. If there were no stress, the no-rotation constraints associated with the edges would be lifted, and the tissue

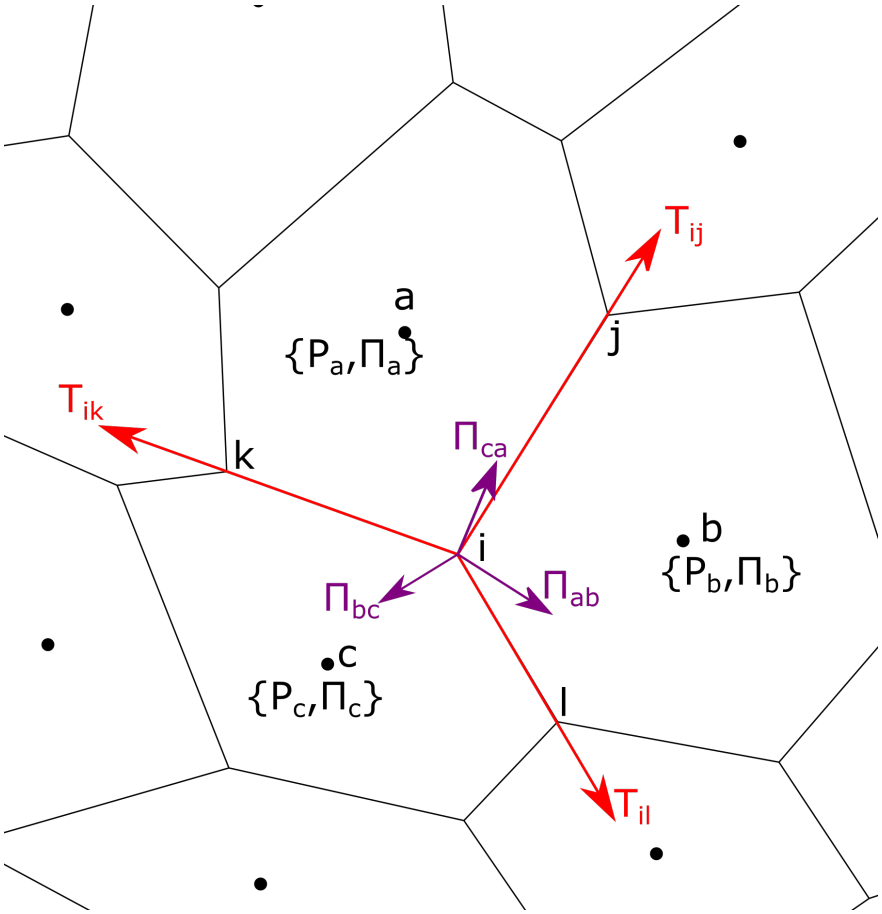

Figure 2.1: A schematic of the variables used in the force-balance condition Eq. (2.7,2.10). The forces on vertex i caused by the tension on the edges are shown as red arrows, and the forces due to the pressure of the cells are shown as purple arrows.

would be under-constrained, with an extensive number of floppy modes.

2.2.3 Force-balance condition

The fact that the force equilibrium states in both the VM and the ATN are stressed requires that any choice of the state we choose to expand around, and study topological modes, needs to satisfy force balance.

The force balance condition can be derived by requiring $O(\vec{u})$ terms in the elastic energy to vanish [Eq. (2.1) for the VM and Eq. (2.2) for the ATN]. As we derive in detail in App. 2.5.1, for the VM, after dropping area terms, this condition takes the form

$$T_{ij}\hat{l}_{ij} + T_{ik}\hat{l}_{ik} + T_{il}\hat{l}_{il} = 0, \tag{2.7}$$

for each site i, where as we defined above, $\hat{l}_{ij}, \hat{l}_{ik}, \hat{l}_{il}$ are the edge directions from vertex i to vertices j, k, l, which are the nearest neighbors of i. In addition,

$$T_{ij} = T_a + T_b, \quad T_{ik} = T_a + T_c, \quad T_{il} = T_b + T_c, \tag{2.8}$$

are the tensions on the edges ij, ik, il respectively, originating from the cortical tension T_a, T_b, T_c from the cells a, b, c. The cortical tension of a cell f can be calculated as

$$T_f = \frac{\partial E_f}{\partial P_f} \tag{2.9}$$

for the VM.

In the ATN, as we discussed above, the Maxwell condition is satisfied when the area term is included, so the force balance condition on vertex i is given by

$$\begin{aligned} &T_{ij}\hat{l}_{ij} + T_{ik}\hat{l}_{ik} + T_{il}\hat{l}_{il} \\ &+ \frac{1}{2}\Pi_{ab}\hat{n}_{ab}l_{ij} + \frac{1}{2}\Pi_{bc}\hat{n}_{bc}l_{il} + \frac{1}{2}\Pi_{ca}\hat{n}_{ca}l_{ik} = 0 \end{aligned} \tag{2.10}$$

where $\Pi_{ab} = \Pi_a - \Pi_b$, $\Pi_{bc} = \Pi_b - \Pi_c$, $\Pi_{ca} = \Pi_c - \Pi_a$ are the differences of pressures Π_a, Π_b, Π_c of cells a, b, c respectively. The pressure differences exert effective forces on the vertices because the vertex positions are the only degrees of freedom in the vertex model. Thus, all terms in the energy, including the terms involving cell area that give rise to the pressures, must translate into forces on the vertices. Physically, one can think of these forces on the vertices as arising from a pressure difference that acts at each point along an edge, giving rise to a net force $\Pi_{ab}\hat{n}_{ab}l_{ij}$ on edge ij after integration along the edge. This force tries to move the edge perpendicular to itself; as the position of the edge is completely specified by the positions of the two vertices at its ends, this is equivalent to exerting the force on each vertex given in Eq. (2.10). $\hat{n}_{ab}$, $\hat{n}_{ca}$, $\hat{n}_{bc}$ are the unit vectors normal to edge ij of length l_{ij} pointing from cell a to cell b, edge ik of length l_{ik} pointing from cell c to cell a, and edge il of length l_{il} pointing from cell b to cell c respectively, as shown in Fig. 2.1. The 3 terms in the second row of Eq. (2.10) represent the force on the vertex that comes from the pressure difference of the 3 adjacent cells.

It is worth noting that the tensions T_{ij}, T_{ik}, T_{il} in the ATN are independent variables for each edge, unlike the tensions in the VM which are related to one another via Eq. (2.8).

To summarize, the two main differences between the VM and the ATN, regarding mechanics around an equilibrium state, are that (i) the perimeter does not need to remain constant for ZMs in the ATN—the edges adjust to their preferred tensions instead of returning to the preferred perimeter, and thus the area term is included in order to bring the model to the Maxwell condition, and

(ii) tensions on edges in the ATN are independent on each edge, rather than determined by cortical tensions which are variables associated with cells. As we can see in the next section, we find this condition important in allowing the system to become topologically polarized, in the cases we studied.

2.3 Topological mechanics

In this section we investigate topological mechanics in the VM and the ATN and discuss a phase diagram of the ATN showing where topologically polarized phases arise as a function of the architecture of the cell sheet.

2.3.1 Compatibility and equilibrium matrices

The compatibility (C) and equilibrium ($\mathbf{Q}$) matrices are the starting point to describe topological mechanics in Maxwell networks. In simple ball-and-spring networks, these matrices map between degrees of freedom space and constraints space, and their null spaces give ZMs and SSSs, respectively [1].

For an epithelial cell sheet, the compatibility and equilibrium matrices need to be generalized to describe the constraints that are more complicated in nature compared to simple ball-and-spring networks.

For the VM, as we discussed above, the constraints come from the no-rotation condition of each edge and the perimeter of each cell, so the matrix is given by

$$\mathbf{C} \cdot u = \begin{pmatrix} e^{\perp} \\ \Delta P \end{pmatrix} \tag{2.11}$$

whereas the mapping by the $\mathbf{Q}$ matrix is such that

$$\mathbf{Q} \cdot \begin{pmatrix} t^{\perp} \\ T_P \end{pmatrix} = f \tag{2.12}$$

where $e^{\perp}$ and $t^{\perp}$ are E-dimensional vectors of transverse motion (i.e., rotation) of and force on all the edges, ΔP and T_p are F-dimensional vectors of the changes of perimeters and cortical tensions of all the cells, u and f are $2V$-dimensional vectors of the displacements of and forces on the vertices. Because $F + E = 2V$, both $\mathbf{C}$ and $\mathbf{Q}$ are $2V \times 2V$ dimensional square matrices.

It may appear confusing to see transverse forces $t^{\perp}$ on edges, whereas in the elastic energy the edges just bear cortical tension. A way to understand it is that we are expanding around a

stressed state, where the edges already carry an equilibrium stress T. Displacements of vertices cause rotation of edges $e^{\perp}$ which leads to a *transverse change* to the tensions, which is $t^{\perp}$. This change of tension is perpendicular to the *edge direction in the reference state*, making it $t^{\perp}$, but the total tension is along the displaced edge direction. Thus, $t^{\perp}$ is allowed to exist as a state of self-stress.

In the ATN, the $\mathbf{C}$ and $\mathbf{Q}$ matrices are similar to that of the VM, except that the cortical tension is replaced by an area constraint,

$$\mathbf{C} \cdot u = \begin{pmatrix} e^{\perp} \\ \Delta A \end{pmatrix}, \tag{2.13}$$

$$\mathbf{Q} \cdot \begin{pmatrix} t^{\perp} \\ \Pi \end{pmatrix} = f, \tag{2.14}$$

where ΔA and Π are F dimensional vectors of changes of area and pressure of all the cells.

In both models, similar to the ball-and-spring network models, we have $\mathbf{C} = \mathbf{Q}^T$. In the VM, because the elastic energy is conserved, a dynamical matrix can be defined as

$$\mathbf{D} = \mathbf{QKC}, \tag{2.15}$$

which gives the quadratic expansion of energy around the equilibrium state, and $\mathbf{K}$ is a diagonal matrix includes the values of transverse spring constants $k^{\perp}$ (which comes from tensions on the edges as we show in App. 2.5.1) and the elastic constant of cortical tensions K_P as the diagonal entries for the VM, but the entries for the ATN would be the transverse spring constants $k^{\perp}$ and the area elastic constant K_A. As we discuss below, the actual spring constants are not important for the topological mechanics of these epithelial tissue models (as long as $\mathbf{K}$ is positive definite), as topological mechanics is primarily concerned with topologically protected ZMs and SSSs.

$$E = \frac{1}{2} u \cdot \mathbf{D} \cdot u. \tag{2.16}$$

This conserved elastic energy is not required for our discussions of topological modes.

The null-space of the $\mathbf{C}$ matrix and the $\mathbf{Q}$ matrix give ZMs and SSSs, similar to what happens in regular spring-and-mass networks. In particular, ZMs in the VM are vertex displacements that cause no rotation for the edges and no change in the perimeter of the cells, whereas ZMs in the ATN are vertex displacements that cause no rotation for the edges and no change in the area for the cells. On the other hand, SSSs in the VM are eigenmodes of transverse forces on edges and cortical tensions on cells that leave no net force on any vertices, whereas SSSs in the ATN in this model are eigenmodes of transverse forces on edges and pressure on cells that leave no net force on any vertices.

It is worth noting that these matrices are determined by the $O(u^2)$ terms in the expansion of the elastic energy, as we discussed in Sec. 2.2.2 and App. 2.5.1. The $O(u)$ terms vanish when we expand around an equilibrium reference state, and lead to the force-balance condition, as discussed in Sec. 2.2.3. These $O(u)$ terms do not affect the topological mechanics of the sheet. Instead, they determine what type of reference states are allowed.

2.3.2 Periodic epithelial sheets and topological polarization

To explore topological mechanics in epithelial sheets, we first start from periodic lattices, for convenient analysis of topological states in momentum space. Specifically, we consider the network topology of the tissue to be a honeycomb lattice, i.e., each cell has 6 edges and 3 edges meet at each vertex. Real epithelial tissue can vary both in terms of the number of edges per cell, and the number of edges meeting at a vertex, but we start from this simple model for our analysis of topological mechanics. In particular, we allow the shape of the cells to deviate from a regular hexagon to tune the geometry of the network and introduce topological phases.

Specifically, we focus on the case where each unit cell of the periodic lattice contains two epithelial cells, because inversion symmetry is always preserved if we only have one epithelial cell in the unit cell, and the tissue then cannot have a topologically polarized phase [1].

In this 2-cell unit cell, we have 4 vertices at coordinates $s_1 = (0, 0)$, $s_2 = (1.5, 0)$, $s_3 = (0, \sqrt{3})$, $s_4 = (1.5, \sqrt{3})$ for the critical configuration described in the next section and 6 edges in the basis, and the network is constructed following an oblique Bravais lattice with primitive vectors $\vec{a}_1 = (\frac{3}{2}, \frac{\sqrt{3}}{2}), \vec{a}_2 = (0, 2\sqrt{3})$. The number of degree of freedom per unit cell $n_{DOF} = 8$, and the number of constraints per unit cell $n_C = 6 + 2 = n_{DOF}$ where the 6 represents the 6 no-rotation constraints from the 6 edges, and 2 represents the constraints associated with the two faces (perimeter for the VM and area for the ATN).

To construct the compatibility matrix, we start from the ZM conditions discussed in Sec. 2.2.2, namely, Eqs. (2.3, 2.5) for the VM, and Eqs. (2.3, 2.4) for the ATN. Using these conditions, we can construct compatibility matrices $C(\mathbf{q})$ in momentum space that satisfy the mapping described in Eq. (2.11) for the VM and Eq. (2.13) for the ATN. The null space of these compatibility matrices give the ZMs of these models. The details of the compatibility matrix are given in the App. 2.5.2.

The topological polarization can then be determined from these compatibility matrices, via the calculation of the winding numbers of $\det C(\mathbf{q})$ around the first Brillouin zone [1],

$$\mathcal{N}_i = \frac{1}{2\pi} \oint_{C_i} d\mathbf{q} \cdot \nabla_{\mathbf{q}} \operatorname{Im} \ln \det C(\mathbf{q}), \tag{2.17}$$

where the two paths C_1, C_2 wrap the first Brillouin zone along the two reciprocal vectors $\vec{b}_1, \vec{b}_2$.

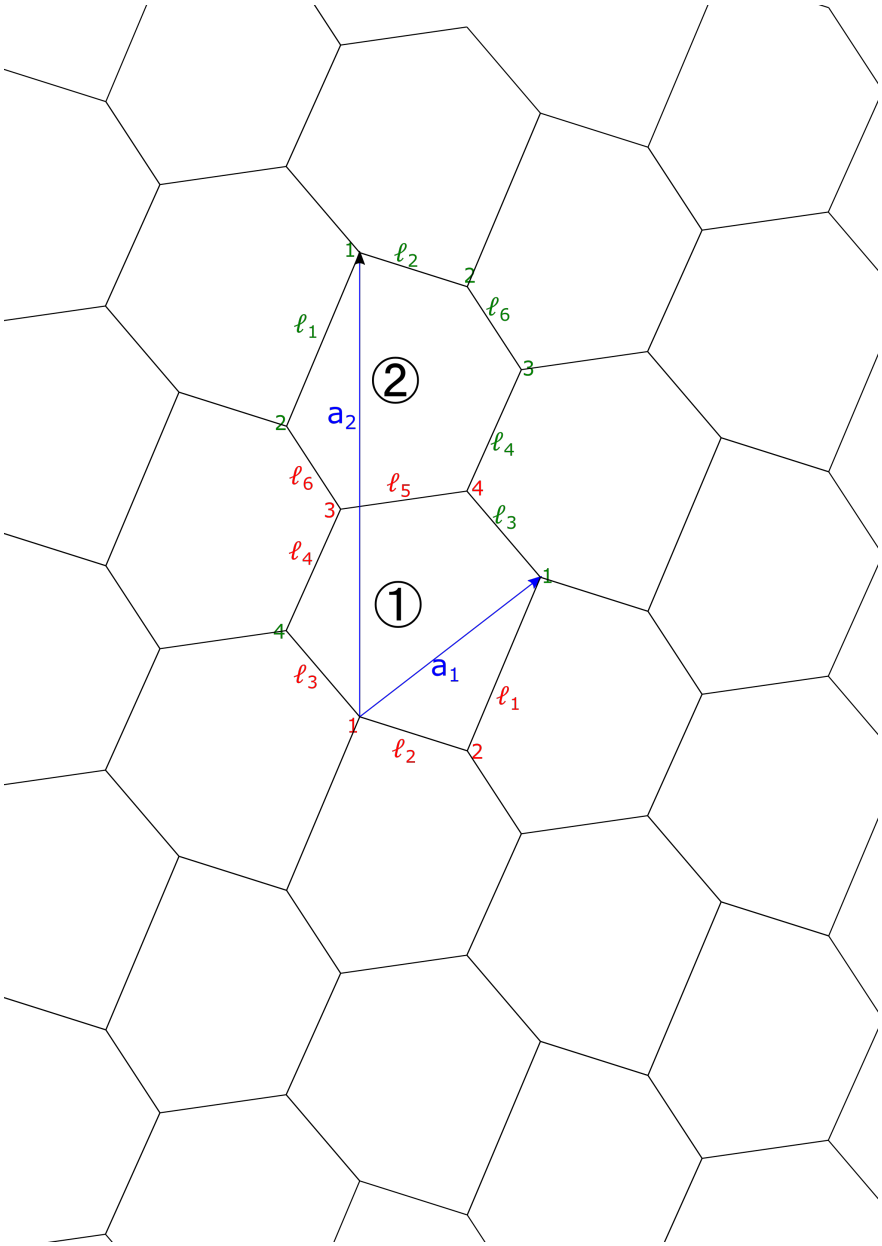

Figure 2.2: An epithelial tissue sheet taking a periodic lattice structure with two cells ① and ② per unit cell. The basis contains 4 vertices and 6 edges as labeled in red. The primitive vectors $\vec{a_i}$ are labeled in blue. The same vertices and edges that are translated according to the primitive vectors are labeled in green.

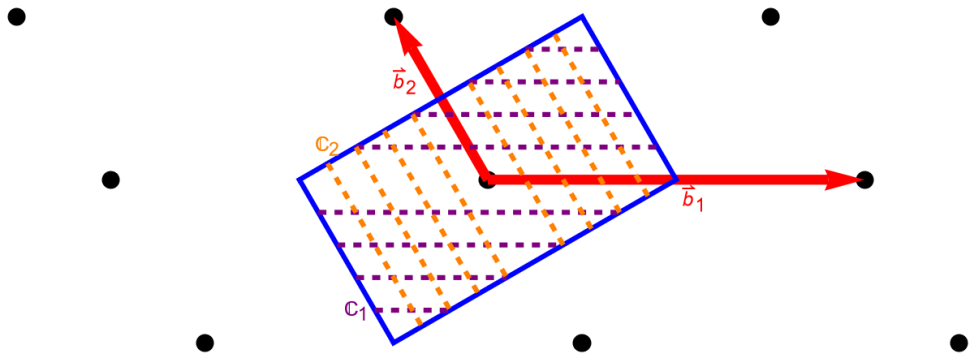

Figure 2.3: A representation of the first Brillouin zone and the contours C_1, C_2 taken for the integral in Eq. (2.17). The black dots are the reciprocal lattice sites, the red arrows are the reciprocal lattice vectors $\vec{b}_1, \vec{b}_2$, and the region enclosed by the blue lines is the 1^{st} Brillouin zone. The representation of paths of direction C_1 are labeled with the dashed purple lines and the paths of direction C_2 are labeled with the dashed orange lines. The reason we take multiple contours along each direction is that we need to identify potential changes of topological winding numbers across different contours along the same direction to identify the existence of Weyl points.

And a representation of the contour is shown in Fig. 2.3. A topological polarization can then be defined

$$\vec{R}_T = -\sum_i n_i \vec{a}_i, \tag{2.18}$$

where $\vec{a}_i$ are the 2 primitive vectors. Here the two integers (n_1, n_2) are related to the two winding numbers calculated above by a constant shift, $n_i = \mathcal{N}_i + \Delta_i$, that accounts for the asymmetry of the choice of the unit cell (the "gauge degree of freedom" as discussed in Ref. [1]), such that $\vec{R}_T$ provides a symmetric description of the polarization. For the choice of unit cell we use, as described in Fig. 2.2, $(\Delta_1, \Delta_2) = (2, -1)$. This is chosen such that the unpolarized case has $\vec{R}_T = 0$.

2.3.3 Critical configurations

We start our analysis of topological phases in these lattices by identifying critical configurations where ZMs are bulk modes. These critical configurations are analogous to the regular square and kagome lattices [53], and the Mikado model with straight fibers [19], where ZMs (other than trivial translations) arise under periodic boundary conditions (PBC).

These critical configurations are vital points to construct a phase diagram for topological boundary modes in these problems. This can be seen from the Maxwell-Calladine index theorem [Eq. (2.6)]. Under PBC, Maxwell system have $N_{DOF} = N_C$ so in general there are no ZMs or SSSs except for the trivial translations. When lattices are at geometric singularities (i.e. critical

configurations), such as bonds forming straight lines, additional SSSs arise under PBC, leading to additional ZMs, because $N_{ZM} - N_{SSS} = 0$ is always satisfied. These ZMs and SSSs are *bulk modes* as opposed to boundary modes, as they satisfy PBC.

Similarly, the VM and the ATN also develop these SSS-ZM pairs under PBC when edges of the cells form straight lines. There are two such critical configurations in the 2-cell unit cell lattice, as shown in Fig. 2.4, and they give rise to bulk ZMs. In these critical configurations, edges in these straight lines can carry equal $t^{\perp}$ which are balanced on all nodes, giving rise to SSSs. The corresponding ZMs are shown in Fig. 2.4, where cells in each straight vertical "strip" shift relative to one another, leaving all edges parallel to their original direction. These ZMs preserve all edge directions, perimeter, and area, so they are ZMs in both the VM and the ATN. Our lattices yield these two types of critical configuration because of our choice of the 2-cell unit cells. Other critical configurations involving wider strips can also arise when one chooses bigger unit cells. Columnar structures of this type are seen in a variety of epithelial tissues [69; 75; 76; 77; 78; 79; 80; 81].

At these critical configurations, the lowest phonon band has $\omega = 0$ lines due to these bulk ZMs, and the momentum space $\omega = 0$ lines are perpendicular to these straight lines in the real-space lattice. The $\omega = 0$ lines of the critical configurations of different straight line directions are shown in Fig. 2.6 (f) and Fig. 2.10 (d). As a result, the topological winding number [Eq. (2.17)] is ill-defined at these critical configurations. The system becomes gapped when the geometry is perturbed, leading to phases with different topological polarizations, as we discuss below.

2.3.4 Polarized Phases

In order to search for topologically polarized phases, we choose to study geometries of cell sheets perturbed around the critical configuration in Fig. 2.4(a) where straight lines of edges form along the $\vec{a}_2$ direction, as it is a simple geometry with high symmetries. In this analysis we find topologically polarized phases in the ATN, which we discuss below. Due to fewer free parameters in choosing force-balanced reference states, the VM does not show any topologically polarized phases. We will comment on this at the end of this section.

To construct a phase diagram for the ATN, we place vertex number 2 (as labeled in Fig. 2.2) at different positions, which breaks the straight lines and lift the bulk ZM-SSS pairs. At each given displacement (x_1, x_2) of vertex number 2 [from the critical state Fig. 2.4(a)], we define a new lattice (which is a distinct reference state), and calculate winding numbers using Eq. (2.17). The result is shown in Fig. 2.5. The phase diagram around critical configuration in Fig. 2.4(b) is included in the App. 2.5.3.

A few interesting features arise in this phase diagram. First, as vertex number 2 moves vertically along the straight lines, the system stays critical, as the bulk modes of shifting cells vertically

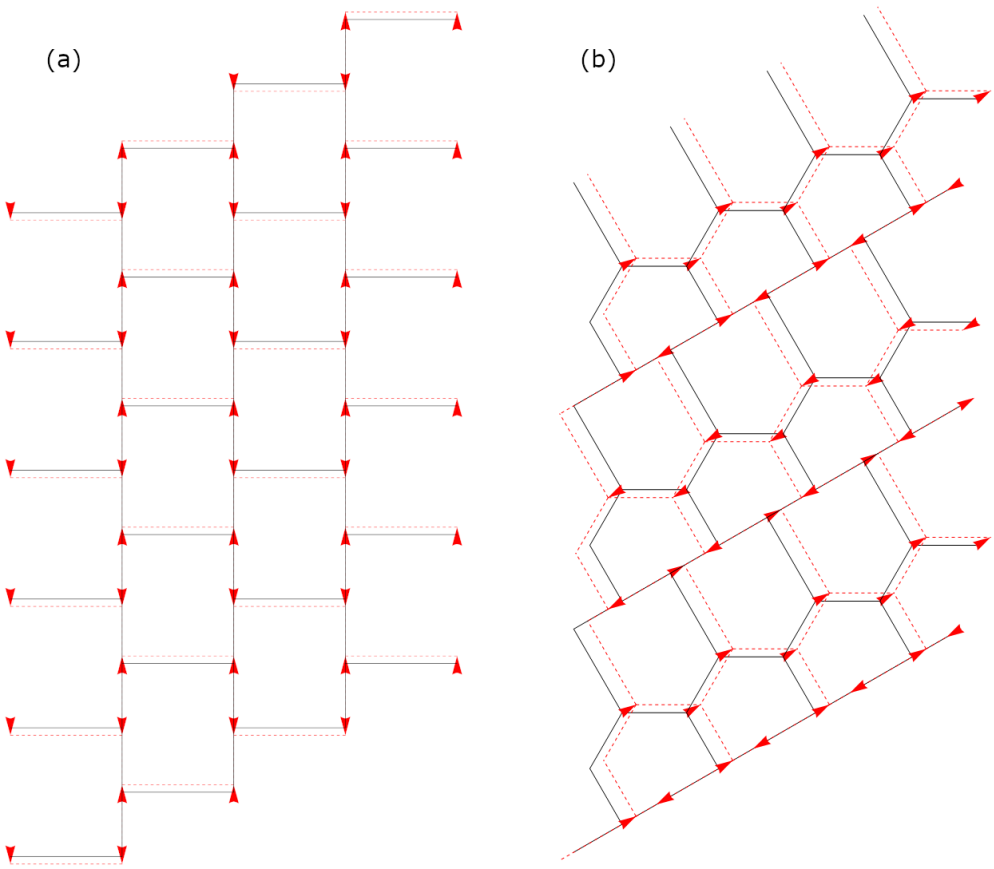

Figure 2.4: Critical configurations with edges of cells forming straight lines along $\vec{a}_2$ (a) and $\vec{a}_1$ (b). Examples of bulk ZMs in these configurations are shown with red arrows (vertex displacements) and dashed lines (deformed configurations).

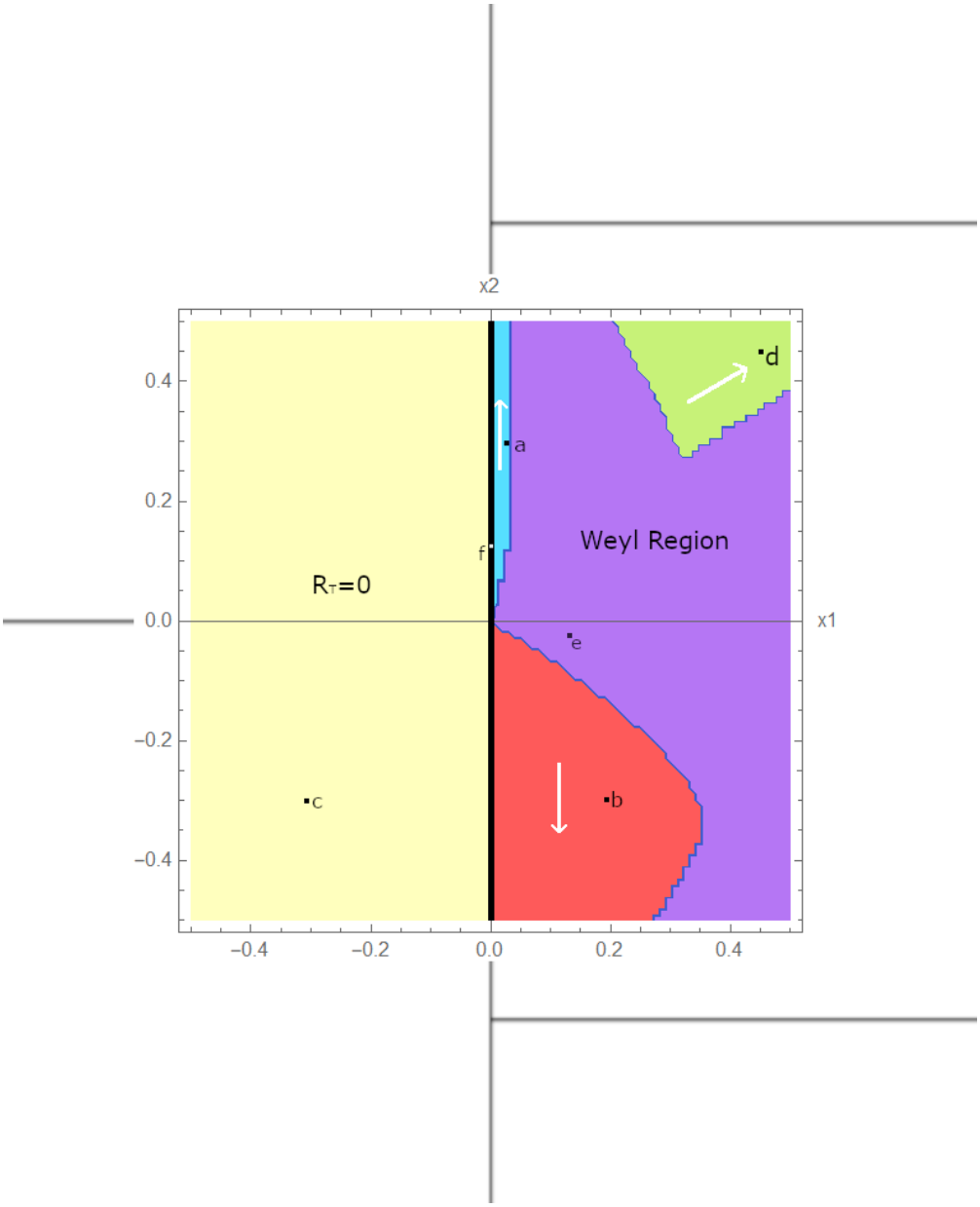

Figure 2.5: Topological phase diagram of the cell sheet lattice as an ATN around critical configuration in Fig. 2.4(a). The geometry of the lattice is such that vertices $1, 3, 4$ stay fixed, while vertex 2 is displaced by (x_1, x_2) which are the axes of the phase diagram. The phase diagram is overlaid on the real space lattice to make the geometry clear. The thick black line marks critical configurations, and 5 different topological phases are observed. The yellow region is un-polarized. The cyan, red, and green regions are topologically polarized with $\vec{R}_T$ along $\vec{a}_2$, $-\vec{a}_2$, and $\vec{a}_1$ respectively, as indicated by the white arrows. In the purple region the lattice displays Weyl points and thus topologically protected bulk floppy modes. Six representative configurations of these regions (marked by black dots) along with their phonon dispersions are shown in Fig. 2.6.

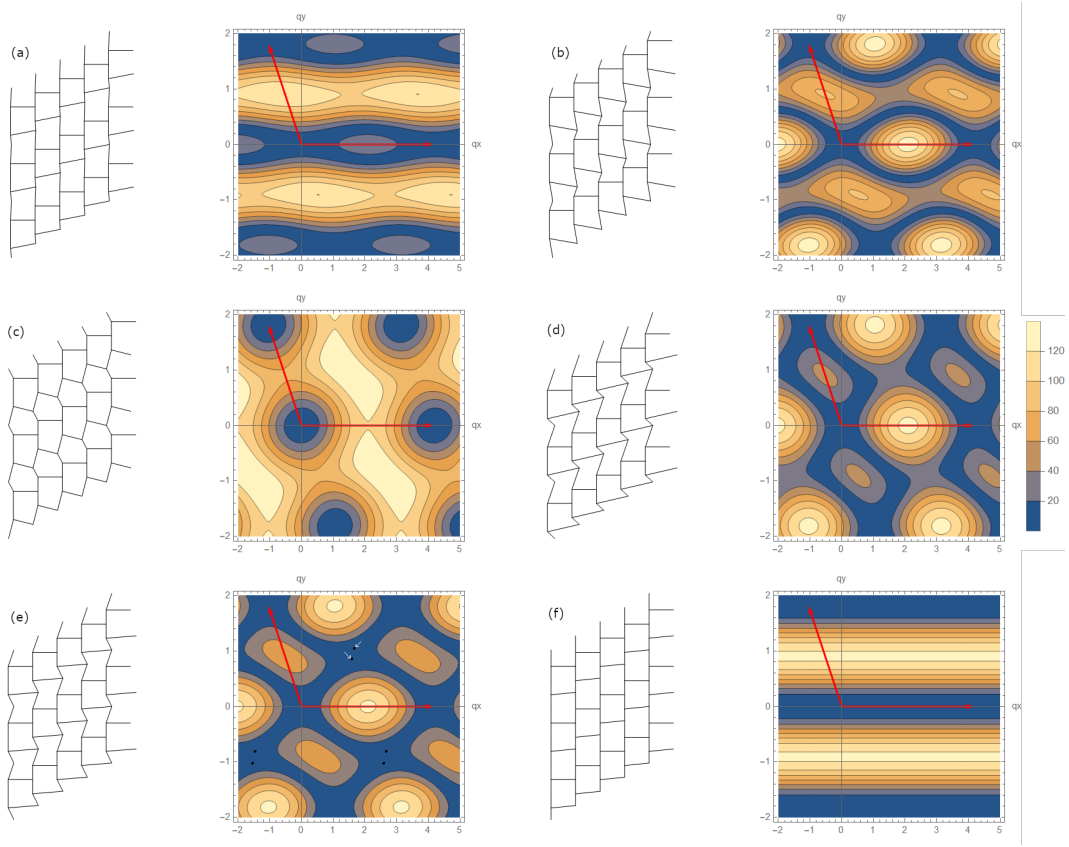

Figure 2.6: Representative examples of cell sheet lattices in different regions of the phase diagram (Fig.2.5). (a) A polarized lattice with $\vec{R}_T = \vec{a}_2$. (b) A polarized lattice with $\vec{R}_T = -\vec{a}_2$. (c) An unpolarized lattice. (d) A polarized lattice with $\vec{R}_T = \vec{a}_1$. (e) A lattice with Weyl modes. (f) A lattice at critical configuration. For each panel, the real space lattice is shown on the left and the phonon dispersion relations (ω as a function of q_x, q_y) is shown on the right. The two red arrows show the reciprocal lattice vectors $\vec{b}_1, \vec{b}_2$. Note the Weyl points in (e) represented as black dots.

remain being ZMs. Second, as vertex number 2 moves to the left, all cells become convex, and the cell sheet is always *unpolarized* ($\vec{R}_T = 0$) in this type of geometry. Third, as vertex number 2 moves to the right, all cells become concave, and the sheet can become polarized up or down, separated by a region where Weyl modes arise. Weyl modes are singularities of the vibrational modes ($\omega = 0$) in the Brillouin zone that are protected by topological winding numbers. In particular, when the integral path in Eq. (2.17) shifts across a Weyl point, the winding number jumps by an integer value, as this contour integral has a nonzero winding number at the Weyl points themselves. As a result, they mark the change of topological polarizations for modes with different wave numbers. These Weyl points appear and annihilate in pairs as the geometry of the system changes [17].

Some representative configurations of these phases and their phonon dispersion relations are shown in Fig. 2.6. The phonon dispersion of the corresponding lattice configurations are shown by calculating $\sqrt{\det D(q_x, q_y)}$ where the spring constant matrix $\mathbf{K}$ is taken to be an identity matrix. We also plot some topological boundary ZMs for configurations with $\vec{R}_T = \pm\vec{a}_2$ [(a,b) in Fig. 2.6] in Fig. 2.7, where the ZMs are localized at the top and bottom edges respectively. To make these plots, we take fixed wave numbers along the lattice boundary parallel to $\vec{a}_1$ and have PBC along this direction. We have open boundary conditions at the top and bottom boundaries and calculate these ZMs. It is visible from these plots that the modes preserve the edge directions and the cell areas, and are indeed ZMs of the sheet.

For each column of unit cells, two ZMs emerge due to the open boundary on the top and the bottom. This can be seen from Fig. 2.2 where cutting an open boundary along $\vec{a}_1$ removes two constraints (one edge and one area) per column of unit cells. In the topologically polarized phases with $\vec{R}_T = \vec{a}_2$ [Fig. 2.6(a)] both modes are localized on the top boundary [Fig. 2.7(a,b)], leaving the bottom boundary rigid because it is ZM free. In the topologically polarized phases with $\vec{R}_T = -\vec{a}_2$ [Fig. 2.6(b)] both modes are localized on the bottom boundary [Fig. 2.7(c,d)]], leaving the top boundary rigid.

It is interesting to note that the decay length of the $\vec{R}_T = \vec{a}_2$ configuration appears to be very long [Fig. 2.7(a)]. This is due to the fact that the polarized phase with $\vec{R}_T = \vec{a}_2$ is a very narrow region on the phase diagram. Note that at the critical phase, the decay length is infinity (the ZMs are bulk modes). As a result, the geometric perturbation of the unit cells in this phase is not large enough to significantly decrease the decay length of the ZMs before hitting Weyl modes configurations.

At critical configurations [Fig. 2.6(f)], as we mentioned above, the ZMs are bulk modes. For these lattices, one of the two ZMs per column is the same as the ZM computed under PBC [Fig. 2.4(a)], whereas the other one involves an interesting "breathing" motion of the columns of unit cells, as shown in Fig. 2.8. One might think of this mode as a boundary mode because of its

seemingly larger magnitude of displacement on the top and bottom. However, this is a bulk ZM, since the displacements increases linearly from the center to the boundaries (instead of exponential growth), resulting in constant strain. The ZMs of the topologically polarized phases can be seen as the evolution and linear combination of these two bulk ZMs at the critical configuration.

All these configurations can satisfy force balance in the ATN, by properly choosing tension of the edges and pressure of the cells. This can be seen by considering these configurations as mechanical networks with central force springs and pressure on cells (as discussed in Sec. 2.2.3). Given the hexagonal topology of the cells and all vertices at $z = 3$, the network is Maxwell regarding pre-stress, so there must be at least two global SSSs that make the system force balance under PBC at any geometry [53]. It is worth pointing out that, by definition, all models in which the only degrees of freedom are the vertices ignore the curvature of the cell edges induced by the pressure difference between the cells, which may be formally justified in the limits that the edges have a large bending stiffness or that the edge tensions are much larger than the forces exerted by pressure differences. In addition, as we mentioned above, topological polarization in these cell sheet lattices requires concave cell shapes. In this situation, force balance at the vertex with the concave angle might typically be expected to require active compression (i.e. negative T_{ij}) on at least one edge. In particular, it is clearly the case that some T_{ij} must be negative if pressure differences between cells are small enough. Although we cannot categorically exclude that some equilibrium configuration with concave cells and large pressure differences exists where all of the tensions are positive, we also have never been able to come up with such a counterexample. We thus hypothesize that topological polarization normally requires negative tensions.

Coming back to the VM, the reason that the VM doesn't show any topological polarization is due to the more constraining force-balance condition in the VM. As shown in Eq. (2.8), instead of freely chosen cell edge tensions as in the ATN, cell edge tensions in the VM come from cortical tensions of the cells, and must satisfy Eq. (2.8). Consequently, the number of free parameters of equilibrium states is reduced. In particular, for the 4 sites in the unit cell, according to the force balance equation in Eq. (2.7) and the cortical tension equation Eq. (2.8), we have

$$-(T_1+T_2)\vec{l_2}+(2T_1)\vec{l_3}+(T_1+T_2)\vec{l_1} = 0, \tag{2.19}$$

$$-(T_1+T_2)\vec{l_2}+(2T_2)\vec{l_6}+(T_1+T_2)\vec{l_1} = 0, \tag{2.20}$$

$$-(T_1+T_2)\vec{l_4}+(2T_2)\vec{l_6}+(T_1+T_2)\vec{l_5} = 0, \tag{2.21}$$

$$-(T_1+T_2)\vec{l_4}+(2T_1)\vec{l_3}+(T_1+T_2)\vec{l_5} = 0, \tag{2.22}$$

where T_1, T_2 are the cortical tensions of the two cells in the unit cell. Eq. (2.20-2.22) impose an additional constraint of the force equilibrium state $(T_1)\vec{l_3} = (T_2)\vec{l_6}$. This extra constraint means that $\vec{l_3}$ is parallel to $\vec{l_6}$ which makes the 2 cells in the unit cell to have almost the same geometry with

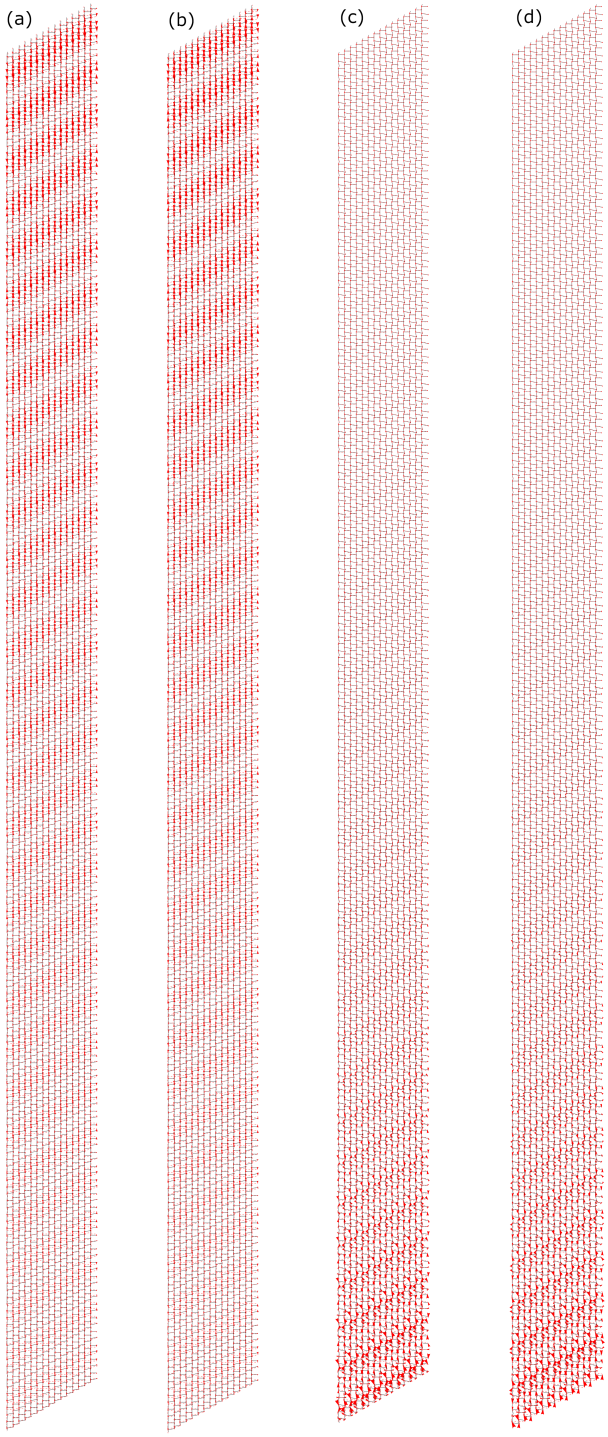

Figure 2.7: Examples of topological ZMs in polarized ATNs. (a-b) A lattice with $\vec{R}_T = \vec{a}_2$ [same as the lattice in Fig. 2.6(a)] shows two ZMs both localized on the top boundary. (c-d) A lattice with $\vec{R}_T = -\vec{a}_2$ [same as the lattice in Fig. 2.6(b)] shows two ZMs both localized on the bottom boundary. The ZMs are calculated with PBC along the $\vec{a}_1$ direction, taking a wavevector $\vec{q}$ such that $\vec{q} \cdot \vec{a}_1 = \pi$.

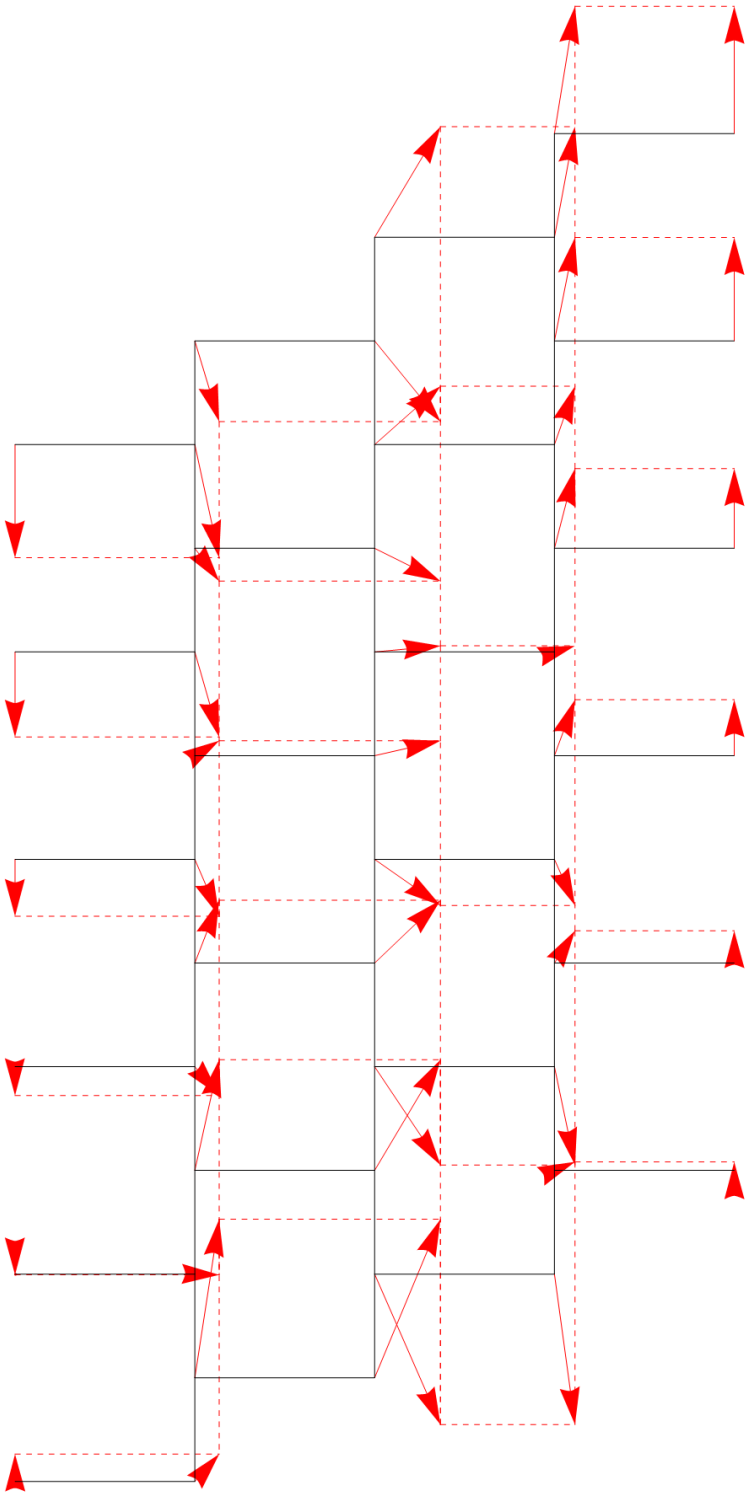

Figure 2.8: The ”breathing” mode at the critical configuration, where the straight strips get thinner and broader in an alternating order. The network is under PBC for the left-right boundary, and open boundary condition for the top-bottom boundary.

only length difference for edges $\vec{l}_3$ and $\vec{l}_6$ (see Fig. 2.2). Thus under inversion around the center of edge $\vec{l}_5$, the unit cell overlaps itself up to only the length difference, with all cell-edge angles preserved. As we discussed above, the only way the unit-cell geometry enters the mechanics of the cell sheet in the VM is through these edge angles, and the lengths of the edges are irrelevant. As a result, the mechanics of the VM with two cells per unit cell always has *inversion symmetry due to force balance*, and thus cannot topologically polarize. The only way to polarize the VM is to either allow larger unit cell (3 or more cells in each unit cell and not under columnar arrangement) or to introduce disorder. Alternatively, force-balance constraints may be lifted by allowing external forces imposed by the substrate, which offers us a larger parameter space to have topologically polarized cell configurations.

The discussions in this section are all based on periodic lattices. They could potentially be extended to generic, disordered cell sheets with the connectivity topology of honeycomb networks. In App. 2.5.4 we sketch a transfer matrix method [19] that can be applied to disordered cell sheets to investigate possible topological phases in future studies. Detailed studies of disordered cell sheets are beyond the scope of this paper.

2.4 Discussion

In this paper, we study topological mechanics in two theoretical models of epithelial tissues, namely the VM and the ATN. We identify topologically polarized phases in the ATN where ZMs and SSSs localize on boundaries of the tissue in a topologically polarized way. In contrast, the VM doesn't support topologically polarized phases in the periodic lattice structures we studied, due to the more constraining nature of its force-balance condition. It is in principle possible that topological polarization could develop in the VM if larger unit cells or disordered configurations are considered, but such configurations are beyond the scope of the current paper.

In order to study topological mechanics in the ATN, we place the system at the Maxwell point with balanced degrees of freedom and constraints. To this end, we consider a generic case where the pressure difference between cells is not ignored so the area constraint needs to be included. We study these cell sheets in a periodic lattice setting of honeycomb topology, and the unit cell consists of two cells, for simplicity. Our results show that all lattices of convex cells are topologically equivalent and do not show any topological polarization. Topologically polarized phases arise when the cells become concave, which usually implies that some cell edges carry active compression rather than tension. These topologically polarized phases are characterized by exponentially localized ZMs and SSSs on boundaries and interfaces pointed to by the topological polarization vector. This indicates that when non-convex cellular shapes are experimentally observed on epithelial tissues, one may expect to discover topologically-polarized mechanical phenomena as we

discuss here. A special note we need to make here is that for the topologically polarized phase to occur, only infinitesimal concavity is needed. In the critical configuration (Fig. 2.4), contraction is essentially off at the horizontal edges (in comparison to the contraction on the vertical edges). Thus, infinitesimal compression is sufficient for the cells to become concave and polarized (see Fig. 2.6). Although active tensions on cell edges are typically contractile, it is possible in some circumstances for passive elastic contributions from the crosslinked cytoskeleton to resist compression, yielding negative effective tensions on timescales relevant for cell motion [82; 83]; similarly, cell-cell adhesion makes a negative contribution to edge tension [84].

Mechanical topological polarization results in strongly asymmetric mechanical responses, similar to what have been observed in spring-and-mass models [14; 15; 16; 53; 19; 20]. In general, topological ZMs and SSSs localize at opposite sides of a topologically polarized system, where the topological polarization $\vec{R}_T$ points to the edge/interface with extra ZMs. In particular, if the topological polarization $\vec{R}_T$ points towards an open edge, it exhibits extra exponentially localized ZMs, while an open edge on the opposite side loses ZMs and may become rigid if all ZMs are polarized to the opposite side. Moreover, interfaces connecting domains of tissue of opposite topological polarizations can host exponentially localized ZMs (SSSs) when there is a net flux of topological polarization $\vec{R}_T$ towards (away from) this interface.

Topologically protected ZMs induce localized softness at boundaries and interfaces of the tissue. Compared to normal tissues, where boundaries are usually softer than the bulk in an isotropic way, topologically polarized tissues exhibit softness in a highly anisotropic manner, where some boundaries (ones opposite to the direction of $\vec{R}_T$) appear to be as rigid as the bulk, and some interfaces (ones with accumulated ZMs due to different $\vec{R}_T$ from domains around them) may be as soft as a normal boundary.

Similarly, topologically protected SSSs induce unusual local stiffness. At the level of linear response, as shown in Refs. [30; 15; 54], when a material is under external load, stress is "attracted" to interfaces with localized SSSs. At the nonlinear level, stress response may be further controlled by cellular rearrangements, as discussed in Refs. [69; 70], but the effect of SSSs may still play an important role in these rearrangements as spots of focused stress. Biologically, this elevated local stress may cause interesting consequences in cells at these interfaces.

In addition, even in the bulk of a topologically polarized tissue far from boundaries or interfaces, the mechanical response to local perturbations (from cell activity or from external forces) can show strong directionality. It has been shown in Ref. [22] that in a topologically polarized mechanical network stress and displacement propagate in opposite directions.

It is worth pointing out that we made the simplifying assumption that having boundaries and interfaces does not interfere with the active stresses in the tissue sheet. Rigorously speaking, force balance may be violated at these boundaries and interfaces. This will lead to local deformations to

re-balance the stress, causing locally perturbed geometry at the boundaries and interfaces. Alternatively, these active stresses can be balanced by external forces from the substrate the cell sheet attaches on (the extracellular matrix) or other biological components in contact with the sheet, so that the homogeneous lattice configurations are maintained. We conjecture that the topological mechanical properties will survive despite these perturbations, given their topological robustness. It has been recently shown that topological mechanical properties are indeed robust against various perturbations from disorder to stress [19], and random damage [54] of the networks. Detailed numerical studies of these cell sheets with actual open boundaries and interfaces will be the subject of future studies.

Biologically, these topologically robust mechanical properties may lead to interesting consequences. When cells are arranged such that ZMs localize at certain boundaries and interfaces, the greatly decreased local stiffness may allow significant changes of cell shape and trigger special biological processes. On the other hand, when cells are arranged such that SSSs localize at certain interfaces, stress significantly increases at these locations, which may trigger processes such as cell proliferation or the cell sheet to buckle out-of-plane at these controlled locations.

2.5 Appendices

2.5.1 Expansion of Elastic Energy

In this appendix we expand the elastic energy of both the VM and the ATN, as stressed elastic media, and derive the force balance condition from the first order terms of the expansion and constraints for ZMs from the second order terms of the expansion.

2.5.1.1 Elastic energy

The change of the elastic energy in both the VM and the ATN can be generically written as

$$dE = \sum_{\langle ij \rangle} \tilde{T}_{ij} dR_{ij} + \sum_{f} \tilde{\Pi}_f dA_f. \tag{2.23}$$

This expression takes the same form as the differential elastic energy of the ATN [Eq. (2.2)], but it also applies to the VM when it is considered an expansion of Eq. (2.1) where the $\tilde{T}_{ij}$'s come from the cortical tensions as we discuss below. We introduce a $2V$ dimensional vector $\mathbf{u} = (u_1^x, u_1^y, \cdots, u_n^x, u_n^y)$ to denote the displacement of all vertices, and expand the elastic energy change up to the 2nd order in $\mathbf{u}$. We add a tilde on the tension and pressure, $\tilde{T}_{ij}, \tilde{\Pi}_f$ to denote that they may contain $\mathcal{O}(u)$ terms.

Between the VM and the ATN, the major difference is reflected in the edge tension T_{ij}. These tensions are controlled by the cortical tensions T_a and T_b of the adjacent cells a and b in the VM, whereas in the ATN they are adjusted by the myosin dynamics on the edge to reach their stall values. Thus, as discussed in Sec. 2.2.1, we assume here that the edge tensions in the ATN are constant,

$$\tilde{T}_{ij} = T_{ij} \tag{2.24}$$

for the ATN but

$$\begin{aligned} \tilde{T}_{ij} &= K_P \left[(P_a - P_0) + (P_b - P_0) + \frac{1}{2} dP_a + \frac{1}{2} dP_b \right] \\ &= T_a + T_b + \frac{K_P}{2} (dP_a + dP_b) \end{aligned} \tag{2.25}$$

for the VM, where the cell perimeters are to be evaluated at the equilibrium configuration. This expression comes from an expansion of the cortical tension term of Eq. (2.1) around a stressed state with "pre-stretch" $P_f - P_0$. The change of perimeter for each cell can be expressed in terms of the displacement field $\mathbf{u}$. To second order we have

$$dP_f = \mathbf{u} \cdot \nabla P_f + \frac{1}{2} \big(\mathbf{u} \cdot \nabla \nabla^T P_f \cdot \mathbf{u}^T \big) \tag{2.26}$$

where $\nabla = (\partial_1^x, \partial_1^y, \cdots, \partial_n^x, \partial_n^y)$ and $\nabla \nabla^T$ is the Hessian matrix. Here the differential is taken with respect to $\mathbf{u}$ so that $\partial_1^x = \partial / \partial u_1^x$.

Since the perimeter $P_f = \sum_{\langle ij \rangle} R_{ij}$, the derivative for the perimeter dP_f in Eq. (2.26) can be rewritten as

$$dP_f = \sum_{\langle ij \rangle} \mathbf{u} \cdot \nabla R_{ij} + \frac{1}{2} \big(\mathbf{u} \cdot \nabla \nabla^T R_{ij} \cdot \mathbf{u}^T \big). \tag{2.27}$$

The area contributions are treated the same in both models including the change in pressure due to the displacements $\mathbf{u}$,

$$\tilde{\Pi}_f = K_A \left[(A_f - A_0) + \frac{1}{2} dA_f \right] = \Pi_f + \frac{K_A}{2} dA_f \ , \tag{2.28}$$

where A_f is to be evaluated at mechanical equilibrium. This expression comes from an expansion of the area term of Eq. (2.1) around a stressed state with "pre-area-expansion" $A_f - A_0$. The change of cellular area dA_f can be expanded as (to second order)

$$dA_f = \mathbf{u} \cdot \nabla A_f + \frac{1}{2} \big(\mathbf{u} \cdot \nabla \nabla^T A_f \cdot \mathbf{u}^T \big) \tag{2.29}$$

Thus, combining Eq. (2.25) to Eq. (2.29) we obtain the 2nd order expansion of dE with respect to the displacement field $\mathbf{u}$ in the VM as

$$\begin{aligned} dE_{\text{VM}} = &\sum_{\langle ij \rangle} (T_a + T_b)(\mathbf{u} \cdot \nabla R_{ij}) + \frac{K_P}{2}[(\mathbf{u} \cdot \nabla (P_a + P_b))(\mathbf{u} \cdot \nabla R_{ij})] + \frac{(T_a + T_b)}{2}\big(\mathbf{u} \cdot \nabla \nabla^T R_{ij} \cdot \mathbf{u}^T\big) \\ &+ \sum_f \Pi_f (\mathbf{u} \cdot \nabla A_f) + \frac{K_A}{2}(\mathbf{u} \cdot \nabla A_f)^2 + \frac{1}{2}\Pi_f \big(\mathbf{u} \cdot \nabla \nabla^T A_f \cdot \mathbf{u}^T\big) + \mathcal{O}\big(\mathbf{u}^3\big) \end{aligned} \tag{2.30}$$

Similarly, for the ATN, we have the energy expansion

$$\begin{aligned} dE_{\text{ATN}} = &\sum_{\langle ij \rangle} T_{ij} (\mathbf{u} \cdot \nabla R_{ij}) + \frac{T_{ij}}{2}\big(\mathbf{u} \cdot \nabla \nabla^T R_{ij} \cdot \mathbf{u}^T\big) \\ &+ \sum_f \Pi_f (\mathbf{u} \cdot \nabla A_f) + \frac{K_A}{2}(\mathbf{u} \cdot \nabla A_f)^2 + \frac{1}{2}\Pi_f \big(\mathbf{u} \cdot \nabla \nabla^T A_f \cdot \mathbf{u}^T\big) + \mathcal{O}\big(\mathbf{u}^3\big) \end{aligned} \tag{2.31}$$

2.5.1.2 Force-balance condition

The force balance condition comes from the fact that the expansions of Eq. (2.30) and (2.31) must have vanishing $\mathcal{O}(u)$ terms, so that there is no net force on any vertex. This condition takes the form

$$dE^{(1)} = \sum_{\langle ij \rangle} T_{ij} (\mathbf{u} \cdot (\nabla R_{ij})) + \sum_f \Pi_f (\mathbf{u} \cdot \nabla A_f) = 0 \tag{2.32}$$

for any choice of the displacement field $\mathbf{u}$. This equation is exactly the force balance condition described in Eq. (2.10) of the main text for the ATN. For the VM, we keep only the first term in Eq. (2.32), because we drop the area term in order to satisfy Maxwell's condition. This leads to Eq.(2.7) of the main text.

2.5.1.3 The Hessian

Now we turn to examine the $\mathcal{O}(u^2)$ terms in the expansions and identify the constraints. For the VM, as discussed in the main text, we only treat the cortical tension as dominant contribution to the elastic energy in order to place the model to the Maxwell condition. The 2nd order terms in Eq.(2.30) are thus

$$dE^{(2)}_{\text{VM}} = \sum_{\langle ij \rangle} \frac{K_P}{2}[(\mathbf{u} \cdot \nabla (P_a + P_b))(\mathbf{u} \cdot \nabla R_{ij})] + (T_a + T_b)\big(\mathbf{u} \cdot \nabla \nabla^T R_{ij} \cdot \mathbf{u}^T\big) \tag{2.33}$$

The $\mathcal{O}(u^2)$ terms for the ATN from Eq. (2.31) are

$$dE^{(2)}_{\text{ATN}} = \sum_{\langle ij \rangle} \frac{T_{ij}}{2}\big(\mathbf{u}\cdot\nabla\nabla^T R_{ij}\cdot\mathbf{u}^T\big) + \sum_f \frac{K_A}{2}(\mathbf{u}\cdot\nabla A_f)^2 + \frac{1}{2}\Pi_f\big(\mathbf{u}\cdot\nabla\nabla^T A_f\cdot\mathbf{u}^T\big) \tag{2.34}$$

These $\mathcal{O}(u^2)$ terms lead to an elastic energy that consists of all complete square terms. Because these complete square terms must all be zero to make the elastic energy vanish, they provide constraints discussed Sec. 2.2.2 in the main text. We derive these complete square terms below.

For a cell f modeled as an V_f-polygon, the perimeter and area can be written as

$$P_f = \sum_{i=1}^{V_f} l_i \tag{2.35}$$

$$A_f = \frac{1}{2}\sum_{i=1}^{V_f-1}\sum_{j>i}^{V_f-1}(l_j^x l_i^y - l_j^y l_i^x), \tag{2.36}$$

where $\vec{l}_i = \vec{r}_{i+1} - \vec{r}_i + \vec{u}_{i+1} - \vec{u}_i$ is the length of edge i of face f the same way as defined in Sec. 2.2. Thus the expansion on perimeter and area can be arranged in orders of u as:

$$l_i = l_i^{(0)} + l_i^{(1)} + l_i^{(2)} + \mathcal{O}\Big(l_i^{(3)}\Big) \tag{2.37}$$

where

$$l_i^{(0)} = |\vec{r}_{i+1} - \vec{r}_i| \tag{2.38}$$

$$l_i^{(1)} = \mathbf{u}\cdot\nabla l_i = (\vec{u}_{i+1} - \vec{u}_i)\cdot\hat{n}_i \tag{2.39}$$

$$l_i^{(2)} = \mathbf{u}\cdot\nabla\nabla^T l_i\cdot\mathbf{u}^T = \frac{1}{2l_i}|\hat{n}_i\times(\vec{u}_{i+1} - \vec{u}_i)|^2 \tag{2.40}$$

with $\hat{n}_i$ being the unit vector of $\vec{l}_i^{(0)}$, which is the bond direction before displacements. Subjecting Eq. (2.39) - (2.40) into Eq. (2.30) and (2.31) allows us to find explicit expressions in terms of the displacements $\mathbf{u}$.

For the VM, the 1st quadratic term in Eq. (2.30) can be rearranged to become a sum over faces

$$\sum_{\langle ij\rangle}\frac{K_P}{2}[(\mathbf{u}\cdot\nabla(P_a+P_b))(\mathbf{u}\cdot\nabla R_{ij})] = \sum_f \frac{K_P}{2}\left[\sum_i^n l_i^{(1)}\right]^2. \tag{2.41}$$

The 2nd term after the edge to face summation rearrangements becomes

$$\sum_{\langle ij \rangle} (T_a + T_b)\big(\mathbf{u} \cdot \nabla\nabla^T R_{ij} \cdot \mathbf{u}^T\big) = \sum_f T_f \sum_{i=1}^{n} l_i^{(2)} \tag{2.42}$$

where T_f is the cortical tension on cell f.

It is obvious now that all $\mathcal{O}(u^2)$ terms in the elastic energy of the VM can be arranged into these complete square terms, the total number of which is equal to $F + E$. For a ZM which leaves the elastic energy zero, each of the complete square terms need to vanish. We thus arrive at ZM conditions for the VM

$$\sum_{i}^{V_f} (\vec{u}_{i+1} - \vec{u}_i) \cdot \hat{n}_i = 0 \tag{2.43}$$

$$\hat{n}_i \times (\vec{u}_{i+1} - \vec{u}_i) = 0 \tag{2.44}$$

which are Eq. (2.5) and (2.3) in the main text. These constraints are generically linearly independent unless the geometry is fine-tuned such that a singularity arises.

We can do a similar analysis for the ATN, where we find that the 1st term in Eq. (2.31)

$$\sum_{\langle ij \rangle} \frac{T_{ij}}{2}\big(\mathbf{u} \cdot \nabla\nabla^T R_{ij} \cdot \mathbf{u}^T\big) \tag{2.45}$$

result in exactly the same ZM condition as Eq. (2.44). The 2nd term

$$\sum_f \frac{K_A}{2}(\mathbf{u} \cdot \nabla A_f)^2 \tag{2.46}$$

has the completed square on $\mathbf{u} \cdot \nabla A_f$, which leads to the ZM condition described in Eq. (2.4) of the main text. Interestingly, the 3rd term in Eq. (2.31)

$$\frac{1}{2}\Pi_f\big(\mathbf{u} \cdot \nabla\nabla^T A_f \cdot \mathbf{u}^T\big) \tag{2.47}$$

only depends on the boundary displacements, because it becomes the variation of the total area of the whole sheet after summing over all faces. Explicitly, the Hessian of the area $\nabla\nabla^T A_f$ can be

written in a matrix form as

$$\nabla\nabla^T A_f = \begin{pmatrix} 0 & -1 & 0 & 0 & 0 & 1 \\ 1 & 0 & -1 & 0 & 0 & 0 \\ 0 & 1 & 0 & -1 & 0 & 0 \\ 0 & 0 & 1 & 0 & -1 & 0 \\ 0 & 0 & 0 & 1 & 0 & -1 \\ -1 & 0 & 0 & 0 & 1 & 0 \end{pmatrix} \tag{2.48}$$

using the sites r_i of a face as the basis where $i \in [1, 6]$. Thus, this term vanishes automatically for any internal vertex and does not provide a new constraint. The total number of constraints in the ATN is also $F + E$, placing it at the Maxwell point. One way to physically understand the vanishing of this term is that the total area of the cellular sheet would not change under the displacement of internal vertices.

2.5.2 Compatibility Matrix

2.5.2.1 Compatibility matrix of the Active Tension Network

The compatibility matrix for the ATN can be constructed according to the ZM conditions in Eq. (2.3) and Eq. (2.4). For the unit cell construction in Fig. 2.2, the momentum space compatibility matrix $\mathbf{C}(\mathbf{k})$ is an 8×8 matrix because we have 4 sites, 2 faces and 6 edges in a unit cell. From the condition Eq. (2.3), we have 6 constraints for ZMs in the ATN,

$$\hat{n}_1 \times \left(\vec{u}_2 - e^{ik_1}\vec{u}_1\right) = \mathbf{e}_1^{\perp} \tag{2.49}$$

$$\hat{n}_2 \times \left(\vec{u}_1 - \vec{u}_2\right) = \mathbf{e}_2^{\perp} \tag{2.50}$$

$$\hat{n}_3 \times \left(e^{-ik_2}\vec{u}_4 - \vec{u}_1\right) = \mathbf{e}_3^{\perp} \tag{2.51}$$

$$\hat{n}_4 \times \left(\vec{u}_3 - e^{-ik_2}\vec{u}_4\right) = \mathbf{e}_4^{\perp} \tag{2.52}$$

$$\hat{n}_5 \times \left(\vec{u}_4 - \vec{u}_3\right) = \mathbf{e}_5^{\perp} \tag{2.53}$$

$$\hat{n}_6 \times \left(e^{i(k_1-k_2)}\vec{u}_2 - \vec{u}_3\right) = \mathbf{e}_6^{\perp} \tag{2.54}$$

And from the area conditions in Eq. (2.4), we have 2 more constraints for ZMs in the ATN,

$$\begin{aligned}
&\left(\vec{u}_2 - e^{ik_1}\vec{u}_1\right) \times \left(\vec{l}_2 + \vec{l}_3\right) + \left(\vec{u}_1 - \vec{u}_2\right) \times \left(-\vec{l}_1 + \vec{l}_3\right) \\
&- \left(e^{-ik_2}\vec{u}_4 - \vec{u}_1\right) \times \left(\vec{l}_2 - \vec{l}_1\right) + \left(\vec{u}_3 - e^{-ik_2}\vec{u}_4\right) \times \left(\vec{l}_5 - \vec{l}_3\right) \\
&+ \left(\vec{u}_4 - \vec{u}_3\right) \times \left(-\vec{l}_3 - \vec{l}_4\right) \\
&- \left(e^{ik_1}\vec{u}_1 - \vec{u}_4\right) \times \left(\vec{l}_4 + \vec{l}_5\right) = \Delta A_1
\end{aligned} \tag{2.55}$$

and

$$\begin{aligned}
&\left(\vec{u}_4 - e^{ik_1}\vec{u}_3\right) \times \left(\vec{l}_6 - \vec{l}_5\right) + \left(\vec{u}_3 - \vec{u}_4\right) \times \left(\vec{l}_6 + \vec{l}_4\right) \\
&- \left(e^{i(k_1-k_2)}\vec{u}_2 - \vec{u}_3\right) \times \left(-\vec{l}_4 - \vec{l}_5\right) \\
&+ \left(e^{ik_2}\vec{u}_1 - e^{i(k_1-k_2)}\vec{u}_2\right) \times \left(-\vec{l}_2 - \vec{l}_6\right) \\
&+ \left(e^{ik_2}\vec{u}_2 - e^{ik_2}\vec{u}_1\right) \times \left(\vec{l}_1 - \vec{l}_6\right) \\
&- \left(e^{ik_1}\vec{u}_3 - e^{ik_2}\vec{u}_2\right) \times \left(-\vec{l}_1 - \vec{l}_2\right) = \Delta A_2
\end{aligned} \tag{2.56}$$

Putting the 8 equations from Eq. (2.49) - Eq. (2.56) together results in the compatibility matrix of size 8×8 in the basis of $\{u_i^x, u_i^y\}$ where $i = 1, 2, \cdots, 4$ with each constraint in each row, and each degrees of freedom in each column. The determinant of this matrix is used to compute the topological polarization. In these equations, we defined the shorthand $e^{ik_1} \equiv e^{i\vec{k}\cdot\vec{a}_1}$, $e^{ik_2} \equiv e^{i\vec{k}\cdot\vec{a}_2}$, which are the Bloch factors of the lattice.

2.5.2.2 Compatibility matrix of the VM

Similarly, we can construct the compatibility matrix for the VM using Eq. (2.3) and Eq. (2.5). The bond rotation constraint Eq. (2.3) have the same 6 equations as shown in Eqs. (2.49 - 2.54). However, the perimeter conservation Eq. (2.5) gives us 2 constraints,

$$\begin{aligned}
&\left(\vec{u}_2 - e^{ik_1}\vec{u}_1\right) \cdot \vec{l}_1 + \left(\vec{u}_1 - \vec{u}_2\right) \cdot \vec{l}_2 + \left(e^{-ik_2}\vec{u}_4 - \vec{u}_3\right) \cdot \vec{l}_3 \\
&+ \left(\vec{u}_3 - e^{-ik_2}\vec{u}_4\right) \cdot \vec{l}_4 + \left(\vec{u}_4 - \vec{u}_3\right) \cdot \vec{l}_5 + \left(e^{ik_1}\vec{u}_1 - \vec{u}_4\right) \cdot \vec{l}_6 = \Delta P_1
\end{aligned} \tag{2.57}$$

$$\begin{aligned}
&\left(\vec{u}_4 - e^{ik_1}\vec{u}_3\right) \cdot \vec{l}_1 + \left(\vec{u}_3 - \vec{u}_4\right) \cdot \vec{l}_2 + \left(e^{i(k_1-k_2)}\vec{u}_2 - \vec{u}_3\right) \cdot \vec{l}_3 \\
&+ \left(e^{ik_2}\vec{u}_1 - e^{i(k_1-k_2)}\vec{u}_2\right) \cdot \vec{l}_4 + \left(e^{ik_2}\vec{u}_2 - e^{ik_2}\vec{u}_1\right) \cdot \vec{l}_5 + \left(e^{ik_1}\vec{u}_3 - e^{ik_2}\vec{u}_2\right) \cdot \vec{l}_6 = \Delta P_2.
\end{aligned} \tag{2.58}$$

The 8×8 compatibility matrix of the VM is constructed using Eqs. (2.49 - 2.54), (2.57), and (2.58) again in the basis of $\{u_i^x, u_i^y\}$.

2.5.3 Topological Phase Diagram of Networks Close to Critical Configurations Along $\vec{a}_1$

In Fig. 2.4 we show two critical configurations with bonds forming straight lines, allowing bulk ZMs where cells translate along strips along $\vec{a}_2$ (a) or $\vec{a}_1$ (b). In the main text, we discussed the phase diagram around the critical configuration (a).

We have done similar analysis of configurations around critical configuration (b), and the results are shown in Fig. 2.9. Similarly, the sheet is unpolarized when all cells are convex. When the cells become concave, configurations of $\vec{R_T} = \pm\vec{a}_1$, as well as a region with Weyl points show up. We show some examples of the geometry of these phases in Fig. 2.10.

It is interesting to note here that because 4 constraints per unit cell are removed when a vertical cut is introduced on the lattice to generate an open boundary along $\vec{a}_2$ (so as to show the topological polarization along $\vec{a}_1$), 4 instead of 2 ZMs are generated per unit cell. Therefore, topological polarization $\vec{R_T} = \pm\vec{a}_1$ indicates that the ratio of ZMs at the left and right boundary have ratios of $1:3$ or $3:1$ instead of $0:4$ or $4:0$. As a result, we do not observe any boundary becoming completely ZM free in this case, unlike the phase diagram we discussed in the main text, where the top or the bottom boundaries can be free of ZMs.

2.5.4 Transfer Matrix for Disordered Cell Sheets

In this appendix we develop a transfer matrix method for ZMs in cell sheets, which can be applied to *disordered* cell sheets to conveniently derive the ZM at given boundary conditions. The transfer matrix for the VM and the ATN can be derived in similar ways, thus we show both derivations in this appendix.

In this transfer matrix construction, we assume that each cell is a hexagon (of arbitrary shape) and each vertex has three edges meeting at it, so the sheet still has the topology of a honeycomb lattice, but no periodicity is required for the shapes of the cells. The constructed transfer matrix will enable us to derive the ZM displacements of the three "outgoing" edges from the ZM displacements of the three "incoming" edges. Therefore by propagating this transfer matrix through the whole cell sheet, where each hexagonal cell has three in-flux and three out-flux, we can compute the ZM of the whole sheet.

To derive this transfer matrix method, we consider one cell and establish the edge conventions as shown in Fig. 2.11. Same as in Eq. (2.4), we define $\vec{\mathcal{U}}_i = \vec{u}_{i+1} - \vec{u}_i$ as the relative displacement between the neighboring vertices. Because the ZM cannot rotate the edges [Eq.(2.3)], these vectors $\vec{U}_i$ only have components parallel to the original edge direction

$$\mathcal{U}_i^{\parallel} = \vec{\mathcal{U}} \cdot \hat{l}_{i,i+1}, \tag{2.59}$$

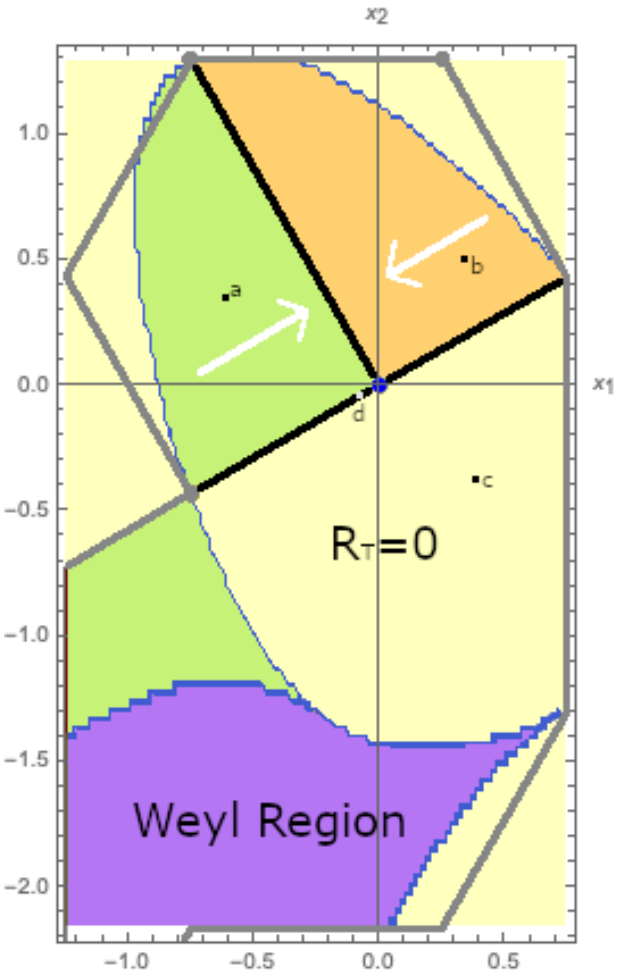

Figure 2.9: Phase diagram for changing site 2 coordinate in Case 1 with the same representation style as Fig. 2.5. The gray boundary labels the outbound of the unit cell with the 3 stationary sites besides vertex 2. The thick black line marks critical configurations, and 5 different topological phases are observed. The yellow region is un-polarized. The cyan, and red regions are topologically polarized with $\vec{R}_T$ along $\vec{a}_1$, and $-\vec{a}_1$ respectively, where the white arrows mark $\vec{R}_T$. In the purple region the lattice displays Weyl points and thus topologically protected bulk floppy modes. Four representative configurations of these regions (marked by black dots) are shown in Fig. 2.10.

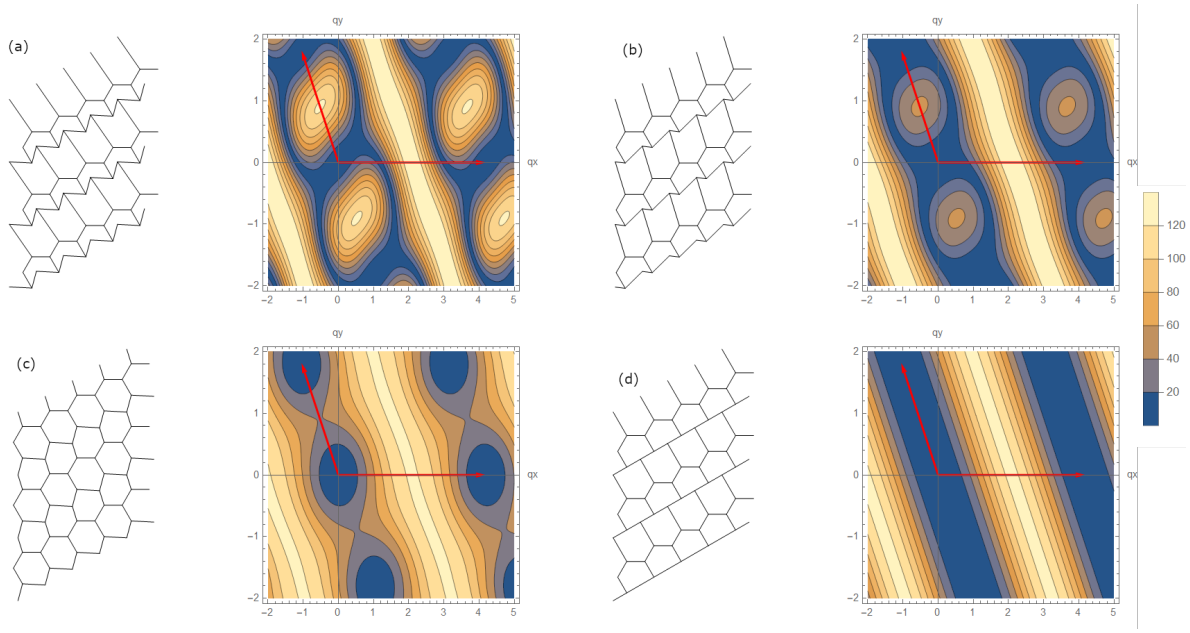

Figure 2.10: Representative examples of cell sheet lattices in different regions of the phase diagram (Fig. 2.9) with the same style as Fig. 2.6. (a): A polarized lattice with $\vec{R}_T = \vec{a}_1$. (b): A polarized lattice with $\vec{R}_T = -\vec{a}_1$. (c): An unpolarized lattice. (d): A lattice at critical configuration.

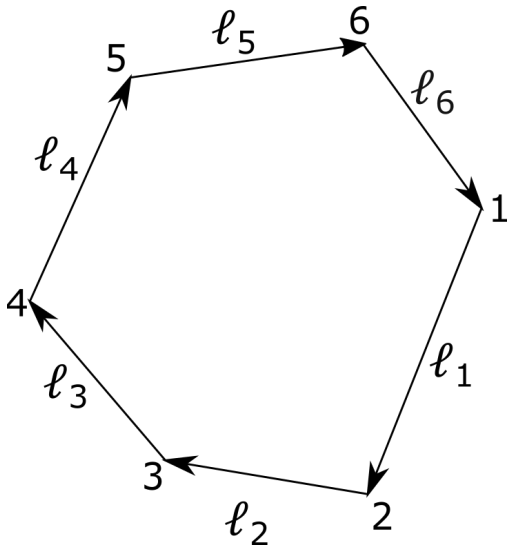

Figure 2.11: The convention used in establishing the Transfer Matrix, sites and edges are labeled as in the figure, and edge directions are chosen to be in the clockwise direction.

where $\hat{l}_{i,i+1}$ is the direction of the edge connecting vertices i and $i+1$.

At each cell, we assume there are three known displacements $\{\mathcal{U}_1^{\parallel}, \mathcal{U}_2^{\parallel}, \mathcal{U}_3^{\parallel}\}$, and we will derive three unknown displacements $\{\mathcal{U}_4^{\parallel}, \mathcal{U}_5^{\parallel}, \mathcal{U}_6^{\parallel}\}$. From the fact that the hexagonal cell has to remain closed, we have

$$\sum_{i=1}^{V_f} \mathcal{U}_i^{\parallel} \hat{l}_{i,i+1} = 0. \tag{2.60}$$

This gives us two equations, because it is a vectorial equation. One more equation for ZMs comes from the perimeter conservation condition in Eq. (2.5) in the VM

$$\sum_{i=1}^{V_f} \vec{\mathcal{U}} \cdot \hat{l}_{i,i+1} = \sum_{i=1}^{V_f} \mathcal{U}_i^{\parallel} = 0 \tag{2.61}$$

and from the area preservation condition in Eq. (2.4) in the ATN.

$$\sum_{i=1}^{V_f-1} \sum_{j>i}^{V_f-1} \left(\vec{\mathcal{U}}_j \times \vec{\mathcal{L}}_i - \vec{\mathcal{U}}_i \times \vec{\mathcal{L}}_j \right) = 0. \tag{2.62}$$

Equations (2.60) - Eq. (2.62) allow us to write a transfer matrix $\mathbf{M}$ for both models such that

$$\mathbf{M} \cdot \begin{pmatrix} \mathcal{U}_1^{\parallel} \\ \mathcal{U}_2^{\parallel} \\ \mathcal{U}_3^{\parallel} \end{pmatrix} = \begin{pmatrix} \mathcal{U}_4^{\parallel} \\ \mathcal{U}_5^{\parallel} \\ \mathcal{U}_6^{\parallel} \end{pmatrix} \tag{2.63}$$

The transfer matrix $\mathbf{M}$ takes the form of a square non-symmetric matrix for both models. In the VM,

$$\mathbf{M}_{VM} = -\begin{pmatrix} 1 & 1 & 1 \\ \cos\theta_4 & \cos\theta_5 & \cos\theta_6 \\ \sin\theta_4 & \sin\theta_5 & \sin\theta_6 \end{pmatrix}^{-1} \cdot \begin{pmatrix} 1 & 1 & 1 \\ \cos\theta_1 & \cos\theta_2 & \cos\theta_3 \\ \sin\theta_1 & \sin\theta_2 & \sin\theta_3 \end{pmatrix} \tag{2.64}$$

where θ_i are the angles of the edges $\mathcal{L}_{i,i+1}$ in the Cartesian coordinate system. The transfer matrix $\mathbf{M}$ for the ATN has a similar form as Eq. (2.64), with the elements in the first row replaced by the terms given by Eq. (2.62).

$$\mathbf{M}_{ATN} = -\begin{pmatrix} \cos\theta_4\left(\mathcal{L}_5^y+\mathcal{L}_6^y\right)-\sin\theta_4\left(\mathcal{L}_5^x+\mathcal{L}_6^x\right) & \cos\theta_5\left(\mathcal{L}_6^y-\mathcal{L}_4^y\right)-\sin\theta_5\left(\mathcal{L}_6^x-\mathcal{L}_4^x\right) & -\cos\theta_6\left(\mathcal{L}_4^y+\mathcal{L}_5^y\right)+\sin\theta_6\left(\mathcal{L}_4^x+\mathcal{L}_5^x\right) \\ \cos\theta_4 & \cos\theta_5 & \cos\theta_6 \\ \sin\theta_4 & \sin\theta_5 & \sin\theta_6 \end{pmatrix}^{-1} \cdot \begin{pmatrix} \cos\theta_1\left(\mathcal{L}_2^y+\mathcal{L}_3^y\right)-\sin\theta_1\left(\mathcal{L}_2^x+\mathcal{L}_3^x\right) & \cos\theta_2\left(\mathcal{L}_3^y-\mathcal{L}_1^y\right)-\sin\theta_2\left(\mathcal{L}_3^x-\mathcal{L}_1^x\right) & -\cos\theta_3\left(\mathcal{L}_1^y+\mathcal{L}_2^y\right)+\sin\theta_3\left(\mathcal{L}_1^x+\mathcal{L}_2^x\right) \\ \cos\theta_1 & \cos\theta_2 & \cos\theta_3 \\ \sin\theta_1 & \sin\theta_2 & \sin\theta_3 \end{pmatrix} \tag{2.65}$$

These transfer matrices can be used to propagate the ZM across the whole sheet cell by cell from

given boundary conditions, as shown in Fig. 2.12.

To study topological mechanics, we again start from the bulk ZM configuration shown in Fig. 2.4(a), where $\vec{\mathcal{U}}_1 \parallel \vec{\mathcal{U}}_3 \parallel \vec{\mathcal{U}}_4 \parallel \vec{\mathcal{U}}_6$. In this configuration, both $\mathbf{M}_{VM}$ and $\mathbf{M}_{ATN}$ yield one ZM with eigenvalue $\lambda_1 = -1$ with a corresponding eigenvector $\vec{\nu}_1 = \begin{pmatrix} 1 \\ 0 \\ 1 \end{pmatrix}$ for the $\mathcal{U}_i^{\parallel}$. This is clearly the bulk ZM depicted in Fig. 2.4(a), where edges 2 and 5 shift vertically.

However, the other two eigenmodes of this 3×3 transfer matrix do not correspond to simple decompositions of other edges of this cell. Specifically in ATN, one of these two modes represents vertical shifts of neighboring columns with an eigenvalue $\lambda_2 = 1$, whereas the other one represents a horizontal broadening or narrowing of the network that has a corresponding eigenvalue $\lambda_3 = \frac{|\mathcal{L}_5|}{|\mathcal{L}_2|}$, and this mode captures the "breathing" mode discussed in the main text. This differs from other simpler cases of transfer matrices for topological mechanics where modes symmetrically separate, making it transparent to study ZM decay in different directions in those systems [19; 20].

For the rest of this appendix, we introduce perturbations to the vertex positions and examine how the eigenvalues of the transfer matrix change. In particular, we focus on the first mode which has eigenvalue $\lambda_1 = -1$ at the critical configuration. The sign of its first order correction $\delta\lambda_1$ indicates the directions of decay in the ZM.

We use first order perturbation theory to find $\delta\lambda$ as a function of the geometric perturbation of the vertex positions. However, due to the non-symmetric nature of the transfer matrix, the first order perturbation method needs a slight modification from the usual perturbation theory because the left and right eigenvectors of the matrix are not identical.

In first order perturbation theory for symmetric matrices, the perturbation to the eigenvalues take the form $E^{(1)} = \left\langle \psi^{(0)} \middle| \delta E \middle| \psi^{(0)} \right\rangle$. However for non-symmetric matrices, it takes the form

$$\delta\lambda_i = \frac{\vec{\mu^{\intercal}}_i^0 \delta\mathbf{M} \vec{\nu}_i^0}{\vec{\mu^{\intercal}}_i^0 \vec{\nu}_i^0}$$

where $\vec{\mu^{\intercal}}_i^0, \vec{\nu}_i^0$ are the left and right eigenvectors of the unperturbed matrix $\mathbf{M}$. The derivation of this form is supplied as the following.

With some small geometric change from the critical configuration, the transfer matrix $\mathbf{M}$ can be written as

$$\mathbf{M} = \mathbf{M}^0 + \delta\mathbf{M}, \tag{2.66}$$

the eigenvalues λ_i can be expanded to the first order as

$$\lambda_i \approx \lambda_i^0 + \delta\lambda \tag{2.67}$$

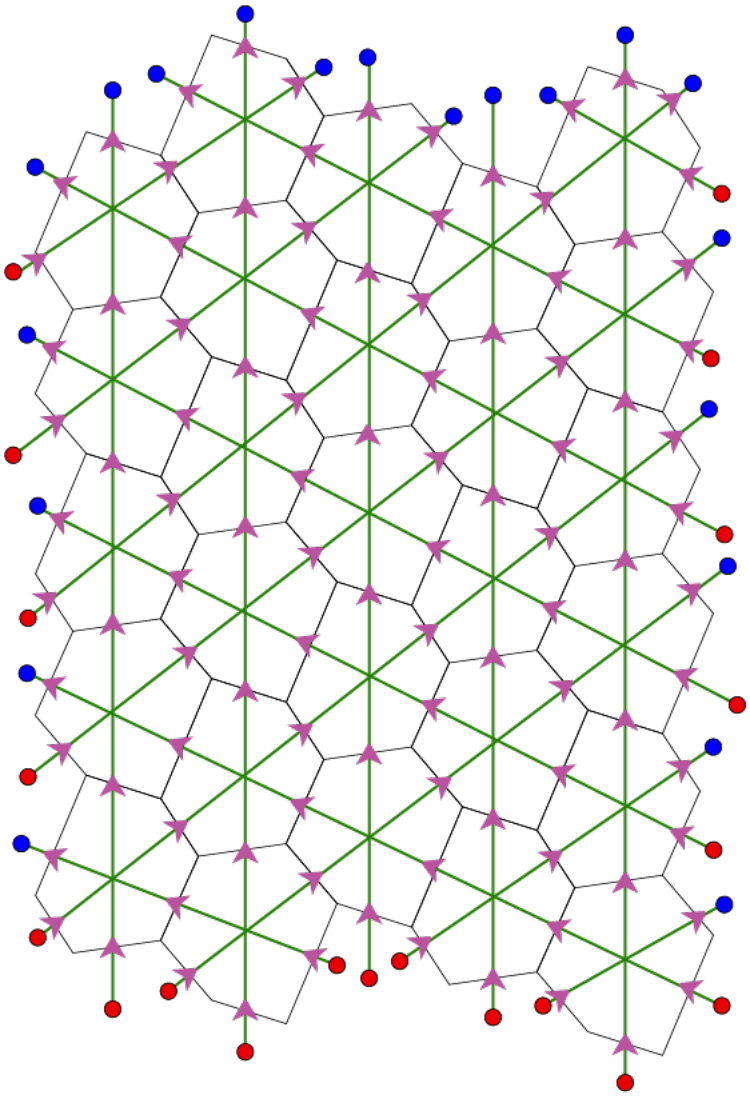

Figure 2.12: An illustration of how the transfer matrix can use the ”incoming” edges to solve for the ”outgoing” edges on a sheet of hexagonal cells for ZMs. The red dots label the “incoming” edges, where $\mathcal{U}_i^{\parallel}$ are given by boundary conditions, and the blue dots represent the “outgoing” edges where $\mathcal{U}_i^{\parallel}$ are calculated. Across each cell, the transfer matrix allows us to find out the ZM at the three outgoing edges as functions of the ZM at the three incoming edges, and the direction of the ZM solution propagation is labeled by the magenta arrows across cell edges. The choice of the in and out directions is not unique on the sheet, and depends on which boundaries are fixed. The total number of incoming edges (red dots) is equal to the total number of ZMs of the whole sheet, so determining $\mathcal{U}_i^{\parallel}$ at these edges determines the ZM of the whole sheet.

and the right eigenvectors $\vec{\nu}_i$ can be expanded to the first order as

$$\vec{\nu}_i \approx \vec{\nu}_i^0 + \vec{\delta\nu} \tag{2.68}$$

where $\mathbf{M}^0$, λ_i^0, and $\vec{\nu}_i^0$ are the transfer matrix and its eigenvalues and eigenvectors when the geometry is at the critical configuration, so that we know $\mathbf{M}^0\vec{\nu}_i^0 = \lambda_i^0\vec{\nu}_i^0$.

With these expansions, we have

$$\big(\mathbf{M}^0 + \delta\mathbf{M}\big)\Big(\vec{\nu}_i^0 + \vec{\delta\nu}_i\Big) = \big(\lambda_i^0 + \delta\lambda_i\big)\Big(\vec{\nu}_i^0 + \vec{\delta\nu}_i\Big). \tag{2.69}$$

Multiplying out the terms and keep to the first order, we get

$$\mathbf{M}^0\vec{\nu}_i^0 + \mathbf{M}^0\vec{\delta\nu}_i + \delta\mathbf{M}\vec{\nu}_i^0 = \lambda_i^0\vec{\nu}_i^0 + \lambda_i\vec{\delta\nu}_i + \delta\lambda_i\vec{\nu}_i^0. \tag{2.70}$$

The first terms cancel on both sides, so it becomes

$$\mathbf{M}^0\vec{\delta\nu}_i + \delta\mathbf{M}\vec{\nu}_i^0 = \lambda_i\vec{\delta\nu}_i + \delta\lambda_i\vec{\nu}_i^0. \tag{2.71}$$

Now suppose $\vec{\mu}_i^0$ is the left eigenvector of $\mathbf{M}^0$ with the eigenvalue λ_i, such that $\vec{\mu^\intercal}_i^0\mathbf{M}^0 = \vec{\mu^\intercal}_i^0\lambda_i$, or equivalently, $\mathbf{M}^\intercal\vec{\mu}_i^0 = \lambda_i^0\vec{\mu}_i^0$. Dotting this left eigenvector on both sides of the equation gives us

$$\vec{\mu^\intercal}_i^0\mathbf{M}^0\vec{\delta\nu}_i + \vec{\mu^\intercal}_i^0\delta\mathbf{M}\vec{\nu}_i^0 = \vec{\mu^\intercal}_i^0\lambda_i\vec{\delta\nu}_i + \vec{\mu^\intercal}_i^0\delta\lambda_i\vec{\nu}_i^0 \tag{2.72}$$

Now we can cancel out the first term on both sides again based on the property of the left eigenvectors $\vec{\mu}_i^0$, so we are left with

$$\vec{\mu^\intercal}_i^0\delta\mathbf{M}\vec{\nu}_i^0 = \vec{\mu^\intercal}_i^0\delta\lambda_i\vec{\nu}_i^0 \tag{2.73}$$

Rearranging the equation, we have

$$\delta\lambda_i = \frac{\vec{\mu^\intercal}_i^0\delta\mathbf{M}\vec{\nu}_i^0}{\vec{\mu^\intercal}_i^0\vec{\nu}_i^0} \tag{2.74}$$

which is the first order correction to the eigenvalue λ_i of the transfer matrix.

This perturbation theory can potentially be used to study how ZMs exponentially grow or decay in disordered cell sheets. We applied this method to the periodic lattices we studied in the main text, and the results are consistent between the momentum space calculation described in the main text and the transfer matrix calculation. As we choose lattices in each topological phase in Fig. 2.5, the sign changes of $\delta\lambda$ agrees with the winding number jumps.

CHAPTER 3

Stress Control in Maxwell Lattices with Non-Ideal Springs

This chapter summarizes the work written in the manuscript "Stress Control in Non-Ideal Maxwell Lattices via Geometry" co-authored by Harry Liu, A. Nafis Arafat, Ethan Stanifer, Siddhartha Sarkar, and Xiaoming Mao. under preparation. The finalized version in the future publication may appear with more contexts than this Chapter.

3.1 Introduction

How materials respond to applied forces has been a crucial question to understand since ancient times when stable and robust machinery was desired. In the past decades, the role geometry plays in mechanical responses has begun to grasp the attention, and a set of materials named mechanical metamaterial, in which the mechanical properties are controlled by geometry, has been developed [85; 86; 87; 88; 89]. These innovative materials are invariant in composition and scale because of the consistency in geometry, and they offer many interesting engineering opportunities as they can possess many interesting features that sometimes do not appear in natural materials such as negative Poisson's ratio [90] and negative stiffness [91]. Among different mechanical metamaterials, a special class named Topological Mechanical Metamaterials (TMMs) in which the mechanical responses are governed by topology, making them robust and immune to defects [1; 30; 53]. TMMs can be realized in many different physical systems [86; 16], opening up opportunities to study many new fascinating physical phenomena and to engineer intriguing new applications [15; 92; 54; 23]. Among these interesting phenomena, one particular feature is the focusing of stress at the domain wall when two topologically distinct domains are connected together. The fact that stresses in the structure are focused at the domain wall provides protection against fracturing sites in the structure [54].

At the linear level, it was understood that a lattice can have both zero energy modes (ZMs) which allow the lattice to deform without energy cost, and states of self-stress (SSSs) which allow

the lattice to carry tensions without causing net force on the sites [1]. The ZMs and SSSs are related by the Maxwell-Calladine index, which is given by the number of degrees of freedom and the number of constraints in the lattice [29]. The SSSs supply a backbone for the lattices in response to external stresses [93] and offers an understanding of the aforementioned stress focusing and fracture protection phenomena [54].

Besides the theoretical advancement in TMMs and the proposed applications based on them, efforts have been made toward the engineering and manufacturing of TMMs [86; 28; 94; 34; 39]. One known difficulty in completing these tasks is the energy cost associated with hinge bending [86; 28; 34; 39], which is not captured in the theory of TMMs as free joints are assumed. The non-zero bending stiffness of the hinges has diminishing effects on the mechanical properties predicted by theory. It causes an elevation of the band for the ZMs, thus making them no longer zero energy, which leads to low contrast between the predicted hard and soft boundaries of the lattice [54]. It can also intensify the stresses at the joints away from where the SSSs are localized, which masks the focusing effect of the stress responses, and in the extreme case, causes fracturing at the sites instead of bonds [95; 5]. Despite the undesired engineering and manufacturing challenges it brings, the bending stiffness at the joints offers a new perspective for controlling the transformations of the lattices, through which the lattice is able to switch between topological domains [16].

To further understand the effect of the bending stiffness at the hinges and to design a simple way to minimize the negative effects it brings while maintaining the overall topological mechanical properties desired, we use both the Angular Spring Model (AS) and the Next-Nearest-Neighbor Model (NNN) in this study to numerically study the effect of bending stiffness on the domain wall stress focusing and to analytically understand the stress response at the hinges. Then by incorporating the AS and NNN springs, we manipulate the generalized kagome unit cell to minimize the excessive stress away from the domain wall, as well as to tune the stress responses according to the given strains. By minimizing the hinge stresses, site fracturing, which is seen more often in lattice structures, can be reduced. Whereas the tuning of stress responses with different given strains provides an opportunity for engineering TMMs that are suitable for different applications.

3.2 The Models and Simulations

When considering the manufacturing of TMMs, a continuum approach is usually required to study the hinge material effects on the topologically protected mechanical responses of the TMMs. However, to capture the hinge bending effect to the simplest level, an angular spring model (AS) and a linear level approximation of AS, the next nearest spring model (NNN) is sufficient and simple to conduct a numerical study on.

In this section, we first discuss how the structure's response caused by external strains can be projected and understood through the SSSs, which gives us an analytical expectation of the stress profile of the regular kagome network. Then we subsequently introduce the AS and NNN models, demonstrate the numerical results on the stress distribution in the network after the angular or the NNN springs are added, and explain how they reflect the leading order of the continuum description. In the last part of this section, we demonstrate the different stress responses of networks when different strains are given.

3.2.1 States of Self-stresses and Strain Projection

For a Maxwell lattice of N sites and N_c bonds in d dimensions, the elastic energy can be written as

$$H = \sum_{\langle ij \rangle \in NN} \frac{k_{ij}}{2} \left(\vec{l}_{ij} - \vec{l}_{ij}^{0} \right)^2 \tag{3.1}$$

for springs $\vec{l}_{ij} = \vec{r}_i - \vec{r}_j + \vec{u}_i - \vec{u}_j$, where $\vec{u}_i$ and $\vec{u}_j$ are the displacements of the sites $\vec{r}_i$ and $\vec{r}_j$ that the spring $\vec{l}_{ij}$ connects, with lengths $l_{ij} = \left| \vec{l}_{ij} \right|$, springs constant k_{ij}, and rest lengths $l_{ij}^0 = |\vec{r}_i - \vec{r}_j|$. The energy is summed over all nearest neighbor (NN) bonds. To the linear level, the elastic energy is approximated as

$$H = \frac{1}{2} \vec{u} \cdot \mathbf{D} \cdot \vec{u} \tag{3.2}$$

where $\vec{u}$ is the displacement field of the lattice, $\mathbf{D} = \mathbf{C}^\intercal \cdot \mathbf{k} \cdot \mathbf{C} = \mathbf{Q} \cdot \mathbf{k} \cdot \mathbf{Q}^\intercal$ is the dynamical matrix, in which $\mathbf{k}$ is the diagonal matrix with springs constants as of all bonds as its entries, $\mathbf{C}$ is the compatibility matrix that relates the dN-dimensional site displacement vectors $\vec{u}$ to the N_c-dimensional vector of bond extensions $\vec{e}$, and $\mathbf{Q} = \mathbf{C}^\intercal$ is the equilibrium matrix that relates the N_c-dimensional bond tensions $\vec{t}$ to the dN-dimensional vector of forces on sites [1]:

$$\mathbf{C} \cdot \vec{u} = \vec{e}, \quad \mathbf{Q} \cdot \vec{t} = \vec{f}. \tag{3.3}$$

The entries of the $\mathbf{C}$ matrix are determined by the equation for the extension of the springs $\vec{l}_{ij}$:

$$e_{ij} = \hat{l}_{ij} \cdot (\vec{u}_i - \vec{u}_j), \tag{3.4}$$

where $\hat{l}_{ij}$ is the unit vector of the spring $\vec{l}_{ij}$. The null space of $\mathbf{C}$ gives the ZMs as it represents a set of site displacements that cause no bond extensions, and the null space of the $\mathbf{Q}$ represents SSSs as it represents a set of bond tensions that cause no net force on the sites.

The stress focusing can be understood through the SSSs of the network, and a projection of the external strains onto the states of self-stresses [54]. In real space, $\mathbf{C}$ and $\mathbf{Q}$ can be separated into

the bulk (denoted by the subscript V) and boundary (denoted by the subscript ∂V) contributions. Separating the contributions from the bulk and the boundary, we have

$$\vec{f}_V = \mathbf{Q}_V \vec{t} \tag{3.5}$$

$$\vec{e} = \mathbf{C}_V \vec{u}_V + \mathbf{C}_{\partial V} \vec{u}_{\partial V}, \tag{3.6}$$

where boundary displacement $\vec{u}_{\partial V}$ is given. Then we can solve under force balance $\vec{f}_V = \mathbf{Q}_V \vec{t} = 0$ for $\vec{t}$, which is a linear combination of the null space of $\mathbf{Q}_V$ (the SSSs of the bulk), i.e. $\vec{t} = \sum_i a_i \vec{s}_i$, where $\vec{s}_i$ is a complete orthonormal basis of the SSSs. The tensions can be then further simplified to [54]

$$\vec{t} = \sum_{i,j} \left[\left(\mathbf{s}\, \mathbf{k}^{-1} \mathbf{s} \right)^{-1} \right]_{ij} (s_j \cdot \mathbf{C}_{\partial V} \vec{u}_{\partial V}) s_i, \tag{3.7}$$

where $\mathbf{s}$ is the matrix whose column are the SSSs $\vec{s}_i$.

For a homogeneous system with translation symmetry, it is easier to work with the compatibility matrix in Fourier space $\mathbf{C}(\mathbf{q})$, which is $n_c \times nd$ matrix, (where n_c is the number of bonds per unit cell and n is the number of sites per unit cell). AS shown in the seminal paper by Kane and Lubensky [1], for a system with a domain wall between two different Maxwell lattices, the number of SSSs localized at a the domain wall can be calculated from the properties of the $\mathbf{C}(\mathbf{q})$ matrices of each Maxwell lattice; below we describe this briefly and discuss the consequences for our specific system shown in Fig. 3.1(a).

From the compatibility matrix $\mathbf{C}(\mathbf{q})$ of a homogeneous lattice at the Maxwell point (i.e., $n_c = nd$) in Fourier space, the dynamical matrix can be obtained as $\mathbf{D}(\mathbf{q}) = \mathbf{C}^\dagger(\mathbf{q})\mathbf{C}(\mathbf{q})$ (where we chose the spring constants and the masses of the particles to be 1 for simplicity). The normal mode frequencies of the lattice $\omega^2(\mathbf{q})$ are the eigenvalues of the Dynamical matrix $\mathbf{D}(\mathbf{q})$. Kane and Lubensky [1] defined a 'square root' of the dynamical matrix, which in reciprocal space takes the following form:

$$\mathcal{H}(\mathbf{q}) = \begin{pmatrix} \mathbf{0} & \mathbf{C}^\dagger(\mathbf{q}) \\ \mathbf{C}(\mathbf{q}) & \mathbf{0} \end{pmatrix}. \tag{3.8}$$

For every nonzero eigenvalue $\omega^2(\mathbf{q})$ of $\mathbf{D}(\mathbf{q})$, $\mathcal{H}(\mathbf{q})$ has two eigenvalues $\pm\omega(\mathbf{q})$. The zero modes of $\mathcal{H}(\mathbf{q})$ include nullspace of $\mathbf{C}(\mathbf{q})$ (zero modes – ZMs) and nullspace of $\mathbf{C}^\dagger(\mathbf{q})$ (states of self stress – SSSs), whereas the zero modes of $D(\mathbf{q})$ include the ZMs. Maxwell Calladine theorem [29] dictates that the number of ZMs (n_0) and number of SSSs (n_s) are equal ($n_0 = n_s$) for a Maxwell lattice. The matrix $\mathcal{H}(\mathbf{q})$ has the property that $S\mathcal{H}(\mathbf{q})S = -\mathcal{H}(\mathbf{q})$, where $S = \text{Diag}\{\mathbb{1}, -\mathbb{1}\}$. This property is known as chiral (or sublattice) (anti)symmetry in the literature. Also, it is easy to check that $\mathcal{H}(\mathbf{q})$ has time-reversal symmetry: $\mathcal{H}(\mathbf{q}) = \mathcal{H}^*(-\mathbf{q})$, where * is complex conjugation. These two symmetries put the matrix $\mathcal{H}(\mathbf{q})$ in BDI class of Altland Zirnbauer (AZ) classification [96].

According to the AZ periodic table [97] BDI (or AIII if we exclude time-reversal symmetry) class has a $\mathbb{Z}$ topological index in 1D. Hence, a topological polarization vector $\mathbf{R}_T$ of a 2D Maxwell lattice can be defined as

$$\begin{aligned} \mathbf{R}_T &= \sum_i n_i \mathbf{a}_i, \\ n_i &= \frac{1}{2\pi i} \oint_{\mathbf{q}\to\mathbf{q}+\mathbf{G}_i} d\mathbf{q} \cdot \nabla_{\mathbf{q}} \log\det \mathbf{C}^{\dagger}(\mathbf{q}), \end{aligned} \tag{3.9}$$

where $\mathbf{a}_i$ are the lattice vectors, $\mathbf{G}_i$ are the reciprocal lattice vectors such that $\mathbf{G}_i \cdot \mathbf{a}_j = 2\pi\delta_{ij}$, and $n_i \in \mathbb{Z}$. Note that this definition of polarization is only applicable if the $\mathbf{C}(\mathbf{q})$ is a square matrix with $n_c = nd$ or in other words the lattice is Maxwell. Also, we assumed that there are no bulk ZMs (except the uniform translations); hence, the integers n_i do not depend on $\mathbf{q}$. It was shown in [1] that at a domain wall between two Maxwell lattices the total number of ZMs at the domain wall at every wave number q parallel to the domain wall is given by

$$n_{dw} = \frac{1}{2\pi}\mathbf{G} \cdot (\mathbf{R}_T^L - \mathbf{R}_T^R), \tag{3.10}$$

where the superscripts L and R denote systems on the left and right of the domain wall respectively, $\mathbf{G}$ is the smallest reciprocal lattice vector pointing from left to right of the domain wall, and we assumed that the polarizations for both systems were calculated in the same gauge. Note that if this number is positive, it counts the number of ZMs, whereas if the number is negative, its absolute value counts the number of SSSs [1].

For the system shown in Fig. 3.1(a), $\mathbf{R}_T^L = -\mathbf{a}_1$, $\mathbf{R}_T^R = \mathbf{a}_1$ and $\mathbf{G} = 2\mathbf{G}_1 - \mathbf{G}_2$ (where $\mathbf{a}_1 = (1, 0)$, $\mathbf{a}_2 = (-0.5, 0.7)$, $\mathbf{G}_1 = 2\pi(1, 1/1.4)$, $\mathbf{G}_2 = 2\pi(0, 1/0.7)$); consequently $n_{dw} = -4$, which implies that there are 4 SSSs at each wavenumber q parallel to the domain wall. However, the projection of homogeneous strains on the SSSs are only nonzero for SSSs at wave-number $q = 0$ [54]. Moreover, among the 4 SSSs that should be there at $q = 0$ (see Fig. 3.1(b-e)), two SSSs (Fig. 3.1(d-e)) get lifted to finite energy when the system is finite in x-direction due to the fact that they have large penetration depth (i.e., decay length away from the domain wall), whereas the two which have small penetration depth (Fig. 3.1(b-c)) remain at zero energy [1]. Under the application of uniaxial stress (as shown in Fig. 3.1(a)), these two SSSs (which are highly localized near the domain wall) carry most of the load; consequently we see stress focusing in Fig. 3.1(a). (The fact that there has to be at least two SSSs at $q = 0$ is protected by translation symmetry, which implies that there are two zero modes at $q = 0$, and consequently two SSSs). Moreover, the localized SSS in Fig. 3.1(c) has both tensions and compressions (red and blue colored bonds, respectively); hence the projection of an affine uniaxial strain on it is negligible compared to the projection of the affine uniaxial strain in the SSS in Fig. 3.1(b). This is why the numerical result in

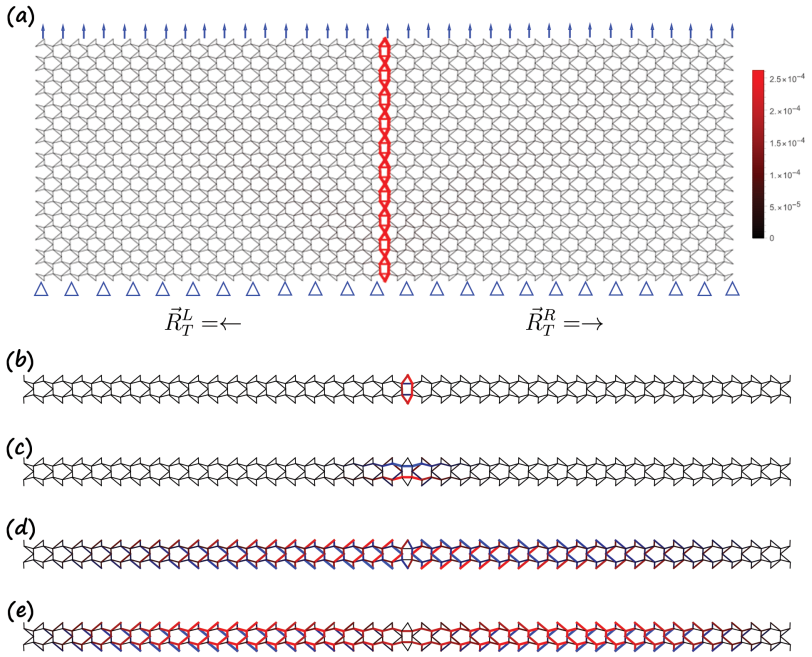

Figure 3.1: Comparison between simulation and the supercell analysis results. (a): A energy minimized simulation by fixing the bottom boundary and giving a vertical displacement on all sites at the top boundary with a magnitude $u = 10^{-3}$. The left and right boundaries are entirely free, and sliding is allowed for the top and bottom boundaries. The triangle marks the fixed boundary and the arrows mark the displaced boundary. The topological polarization vectors $\vec{R_T}$ for the left and right domains are shown with arrows. The intensity of the red color and the thickness of the bonds both increase with the magnitude of stress on the bonds. The maximum stress in the response $t_{max} = 2.6 \times 10^{-4}$ in units of force. (b), (c), (d), (e): 4 states of Self-stress calculated from the supercell analysis. each supercell is periodic in $\hat{y}$-direction and open in $\hat{x}$-direction. The SSSs are all calculated at $\mathbf{q} = 0$. The red and blue represent tension and compression for the SSS respectively, and the thicknesses are proportional to the magnitudes on the bonds. The SSSs in (b) and (c) remain at zero energy thus contributing to the stresses at the domain wall as shown in (a), but the SSSs in (d) and (e) are elevated into the bulk with a large penetration depth due to the open boundaries.

Fig. 3.1(a) closely resembles the SSS in Fig. 3.1(b).

A numerical simulation is then performed to compare with the super-cell analysis. In the simulation, an axial displacement of $10^{-3} \ll 1$ in $\hat{y}$-direction is applied to all sites at the top boundary, and sites on the bottom boundary are pinned in the $\hat{y}$-direction while the left and right boundaries are left open. Clear stress focusing on the domain is seen in the simulation, as well as a match with the SSSs from the super-cell analysis, as shown in Fig. 3.1.

3.2.2 Angular Spring Model

One model we have used to capture the bending stiffness at the sites is the Angular Spring Model (AS). The model associates an energy cost to the angular change from the rest angles with quadratic form.

$$H_\theta = \sum_{i,jk} \frac{\kappa_{\theta_{i,jk}}}{2} \left(\theta_{i,jk} - \theta^0_{i,jk}\right)^2 \tag{3.11}$$

where $\kappa_{\theta_{i,jk}}$ and $\theta^0_{i,jk}$ are the angular spring constant and the rest angle for angle $\theta_{i,jk}$ formed by the central site i and it's neighboring sites j, k. From the AS energy function, the forces on the particles i, j, k from each angle

$$F_{l\alpha} = -\sum_{\{i,jk\}} \kappa_{\theta_{i,jk}} \left(\theta_{i,jk} - \theta^0_{i,jk}\right) \frac{\partial \theta_{i,jk}}{\partial x_{l\alpha}}. \tag{3.12}$$

can be calculated by taking the first derivative of 3.11 to reflect the bending stresses in the lattice. A detailed full expression of the AS force and the angle convention we used can be found in the appendix 3.5.1. The AS energy and the AS force are then implemented into an energy minimization method with the minimization of the regular linear springs of the lattice to find the equilibrium state and then calculate the tensions in the lattice, for both the nearest neighbor (NN) bonds and the AS.

Compared to Fig. 3.1, the inclusion of AS elevates the maximal stress on the domain wall, as well as the stress at sites away from the domain wall even with an AS constant $\kappa_\theta = 10^{-4}$ when the regular bond has a spring constant $k = 1$, where we have taken for simplicity that there is no difference among all regular bonds $k_{ij} = k$ and all the AS $\kappa_{\theta_{i,jk}} = \kappa_\theta$. The tension profile also shows an inhomogeneous distribution of the AS stress across the lattice, which signifies acute points of high-stress bearing, and these sites would be more probable to fracture compared to others. Furthermore, the total stresses at all sites increase with an increasing AS constant κ_θ as shown in Fig. 3.2(b) and (c), and eventually the stress away from the domain rises up to magnitudes comparable to the stress at the domain wall so the stress focusing effect at the domain wall gets masked. Such a masking phenomenon happens when $\kappa_\theta \approx 10^{-2}$

The AS model successfully captures the expected masking effect of the focused stress from bending stiffness at the hinges, but due to its nature of a multi-body interaction for the angles, it is slightly difficult to design and control the geometric parameters of the lattice to minimize the inhomogeneous AS stress distribution as well as the masking threshold of the focused stress at the domain wall. Therefore, to capture the essential information given by the AS model to the simplest level, a next-nearest-neighbor model (NNN) is used instead of the full AS model.

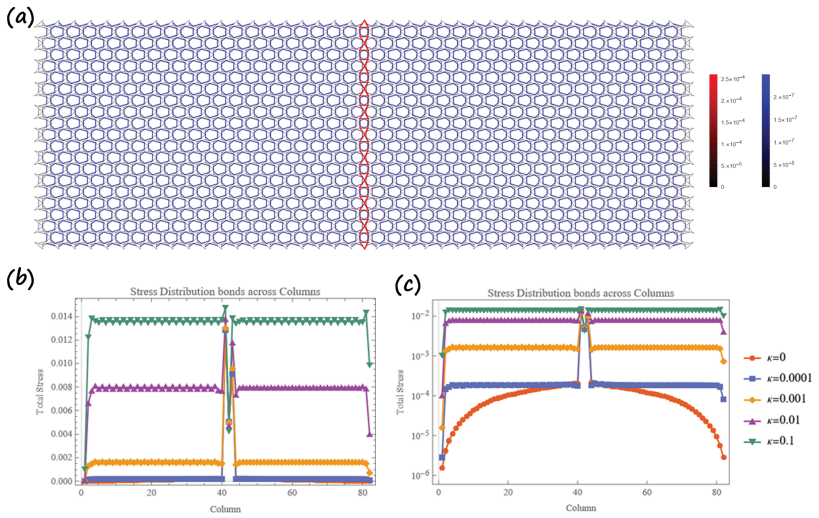

Figure 3.2: Vertical pull simulation with the inclusion of angular springs (AS). (a): An energy minimization simulation as the one described in Fig. 3.1(a), but with the inclusion of angular spring constant$\kappa_\theta = 10^{-4}$. The maximum tension on the NN bonds is $t^{NN}_{max} = 2.59 \times 10^{-4}$ in the units of force, and $t^{AS}_{max} = 2.48 \times 10^{-7}$ on the AS. The NN bonds are labeled in red, while the AS are represented in blue. The intensity of the color increases with the stress magnitude. (b): The total stress on bonds across columns in the lattice. The stresses on the vertical axis are shown on a linear scale, and the horizontal axis labels the column index of the lattice. The spiking of stress magnitude at the domain wall is shown in this figure. (c): The total stress on bonds across columns on a log scale, which shows the drastic increase of stress away from the domain wall as κ_θ increases.

3.2.3 Next-Nearest-Neighbor Model

In the regime of small angle bending $\theta \ll 1$, the NNN model and AS model are approximately the same as each AS is modeled to be a spring that connects the two sites $\vec{r}_j$ and $\vec{r}_k$ at the ends of the angle centered at site $\vec{r}_i$. The energy associated with the NNN bonds is written as

$$H_{NNN} = \sum_{\langle j,k\rangle \in NNN} \frac{\kappa_{jk}}{2}\left(\vec{l}_{jk} - \vec{l}^{\,0}_{jk}\right)^2. \tag{3.13}$$

It takes the same form as Eq. (3.1), but we now take the site pairs $\vec{r}_j$ and $\vec{r}_k$ that are next-nearest-neighbors. For simplicity, we again assume the NNN spring constants are homogeneous across the lattice, i.e. $\kappa_{jk} = \kappa_{NNN}$. The AS constant κ_θ and NNN constant κ_{NNN} are related by a geometric parameter which is determined by the geometry of the unit cell, as it shows how much an NNN

spring changes in length as the corresponding angle changes:

$$\kappa_{NNN} = -\frac{l_{ij} l_{ik} \sin\theta}{\sqrt{l_{ij}^2 + l_{ik}^2 - 2 l_{ij} l_{ik} \cos\theta}} \kappa_\theta. \tag{3.14}$$

The same numerical simulation as for the AS model is done for the NNN model as well, and the results in Fig. 3.3 show apparent similarity with the AS model. The stress focusing is apparent at the domain wall, as well as a distribution of NNN stress away from the domain wall is observed that preserves a similar pattern as the AS stress. The masking effect on the stress focusing is also observed as κ_θ increases in magnitude, however, the elevation of the magnitudes of the stress away from the domain wall in the NNN model is slower than in the AS model because NNN only captures the lowest order effect of the AS model. Nevertheless, the NNN model enables us an easy way to understand the effect of bending stiffness at the hinges as well as to design new geometries to lower the bending stresses while maintaining the stress-focusing effect at the domain wall.

The fact that the total stress at every cell increases with increasing κ_{NNN} in Fig. 3.3(b-c) can be explained as follows. With the addition of the 6 NNN bonds per unit cell, the number of constraints in each unit cell is 6 more than the number of degrees of freedom. As a consequence, for the homogeneous system on either side of the domains, the matrix $\mathbf{Q}(\mathbf{q}) \equiv \mathbf{C}^\dagger(\mathbf{q})$ is 6×12, which implies that there are $12-6 = 6$ SSSs at every $\mathbf{q}$. These extra SSSs can carry some of the load from external strain. To see this we create a supercell with a domain wall between two homogeneous systems (as shown in Fig. 3.3(d)) with $N_0 = 20$ domain wall compatible unit cells (note that a domain wall compatible unit cell has twice as many degrees of freedom as a primitive unit cell) on each side of the domain wall. In total there are $6\times 2N_0+1 = 241$ particles (482 degrees of freedom) and 954 bonds. We apply an open boundary condition in the x-direction and the Bloch-periodic boundary condition in the y-direction. Due to the excess of bonds ($954-482 = 472$), at every wave number q parallel to the domain wall there are 472 bulk SSSs. At $q = 0$, the number of SSSs is 474 (the extra two are due to translation symmetry). Among these 474 SSSs, 2 are localized at the domain wall (these were present in the nearest neighbor model), and 472 are bulk SSSs appearing due to excess of bonds at every unit cell. In principle, an affine uniaxial strain will be carried by all of these SSSs. However, when the ratio of the bond stiffness $\kappa_{NNN}/k_{NN} \ll 1$, the projection of bond tensions corresponding to the affine uniaxial strain on the bulk SSSs is much smaller than on the domain wall SSSs (which are supported by the nearest neighbor bonds since they were present in the nearest neighbor model), consequently most of the stress would be concentrated at the domain wall. As we increase κ_{NNN}/k_{NN}, the projection of bond tensions corresponding to the affine uniaxial strain on the bulk SSSs increases, and we see more even distribution everywhere in the system. To make this argument quantitative, we apply an affine uniaxial strain ϵ_{yy} to the supercell, and calculate the bond tensions at equilibrium for different values of κ_{NNN}/k_{NN}. To

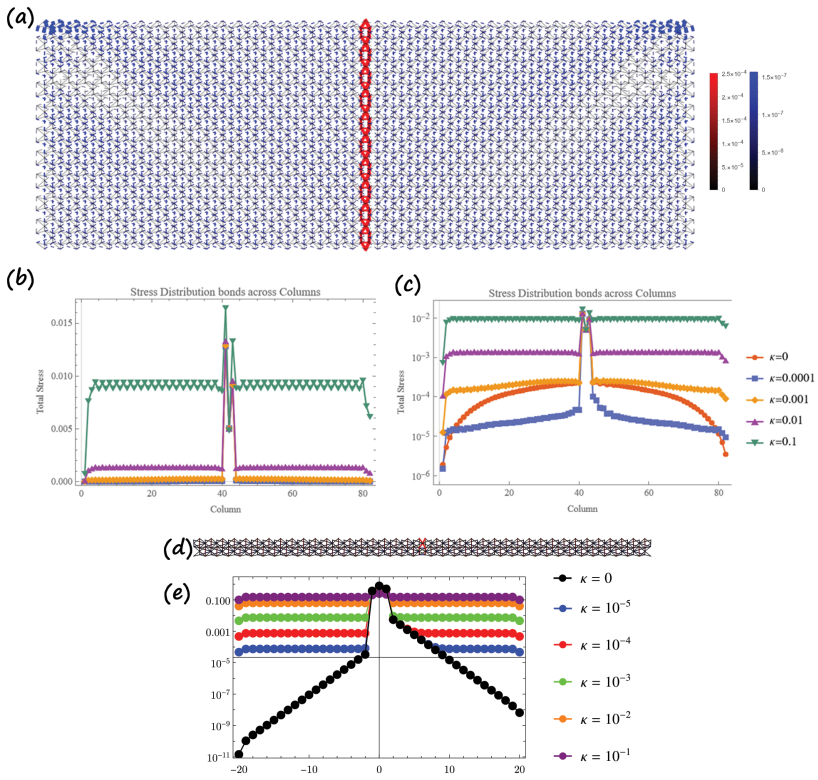

Figure 3.3: Vertical pull simulation with the inclusion of NNN springs. (a): An energy minimization simulation as the one described in Fig. 3.2(a), but with the inclusion of NNN spring constant$\kappa_{NNN} = 10^{-4}$. The maximum tension on the NN bonds is $t_{max}^{NN} = 2.55 \times 10^{-4}$ in the units of force, and $t_{max}^{NNN} = 1.56 \times 10^{-7}$ on the NNN bonds. The NN bonds are labeled in red, while the NNN bonds are represented in blue. The intensity of the color increases with the stress magnitude. (b): The total stress on bonds across columns in the lattice. The stresses on the vertical axis are shown on a linear scale, and the horizontal axis labels the column index of the lattice. The spiking of stress magnitude at the domain wall is shown in this figure. (c): The total stress on bonds across columns on a log scale, which shows the drastic increase of stress away from the domain wall as κ_{NNN} increases. The similarity with Fig. 3.2 is observed in this figure, validating the proximity between the AS and NNN spring models. (d): A representation of the SSS calculated by the supercell analysis with a periodicity in y after the inclusion of the NNN springs. The NN springs stress is represented in red and the NNN stress in blue, with the color intensity proportional to the magnitude of the stress. (e): Stress in unit cells plotted across the columns in a log scale from the supercell analysis with periodicity in y, which is analogous to (c) from the numerical simulation.

do that, we first note that under strain ϵ_{yy}, i^{th} bond gets stretched by amount $e_{\text{aff},i} = \epsilon_{yy} \sin^2 \theta_i$, where θ_i is the angle between i^{th} bond and the x-direction. Defining $\mathbf{e}_{\text{aff}}$ as the vector of the affine

elongations $e_{\text{aff},i}$, one can show that vector of the bond tensions $\mathbf{t}$ to be [30]

$$\mathbf{t} = \sum_i \left(\left[\left(\mathbf{K}^{-1} \right)_{ss} \right]^{-1} \mathbf{e}_{\text{aff},s} \right)_i \mathbf{s}_i, \tag{3.15}$$

where $\mathbf{s}_i$ are the SSSs, $\mathbf{e}_{\text{aff},s}$ is vector of projections $e^i_{\text{aff},s} = \mathbf{e}_{\text{aff}} \cdot \mathbf{s}_i$, $\left(\mathbf{K}^{-1}\right)_{ss} = [\mathbf{s}]^T \mathbf{K}^{-1} [\mathbf{s}]$ where $\mathbf{K}$ is the matrix of bond stiffness and $[\mathbf{s}]$ is the matrix consisting of column vectors $\mathbf{s}_i$. Fig. 3.3(e) shows the resultant bond tensions as a function of position for different value κ_{NNN} (we chose $k_{NN} = 1$ and $e_{yy} = 1$ for this calculation). When $\kappa_{NNN} = 0$, we see that bond tensions decay exponentially away from the domain wall (the black curve in Fig. 3.3(e)) meaning that the stress is only carried by the SSSs (see Fig. 3.1(b)) localized at the domain wall. As we turn on κ_{NNN}, the bond tension becomes constant (Fig. 3.3(e)) away from the domain wall because of nonzero projection of the affine strain onto the bulk SSSs, and the value of this constant increases with increasing κ_{NNN}.

3.2.4 Responses of Different Strains

Furthermore, we examined the behavior of the lattice under different loaded strains, here we show the effect of gravity, dipole force, and gravity in a kagome lattice with SSS domain walls in Fig. 3.4.

To simulate the lattice under gravity, we give an initial force to all the sites in the lattice, while fixing the bottom boundary of the lattice in $\hat{y}$-direction. The energy minimized result shows that the SSSs focused at the domain wall are excited and a clear stress focusing is seen at the domain wall. The effect of gravity would give a strain to the lattice in the $\vec{y}$-direction, which has projection to the SSSs at the domain wall, and causes the excitement of the SSSs and the appearance of stress focusing at the domain wall.

The shear strain is simulated by giving an affine simple shear strain to the lattice by giving a gradually increasing displacement in $\hat{x}$-direction from the bottom boundary to the top boundary up to a maximum distance $u_{max} = 10^{-3}$ with the bottom boundary and the top boundary then fixed, then the lattice relaxes to the equilibrium configuration. The resulting stress in the lattice responding to the shear strain shows no stress focusing on the domain wall as the shear strain does not project to the SSSs of the lattice. However, as we will show in Sec. 3.3.3, the projection of the shear strain onto an SSS can happen to demonstrate stress focusing on the domain wall when the domain wall is designed to be tilted instead of vertical. Furthermore, examining the pattern of tension and compression, they are mirror symmetric against both the domain wall and the middle horizontal row. Which is caused by force balance.

The dipole force is simulated by giving tension forces at the opposite sites of a chosen bond

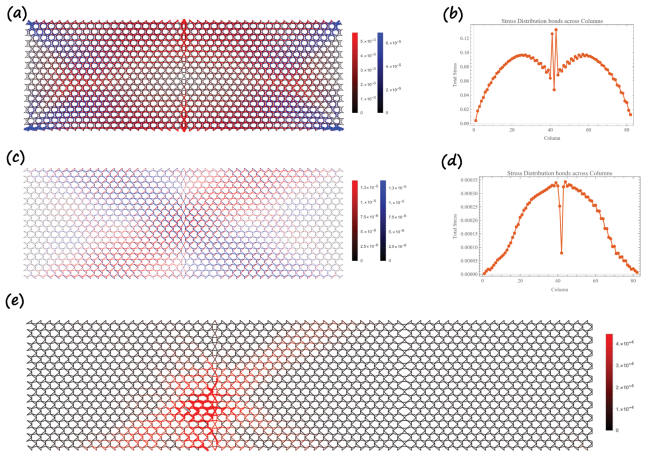

Figure 3.4: Kagome lattice with SSS domain wall under different given strains. The lattice configuration is identical to the one used in Fig. 3.1, Fig. 3.2, and Fig. 3.3. (a): The gravitational effect on the lattice with angular springs. The mass of sites are identically $m = 5 \times 10^{-6}$, and the angular spring constants are $\kappa_\theta = 10^{-4}$ in unit of force/angle. The response NN stress is shown in red, and the AS response is shown in blue. The thickness and the color intensity of the bonds are proportional to the magnitude of the stress. The response shows a maximum NN stress $t^{NN}_{max} = 5.56 \times 10^{-3}$ concentrated at the domain wall, and a maximum AS stress $t^{AS}_{max} = 6.85 \times 10^{-5}$ concentrated at the lattice corners. The concentration of stress at the domain wall demonstrates the excitation of SSSs in the lattice by gravity, which is more clearly seen in (b). (b): The total stresses of bonds for each column, the peak in the middle represents the large stress bearing by the domain wall. (c): The kagome lattice under a simple shear with NN bonds only. The lattice is given an affine shear with the maximum displacement at the top boundary to the right with a magnitude $u_{max} = 10^{-3}$, which is roughly 1.5×10^{-3} times of the bond lengths, then the top boundary and the bottom boundaries are both clamped after the simple shear strain is given. The response in the network is separated into tension and compression, where tension is shown in red and compression is shown in blue. The thickness and the color intensity of the bonds are proportional to the magnitudes of the tension and compression. The maximum tension and the maximum compression are equal in magnitude $t^t_{max} = t^c_{max} = 1.36 \times 10^{-5}$ in the lattice. (d): The total stresses of bonds across columns, the absolute magnitudes of the tension and compression are summed for each column. The drop of stress magnitude at the domain wall indicates there is no excitation of the SSSs at the domain wall, thus no stress focusing. (e): The response of the lattice with NN bonds only after a dipole force is given on a bond close to the SSS domain wall. The dipole force is given by setting the rest length of the chosen bond (colored in cyan) to be 1.05 times the original length in the lattice, thus exerting equal and opposite forces on the two sites the bond connects, and the top and the bottom boundaries are fixed in this simulation as sliding boundaries would cause the lattice to relax to a configuration with only overwhelming stress on the bond exerting dipole force. The stress response of the lattice is colored in red, with the bond thickness and color intensity proportional to the magnitude of the stress. The maximum stress in the response $t_{max} = 4.4 \times 10^{-4}$.

while holding the top and bottom boundaries fixed in the $\hat{y}$-direction. Different stress responses were observed given the location of the dipole force applied relative to the domain walls. However, a generic profile of concentrated stress appears around where the dipole forces are applied. Furthermore, a screening effect provided by the domain wall appears, as the stresses reduce in magnitude after passing through the domain wall (shown in Fig. 3.4(e)). This effect can be understood through an earlier study on the dipole force in kagome lattice, in which a polarized strain and stress responses are shown [22], and the strain caused by the dipole force, when gets close to the domain wall, would have components projected to the SSSs, thus having stress concentrated at the domain wall rather than the domain past it.

The tests involving different strain conditions applied to the lattice show that SSSs would only be excited by the applied strain if components of the strain can be projected to the SSSs, which leads to a further design of lattices that focus stresses on the domain wall when responding to different strains, and the shear strain is of the main consideration in this case.

3.3 Kagome Lattice Design

To design a kagome lattice that lowers the focused stress at the domain wall as well as the bending stresses at the hinges or a lattice with domain walls that focus stress when responding to different strains, we examine a generalized kagome lattice unit cell that includes both the regular bonds and the NNN bonds and adopt the parameters $X = (x_1, x_2, x_3; z)$ that labels the "zigzagging" along three vectors of the unit cell and the dilation of the unit cell illustrated in the work that first theorized topological mechanics [1]. We then examine the effect of the parameters X on the kagome lattice formed by the NNN lattice as well to control the stress on the NNN bonds.

3.3.1 Generalized Kagome Lattice

In the generalized kagome lattice (GKL), as the NNN bonds are also included, for the 3 sites in the unit cell, 2 additional bonds are attached to each site, thus making the total number of bonds 12, 6 for the regular bonds and 6 NNN bonds, as shown in Fig. 3.5. Another observation of the kagome lattice with NNN inclusion is that the network formed by only NNN bonds is constructed by a kagome lattice that is different from the kagome lattice formed by the regular bonds. Furthermore, it is constructed by 3 layers of the same kagome lattice shifted by the primitive vector $\vec{a}_1$ of the regular kagome lattice, and its geometry changes according to the kagome lattice formed by the regular bonds.

For the regular bonds, according to the parameters $X = (x_1, x_2, x_3; z)$, x_i "zigzags" the bonds along vector $\vec{a}_i$ while maintaining the bonds in the other 2 directions straight, while z uniformly

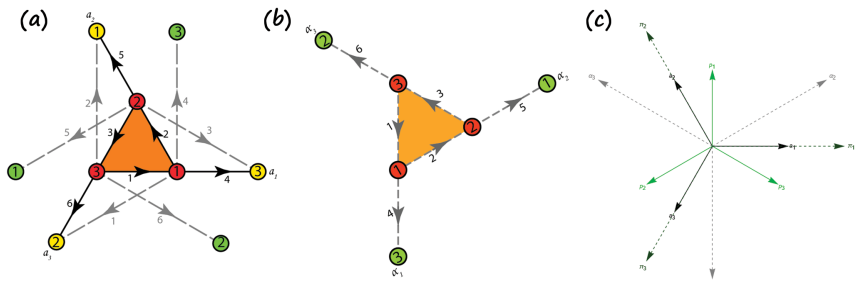

Figure 3.5: (a): Unit cell of the GKL, the black solid lines represent the regular bonds and the gray dashed one the NNN bonds. The red sites are the sites in this unit cell and the green and yellow ones represent the same sites in the neighboring unit cells. $\vec{a}_1$ and $\vec{a}_2$ are the 2 primitive unit vectors, and $\vec{a}_3 = -(\vec{a}_1 + \vec{a}_2)$ completes the 3-fold symmetric basis for the parameters $X = (x_1, x_2, x_3; z)$. The 3 sites of the unit cell labeled in red have positions $\vec{r}_1 = \vec{a}_1/2$, $\vec{r}_2 = -\vec{a}_3/2$, and $\vec{r}_3 = 0$. (b): Unit cell of the NNN kagome lattice that composes one of the three layers of NNN network. The red sites are the sites in this unit cell and the green ones represent the same sites in the neighboring unit cells. The dashed gray lines represent the bonds in the NNN kagome unit cell, $\vec{\alpha}_1$ and $\vec{\alpha}_2$ are the 2 primitive unit vectors, and $\vec{\alpha}_3 = -(\vec{\alpha}_1 + \vec{\alpha}_2)$ completes the same 3-fold symmetric basis for the parameters $X = (x_1, x_2, x_3; z)$ that can introduce symmetric twisting of the NNN kagome unit cell. The 3 sites of the unit cell labeled in red have positions $\vec{\rho}_1 = \vec{a}_1/2$, $\vec{\rho}_2 = -\vec{a}_3/2 + \vec{a}_1$, and $\vec{\rho}_3 = -\vec{a}_3$. (c): The primitive vectors and their $\pi/2$ rotated counterparts. The primitive vectors $\vec{a}_i$ of the NN lattice with the convention shown in (a) is shown in solid black arrows, and their perpendicular counterparts $\vec{p}_i$ are shown in solid green arrows. The primitive vectors $\vec{\alpha}_i$ of the NNN lattice unit cell in (b) are labeled by dashed gray arrows, with their perpendicular counterparts $\vec{\pi}_i$ labeled in dashed dark green arrows. The relation of NN and NNN lattice primitive vectors are that $\vec{a}_i$ align exactly with $\vec{\pi}_i$, and $\vec{p}_i$ align with $\vec{\alpha}_i$ but with opposite directions.

dilates the unit cell. The new sites $\vec{R}_i$ from the transformation of the sites $\vec{r}_i$ is given by

$$\vec{R}_i = \vec{r}_i - \sqrt{3} x_i \vec{p}_i + x_{i-1}\vec{a}_{i+1} + \frac{z}{\sqrt{3}}\vec{p}_{i-1}, \tag{3.16}$$

Where $\vec{p}_i$ are $\vec{a}_i$ rotated by $\frac{\pi}{2}$ counterclockwise such that $\vec{a}_i \cdot \vec{p}_i = 0$ (shown in Fig. 3.5(c)), and the subscripts $i = 1, 2, 3$ are cyclic. This parameterization also offers a simple way to calculate the topological polarization vector as $\vec{R_T} = \frac{1}{2}\sum_{i=1}^{3} Sgn(x_i)\vec{a}_i$ [1; 53].

As for the NNN bonds, it can also be reorganized into a symmetric convention similar to the one for the regular bonds shown in Fig. 3.5(a), and in this convention for defining the NNN bonds unit cell, the primitive vectors for the NNN kagome lattice align with those of the regular bond kagome lattice, as shown in Fig. 3.5(b). The sites $\vec{r}_i^{NNN}$ in this convention are transformed to the new coordinates $\vec{R}_i^{NNN}$ as

$$\vec{R}_i^{NNN} = \vec{r}_i^{NNN} + x_i\vec{\alpha}_i + \frac{1}{\sqrt{3}} x_{i-1}\vec{\pi}_{i+1} - \frac{z}{3}\vec{\alpha}_{i-1} \tag{3.17}$$

by the same parameters $X = (x_1, x_2, x_3; z)$. In the NNN unit cells shown in Fig. 3.5(b), the X parameter changes the NNN bonds in a way such that x_i keep the bonds along $\vec{\alpha}_i$ straight while making the bonds in the other 2 directions $\vec{\alpha}_{i-1}$ and $\vec{\alpha}_{i+1}$ "zigzagged", and the parameter z introduces a rotation to the basis triangle around its center.

With the understanding of these rules, we are able to design lattices of different types by desire. We can not only change the geometry such that the maximum stress in the lattice is reduced, but also a lattice that focuses the stress for shear strain.

3.3.2 Stress Lowering Lattice

According to the rules elaborated in section 3.3.1, a lattice that lowers the maximum stress as well as changes the stress distribution can be designed by choosing appropriate X parameters. One of such configurations is shown below in Fig. 3.6

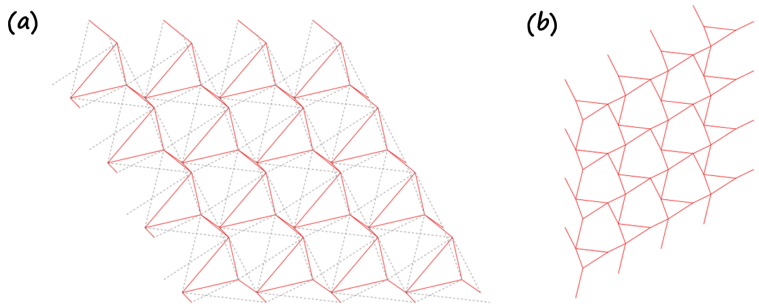

Figure 3.6: The designed twisted kagome lattice that lowers the stress on both NN and NNN bonds, as well as homogenizes the NNN stress in the lattice. (a) A 4×4 twisted kagome lattice is shown in red solid lines, with the NNN connection shown in dashed gray lines. (b) The kagome lattice composed by the NNN bonds in this designed lattice is shown in (a). The red bonds can be matched back to the gray dashed bonds in (a)

By doing so, we successfully lowered the maximum tension in NN bonds from $t_{old}^{NN} = 2.55 \times 10^{-4}$ to $t_{new}^{NN} = 1.68 \times 10^{-4}$, as shown in Fig. 3.7, the figure also illustrates the homogenization of the NN bond tensions in the lattice as the previously observed concentration of NNN stress at the corners of the old lattice in Fig. 3.3 no longer appears. Furthermore, the maximum tension of the NNN bonds was reduced from $t_{old}^{NNN} = 1.56 \times 10^{-7}$ to $t_{new}^{NNN} = 1.49 \times 10^{-7}$, as shown in Fig. 3.7.

3.3.3 Shear Focusing Lattice

The results in Sec. 3.2.4 show that the vertical domain wall does not show any signs of stress-focusing on the domain wall, the affine shear strain is odd parity under reflection about the mirror along the domain wall, whereas the SSSs (see Fig. 3.1(b-c)) are even under the mirror; hence the

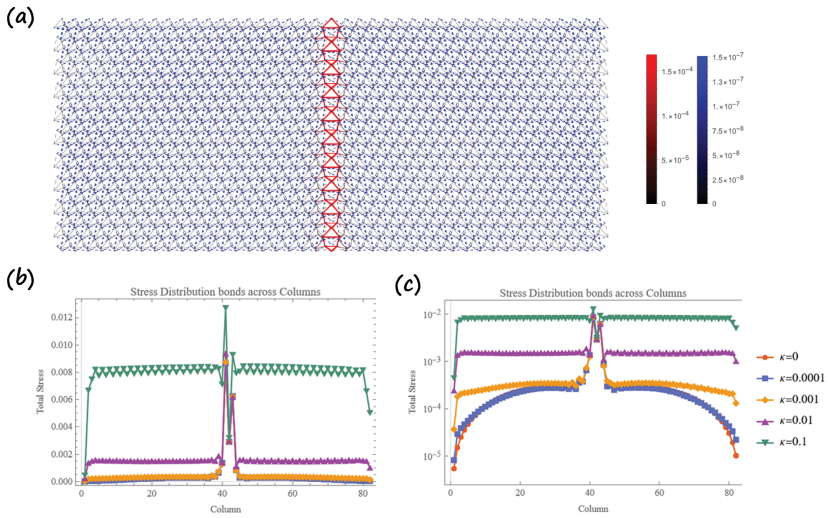

Figure 3.7: Vertical pull simulation with the inclusion of NNN springs on an engineered kagome lattice to lower the stress. (a): An energy minimization simulation as the one described in Fig. 3.2(a) and Fig. 3.3, the NNN spring constant is kept at $\kappa_{NNN} = 10^{-4}$. The maximum tension in the result on the NN bonds is $t_{NN} = 1.68 \times 10^{-4}$ in the units of force, and $t_{NNN} = 1.49 \times 10^{-7}$ on the NNN bonds. The NN bonds are labeled in red, while the NNN bonds are represented in blue. The intensity of the color increases with the stress magnitude. (b): The total stress on bonds across columns in the lattice. The stresses on the vertical axis are shown on a linear scale, and the horizontal axis labels the column index of the lattice. The spiking of stress magnitude at the domain wall is shown in this figure. (c): The total stress on bonds across columns on a log scale. The fact of insignificantly small elevation of the stress away from the domain wall when the NNN springs constant rises from $\kappa = 0$ to $\kappa = 10^{-4}$ compared to the contrast shown in Fig. 3.3(c) demonstrates small or no excitation to the extra SSS caused by the NNN springs in this new lattice, thus without the observation of stress plateauing away from the domain wall.

projection of the shear onto the SSSs is negligible (note that the system is almost mirror symmetric about the domain wall i.e., the mirror symmetry is broken only perturbatively). However, if we make the domain wall slanted (see Fig. 3.8), the mirror is broken. Now the shear strain will have nonzero projections on the SSSs localized the domain wall.

The focused stress on the diagonal domain wall is shown in Fig. 3.8. Compared to Fig. 3.4(c), the response on the two regions is no longer mirror-symmetric, and the large stress is focused on the diagonal domain wall due to the projection of the strain onto SSSs. The maximum tension $t^t_{max} = 1.6 \times 10^{-5}$ and the maximum compression $t^c_{max}) = 7.6 \times 10^{-6}$ are no longer the same in the lattice and are dependent on the shear direction. The tension becomes more prominent if the shearing direction is the $+\hat{x}$-direction and compression if the shearing direction is the $-\hat{x}$-

direction.

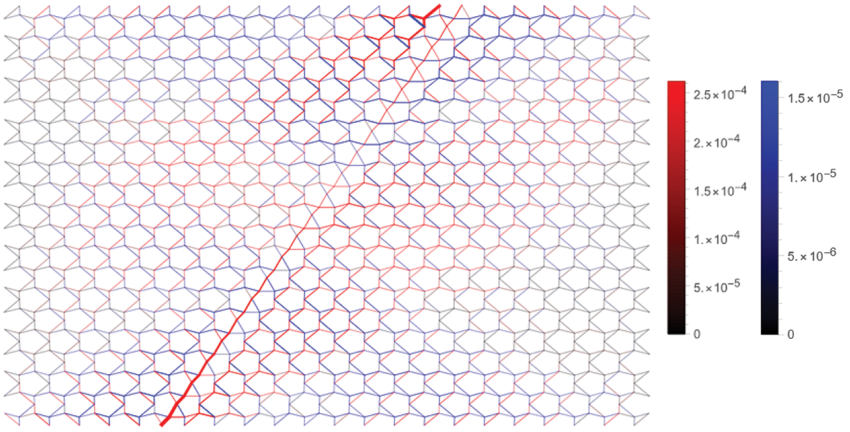

Figure 3.8: A kagome lattice with the same unit cell as in Fig. 3.1, but with a diagonally oriented domain wall between the oppositely polarized regions. A stress focusing shows up again in the lattice when the domain wall is tilted compared to Fig. 3.4(c). The lattice is sheared the same way as described for Fig. 3.4(c) as well. The maximum tension $t^t_{max} = 1.6 \times 10^{-5}$ and the maximum compression $t^c_{max}) = 7.6 \times 10^{-6}$ are no longer identical, and whether tension or compression is focused at the diagonal domain wall is related to the shearing direction, the domain wall focuses tension if the shearing direction is the $+\hat{x}$-direction and compression if the shearing direction is the $-\hat{x}$-direction.

3.4 Discussion

In this manuscript, we explored the effect of bending stiffness on topologically polarized kagome lattices, especially focusing on the effect on states of self-stress in the lattices by examining a vertical pulling test for a lattice with a domain wall between oppositely topologically polarized regions. The inclusion of bending stiffness is done through two approximate models, namely the angular spring (AS) model and the next nearest neighbor (NNN) spring model additional to the nearest neighbor (NN) springs in the original lattice. The proximity of these two models are demonstrated, and on top of that, they both show a masking effect on stress concentration at the SSS domain wall as the NNN spring constant or angular spring constant increases. This observation is explained by examining the additional SSS in the lattice caused by the additional NNN bonds, and the same reason causes the plateauing of stress away from the domain wall. At the same time, we examined the same lattice under different loading conditions. We observed that the SSS is excited under gravity, thus the stress in the lattice is focused on the SSS domain wall. On the other hand, we also observed that the stress focusing at the domain wall disappears when

a simple shear is given to the lattice, which matches the prediction given by analyzing the projection of shear strain onto the SSSs. We have also observed a directional response of the lattice as reported in ref. [22] as well as a stress screening effect by the SSS domain wall.

Moreover, efforts were made in analyzing the NN and NNN lattice construction to design lattices that lower stress or concentrate stress on the domain wall against shear strains. By changing the twisting parameters of kagome unit cells to make the topological polarization of the kagome lattices composed by the NN and NNN bonds no longer opposite, a kagome lattice has a lower stress response against a vertical loading was achieved. And by tilting the SSS domain wall to a diagonal direction in the lattice to make the projection of pure strain onto the SSSs non-zero, a domain wall that focuses stress against shearing was achieved.

This study of the effect of bending stiffness and response to different strain loading of the topological mechanical lattice can contribute greatly to the engineering and designing of topological mechanical metamaterials (TMMs). The understanding of bending stiffness would help with the additive manufacturing of TMMs, as they provide insight into selecting the hinge fillet materials as well as the geometry when the ideal lattice model is translated to a continuum material. The understanding of shear strain projection onto SSSs and the successful designing of a kagome lattice that focuses stress against shear open up a new direction in designing TMMs, as it shows the ability of possible fracture projection not only against vertical loading but against shear as well.

3.5 Appendices

3.5.1 Angular Spring Model Energy and Forces

Energy from the angular spring differs from usual springlike interactions because it requires us to consider multiple particle positions. We represent these triples with $\{i, jk\}$ where i represents the central particle and j and k represent the side particles. A diagram of the angle composed by central particle 0 and particles x and y is shown in Fig. 3.9.

The energy of bending can be written as a springlike interaction on this angle:

$$U = \sum_{\{i,jk\}} \frac{\kappa_{i,jk}}{2} \left(\theta_{i,jk} - \theta^0_{i,jk}\right)^2 \tag{3.18}$$

where $\theta_{i,jk}$ and $\theta^0_{i,jk}$ are the current and rest angles associated with the triple $\{i, jk\}$ and $\kappa_{i,jk}$ is the angular stiffness of this bending bond.

This angle can be measured from the positions of the particles with $\theta_{i,jk} = arccos(\hat{r}_{ij} \cdot \hat{r}_{ik})$ where $\hat{r}_{ij}$ and $\hat{r}_{ik}$ are the unit vectors of the two bond vectors that form the angle $\theta_{i,jk}$. As discussed, this suffers from a limited range of 0 to π. We can investigate reflex angles via utilization of the

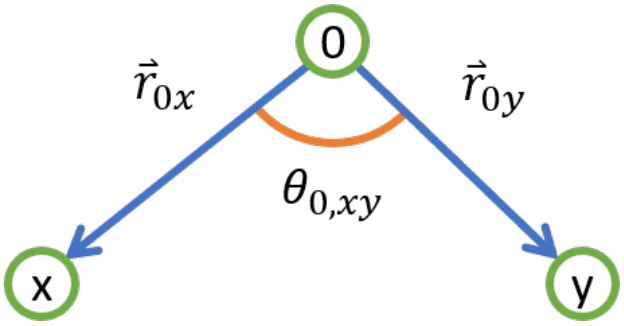

Figure 3.9: A simple diagram of a three-particle subsystem highlighting the angle $\theta_{0,xy}$ between bond vectors $\vec{r}_{0x}$ and $\vec{r}_{0y}$ among particles 0, x, and y.

cross product as well as the dot product:

$$\theta_{i,jk} = \pi + sgn\left(\overrightarrow{r}_{ij} \times \overrightarrow{r}_{ik}\right)\left(arccos(\hat{r}_{ij} \cdot \hat{r}_{ik}) - \pi\right). \tag{3.19}$$

This measure has a range from 0 to 2π. Therefore, $\left(\theta_{i,jk} - \theta^0_{i,jk}\right)$ ranges from $-\theta^0_{i,jk}$ to $\left(2\pi - \theta^0_{i,jk}\right)$. It is also important to note that $\theta_{i,jk} = 2\pi - \theta_{i,kj}$.

The force on each particle of the AS via the first derivative of the energy is:

$$F_{l\alpha} = -\sum_{\{i,jk\}} \kappa_{i,jk}\left(\theta_{i,jk} - \theta^0_{i,jk}\right)\frac{\partial\theta_{i,jk}}{\partial u_{l\alpha}}. \tag{3.20}$$

This derivative of the angle with respect to particle motion is given by

$$\frac{\partial\theta_{i,jk}}{\partial u_{l\alpha}} = -\frac{sgn\left(\overrightarrow{r}_{ij} \times \overrightarrow{r}_{ik}\right)}{\sqrt{1-(\hat{r}_{ij}\cdot\hat{r}_{ik})^2}}\left(\frac{\delta_{jl}-\delta_{il}}{r_{ij}}(\hat{r}_{ik,\alpha} - (\hat{r}_{ij}\cdot\hat{r}_{ik})\hat{r}_{ij,\alpha}) + \frac{\delta_{kl}-\delta_{il}}{r_{ik}}(\hat{r}_{ij,\alpha} - (\hat{r}_{ij}\cdot\hat{r}_{ik})\hat{r}_{ik,\alpha})\right). \tag{3.21}$$

The force derivative $\frac{\mathrm{d}}{\mathrm{d}u}$is taken with respect to the displacements of the sites $\vec{u}$ away from their equilibrium positions, and α labels the x and y components of the force. We do not need to concern ourselves with the derivative of the sign function as this only gives a delta function when the angle is π due to the singularity.

Note that there is no force if the angle is at the rest length. However, if the bond is bent, there is a force not only on the external particles but also on the central particle, which is only symmetric if the distances between particles are the same.

We can simplify this equation using orthogonal vectors in 2d. For a given vector $\overrightarrow{V}$, the orthogonal vector is provided by

$$\overrightarrow{V}^{\perp} = \begin{pmatrix} -V_y \\ V_x \end{pmatrix}. \tag{3.22}$$

The force on any particle due to the angular bonds is therefore given by

$$F_{l\alpha} = \sum_{\{i,jk\}} \kappa_{i,jk} \left(\theta_{i,jk} - \theta^0_{i,jk}\right) \left(\frac{(\delta_{jl} - \delta_{il})\hat{r}^{\perp}_{ij,\alpha}}{r_{ij}} - \frac{(\delta_{kl} - \delta_{il})\hat{r}^{\perp}_{ik,\alpha}}{r_{ik}} \right). \tag{3.23}$$

3.5.2 κ_θ to κ_{NNN} conversion

By examining an angle's geometric relations, we can build a conversion relation between the AS spring constant and the NNN spring constant. We do so by examining the conversion between the small angle change $\delta\theta$ of the angle θ between bonds $\vec{r}_{ij}$ and $\vec{r}_{ik}$ and the change of length δl of bond $\vec{r}_{jk}$ between sites j and k, which is the NNN springs bond that the AS of angle θ is approximated as. A diagram of the geometry is shown in Fig. 3.10

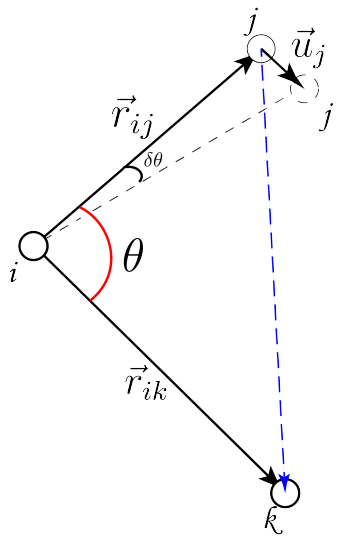

Figure 3.10: A representation of the AS angle θ (shown in red) between bonds $\vec{r}_{ij}$ and $\vec{r}_{ik}$, and the approximated NNN bond $\vec{r}_{jk}$ (shown in dashed blue line). The angle is changed by $\delta\theta$ when the site j is moved by a small displacement $\vec{u}_j$.

As Fig. 3.10 shows, the angle θ is changed by $\delta\theta$ when the site j goes through a small displacement $\vec{u}_j$, however, as the displacement is small, we approximate the length $r_{ij} = |\vec{r}_{ij}|$ remains unchanged as the angle is rotated. Then the length change δl for the bond length $r_{jk} = |\vec{r}_{jk}|$ can be written as

$$\delta l = \sqrt{r_{ij}^2 + r_{ik}^2 - 2r_{ij}r_{ik}\cos(\theta)} - \sqrt{r_{ij}^2 + r_{ik}^2 - 2r_{ij}r_{ik}\cos(\theta - \delta\theta)} \tag{3.24}$$

Taking the deformation angle $\delta\theta$ to be small and expand Eq. (3.24) to linear order in $\delta\theta$, we have

$$\delta l \approx \frac{r_{ij} r_{ik} \sin(\theta)}{\sqrt{r_{ij}^2 + r_{ik}^2 - 2 r_{ij} r_{ik} \cos(\theta)}} \delta\theta, \tag{3.25}$$

where $r_{ij} = |\vec{r}_{ij}|$ and $r_{ik} = |\vec{r}_{ik}|$ are the lengths of the two bonds which the angle θ is composed of. And by this geometric relation between the length change of the NNN spring δl and the angle change $\delta\theta$, we conclude with the relation Eq. (3.14) between the AS constant κ_θ and the NNN spring constant κ_{NNN} in Sec. 3.2.3.

3.5.3 Numerical Methods

There are two numerical methods used in the simulations. For the simulations with NN and NNN springs, a simple gradient descent method was used. This implementation calculates the force of the nodes in the system and displaces them following the force gradient until an error tolerance of 10^{-7} is reached. As for the simulation including AS, a *Fast Inertial Relaxation Engine (FIRE)* algorithm is used to handle the non-linear multi-particle interactions and to accelerate the computation. For the *FIRE* algorithm, not only the force gradient $\vec{F}$ is calculated, but also the velocity $\vec{v}$ and its dot product with the force $P = \vec{F} \cdot \vec{v}$. Then the direction and the speed of the descent are controlled by P.

CHAPTER 4

Multi-stable Topological Mechanical Metamaterials

This chapter summarizes the work *"Multistable Topological Mechanical Metamaterials"* co-authored by Haning Xiu, Harry Liu, Andrea Poli, Guangchao Wan, Kai Sun, Ellen M. Arruda, Xiaoming Mao, and Zi Chen under submission to PNAS, and posted on arXiv as *arXiv:2207.05826*.

4.1 Introduction

Synthetic mechanical metamaterials have been demonstrated to exhibit exotic physical and mechanical properties such as negative Poisson's ratio [90], negative compressibility [91], and programmable nonlinearity [87; 98]. One group of mechanical metamaterials, Maxwell lattices, has been extensively studied in recent years due to their proximity to mechanical instability and interesting topological edge floppy modes and states of self-stress [16; 1; 30; 53], leading to a wide collection of fascinating phenomena and applications including focused stress and fracture protection, phonon waveguide, phonon diode, and tunable stability [87; 95; 54; 20; 19; 99; 24; 15]. The distorted kagome lattice, one of the typical Maxwell lattices, has been the focus of extensive research due to its rich mechanical properties in various topological states [100; 101; 102; 92; 103; 23]. By tuning the geometry of unit cells, a distorted kagome lattice can exhibit peculiar mechanical behaviour protected by the topology of the compatibility matrix in momentum space. Recent research [16] showed the feasibility of changing the topological phase of a kagome lattice by varying a single geometric parameter, i.e., the angle between the two triangles in the unit cells; such transformation is done using a homogeneous soft strain that is intrinsic to the lattice, called the Guest-Hutchinson Mode [31]. The topological transition induced by this soft strain leads to dramatic changes in the surface stiffness of the lattice, desirable for many applications from impact mitigation to non-reciprocal wave propagation [23]. However, experimental realization of this soft strain transformation has been challenging, due to the proximity of these lattices to mechanical instability, which leads to inhomogeneities in deformation as well as nonlinear buckling of the lattice geometry during the transformation. This challenge makes it difficult for Maxwell

lattices to become practical multi-functional materials and potential innovative reprogrammable mechanological metamaterials (ReMM) [104; 105; 106].

To address this, here we introduce bistability, for the first time, to topological Maxwell lattices by adding a spring to each unit cell. This novel design achieves swift and homogeneous transformation between topologically polarized [1] and non-polarized phases, characterized by dramatically different mechanical properties, and meanwhile it generates programmable mechanical stiffnesses including effective normal stiffness and shear stiffness that do not exist in conventional Maxwell lattices. In the design we present here, the added spring connects the centers of two bonds in each unit cell, thereby creating two stable states that lie symmetrically on either side of the critical state that separates the topologically polarized and nonpolarized phases (Fig 1). Compared to the design in Ref. [16] in which the lattice continuous transforms along the soft strain direction, the bistability introduced at the unit cell level here offers well-defined stable states (two for each unit), leading to much better control of the lattice transformation, as well as rich opportunities in programming multistability and related multifunctionalities in the material. Both theoretically and experimentally, with good agreement, we show that the surface stiffness in one state is significantly different from the other. We then characterize how the spring constant of the added springs controls the stiffness of the soft surface. We further demonstrate experimentally that the bistability of these units greatly improves the controllability of the lattice during the transformation from one state to the other, realizing swift, drastic, and reversible change of surface stiffness. Beyond these distinct characteristics, such as maintaining mechanical properties of conventional Maxwell lattices and generating mechanical stiffnesses, these multistable Maxwell lattices open a suite of new opportunities for combining topological mechanics with nonlinearity. The multistable lattice we designed shows intriguing spatial patterns that feature drastically different structures separated by an interface; each side adopts one of the two stable states whereby the interface depends on various factors from the width of the strip to the unit cell design, creating a new set of controllable spatially patterned materials. The proposed multi-stable Maxwell lattice can be further used to design and innovate ReMM. Our new technique facilitates the development of mechanical computing systems, neuromorphic metamaterials, controlled morphing systems, flexible robotics, bioinspired control, and distributed intelligence [104; 105; 106; 107; 108; 109].

4.2 Results

4.2.1 Topological polarization and multistability of Maxwell lattices

Mechanical stability of a frame to linear order can be characterized using zero modes (ZMs) and states of self-stress (SSSs). A ZM is a set of displacements of the lattice sites that cause no

change of bond length, and an SSS is a set of tension/compression on bonds that cause no net force on lattice sites. Maxwell proposed, and Calladine later modified, an index that accounts for the difference between the degrees of freedom of a network and the number of constraints, which is equal to the difference between the number of ZMs and SSSs [1; 6; 29]. In the special case when the number of degrees of freedom exactly equals the number of constraints in the bulk, the mechanical network is at the verge of instability, and such a network is called a Maxwell network. For lattices with point-like sites and central-force bonds ("ball-and-spring" structures) this criterion takes the form that the average coordination number of the network is $\langle z \rangle = 2d$, where d is the dimension of the network, leading to $\langle z \rangle = 4$ in two dimensions. One of the typical lattices that satisfies the Maxwell criterion is the kagome lattice and its various distorted versions, which contains 3 sites and 6 bonds in its unit cell, satisfying $\langle z \rangle = 4$ (each bond connects two sites). In Fig. 4.1(a), one such unit cell is shown as a combination of triangles A and B, and the specific side lengths of triangles A and B we use in this paper are (0.4, 0.8, 1), (0.5, 0.7, 1). The geometric structure of the ML is defined by the chosen lengths of the six sides of the two component triangles in order to have significant topological polarization properties, and the calculations of topological polarization in the following are all based on this choice. In the limit that the bonds of the lattices are rigid, only one internal degree of freedom, the relative rotation between the two triangles (the twisting angle), α, remains for this unit cell.

The mechanics of boundaries, interfaces, and defects for Maxwell lattices are governed by a "topological polarization" R_T introduced by Kane and Lubensky [1]. This topological polarization is determined by the geometry of the unit cell and can be computed via winding numbers of the compatibility matrix of the lattice in the momentum space. Boundaries and interfaces where R_T points towards gain topologically protected, exponentially localized ZMs, and by contrast, interfaces where R_T points away gain SSSs. Such topological polarization leads to remarkable mechanical effects owing to asymmetric surface stiffness and stress focusing [54; 15]. In Ref. [16], it is shown that changing the geometry of the unit cell via the Guest-Hutchinson mode (which alters the angle between triangles A and B homogeneously across the lattice) changes the topological polarization, thus switching the mechanical properties of the boundaries and interfaces.

In particular, this distorted kagome lattice experiences such topological transitions at three critical angles, α_{a_2}, α_{a_1}, and $\alpha_{a_2-a_1}$ (Fig. 4.1(b), where subscripts of are the lattice directions where bonds align into straight lines at the transition). When $\alpha < \alpha_{a_2}$ or $\alpha > \alpha_{a_2-a_1}$, the lattice is non-polarized ($R_T = 0$, where all boundaries are soft), and as changes between α_{a_2} and $\alpha_{a_2-a_1}$, the lattice exhibits a topological polarization. There are two specific polarized phases where $R_T = a_2$ and $R_T = a_2 - a_1$ (following the same symmetric gauge used in Refs [16; 1]) separated by the critical angle α_{a_1}.

To achieve multistability of the lattice and convenient operation of topological polarization

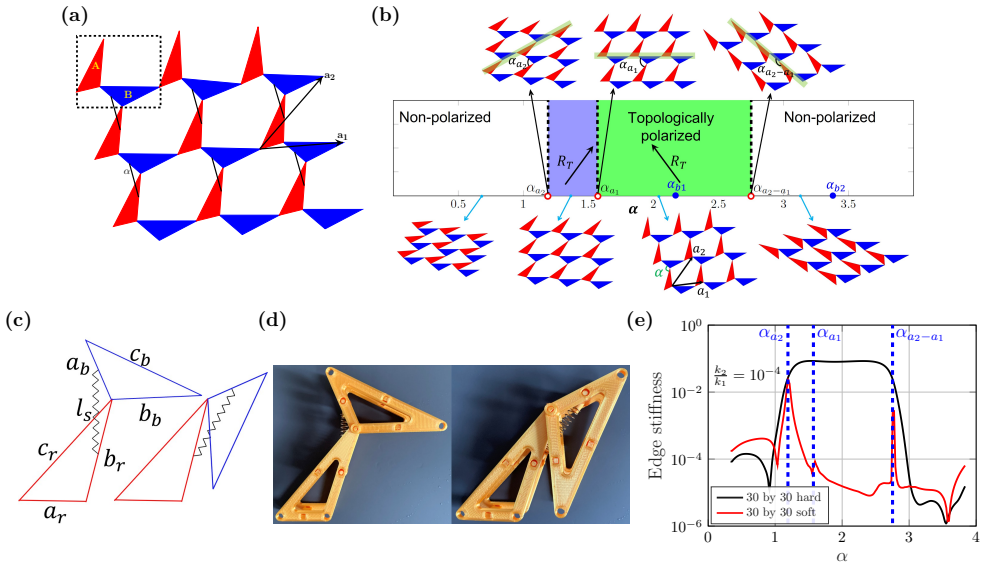

Figure 4.1: Schematic of the multistable Maxwell lattice and its topological polarization. (a) Schematic of a section of a Maxwell lattice having bistable units with 3×3 unit cells. Each unit cell (dashed box) consists of triangles A and B that are hinge-connected, and added springs are indicated by black lines between the triangles. The primitive vectors are $\vec{a}_1$ and $\vec{a}_2$. (b) Topological transitions of a distorted kagome lattice. Three angles, α_{a_2}, α_{a_1}, and $\alpha_{a_2-a_1}$ correspond to cases where the sides of the triangles A and B align (light green stripes) and represent the critical angles that separate distinct topologically polarized phases. The angles $\alpha_{b_1} = 2.0984$ and $\alpha_{b_1} = 3.4052$ indicate two equilibria (one in the polarized phase and the other in the non-polarized phase) of the lattice with bistable units, in which the springs are relaxed. These are the two equilibria for the configuration in the rest of this paper as well. (c) Two stable equilibria with notations of the triangles of a bistable unit with a spring. a_r, b_r, and c_r are side lengths of triangles A, while a_b, b_b, and c_b represent side lengths of triangles B. l_s is the length of the undeformed spring. (d) 3D printed unit cell with a spring showing bistable equilibria. (e) Numerical surface stiffness versus the twisting angle, α, of a 30×30 distorted kagome lattice [as shown in (a)] with bistable units. The surface stiffness is normalized by bond stiffness k_1 (here $k_1 = 1$), and the spring constant is $k_2/k_1 = 10^{-4}$. The stiffness of the hard edge increases significantly as α falls within α_{a_2} and $\alpha_{a_2-a_1}$, and floppy modes move the opposite edge.

transformation, bistable units are created in which auxiliary springs (with low stiffness shown by black lines in Fig. 4.1(a) and (c)) are added to connect the centers of two bonds in each unit cell. Fig. 4.1(c) indicates the two stable equilibria of a unit cell: one is located in the polarized phase, and the other in the non-polarized phase (3D printed bistable unit cell is shown in Fig. 4.1(d)). The added bistability of each unit facilitates the lattice transition between the two equilibria via the Guest-Hutchinsin modes. As the rest length of the springs, which is lower than the half length of $(a_b + b_r)$, changes, the angle of the homogeneous zero-energy configuration of the lattice, α, is tuned. When the bistable lattice goes through a transition to the polarized phases, there is a dramatic increase of the edge stiffness at the edge opposite to the polarization direction (Fig. 4.1e), preserving the topological effect observed in lattices without bistable units [16]. The procedures to measure the edge stiffness will be discussed in the Results section and in Fig. 4.3. Moreover, these bistable units dramatically decrease the number of ZMs of the lattice with $n \times m$ unit cells from $2n + 2m - 3$ to 2 (rigid rotations of the dangling triangles in the top-left and bottom-right unit cells). Although this change effectively rigidifies the lattice, we show below that because these springs are much softer than the triangles, the lattice is still close to the Maxwell point and the topological properties are well-preserved [73]. Theoretical analysis, numerical computations, and experimental validation of this bistable design will be discussed in the following section to characterize how mechanical properties of the lattice are affected by the springs.

4.2.2 Surface mechanical properties of multistable Maxwell lattices

In this section we discuss the effects of the springs, which are added to induce bistability, on the surface mechanical properties of the lattice and on the generated mechanical stiffnesses for the lattice. We show that, interestingly, the stiffness of the soft edge increases linearly with the stiffness of the spring, whereas the stiffness of the rigid edge is insensitive to the spring constant. Additionally, the springs generate mechanical stiffness when transforming the lattice from one state to another.

A Maxwell lattice of $n \times m$unit cells is created to quantify the surface stiffness of the lattice during the topological polarization transitions. To investigate how the bistable units affect the mechanics of the lattice, linearized surface stiffnesses are calculated and compared with the results of the same lattice without bistable units (Fig. 4.3(b)). First, we start from the nonlinear elastic energy of the lattice by fixing the rest length of the spring l_s (for a given angle α). It is written as

$$E = \sum_i \sum_{j=1}^{6} \frac{k_1}{2}(l_{ij} - l_{ij0})^2 + \sum_k \frac{k_2}{2}(l_k - l_s)^2 \tag{4.1}$$

where i and k label the unit cells and j labels the 6 bonds (edges of triangles) in each unit cell,

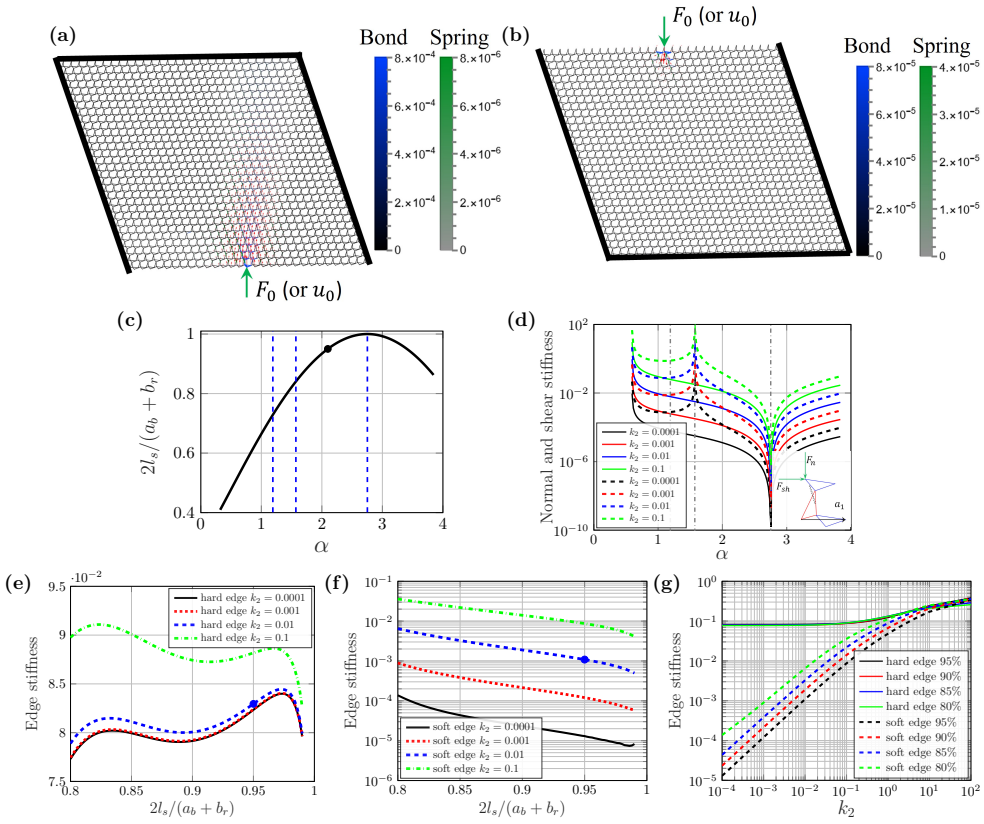

Figure 4.2: Parametric study of surface stiffness. Deformed lattice of 30 by 30-unit cells given displacement at the (a) hard (bottom of the lattice) or (b) soft (top of the lattice) boundary for calculating edge stiffness. The displacement field of the sites are represented by red arrows with longer arrows corresponding to larger displacements. The tension/compression on the bonds and springs are shown in blue and green respectively with higher magnitudes corresponding to more visible colors and thicker lines. The springs are at their rest length, which is 95% of $(a_r + b_b)/2$, and $k_2/k_1 = 0.001$ with $k_1 = 1$. (c) Rest length of springs $(2l_s/(a_b + b_r))$ with respect to the twisting angle α. The black dot is the configuration where the rest length is 95% of $(a_r + b_b)/2$, and this configuration is also used in Fig. 4.3. (d) Normal (solid) and shear (dashed) stiffness versus the twisting angle α. The normal and shear stiffnesses are calculated for the force applied perpendicular and parallel to the primitive vector of a_1, respectively. Surface stiffness of (e) hard and (f) soft edges against the rest length of the bistable unit for different spring stiffness ($k_1 = 1$ for all cases). Blue dots in (e) and (f) are the configurations of the deformed lattice in (a) and (b). (g) Edge stiffness of hard and soft edges versus the stiffness, k_2, for multiple rest lengths of springs. As k_2 increases, the stiffnesses of the top and bottom edges tend to converge. The stiffness and k_2 are non-dimensionalized by k_1.

l_{ij0} and l_{ij} are the rest and current lengths of each bond, respectively, l_k represents the length of the spring in its current state. The stiffnesses of the bonds and the added springs are taken to be k_1 and k_2 respectively. In the limit of small strain, we work with a linearized theory, i.e., we keep terms to the quadratic order in site displacements in the elastic energy. More details about the elastic energy and the linearization in a unit cell can be found in the Supplementary Note. To perform the test, three out of four boundaries of the lattice are fixed, and the remaining boundary is free to be given a small displacement $\vec{U}_i$ at the center site i (Fig. 4.3 (a)-(b)), the direction of which is perpendicular to the bottom edge (a_1 vector direction). The linear conjugate gradient method is used to solve the minimal energy of the lattice and the surface stiffness is calculated as the ratio between force and displacement $\left|\vec{F}_i\right| / \left|\vec{U}_i\right|$ for the site being pressed. All the surface stiffnesses are non-dimensionalized by the stiffness of the bond k_1, and k_1 is 1 for all simulations. It is worth noting that the topological effect of the stiffness is robust and the detail of the probe is not important. The displacement $\vec{U}_i$ in response to a force $\vec{F}_i$ at site i can be formally written in terms of a sum over normal modes $\vec{u}_{i,j}$ as

$$\vec{U}_i = \sum_j \frac{\vec{u}_{i,j}\left(\vec{u}_{i,j} \cdot \vec{F}_i\right)}{\Lambda_j} \tag{4.2}$$

where Λ_j is the dynamical matrix ($\mathbf{K}$) eigenvalue of the normal mode j. Topological floppy modes are characterized by $\Lambda_j \to 0$ and $\vec{u}_{i,j}$ exponentially localized at selected edges, giving rise to dramatically different responses to local probes at opposite edges, regardless of the details of the probe (see SI for numerical tests using different types of probes).

The springs not only introduce bistability, but also result in significant mechanical stiffnesses for the lattice, such as effective normal stiffness and effective shear stiffness of a 2D lattice; here the effective normal stiffness, k_n, is defined as the ratio between the force and the displacement in the direction perpendicular to the primitive vector of a_1, as the lattice undergoes uniform twisting, and the effective shear stiffness, k_{sh}, is defined as the ratio between the force and the displacement in the direction parallel to a_1:

$$k_n = k_2 \frac{b_r^2 \sin^2(\alpha + \psi_{ar})}{8 l_s^2 \cos^2(\pi - \psi_{bb}) |\cos\phi|} \tag{4.3}$$

$$k_{sh} = k_2 \frac{b_r^2 \sin^2(\alpha + \psi_{ar})}{8 l_s^2 \cos^2(\pi - \psi_{bb}) |\sin\phi|} \tag{4.4}$$

where b_r is a side length of triangle A, ψ_{ar} and ψ_{bb} are inner angles of the triangles, and ϕ is the angle between the vector of a_1 and the side of c_b . More information on the mechanical stiffness is shown in the Supplementary Note. Here, the elastic and shear stiffnesses have linear relationships

to the spring constant k_2 and are also dependent on the initial twisting angle α, shown in Fig. 4.2(d). When $k_2 = 0$, both k_n and k_{sh} are zero and the lattice transformation between topological states is a purely soft one as discussed in Ref [16].

The surface stiffness of the lattice depends on the rest length and spring constant of the added springs, as well as the configuration of the lattice. We first study the effect of the spring's rest length on the surface stiffness. By varying the rest length of the springs between $80\% - 99\%$ of $(a_b + b_r)/2$, we tune the two equilibria between far from the topological transition to close to the transition (Fig. 4.2(c)). We use the linearized method described above to measure the edge stiffness of a 30×30 multistable lattice at different rest lengths and different k_2 values (Fig. 4.2(e)-(f)), starting from the topologically polarized equilibrium state. Our results show that the stiffnesses of the hard edges are not sensitive to the rest length of the springs, as long as the lattice is placed at its equilibrium in the polarized phase, whereas the soft-edge stiffness has a monotonic decrease of an order of magnitude when the rest length of the spring increases by 20% of $(a_b + b_r)/2$.

We then study the effect of changing spring constant k_2 on the edge stiffness (Fig. 4.2(g)). We found that the stiffnesses for both hard and soft edges monotonically increase as k_2 increases, but the soft edge is more sensitive to k_2. The magnitude of k_2 ranges from 10^{-4} to 100 and the stiffness of bonds stays at $k_1 = 1$. Although the edge stiffnesses for different rest lengths show moderate variations, the stiffness for the hard edge increases very slowly when k_2 increases up to 10^{-1}, and then it steeply increases as k_2 continues to increase. The stiffness of the soft edge shows the opposite trend—it increases exponentially when k_2 is raised from 10^{-4} to slightly less than 1 and then increases less sharply afterwards. Because of the different increase of stiffnesses between hard and soft edges, Fig. 4.2(g) shows the stiffness convergence of both edges at large k_2 values (up to 100) for each case. This trend can be understood via the nature of the topological edge modes. In the Maxwell limit ($k_2 = 0$), the edge modes are purely rotations of the triangles. At the soft edge, these are the modes that accommodate the local deformations. As a result, the edge stiffnesses are extremely sensitive to the spring constant k_2, because the topological edge modes distort these springs. At the hard edge, in contrast, there are no topological edge modes, and the local deformation is composed of bulk modes, which distorts both the bonds and the springs in the kagome lattice. When the bonds k_1 are much stiffer than the springs, the hard-edge stiffness is not sensitive to k_2. As k_2 increases to close to or even greater than k_1, the added springs become comparable to the bonds in the unit cells, which will take the lattice away from Maxwell points, and lead to the disappearance of topological polarization of the lattice and the lattice will transition to a conventional stable elastic medium.

We further study the edge stiffness of a Maxwell lattice as it deforms along its Guest mode (labelled by the twisting angle α), which reconfigures the lattice between topological phases (Fig. 4.3). The general shape of these curves is similar to the case of lattices without bistable units

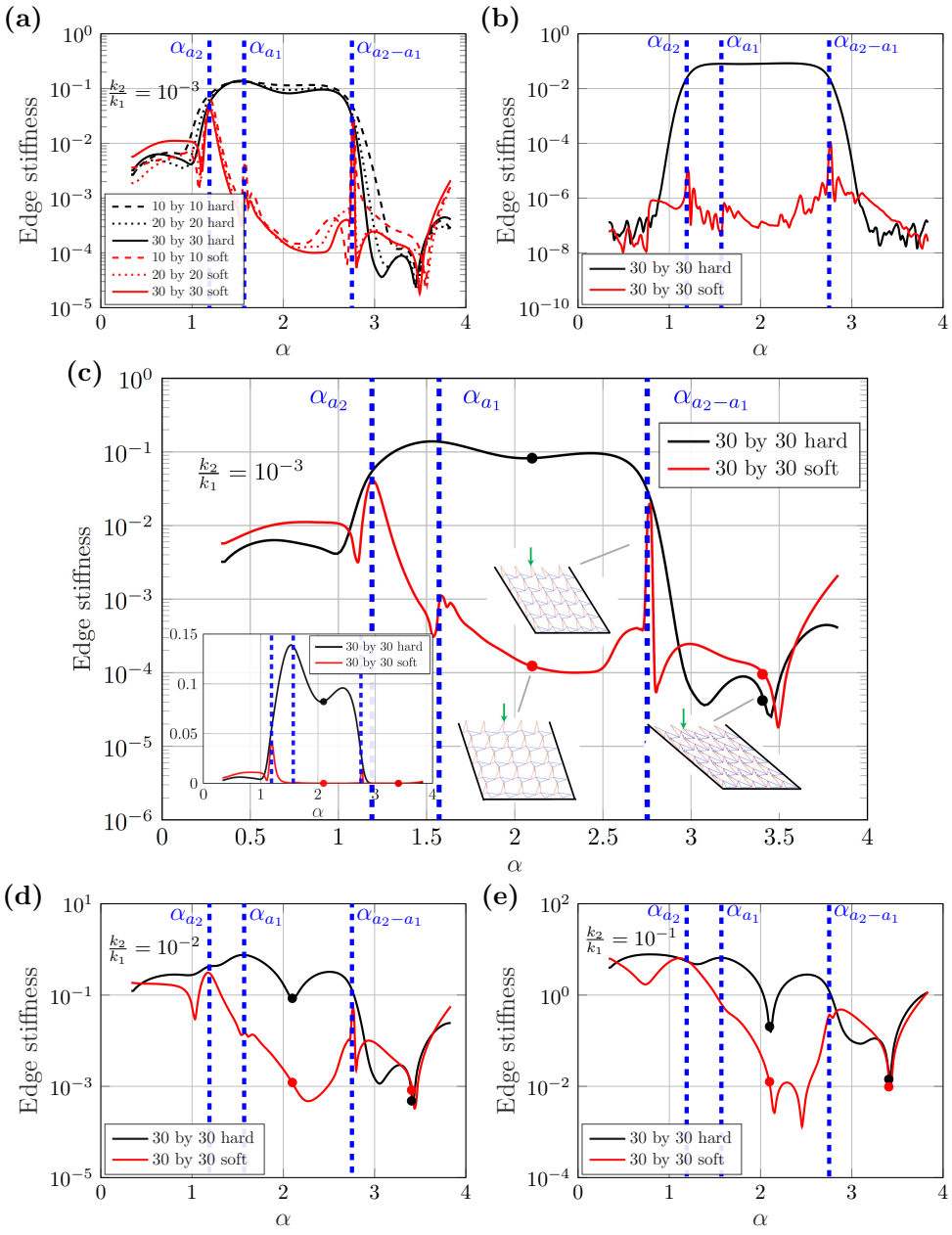

Figure 4.3: Linearized normalized edge stiffness of kagome lattices transitioning between polarized and nonpolarized phases. The bond stiffness k_1 is 1 for all simulations. (a) Edge stiffness of top and bottom edges from 10×10, 20×20 and 30×30 kagome lattices with structures and dimensions shown in Fig. 4.1. The rest length of the spring is set as 95% of $(a_r + b_b)/2$, and the lattice is held at different configurations (labelled by angle) by three boundaries with the edge stiffness measured at the fourth boundary. The spring constant k_2 is 0.001. (b) Edge stiffness of a 30×30 kagome lattice without bistable units ($k_2 = 0$). (c-e) Edge stiffness of a 30×30 kagome lattice with different k_2/k_1. (c) $k_2/k_1 = 0.001$, (d) $k_2/k_1 = 0.01$, and (e) $k_2/k_1 = 0.1$. Black and red dots indicate the specific surface stiffness at the equilibrium twisting angles, α_0, where the spring is relaxed, one located in the topologically polarized phase and the other in the non-polarized phase. An inset in (c) is a linear scale plot of edge stiffness for $k_2/k_1 = 0.001$.

(Fig. 4.3(b)). However, the lattice is only in force balance at the two equilibria (red and black dots in Fig 4.3), due to these bistable units. In all other configurations, the lattice is held at the boundary, and then relaxed to adopt an inhomogeneous and stressed reference state (via a minimization of the nonlinear elastic energy). We then expand the elastic energy around these inhomogeneous stressed states and use the linearized theory to calculate the edge stiffness. The hard-edge stiffness increases prominently when k_2/k_1 is large for the polarized Maxwell lattice resulting from the initial non-zero energy state of the lattice, except for the state in which the auxiliary springs are undeformed. The analysis of the boundary stiffness shows that the topological polarization of Maxwell lattices is well-preserved upon the incorporation of the springs. Furthermore, both the surface stiffness and the lattice elasticity can be programmed by tuning the properties of these added springs.

We support this computational observation by theoretical analysis. It was shown in Refs. [73; 74] that topological polarization can emerge in continuum elasticity theories with strain gradient terms. Here we apply the formulation of Ref. [73] which provides a treatment of additional weak interactions (the added springs for bistability in this case) beyond Maxwell connectivity. We take the linearized theory at the configuration where the lattice is polarized without the added springs (the Maxwell limit), and examine the topological polarization with the added springs at varying spring constant ratio k_2/k_1. In particular, we take the 7×6 dimensional compatibility matrix in momentum space $\mathbf{C}_{\vec{k}}^{lattice}$ (from the 6 nearest-neighbor springs and 1 added spring), reduce it to a 7×2 dimensional renormalized compatibility matrix $\tilde{\mathbf{A}}_{\vec{k}}^{lattice}$ by integrating out the 5 high energy bands and keeping only the lowest 2 bands (acoustic branches), and convert it to a continuum theory with a 2×2 dimensional compatibility matrix $\mathbf{C}^{continuum}(\vec{k})$ via an LDLT decomposition. The last step requires that one eigenvalue of the elastic moduli matrix (3×3 in the Voigt notation) of the 2D lattice is much smaller than the other 2, a measure of how far the lattice is from the Maxwell point. We then calculate the topological index, the frequencies, and the penetration depths of the edge modes from the $\mathbf{C}^{continuum}(\vec{k})$ matrix.

Interestingly, our calculation shows that the topological polarization remains unchanged as we increase k_2/k_1, compared to the Maxwell limit ($k_2/k_1 = 0$). Instead, as k_2/k_1 becomes large, it is the small eigenvalue of the elastic moduli matrix becoming comparable with the other two, invalidating the definition of the topological polarization. As shown in Fig. 4.4, the 3 eigenvalues of the elastic moduli matrix become comparable as k_2/k_1 1. Concurrently, the solved penetration depths of one of the edge modes diverge at this point. This indicates that this edge mode is merged into the bulk bands. This is in good agreement with the numerical results of edge stiffness in Fig. 4.2(g), where the topological asymmetry vanishes around k_2/k_1 1.

Therefore, we show via this continuum theory that as long as the springs added for bistability are weak ($k_2/k_1 \ll 1$), the topological polarization and the resulting asymmetric edge stiffnesses

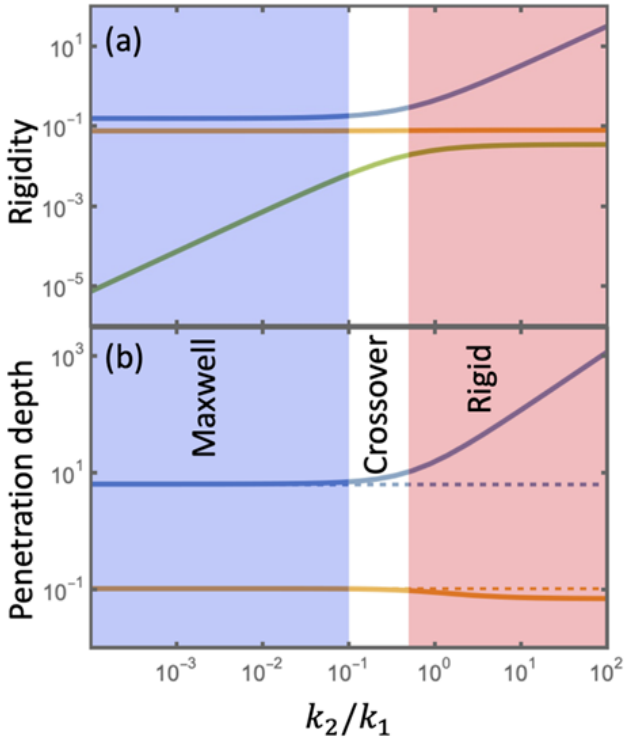

Figure 4.4: Continuous theory of topological mechanics in Maxwell lattices in the presence of bistable spring, k_2. (a) Eigenvalues of the elastic moduli matrix (measured in the unit of k_1) as functions of k_2/k_1. (b) Penetration depths of the two edge modes as functions of k_2/k_1. Dashed lines in (b) indicate the penetration depths at the ideal Maxwell limit $k_2 = 0$. Here the penetration depths are characterized as the parameter b in the zero-mode solution of the decay rate $q_y'' = q_x^2/b$, so the physical penetration depth is b/q_x^2, depending on the wave vector along the edge. For $k_2/k_1 < 0.1$, one of the eigenvalues is significantly smaller than the other two, and the continuous theory exhibits the same topological index and penetration depths as the ideal Maxwell limit. Beyond this point, the smallest eigenvalue becomes comparable with the other two, and the system undergoes a crossover towards the rigid regime, for which the continuous topological theory is no longer valid.

are well preserved.

4.2.3 Reconfigurable interface between topologically distinct states of a multistable Maxwell lattice

The introduction of multistability to a Maxwell lattice offers new opportunities for studying intriguing structural features from topological interfaces to defects, as well as their reconfigurability. As an important first step in understanding heterogeneous states in multistable Maxwell lattices, here we study the static interface between topologically polarized and unpolarized phases in a multistable lattice.

For a homogenous multistable Maxwell lattice, as a shear strain is applied from one boundary of the lattice, a portion of the lattice undergoes a topological transition from one topological state to another. However, due to the different primitive vectors between the two lattice domains in different topological states (Fig. 4.5(i)), the interface bears geometric frustration, and interesting questions arise in terms of the equilibrium configurations of the lattice. To understand the profile of the interface in the static limit, a numerical study using energy minimization is conducted. We set up the initial configuration such that two lattice domains in distinct topological phases, namely, one unpolarized ($R_T = 0$) and one polarized ($R_T = a_2 - a_1$), are connected. Depending on which domain is placed on the top, we have either a SSS interface or a ZM interface [1]. As mentioned above, because the lattice vectors of the two domains along the interface are in general different, in order to connect them, we elongated some bonds in the initial condition, and then let the lattice evolve according to (nonlinear) energy minimization to reach the equilibrium configuration. As a result, interesting interface configurations show up, as shown in Fig. 4.5.

The lattice-vector mismatch between the two domains causes interesting profiles where the interface curves and widens in all cases. This curvature shares similarities with curved thin elastic bodies in continuum elasticity due to frustration [110; 35; 111]. Another key feature is that the exact interface profile depends on the initial configuration, i.e., how the two domains are connected initially, because the energy minimization could lead to multiple local minima given the complexity of the energy landscape. The initial configuration to create interface profiles in Fig. 4.5 is described in the supplementary materials.

The study of the interface profile reveals a geometric frustration when this multistable lattice transforms from one topological state to another via an interface. When the whole lattice transforms uniformly, there is no geometric frustration, but as we described above, when this transition occurs across the lattice with an interface, the lattice vector mismatch causes frustration and internal stress, giving rise to interesting profiles. While such a transition is often dynamic (i.e., as the lattice is triggered by an impact from one end and the transformation propagates through the

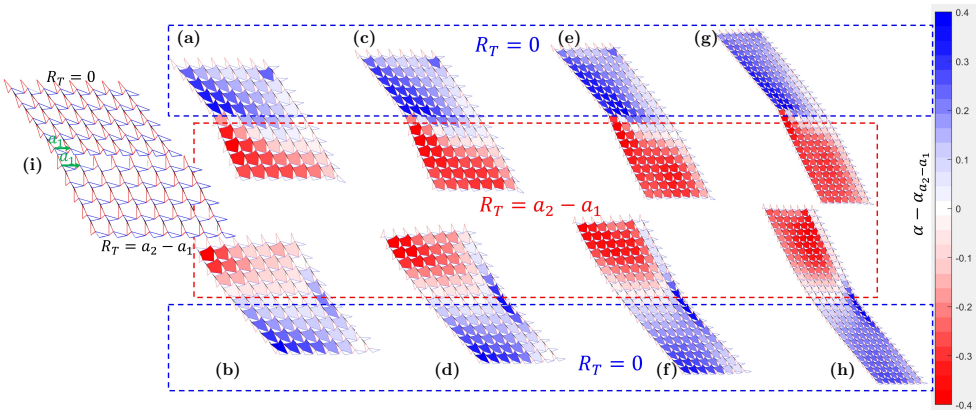

Figure 4.5: Reconfiguration interfaces of multistable topological kagome lattices. Reconfiguration interface of (a-b) 10×8, (c-d) 14×8, (e-f) 20×8, and (g-h) 30×8 kagome lattices based on minimization of nonlinear elastic energy of the lattice. (a, c, e, g) Initial configurations of the lattices have non-polarized domains at the top area of the lattice and polarized domains at the bottom area, respectively (forming a zero-mode interface). (b, d, f, h) Initial configuration presents that the non-polarized area is at the bottom while the polarized area is on the top part of the lattice, creating a self-stress-state interface. (i) Two uniform lattices with different primitive vectors are shown to illustrate fitting them together while with different widths. Examples of initial configurations are shown in Supplementary Materials, Figure. 4.9. The colormap is used for the differences of the twisting angles α between unit cells, and $\alpha_{a_2-a_1}$—positive values (in blue) indicate non-polarized unit cells, and negative (in red) represent polarized unit cells. $\alpha - \alpha_{a_2-a_1} = \pm 0.2$ imply the unit cell is at its bistable equilibrium in which the spring is relaxed ($\alpha_0 = 2.95$ and $\alpha_0 = 2.55$).

lattice), we have chosen to focus on the statics in this study; the dynamics of this interface profile will require further study to achieve a deeper understanding of how this geometric frustration interplays with waves of stress.

4.2.4 Experiments on multistable hinged Maxwell lattices

A prototype of a 3D-printed lattice is used for experimental demonstration of the theoretical findings in the previous sections. The lattice consisting of 6-unit cells in both length and width are assembled with bistable units, where the added springs are incorporated between two triangles from adjacent unit cells (one unit cell with spring embedded is shown Fig. 4.1(d)). Fig. 4.6(a) shows the combined lattice transitioning from the non-polarized domain to the polarized domain via soft twisting manually [16]. This process experimentally demonstrates the ease of manipulation of topological transformation, where the lower left of the lattice is held by one hand and the upper right corner can be pulled diagonally using the other hand. Compared with the similar manipulation in the previous study [16], where the Guest mode has to be realized by a uniform dilation which is difficult to control, the multistable lattice efficiently improves the twisting manipulation and speeds up the transition process.

The experimental setup for measuring the surface stiffness of the lattice is shown in Fig. 4.6(b) and the corresponding force/stiffness versus displacement results for two opposite edges are given in Fig. 4.6(c) and (d). Tips on three of four edges are bonded to the ground using hook-and-loop self-adhesive tapes (also adding superglue to prevent edges slipping) and the last edge is a free boundary for applying mechanical loads for testing. Fig. 4.6(b) demonstrates the large pushing force needed (43.7 N) when a displacement (here 20 mm) is given at a tip of the hard edge, as well as the small deformations as a result, while a more distinct shape change is observed when it is pushed at the tip from the soft edge, and the corresponding force (0.86 N for 19 mm) is roughly 2% of the one at the hard edge. The edge stiffness (the ratio of force to displacement) is calculated and presented in Fig. 4.6(c). The mechanical test is implemented within the regime where the hinges start to bear mechanical forces. More details of the differences between theoretical and experimental stiffness are explained in the Supplementary Note. Fig. 4.6(d) illustrates that there are roughly two orders of magnitude difference between the stiffness of the hard and soft edges (when a pushing load is given). The experimental results are further proofs that the polarized multistable lattice maintains the property where the surface stiffness of the hard edge sharply increases and becomes much higher than that of the soft edge.

Through a set of 3D-printed Maxwell lattices, it is verified that the transformation of the lattice can be done through merely soft twisting of the network and the final angles of the unit cells are guaranteed to be nearly homogenous as they are controlled by the energy minimum of the springs.

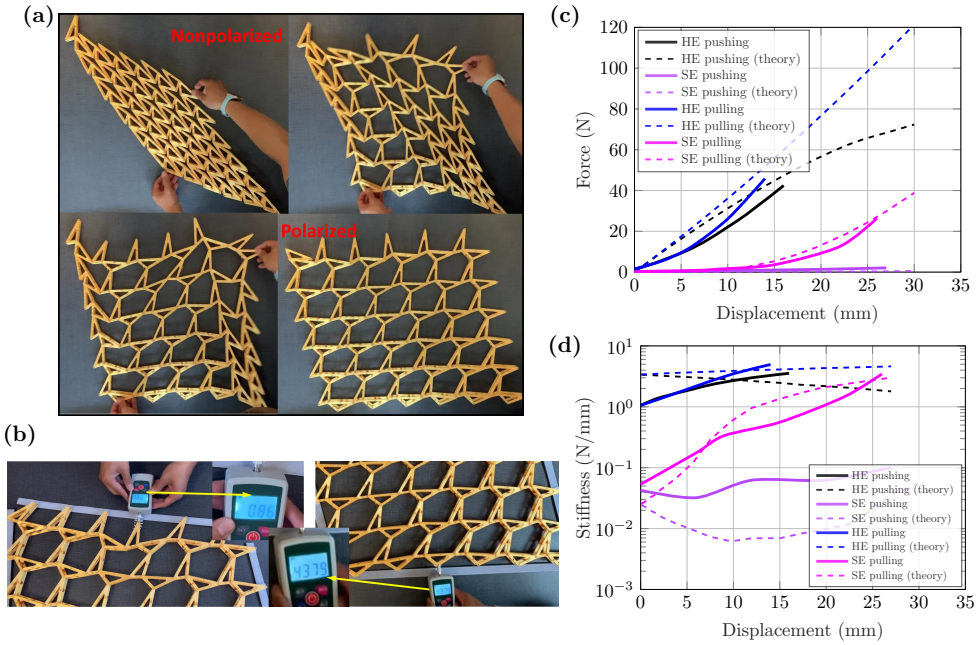

Figure 4.6: Experimental validation on topological transition and surface stiffness. (a) Topological transition (swift twist of angles) from non-polarized phase to polarized phase for a 6×6-unit cell lattice. (b) The comparison of forces needed to push the tips of two opposite edges at given displacements. The hard edge is pushed to 20 mm which needs over 43 N, while 19 mm is given for the soft edge needing only 0.86 N. (c) Force and (d) corresponding edge stiffness against displacement for two edges. The black (blue) line indicates the hard edge undergoes a pushing (pulling) load, while the red (magenta) represents soft edges applied by a pushing (pulling) force. Solid and dashed lines are used to distinguish theoretical results and experimental data.

Furthermore, since the force-displacement curves are measured on both sides of the lattice as it falls in the topologically polarized state, the difference in the edge stiffness on those two sides due to the topological polarization is observed, as well as the hardening due to the addition of the springs.

4.2.5 Experiments on multi-material Maxwell lattice and hingeless bistable unit

To further demonstrate a significant contrast of the edge stiffnesses between two boundaries of the lattice, a multi-material additive manufacturing technique is utilized. In this design, VeroWhite, a stiff material, has been used to construct a solid triangle body for the unit cells to maintain the unit cell structure, and Agilus30, a softer material, has been used as the hinges connecting the triangles in the lattice. The hinges are stiff in response to a tensile force along the hinge axis because the Agilus30 hinge is constrained via its attachment to the stiff Vero-White triangles. The hinges are compliant in bending because the soft Agilus30 is free to bend. During the force vs. displacement measurements of the multi-material lattice, the boundary of interest is probed by a force sensor while the other 3 boundaries are fixed in place. The measurement shows a promising contrast between the edge stiffnesses of the rigid and floppy edges with an average initial stiffness ratio of 16. The experimental set up and the measured force-displacement curves are shown in Fig. 4.7.

This experiment demonstrates that the incorporation of multi-material 3D printing nicely preserves the topological polarization, which was originally defined in the "pin-joint" limit with no bending stiffness. Homogeneous (one-material) 3D printing of Maxwell lattices led to the design of interesting metamaterials for contrasting surface stiffnesses [28; 2; 3]. However, the ratio of the surface stiffness at the hard and soft edges are limited to $\sim< 5$ in these designs, due to significant bending stiffness at the hinges. Multi-material 3D printing presented here offers a creative way to resolve this issue, using soft materials at the hinges, as discussed above. Furthermore, the softness of these hinges may also enable reconfiguration of the lattice between topological phases and the incorporation of the bistable mechanism, and these will be topics for future studies.

With a desire to achieve bistability in the Maxwell lattices through additive manufacturing, a new design of a hingeless bistable unit (Fig. 4.7(c)) is proposed to be incorporated to connect the red and blue triangles in each unit cell. A force displacement test was performed to show the transition between the two stable states of the unit in Fig. 4.6(d). The fact that the force curve drops down to zero and then rises back up as the unit is pushed in a single direction indicates the existence of the second stable state.

However, the integration between the bistable units and the topologically polarized kagome

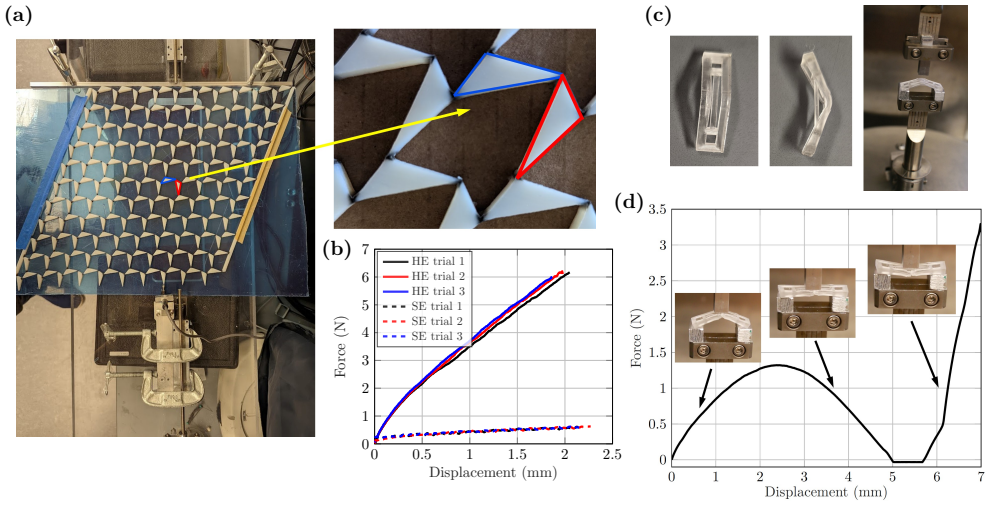

Figure 4.7: Surface stiffness of bistable lattice made by multi-materials and bistable unit design and test. (a) Experimental setup for surface stiffness testing of multi-material Maxwell lattice. A zoom-in panel shows the detailed unit cells and the hinges using soft materials. (b) Force versus displacement for the hard and floppy edges. The solid lines indicate three trials for the hard edge while the dashed lines represent trials for the soft edge. The stiffness ratio between the two edges is averaged by the fitting with 3 trials and is around 16. (c) A bistable hinge, composed of two approximately triangular shaped prisms attached by a flexural hinge, and connected by a thin spring element. Experimental setup for force-displacement testing of the bistable hinge. (d) Force versus displacement for the bistable hinge. The force probe starts from one stable state of the bistable hinge and pushes the structure snapping to the other stable state with a displacement rate of 0.2 mm/s.

lattice has not been achieved yet due to both size limitation and material properties. A lattice with small unit cells such as the one shown in Fig. 4.7(a) cannot accommodate the bistable units as they would be under the printing resolution of the 3D printer, while enlarging the unit cells to incorporate the bistable units would lead to an overall size of the lattice beyond the limitation of the printing platform. A further engineering design needs to be considered to succeed in the integration of bistability and topological kagome lattices through additive manufacturing methods.

4.3 Discussion

In summary, a multi-stable topological mechanical lattice is first-ever created by attaching a spring between two specific edges of the unit cell of a topological kagome lattice. We experimentally and computationally show that the new design of the multistable Maxwell lattice can achieve a controllable and swift transformation between different topological phases with dramatically different mechanical behaviors and enhanced load-bearing capacity (Fig. 4.2(d)). We also studied interfaces between domains of lattices in different topological phases, revealing rich patterns. The asymmetric dynamics of this interface induced by the topological polarization will be interesting topics for future studies, with promising applications in impact control. In addition, we explored additive manufacturing methods to produce multistable lattices, demonstrating that multi-material 3D printing can help achieve edge stiffness ratios much greater than in previous studies, as well as proposing a bistable hingeless unit which can be incorporated into these lattices in future studies.

Multi-stable Maxwell lattices have broad potential applications according to different working circumstances. The edge of the polarized Maxwell lattices with a higher stiffness (hard edge) can be used for ballistic protection and vehicle components acting as load-bearing elements, while the soft edges of the lattices can be used as energy absorption layers and buffers. As the lattice reprograms to the non-polarized phase, both edges become soft, and this effect can be utilized to absorb and store external impact energy. The introduced bistability enables a feasible approach for improving the operation of programmable topological mechanical metamaterials. While in this specific example, bistablity in each unit cell is achieved through an addition of a spring, there are other methods by which bistability or multistability can be introduced including but not limited to strain engineering [112; 113; 114; 115] and mechanical buckling [116], opening important areas for future study. In addition, a valuable extension of the current study is to introduce multistability to 3D topological Maxwell lattices[ref], which exhibit 3 Guest-Hutchinson modes and more interesting modes of transformation, in addition to wide applicability as a structural material.

Moreover, the multistable mechanical metamaterials, with novel mechanical properties and deformation modes, provide a new approach to innovate mechanical computing architectures (both non-volatile and volatile systems). Hence, our study can inspire neuromorphic metamaterials with

unprecedented reprogrammability and controllability, for instance, ReMM that can perform advanced logical functions thanks to the multi-stability and superb reconfigurability of the lattice.

4.4 Materials and Methods

The primary methods used in this work were theoretical analysis combined with experimental validation. Computer-aided programming and numerical computations were implemented via MATLAB. The prototype consisting of 6×6-unit cells was 3D printed using PLA materials by a commercial 3D printer (Ender 3 Pro) and assembled with springs (Uxewll 304 stainless steel) to generate a multistable lattice. A surface stiffness test was implemented using a digital force gauge by pushing and pulling tips at the soft and hard edges.

The experiment on the multimaterial-3D-printed lattice was performed on a platform that employs a constant-speed actuator instrumented with a 1N force sensor (FORT 100). Three boundaries of the sample were fixed on the platform by clamps and tapes, and the force probe indented a selected tip at the open boundary by up to ~ 3 mm.

The hingeless bistable unit was 3D printed with a Nylon material (Ultracur3D ST 45) on a commercial 3D printer (Origin MDK4). The mechanical characterization of the bistable hinge was performed on a dynamic mechanical analyzer (TA RSA3) using a custom fixture to apply pressure to the outer edges of the unit while providing clearance for the spring element.

4.5 Appendices

4.5.1 Note 1: Elastic energy of a unit cell in the lattice

A unit cell chosen to calculate the elastic energy is illustrated on Fig. 4.1(a), where the displacement in x and y directions at each node has added to the unit cell, shown in Fig. 4.8. The bonds of the triangles can be defined as deformable rods with an effective stiffness, k_1, and the stiffness of the spring linking the centers of two bonds is k_2. When the unit cell is deformed associated with the lattice, displacements $\boldsymbol{u}$ of every nodes are generated, resulting in creating elastic energy of the unit cell.

Nodes defined as A, B, C, A', and B' in the unit cell are shared by two triangles either from the same unit cell or from different units. To avoid double counting of these nodes, each unit cell only contains three nodes, A, B, and C, which have notations of $_{i,j}$, representing the unit cell from ith row and jth column of the lattice. Adding nodes from the boundaries, the total number of nodes for a lattice with $n \times m$ unit cells is $6nm + 2n + 2m$. The displacement vector of the unit cell (i, j)

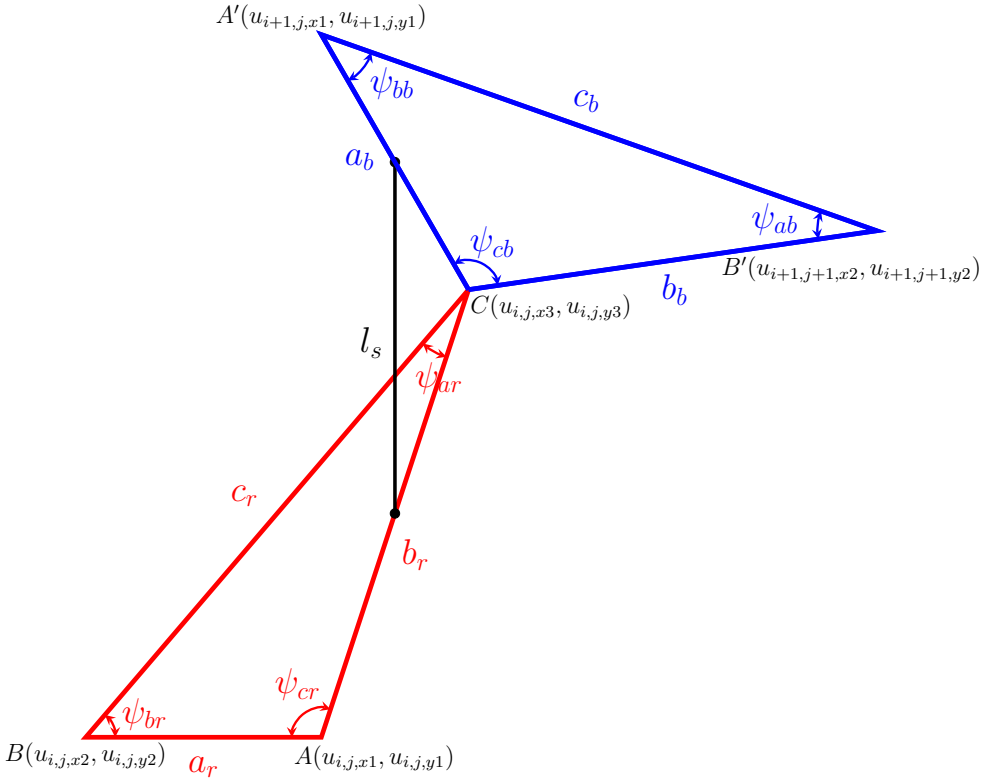

Figure 4.8: A unit cell of a homogeneous lattice with a bistable unit where the internal angle between two triangles is α. Node A, B, A', and B' are shared with the adjacent unit cells, while Node C belongs to the current unit cell corresponding to the α angle.

shown in Fig. 4.8 is defined as

$$\boldsymbol{u} = \Big(u_{i,j,x1}, u_{i,j,x2}, u_{i,j,x3}, u_{i+1,j,x1}, u_{i+1,j+1,x2}, u_{i,j,y1}, u_{i,j,y2}, u_{i,j,y3}, u_{i+1,j,y1}, u_{i+1,j+1,y2}\Big)^T. \tag{4.5}$$

The total elastic energy in the unit cell consisting of the energy from six sides of triangles and the last one from the added spring is given by

$$\begin{aligned}
En = \frac{k_2}{2}\Bigg(\frac{1}{2}\sqrt{\begin{aligned}&[-u_{i,j,x1} + u_{i+1,j,x1} + b_r\cos(\theta+\psi_{bb}+\psi_{cr}) - a_b\cos(\alpha+\theta+\psi_{ar}+\psi_{bb}+\psi_{cr})]^2\\ &+[u_{i,j,y1} - u_{i+1,j,y1} + b_r\sin(\theta+\psi_{bb}+\psi_{cr}) - a_b\sin(\alpha+\theta+\psi_{ar}+\psi_{bb}+\psi_{cr})]^2\end{aligned}} - l_s\Bigg)^2 \\
+\frac{k_1}{2}\Bigg[\Bigg(\sqrt{\begin{aligned}&[-u_{i,j,x1} + u_{i,j,x2} + a_r\cos(\theta+\psi_{bb})]^2\\ &+[u_{i,j,y1} - u_{i,j,y2} + a_r\sin(\theta+\psi_{bb})]^2\end{aligned}} - a_r\Bigg)^2 \\
+\Bigg(\sqrt{\begin{aligned}&[-u_{i,j,x1} + u_{i,j,x3} + b_r\cos(\theta+\psi_{bb}+\psi_{cr})]^2\\ &+[u_{i,j,y1} - u_{i,j,y3} + b_r\sin(\theta+\psi_{bb}+\psi_{cr})]^2\end{aligned}} - b_r\Bigg)^2 \\
+\Bigg(\sqrt{\begin{aligned}&[u_{i,j,x2} - u_{i,j,x3} + a_r\cos(\theta+\psi_{bb}) - b_r\cos(\theta+\psi_{bb}+\psi_{cr})]^2\\ &+[-u_{i,j,y2} + u_{i,j,y3} + a_r\sin(\theta+\psi_{bb}) - b_r\sin(\theta+\psi_{bb}+\psi_{cr})]^2\end{aligned}} - c_r\Bigg)^2 \\
+\Bigg(\sqrt{\begin{aligned}&[-u_{i+1,j,x1} + u_{i,j,x3} + a_b\cos(\alpha+\theta+\psi_{ar}+\psi_{bb}+\psi_{cr})]^2\\ &+[u_{i+1,j,y1} - u_{i,j,y3} + a_b\sin(\alpha+\theta+\psi_{ar}+\psi_{bb}+\psi_{cr})]^2\end{aligned}} - a_b\Bigg)^2 \\
+\Bigg(\sqrt{\begin{aligned}&[-u_{i+1,j+1,x2} + u_{i,j,x3}\\ &+b_b\cos(\alpha+\theta+\psi_{ar}+\psi_{bb}+\psi_{cr}+\psi_{cb})]^2\\ &+[u_{i+1,j+1,y2} - u_{i,j,y3}\\ &+b_b\sin(\alpha+\theta+\psi_{ar}+\psi_{bb}+\psi_{cr}+\psi_{cb})]^2\end{aligned}} - b_b\Bigg)^2 \\
+\Bigg(\sqrt{\begin{aligned}&[-u_{i+1,j,x1} + u_{i+1,j+1,x2} + a_b\cos(\alpha+\theta+\psi_{ar}+\psi_{bb}+\psi_{cr})\\ &-b_b\cos(\alpha+\theta+\psi_{ar}+\psi_{bb}+\psi_{cr}+\psi_{cb})]^2\\ &+[u_{i+1,j,y1} - u_{i+1,j+1,y2} + a_b\sin(\alpha+\theta+\psi_{ar}+\psi_{bb}+\psi_{cr})\\ &-b_b\sin(\alpha+\theta+\psi_{ar}+\psi_{bb}+\psi_{cr}+\psi_{cb})]^2\end{aligned}} - c_b\Bigg)^2\Bigg].
\end{aligned} \tag{4.6}$$

Eq. (4.6) gives the energy of an entire unit cell. However, the total energy of a lattice is the combination of these entire unit cells having added spring and additional unit cells which only include red triangles from the top edge or blue triangles from the bottom. These incomplete unit cells only

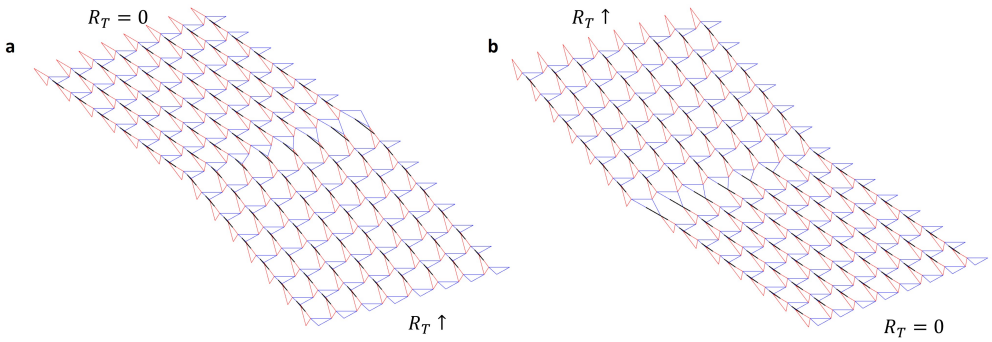

Figure 4.9: initial configurations of a 14×8 lattice with (a) $\boldsymbol{R}_T = \boldsymbol{a_2} - \boldsymbol{a_1}$ at the bottom and $\boldsymbol{R}_T = 0$ at the top, and (b) $\boldsymbol{R}_T = \boldsymbol{a_2} - \boldsymbol{a_1}$ at the top and $\boldsymbol{R}_T = 0$ at the bottom.

have partial terms of energy in Eq. (4.6) which are related to those triangles. Reconfiguration results in Fig. 4.5 are solved by nonlinear minimization of the total elastic energy of the lattice using Eq. (4.6). First, two initial configurations of the lattice are given by two different sets of angles from homogeneous lattices, one located in the polarized domain, and the other in the non-polarized phase. Second, bonds at the interface of two groups of lattices are stretched and connected together to create an entire lattice consisting of these two domains (two examples in Fig. 4.9). Third, the combined lattice is relaxed and the nonlinear minimization (nonlinear conjugate gradient method) is applied to solve this unconstrained problem.

4.5.2 Note 2: Linearized elastic energy of a unit cell

To quantify the surface stiffness of a Maxwell lattice during the polarization transition, it is assumed that the relative deformations of neighboring sites of the lattice is small enough (small $\Delta \boldsymbol{u}$ values) when compared with the geometry of the lattice, and thus the simplified linearized energy of a unit cell, T_{en}, can be used as an approximation instead of the nonlinear energy En. The linearized elastic energy of an entire unit cell represented in Fig. 4.8 is given by

$$T_{en} = \boldsymbol{u}^T \boldsymbol{K}_{en} \boldsymbol{u} + \boldsymbol{F}_{en}^T \boldsymbol{u} + T_{en0}, \tag{4.7}$$

where $\boldsymbol{K}_{en}$ and $\boldsymbol{F}_{en}$ are a 10 by 10 semi positive-definite matrix corresponding to the quadratic term and an 10 by 1 vector relate to the force on the bistable spring away from the rest length l_s,

respectively, at a given α, which have the forms

$$\boldsymbol{K}_{en} = \begin{bmatrix} K_{1,1} & K_{1,2} & K_{1,3} & K_{1,4} & 0 & K_{1,6} & K_{1,7} & K_{1,8} & K_{1,9} & 0 \\ K_{2,1} & K_{2,2} & K_{2,3} & 0 & 0 & K_{2,6} & K_{2,7} & K_{2,8} & 0 & 0 \\ K_{3,1} & K_{3,2} & K_{3,3} & K_{3,4} & K_{3,5} & K_{3,6} & K_{3,7} & K_{3,8} & K_{3,9} & K_{3,10} \\ K_{4,1} & 0 & K_{4,3} & K_{4,4} & K_{4,5} & K_{4,6} & 0 & K_{4,8} & K_{4,9} & K_{4,10} \\ 0 & 0 & K_{5,3} & K_{5,4} & K_{5,5} & 0 & 0 & K_{5,8} & K_{5,9} & K_{5,10} \\ K_{6,1} & K_{6,2} & K_{6,3} & K_{6,4} & 0 & K_{6,6} & K_{6,7} & K_{6,8} & K_{6,9} & 0 \\ K_{7,1} & K_{7,2} & K_{7,3} & 0 & 0 & K_{7,6} & K_{7,7} & K_{7,8} & 0 & 0 \\ K_{8,1} & K_{8,2} & K_{8,3} & K_{8,4} & K_{8,5} & K_{8,6} & K_{8,7} & K_{8,8} & K_{8,9} & K_{8,10} \\ K_{9,1} & 0 & K_{9,3} & K_{9,4} & K_{9,5} & K_{9,6} & 0 & K_{9,8} & K_{9,9} & K_{9,10} \\ 0 & 0 & K_{10,3} & K_{10,4} & K_{10,5} & 0 & 0 & K_{10,8} & K_{10,9} & K_{10,10} \end{bmatrix}_{\alpha}, \tag{4.8}$$

$$\boldsymbol{F}_{en}^{T} = \begin{bmatrix} F_1 & 0 & 0 & F_4 & 0 & F_6 & 0 & 0 & F_9 & 0 \end{bmatrix}_{\alpha}, \tag{4.9}$$

and $T_{en0} = \frac{k_2}{4}\left(a_b^2 + b_r^2 - 2a_b b_r \cos(\alpha + \psi_{ar}) + 4l_s(l_s - \sqrt{a_b^2 + b_r^2 - 2a_b b_r \cos(\alpha + \psi_{ar})})\right)$ is an energy constant resulting from the prestress in the spring, where l_s is the rest length of the added spring.

Coefficients of diagonal terms in the dynamic matrix $\boldsymbol{K}_{en}$ are calculated:

$$K_{1,1} = k_1 \cos^2(\theta + \psi_{bb}) + k_1 \cos^2(\theta + \psi_{bb} + \psi_{cr}) \tag{4.10}$$

$$+ \frac{k_2(b_r \cos(\theta + \psi_{bb} + \psi_{cr}) - a_b \cos(\alpha + \theta + \psi_{ar} + \psi_{bb} + \psi_{cr}))^2}{4(a_b^2 + b_r^2 - 2a_b b_r \cos(\alpha + \psi_{ar}))} \tag{4.11}$$

$$K_{2,2} = k_1 \cos^2(\theta + \psi_{bb}) + \frac{k_1(a_r \cos(\theta + \psi_{bb}) - b_r \cos(\theta + \psi_{bb} + \psi_{cr}))^2}{a_r^2 + b_r^2 - 2a_r b_r \cos(\psi_{cr})} \tag{4.12}$$

$$K_{3,3} = k_1 \cos^2(\theta + \psi_{bb} + \psi_{cr}) + k_1 \cos^2(\alpha + \theta + \psi_{ar} + \psi_{bb} + \psi_{cr}) +$$
$$k_1 \cos^2(\alpha + \theta + \psi_{ar} + \psi_{bb} + \psi_{cr} + \psi_{cb}) + \frac{k_1(a_r \cos(\theta + \psi_{bb}) - b_r \cos(\theta + \psi_{bb} + \psi_{cr}))^2}{a_r^2 + b_r^2 - 2a_r b_r \cos(\psi_{cr})} \tag{4.13}$$

$$K_{4,4} = k_1 \cos^2(\alpha + \theta + \psi_{ar} + \psi_{bb} + \psi_{cr}) +$$
$$\frac{k_2(b_r \cos(\theta + \psi_{bb} + \psi_{cr}) - a_b \cos(\alpha + \theta + \psi_{ar} + \psi_{bb} + \psi_{cr}))^2}{4(a_b^2 + b_r^2 - 2a_b b_r \cos(\alpha + \psi_{ar}))} + \tag{4.14}$$
$$\frac{k_1(a_b \cos(\alpha + \theta + \psi_{ar} + \psi_{bb} + \psi_{cr}) - b_b \cos(\alpha + \theta + \psi_{ar} + \psi_{bb} + \psi_{cr} + \psi_{cb}))^2}{a_b^2 + b_b^2 - 2a_b b_b \cos(\psi_{cb})}$$

$$K_{5,5} = k_1 \cos^2(\alpha + \theta + \psi_{ar} + \psi_{bb} + \psi_{cr} + \psi_{cb}) +$$
$$\frac{k_1(a_b \cos(\alpha + \theta + \psi_{ar} + \psi_{bb} + \psi_{cr}) - b_b \cos(\alpha + \theta + \psi_{ar} + \psi_{bb} + \psi_{cr} + \psi_{cb}))^2}{a_b^2 + b_b^2 - 2a_b b_b \cos(\psi_{cb})} \tag{4.15}$$

$$K_{6,6} = k_1 \sin^2(\theta + \psi_{bb}) + k_1 \sin^2(\theta + \psi_{bb} + \psi_{cr}) + \tag{4.16}$$
$$\frac{k_2(b_r \sin(\theta + \psi_{bb} + \psi_{cr}) - a_b \sin(\alpha + \theta + \psi_{ar} + \psi_{bb} + \psi_{cr}))^2}{4(a_b^2 + b_r^2 - 2a_b b_r \cos(\alpha + \psi_{ar}))} \tag{4.17}$$

$$K_{7,7} = k_1 \sin^2(\theta + \psi_{bb}) +$$
$$\frac{k_1(a_r \sin(\theta + \psi_{bb}) - b_r \sin(\theta + \psi_{bb} + \psi_{cr}))^2}{a_r^2 + b_r^2 - 2a_r b_r \cos(\psi_{cr})} \tag{4.18}$$

$$K_{8,8} = k_1 \sin^2(\theta + \psi_{bb} + \psi_{cr}) + k_1 \sin^2(\alpha + \theta + \psi_{ar} + \psi_{bb} + \psi_{cr}) +$$
$$k_1 \sin^2(\alpha + \theta + \psi_{ar} + \psi_{bb} + \psi_{cr} + \psi_{cb}) + \frac{k_1(a_r \sin(\theta + \psi_{bb}) - b_r \sin(\theta + \psi_{bb} + \psi_{cr}))^2}{a_r^2 + b_r^2 - 2a_r b_r \cos(\psi_{cr})} \tag{4.19}$$

$$K_{9,9} = k_1 \sin^2(\alpha + \theta + \psi_{ar} + \psi_{bb} + \psi_{cr}) +$$
$$\frac{k_2(b_r \sin(\theta + \psi_{bb} + \psi_{cr}) - a_b \sin(\alpha + \theta + \psi_{ar} + \psi_{bb} + \psi_{cr}))^2}{4(a_b^2 + b_r^2 - 2a_b b_r \cos(\alpha + \psi_{ar}))} + \tag{4.20}$$
$$\frac{k_1(a_b \sin(\alpha + \theta + \psi_{ar} + \psi_{bb} + \psi_{cr}) - b_b \sin(\alpha + \theta + \psi_{ar} + \psi_{bb} + \psi_{cr} + \psi_{cb}))^2}{a_b^2 + b_b^2 - 2a_b b_b \cos(\psi_{cb})}$$

$$K_{10,10} = k_1 \sin^2(\alpha + \theta + \psi_{ar} + \psi_{bb} + \psi_{cr} + \psi_{cb}) +$$
$$\frac{k_1(a_b \sin(\alpha + \theta + \psi_{ar} + \psi_{bb} + \psi_{cr}) - b_b \sin(\alpha + \theta + \psi_{ar} + \psi_{bb} + \psi_{cr} + \psi_{cb}))^2}{a_b^2 + b_b^2 - 2a_b b_b \cos(\psi_{cb})}. \tag{4.21}$$

Coefficients of off-diagonal terms in Eq. (4.8) are expressed below:

$$K_{1,2} = K_{2,1} = -k_1 \cos^2(\theta + \psi_{bb}) \tag{4.22}$$

$$K_{1,3} = K_{3,1} = -k_1 \cos^2(\theta + \psi_{bb} + \psi_{cr}) \tag{4.23}$$

$$K_{1,4} = K_{4,1} = \frac{-k_2(b_r \cos(\theta + \psi_{bb} + \psi_{cr}) - a_b \cos(\alpha + \theta + \psi_{ar} + \psi_{bb} + \psi_{cr}))^2}{4(a_b^2 + b_r^2 - 2a_b b_r \cos(\alpha + \psi_{ar}))} \tag{4.24}$$

$$\begin{aligned} K_{1,6} = K_{6,1} = &-k_1 \cos(\theta + \psi_{bb}) \sin(\theta + \psi_{bb}) - k_1 \cos(\theta + \psi_{bb} + \psi_{cr}) \sin(\theta + \psi_{bb} + \psi_{cr}) - \\ &k_2(b_r \cos(\theta + \psi_{bb} + \psi_{cr}) - a_b \cos(\alpha + \theta + \psi_{ar} + \psi_{bb} + \psi_{cr})) \cdot \\ &\frac{(b_r \sin(\theta + \psi_{bb} + \psi_{cr}) - a_b \sin(\alpha + \theta + \psi_{ar} + \psi_{bb} + \psi_{cr}))}{4(a_b^2 + b_r^2 - 2a_b b_r \cos(\alpha + \psi_{ar}))} \end{aligned} \tag{4.25}$$

$$K_{1,7} = K_{7,1} = k_1 \cos(\theta + \psi_{bb}) \sin(\theta + \psi_{bb}) \tag{4.26}$$

$$K_{1,8} = K_{8,1} = k_1 \cos(\theta + \psi_{bb} + \psi_{cr}) \sin(\theta + \psi_{bb} + \psi_{cr}) \tag{4.27}$$

$$\begin{aligned} K_{1,9} = K_{9,1} = &k_2(b_r \cos(\theta + \psi_{bb} + \psi_{cr}) - a_b \cos(\alpha + \theta + \psi_{ar} + \psi_{bb} + \psi_{cr})) \cdot \\ &\frac{(b_r \sin(\theta + \psi_{bb} + \psi_{cr}) - a_b \sin(\alpha + \theta + \psi_{ar} + \psi_{bb} + \psi_{cr}))}{4(a_b^2 + b_r^2 - 2a_b b_r \cos(\alpha + \psi_{ar}))} \end{aligned} \tag{4.28}$$

$$K_{2,3} = K_{3,2} = \frac{-k_1(a_r \cos(\theta + \psi_{bb}) - b_r \cos(\theta + \psi_{bb} + \psi_{cr}))^2}{a_r^2 + b_r^2 - 2a_r b_r \cos(\psi_{cr})} \tag{4.29}$$

$$K_{2,6} = K_{6,2} = k_1 \cos(\theta + \psi_{bb}) \sin(\theta + \psi_{bb}) \tag{4.30}$$

$$\begin{aligned} K_{2,7} = K_{7,2} = &k_1 \cos(\theta + \psi_{bb}) \sin(\theta + \psi_{bb}) + \\ &\frac{k_1(a_r \cos(\theta + \psi_{bb}) - b_r \cos(\theta + \psi_{bb} + \psi_{cr}))(-a_r \sin(\theta + \psi_{bb}) + b_r \sin(\theta + \psi_{bb} + \psi_{cr}))}{a_r^2 + b_r^2 - 2a_r b_r \cos(\psi_{cr})} \end{aligned} \tag{4.31}$$

$$K_{2,8} = K_{8,2} = \frac{k_1(a_r \cos(\theta + \psi_{bb}) - b_r \cos(\theta + \psi_{bb} + \psi_{cr}))(a_r \sin(\theta + \psi_{bb}) - b_r \sin(\theta + \psi_{bb} + \psi_{cr}))}{a_r^2 + b_r^2 - 2a_r b_r \cos(\psi_{cr})} \tag{4.32}$$

$$K_{3,4} = K_{4,3} = -k_1 \cos^2(\alpha + \theta + \psi_{ar} + \psi_{bb} + \psi_{cr}) \tag{4.33}$$

$$K_{3,5} = K_{5,3} = -k_1 \cos^2(\alpha + \theta + \psi_{ar} + \psi_{bb} + \psi_{cr} + \psi_{cb}) \tag{4.34}$$

$$K_{3,6} = K_{6,3} = k_1 \cos(\theta + \psi_{bb} + \psi_{cr}) \sin(\theta + \psi_{bb} + \psi_{cr}) \tag{4.35}$$

$$K_{3,7} = K_{7,3} = \frac{k_1(a_r \cos(\theta + \psi_{bb}) - b_r \cos(\theta + \psi_{bb} + \psi_{cr}))(a_r \sin(\theta + \psi_{bb}) - b_r \sin(\theta + \psi_{bb} + \psi_{cr}))}{a_r^2 + b_r^2 - 2a_r b_r \cos(\psi_{cr})} \tag{4.36}$$

$$\begin{aligned} K_{3,8} = K_{8,3} = & -k_1 \cos(\theta + \psi_{bb} + \psi_{cr}) \sin(\theta + \psi_{bb} + \psi_{cr}) + \\ & - k_1 \cos(\alpha + \theta + \psi_{ar} + \psi_{bb} + \psi_{cr}) \sin(\alpha + \theta + \psi_{ar} + \psi_{bb} + \psi_{cr}) + \\ & - k_1 \cos(\alpha + \theta + \psi_{ar} + \psi_{bb} + \psi_{cr} + \psi_{cb}) \sin(\alpha + \theta + \psi_{ar} + \psi_{bb} + \psi_{cr} + \psi_{cb}) + \\ & \frac{k_1(a_r \cos(\theta + \psi_{bb}) - b_r \cos(\theta + \psi_{bb} + \psi_{cr}))(-a_r \sin(\theta + \psi_{bb}) + b_r \sin(\theta + \psi_{bb} + \psi_{cr}))}{a_r^2 + b_r^2 - 2a_r b_r \cos(\psi_{cr}))} \end{aligned} \tag{4.37}$$

$$K_{3,9} = K_{9,3} = k_1 \cos(\alpha + \theta + \psi_{ar} + \psi_{bb} + \psi_{cr}) \sin(\alpha + \theta + \psi_{ar} + \psi_{bb} + \psi_{cr}) \tag{4.38}$$

$$K_{3,10} = K_{10,3} = k_1 \cos(\alpha + \theta + \psi_{ar} + \psi_{bb} + \psi_{cr} + \psi_{cb}) \sin(\alpha + \theta + \psi_{ar} + \psi_{bb} + \psi_{cr} + \psi_{cb}) \tag{4.39}$$

$$K_{4,5} = K_{5,4} = \frac{-k_1(a_b\cos(\alpha+\theta+\psi_{ar}+\psi_{bb}+\psi_{cr}) - b_b\cos(\alpha+\theta+\psi_{ar}+\psi_{bb}+\psi_{cr}+\psi_{cb}))^2}{a_b^2+b_b^2-2a_bb_b\cos(\psi_{cb})} \tag{4.40}$$

$$K_{4,6} = K_{6,4} = k_2(b_r\cos(\theta+\psi_{bb}+\psi_{cr}) - a_b\cos(\alpha+\theta+\psi_{ar}+\psi_{bb}+\psi_{cr}))\cdot \frac{(b_r\sin(\theta+\psi_{bb}+\psi_{cr}) - a_b\sin(\alpha+\theta+\psi_{ar}+\psi_{bb}+\psi_{cr}))}{4(a_b^2+b_r^2-2a_bb_r\cos(\alpha+\psi_{ar}))} \tag{4.41}$$

$$K_{4,8} = K_{8,4} = k_1\cos(\alpha+\theta+\psi_{ar}+\psi_{bb}+\psi_{cr})\sin(\alpha+\theta+\psi_{ar}+\psi_{bb}+\psi_{cr}) \tag{4.42}$$

$$\begin{aligned} K_{4,9} = K_{9,4} = {} & -k_1\cos(\alpha+\theta+\psi_{ar}+\psi_{bb}+\psi_{cr})\sin(\alpha+\theta+\psi_{ar}+\psi_{bb}+\psi_{cr}) + \\ & - k_2(b_r\cos(\theta+\psi_{bb}+\psi_{cr}) - a_b\cos(\alpha+\theta+\psi_{ar}+\psi_{bb}+\psi_{cr}))\cdot \\ & \frac{(b_r\sin(\theta+\psi_{bb}+\psi_{cr}) - a_b\sin(\alpha+\theta+\psi_{ar}+\psi_{bb}+\psi_{cr}))}{4(a_b^2+b_r^2-2a_bb_r\cos(\alpha+\psi_{ar}))} + \\ & - k_1(a_b\cos(\alpha+\theta+\psi_{ar}+\psi_{bb}+\psi_{cr}) - b_b\cos(\alpha+\theta+\psi_{ar}+\psi_{bb}+\psi_{cr}+\psi_{cb}))\cdot \\ & \frac{(a_b\sin(\alpha+\theta+\psi_{ar}+\psi_{bb}+\psi_{cr}) - b_b\sin(\alpha+\theta+\psi_{ar}+\psi_{bb}+\psi_{cr}+\psi_{cb}))}{a_b^2+b_b^2-2a_bb_b\cos(\psi_{cb})} \end{aligned} \tag{4.43}$$

$$K_{4,10} = K_{10,4} = k_1(a_b\cos(\alpha+\theta+\psi_{ar}+\psi_{bb}+\psi_{cr}) - b_b\cos(\alpha+\theta+\psi_{ar}+\psi_{bb}+\psi_{cr}+\psi_{cb}))\cdot \frac{(a_b\sin(\alpha+\theta+\psi_{ar}+\psi_{bb}+\psi_{cr}) - b_b\sin(\alpha+\theta+\psi_{ar}+\psi_{bb}+\psi_{cr}+\psi_{cb}))}{a_b^2+b_b^2-2a_bb_b\cos(\psi_{cb})} \tag{4.44}$$

$$K_{5,8} = K_{8,5} = k_1 \cos(\alpha + \theta + \psi_{ar} + \psi_{bb} + \psi_{cr} + \psi_{cb}) \sin(\alpha + \theta + \psi_{ar} + \psi_{bb} + \psi_{cr} + \psi_{cb})$$

(4.45)

$$K_{5,9} = K_{9,5} = k_1(a_b \cos(\alpha + \theta + \psi_{ar} + \psi_{bb} + \psi_{cr}) - b_b \cos(\alpha + \theta + \psi_{ar} + \psi_{bb} + \psi_{cr} + \psi_{cb})) \cdot \frac{(a_b \sin(\alpha + \theta + \psi_{ar} + \psi_{bb} + \psi_{cr}) - b_b \sin(\alpha + \theta + \psi_{ar} + \psi_{bb} + \psi_{cr} + \psi_{cb}))}{a_b^2 + b_b^2 - 2a_b b_b \cos(\psi_{cb})}$$

(4.46)

$$K_{5,10} = K_{10,5} = -k_1 \cos(\alpha + \theta + \psi_{ar} + \psi_{bb} + \psi_{cr} + \psi_{cb}) \sin(\alpha + \theta + \psi_{ar} + \psi_{bb} + \psi_{cr} + \psi_{cb}) - k_1(a_b \cos(\alpha + \theta + \psi_{ar} + \psi_{bb} + \psi_{cr}) - b_b \cos(\alpha + \theta + \psi_{ar} + \psi_{bb} + \psi_{cr} + \psi_{cb})) \cdot \frac{(a_b \sin(\alpha + \theta + \psi_{ar} + \psi_{bb} + \psi_{cr}) - b_b \sin(\alpha + \theta + \psi_{ar} + \psi_{bb} + \psi_{cr} + \psi_{cb}))}{a_b^2 + b_b^2 - 2a_b b_b \cos(\psi_{cb})}$$

(4.47)

$$K_{6,7} = K_{7,6} = -k_1 \sin^2(\theta + \psi_{bb}) \tag{4.48}$$

$$K_{6,8} = K_{8,6} = -k_1 \sin^2(\theta + \psi_{bb} + \psi_{cr}) \tag{4.49}$$

$$K_{6,9} = K_{9,6} = \frac{-k_2(b_r \sin(\theta + \psi_{bb} + \psi_{cr}) - a_b \sin(\alpha + \theta + \psi_{ar} + \psi_{bb} + \psi_{cr}))^2}{4(a_b^2 + b_r^2 - 2a_b b_r \cos(\alpha + \psi_{ar}))} \tag{4.50}$$

$$K_{7,8} = K_{8,7} = \frac{-k_1(a_r \sin(\theta + \psi_{bb}) - b_r \sin(\theta + \psi_{bb} + \psi_{cr}))^2}{a_r^2 + b_r^2 - 2a_r b_r \cos(\psi_{cr})} \tag{4.51}$$

$$K_{8,9} = K_{9,8} = -k_1 \sin^2(\alpha + \theta + \psi_{ar} + \psi_{bb} + \psi_{cr}) \tag{4.52}$$

$$K_{8,10} = K_{10,8} = -k_1 \sin^2(\alpha + \theta + \psi_{ar} + \psi_{bb} + \psi_{cr} + \psi_{cb}) \tag{4.53}$$

$$K_{9,10} = K_{10,9} = \frac{-k_1(a_b \sin(\alpha + \theta + \psi_{ar} + \psi_{bb} + \psi_{cr}) - b_b \sin(\alpha + \theta + \psi_{ar} + \psi_{bb} + \psi_{cr} + \psi_{cb}))^2}{a_b^2 + b_b^2 - 2a_b b_b \cos(\psi_{cb})}. \tag{4.54}$$

Additional coefficients in the $\boldsymbol{F}_{en}$ vector are

$$\begin{aligned} F_1 =& k_2(-2l_s + \sqrt{a_b^2 + b_r^2 - 2a_b b_r \cos(\alpha + \psi_{ar})})\cdot \\ & \frac{-b_r \cos(\alpha + \psi_{ar}) + a_b \cos(\alpha + \theta + \psi_{ar} + \psi_{bb} + \psi_{cr})}{2\sqrt{a_b^2 + b_r^2 - 2a_b b_r \cos(\alpha + \psi_{ar})}} \end{aligned} \tag{4.55}$$

$$\begin{aligned} F_4 =& k_2(-2l_s + \sqrt{a_b^2 + b_r^2 - 2a_b b_r \cos(\alpha + \psi_{ar})})\cdot \\ & \frac{b_r \cos(\alpha + \psi_{ar}) - a_b \cos(\alpha + \theta + \psi_{ar} + \psi_{bb} + \psi_{cr})}{2\sqrt{a_b^2 + b_r^2 - 2a_b b_r \cos(\alpha + \psi_{ar})}} \end{aligned} \tag{4.56}$$

$$\begin{aligned} F_6 =& k_2(-2l_s + \sqrt{a_b^2 + b_r^2 - 2a_b b_r \cos(\alpha + \psi_{ar})})\cdot \\ & \frac{b_r \sin(\alpha + \psi_{ar}) - a_b \sin(\alpha + \theta + \psi_{ar} + \psi_{bb} + \psi_{cr})}{2\sqrt{a_b^2 + b_r^2 - 2a_b b_r \cos(\alpha + \psi_{ar})}} \end{aligned} \tag{4.57}$$

$$\begin{aligned} F_9 =& k_2(-2l_s + \sqrt{a_b^2 + b_r^2 - 2a_b b_r \cos(\alpha + \psi_{ar})})\cdot \\ & \frac{-b_r \sin(\alpha + \psi_{ar}) + a_b \sin(\alpha + \theta + \psi_{ar} + \psi_{bb} + \psi_{cr})}{2\sqrt{a_b^2 + b_r^2 - 2a_b b_r \cos(\alpha + \psi_{ar})}}\cdot \end{aligned} \tag{4.58}$$

The lattice also consists of unit cells with only red or blue triangles at the top or bottom edges without bistable units. For a unit cell, $(1, j)$, which only includes a blue triangle at the bottom of the lattice, the displacement vector $\boldsymbol{u}$ only consists of Node A', B', and C in Fig. 4.8, and is represented as

$$\boldsymbol{u} = \left(u_{i+1,j,x1}, u_{i+1,j+1,x2}, u_{i,j,x3}, u_{i+1,j,y1}, u_{i+1,j+1,y2}, u_{i,j,y3}\right)^T. \tag{4.59}$$

The corresponding linearized energy can be written by

$$T_b = \boldsymbol{u}^T \boldsymbol{K}_b \boldsymbol{u}, \tag{4.60}$$

where $\boldsymbol{K}_b$ is a 6 by 6 semi positive-definite matrix and is expressed

$$\boldsymbol{K}_b = \begin{bmatrix} Kb_{1,1} & Kb_{1,2} & Kb_{1,3} & Kb_{1,4} & Kb_{1,5} & Kb_{1,6} \\ Kb_{2,1} & Kb_{2,2} & Kb_{2,3} & Kb_{2,4} & Kb_{2,5} & Kb_{2,6} \\ Kb_{3,1} & Kb_{3,2} & Kb_{3,3} & Kb_{3,4} & Kb_{3,5} & Kb_{3,6} \\ Kb_{4,1} & Kb_{4,2} & Kb_{4,3} & Kb_{4,4} & Kb_{4,5} & Kb_{4,6} \\ Kb_{5,1} & Kb_{5,2} & Kb_{5,3} & Kb_{5,4} & Kb_{5,5} & Kb_{5,6} \\ Kb_{6,1} & Kb_{6,2} & Kb_{6,3} & Kb_{6,4} & Kb_{6,5} & Kb_{6,6} \end{bmatrix}. \tag{4.61}$$

Each coefficient in the $\boldsymbol{K}_b$ is given as follow

$$Kb_{1,1} = k_1 + k_1 \cos^2(\psi_{bb}) \tag{4.62}$$

$$Kb_{2,2} = k_1 + \frac{k_1(c_b - a_b \cos(\psi_{bb}))^2}{a_b^2 + c_b^2 - 2a_b c_b \cos(\psi_{bb})} \tag{4.63}$$

$$Kb_{3,3} = k_1 \cos^2(\psi_{bb}) + \frac{k_1(c_b - a_b \cos(\psi_{bb}))^2}{a_b^2 + c_b^2 - 2a_b c_b \cos(\psi_{bb})} \tag{4.64}$$

$$Kb_{4,4} = k_1 \sin^2(\psi_{bb}) \tag{4.65}$$

$$Kb_{5,5} = \frac{k_1(a_b \sin(\psi_{bb}))^2}{a_b^2 + c_b^2 - 2a_b c_b \cos(\psi_{bb})} \tag{4.66}$$

$$Kb_{6,6} = k_1 \sin^2(\psi_{bb}) + \frac{k_1(a_b \sin(\psi_{bb}))^2}{a_b^2 + c_b^2 - 2a_b c_b \cos(\psi_{bb})}, \tag{4.67}$$

$$Kb_{1,2} = Kb_{2,1} = -k_1 \tag{4.68}$$

$$Kb_{1,3} = Kb_{3,1} = -k_1 \cos^2(\psi_{bb}) \tag{4.69}$$

$$Kb_{1,4} = Kb_{4,1} = -k_1 \cos(\psi_{bb}) \sin(\psi_{bb}) \tag{4.70}$$

$$Kb_{1,6} = Kb_{6,1} = k_1 \cos(\psi_{bb}) \sin(\psi_{bb}) \tag{4.71}$$

$$Kb_{2,3} = Kb_{3,2} = -\frac{k_1(c_b - a_b \cos(\psi_{bb}))^2}{a_b^2 + c_b^2 - 2a_b c_b \cos(\psi_{bb})} \tag{4.72}$$

$$Kb_{2,5} = Kb_{5,2} = \frac{k_1(c_b - a_b \cos(\psi_{bb}))(a_b \sin(\psi_{bb}))}{a_b^2 + c_b^2 - 2a_b c_b \cos(\psi_{bb})} \tag{4.73}$$

$$Kb_{2,6} = Kb_{6,2} = \frac{-k_1(c_b - a_b \cos(\psi_{bb}))(a_b \sin(\psi_{bb}))}{a_b^2 + c_b^2 - 2a_b c_b \cos(\psi_{bb})} \tag{4.74}$$

$$Kb_{3,4} = Kb_{4,3} = k_1 \cos(\psi_{bb}) \sin(\psi_{bb}) \tag{4.75}$$

$$Kb_{3,5} = Kb_{5,3} = \frac{-k_1(c_b - a_b \cos(\psi_{bb}))(a_b \sin(\psi_{bb}))}{a_b^2 + c_b^2 - 2a_b c_b \cos(\psi_{bb})} \tag{4.76}$$

$$Kb_{3,6} = Kb_{6,3} = -k_1 \cos(\psi_{bb}) \sin(\psi_{bb}) + \frac{k_1(c_b - a_b \cos(\psi_{bb}))(a_b \sin(\psi_{bb}))}{a_b^2 + c_b^2 - 2a_b c_b \cos(\psi_{bb})} \tag{4.77}$$

$$Kb_{4,6} = Kb_{6,4} = -k_1 \sin^2(\psi_{bb}) \tag{4.78}$$

$$Kb_{5,6} = Kb_{6,5} = \frac{-k_1(a_b \sin(\psi_{bb}))^2}{a_b^2 + c_b^2 - 2a_b c_b \cos(\psi_{bb})}. \tag{4.79}$$

For a unit cell, (n, j), that only has a red triangle at the top edge, the displacement vector $\boldsymbol{u}$ now has Nodes A, B, and C accordingly. The corresponding semi positive-definite matrix $\boldsymbol{K}_r$ of this

unit cell associated with these displacements is shown below.

$$\boldsymbol{u} = \left(u_{i,j,x1}, u_{i,j,x2}, u_{i,j,x3}, u_{i,j,y1}, u_{i,j,y2}, u_{i,j,y3}\right)^T, \tag{4.80}$$

$$\boldsymbol{K}_r = \begin{bmatrix} K_{1,1r} & K_{1,2} & K_{1,3} & K_{1,6r} & K_{1,7} & K_{1,8} \\ K_{2,1} & K_{2,2} & K_{2,3} & K_{2,6} & K_{2,7} & K_{2,8} \\ K_{3,1} & K_{3,2} & K_{3,3r} & K_{3,6} & K_{3,7} & K_{3,8r} \\ K_{6,1r} & K_{6,2} & K_{6,3} & K_{6,6r} & K_{6,7} & K_{6,8} \\ K_{7,1} & K_{7,2} & K_{7,3} & K_{7,6} & K_{7,7} & K_{7,8} \\ K_{8,1} & K_{8,2} & K_{8,3r} & K_{8,6} & K_{8,7} & K_{8,8r} \end{bmatrix}_\alpha, \tag{4.81}$$

where $K_{i,j}$ is the coefficient from the dynamic matrix $\boldsymbol{K}_{en}$, and $K_{i,jr}$ are given by

$$K_{1,1r} = k_1 \cos^2(\theta + \psi_{bb}) + k_1 \cos^2(\theta + \psi_{bb} + \psi_{cr}) \tag{4.82}$$

$$K_{3,3r} = k_1 \cos^2(\theta + \psi_{bb} + \psi_{cr}) + \frac{k_1(a_r \cos(\theta + \psi_{bb}) - b_r \cos(\theta + \psi_{bb} + \psi_{cr}))^2}{a_r^2 + b_r^2 - 2a_r b_r \cos(\psi_{cr})} \tag{4.83}$$

$$K_{6,6r} = k_1 \sin^2(\theta + \psi_{bb}) + k_1 \sin^2(\theta + \psi_{bb} + \psi_{cr}) \tag{4.84}$$

$$K_{8,8r} = k_1 \sin^2(\theta + \psi_{bb} + \psi_{cr}) + \frac{k_1(-a_r \sin(\theta + \psi_{bb}) + b_r \sin(\theta + \psi_{bb} + \psi_{cr}))^2}{a_r^2 + b_r^2 - 2a_r b_r \cos(\psi_{cr})} \tag{4.85}$$

$$K_{1,6r} = K_{6,1r} = -k_1 \cos(\theta + \psi_{bb}) \sin(\theta + \psi_{bb}) - k_1 \cos(\theta + \psi_{bb} + \psi_{cr}) \sin(\theta + \psi_{bb} + \psi_{cr}) \tag{4.86}$$

$$K_{3,8r} = K_{8,3r} = -k_1 \cos(\theta + \psi_{bb} + \psi_{cr}) \sin(\theta + \psi_{bb} + \psi_{cr}) - \frac{k_1(a_r \cos(\theta + \psi_{bb}) - b_r \cos(\theta + \psi_{bb} + \psi_{cr}))(a_r \sin(\theta + \psi_{bb}) - b_r \sin(\theta + \psi_{bb} + \psi_{cr}))}{a_r^2 + b_r^2 - 2a_r b_r \cos(\psi_{cr})}. \tag{4.87}$$

Compared $K_{i,jr}$ with $K_{i,j}$ at the same position in $\boldsymbol{K}_{en}$, $K_{i,jr}$ does not include the terms related to the energy from the bistable unit.

The total linearized elastic energy, $T = \boldsymbol{u}^T \boldsymbol{K} \boldsymbol{u} + \boldsymbol{F}^T \boldsymbol{u} + T_0$, in Eq. (1) is the sum of the energy from all unit cells, including all those units with or without springs. The composite dynamic matrix K is a linear combination of $\boldsymbol{K}_{en}$, $\boldsymbol{K}_b$ and $\boldsymbol{K}_r$ that forms a $N \times N$ matrix, where $N = 6nm + 2n + 2m$, and the composite vector $\boldsymbol{F}$ is a N by 1 coefficient vector generated from $\boldsymbol{F}_{en}$ of each unit cell. The energy constant, $T_0 = (n-1)mT_{en0}$, is the sum of T_{en0} from $(n-1)m$ unit cells which have bistable units.

4.5.3 Note 3: Linearized mechanical stiffness

Without bistable units, a homogeneous Maxwell lattice can be transformed between different topological polarization domains via strain-free soft twisting. However, during the twisting process, the introduced bistability can generate new mechanical stiffness for the lattice, such as effective elastic and shear stiffness, when the spring is under compressed/elongated.

It is assumed that all bonds of the lattice have infinite stiffness and only added springs generate the elastic energy of the system. Starting from a homogeneous lattice with an initial twisting angle α, the rest length of the added spring is

$$l_s = \sqrt{\frac{a_b^2}{4} + \frac{b_r^2}{4} - \frac{a_b b_r \cos\left(\alpha + \psi_{ar}\right)}{2}}, \tag{4.88}$$

where the side length and inner angle of triangles are shown in Fig 4.8. Fixing the red triangle and given a small displacement, u_x, horizontal to the primitive vector, $\mathbf{a}_1$, (or u_y, perpendicular to $\mathbf{a}_1$) at Node A', the resulting angle change at Node C happens defined as $\delta\alpha$, and the corresponding length of the spring is

$$l = \sqrt{\frac{a_b^2}{4} + \frac{b_r^2}{4} - \frac{a_b b_r \cos\left(\alpha + \delta\alpha + \psi_{ar}\right)}{2}}. \tag{4.89}$$

According to the geometric relation of two triangles in a unit cell, the small displacement u_x and u_y can be rewritten as a function of $\delta\alpha$:

$$\begin{aligned} u_x &= a_b \cos(\pi - \psi_{bb} - \delta\alpha) - a_b \cos(\pi - \psi_{bb}), \\ u_y &= a_b \sin(\pi - \psi_{bb} - \delta\alpha) - a_b \sin(\pi - \psi_{bb}). \end{aligned} \tag{4.90}$$

Since the displacement and angle change is assumed to be small enough, Eqs. (4.89-4.90) can be linearized and are given as:

$$l = l_s(1 + \frac{a_b b_r \sin(\alpha + \psi_{ar})}{2l_s^2}\delta\alpha), \tag{4.91}$$

$$\begin{aligned} u_x &= a_b \sin(\pi - \psi_{bb})\delta\alpha, \\ u_y &= -a_b \cos(\pi - \psi_{bb})\delta\alpha. \end{aligned} \tag{4.92}$$

The pushing force of F_x (F_y) parallel (perpendicular) to the primitive vector of $\mathbf{a}_1$ that twists the lattice can be obtained by calculating the work that equals the total elastic energy of the added spring.

$$\begin{aligned} F_x &= \frac{k_2}{2u_x}\delta l^2, \\ F_y &= \frac{k_2}{2u_y}\delta l^2, \end{aligned} \tag{4.93}$$

where δl is the difference of the current length of spring and the rest length of the spring, which is

$$\delta l = l - l_s = \frac{a_b b_r \sin(\alpha + \psi_{ar})}{2l_s}\delta\alpha. \tag{4.94}$$

Therefore, the effective elastic stiffness and shear stiffness are

$$\begin{aligned} k_{el} &= \frac{F_y}{u_y|\cos\phi|} = k_2\frac{b_r^2\sin^2(\alpha+\psi_{ar})}{8l_s^2\cos^2(\pi-\psi_{bb})|\cos\phi|}, \\ k_{sh} &= \frac{F_x}{u_x|\sin\phi|} = k_2\frac{b_r^2\sin^2(\alpha+\psi_{ar})}{8l_s^2\sin^2(\pi-\psi_{bb})|\sin\phi|}, \end{aligned} \tag{4.95}$$

where ϕ is the angle between the vector of $\mathbf{a}_1$ and the side of c_b, which is given by

$$\arctan\phi = \frac{a_r\sin(\alpha-\psi_{bb}-\psi_{br})}{c_b + a_r\cos(\alpha-\psi_{bb}-\psi_{br})}. \tag{4.96}$$

4.5.4 Note 4: Information on the 3D printed Maxwell lattice

The prototype is designed using SOLIDWORKS and 3D printed using PLA materials via an Ender 3 Pro printer. The material infill density of 10% is used for the 3D printed parts. The spring is selected from commercial Uxewll 304 stainless steel, which has a spring constant of $k_2 = 150$ N/m. Fig. 4.10 shows a 3D-assembled designed unit cell, spring connectors and an example of an assembly of bistable lattice. Two rigid triangles (blue and red in Fig. 4.10a) are jointed at a vertex of each triangle to create a flexible hinge. Thus, the two triangles can be able to freely rotate to each other, so do the triangles in different unit cells. Moreover, the triangles are consisted of two layers, which gives the space for the additional spring embedded into the triangles. This added spring with much lower stiffness can provide an additional constraint of the unit and realize bistable equilibria (shown in Fig. 4.6(a)). The spring connectors (Fig. 4.10b) have raised parts which can hold the spring providing compressive or stretching force.

The effective stiffness k_1 for bonds of unit cells are determined by [117; 118; 119]

$$k_1 = \frac{f}{\Delta L} = 2E\frac{S}{L}, \tag{4.97}$$

where f is the stretching/compression force applied to the bond, ΔL is the stretched/compressed displacement, $E \approx 500$ MPa is the Young's modulus of the PLA material [120; 121; 122] (the infill density, printing speed and temperature, and holes in the part are expected to reduce the Young's modulus of PLA), and $S = 2.5 \times 10^{-6}$ m^2 and L are the cross-sectional area and the length of the bond, respectively. The factor of 2 is due to the double-layered configuration of the printed unit cell. In the experiments, since the length of the each bond are different ($L = 0.09$, 0.036, 0.072,

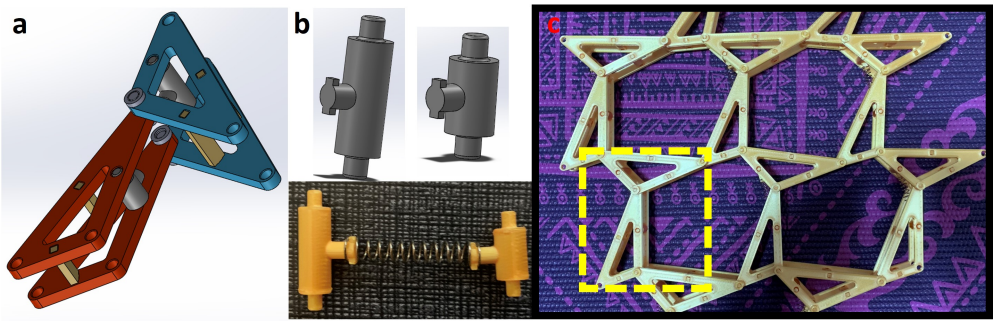

Figure 4.10: (a) 3-dimensional model of a unit cell, (b) 3D modeled and printed spring connectors, and (c) assembled unit cells connected with springs.

0.045, and 0.063 m), k_1 is used to calculate the theoretical results with different values, which are shown as $k_1 = 2.778 \times 10^4$, 6.944×10^4, 3.472×10^4, 5.556×10^4 and 3.968×10^4 N/m. Theoretical force-displacement and stiffness plots in Fig. 4.6(d) are created using these parameters (k_1 and k_2).

The experimental data show a good agreement with theoretical analysis (Fig. 4.6(d)), while there are slight discrepancy. The theoretical stiffness of the hard edge shows an insignificant decrease (no change for the pulling case) as the displacement increases; the experimental data show the increase of stiffness for the hard edge with increasing the displacement. At the low displacement range, the low stiffness is caused by the relative sliding of the fixed boundaries. But at the high displacement area, the friction, generated from the compression between hinges and triangles, dominates over the ratio of the force to displacement, leading to higher edge stiffness. The experimental stiffness of the soft edge (especially for the pushing case) is generally higher than the theoretical one since there are non-negligible surface frictions at the junctions of each unit cell.

Box plots of force-displacement are shown in Fig. 4.11 to illustrate surface stiffness at the soft and hard edge. Each edge is tested 15 times for both pushing and pulling it from the zero-displacement configuration with a displacement no less than 14 mm. The hard edge is around 50 times stiffer than the soft edge (see Fig. 4.6(d)), while in theory, the hard edge can get 100 times stiffer than the soft edge. This discrepancy is because that in a real system, the lattice still has friction at the contacting surfaces and bending stiffness from each triangle, resulting in the reduced difference in edge stiffness between two opposite edges. Nevertheless, these results validate that the added bistable units maintain the property of the surface stiffness of the lattice.

Fig. 4.12a and b show a 3D modeled bistable lattice design and multimaterial-3D-printed test piece, where dark colored hinges (red in (a)) are printed using Agilus30, a softer material, and light white parts are solid triangle bodies using a stiffer material, namely VeroWhite. Dark parts of the lattices are used to create hinges between the solid triangles in the lattice to resemble ideal hinged kagome lattice with zero bending stiffness. The hingeless bistable unit (3D model in Fig. 4.12c) 3D

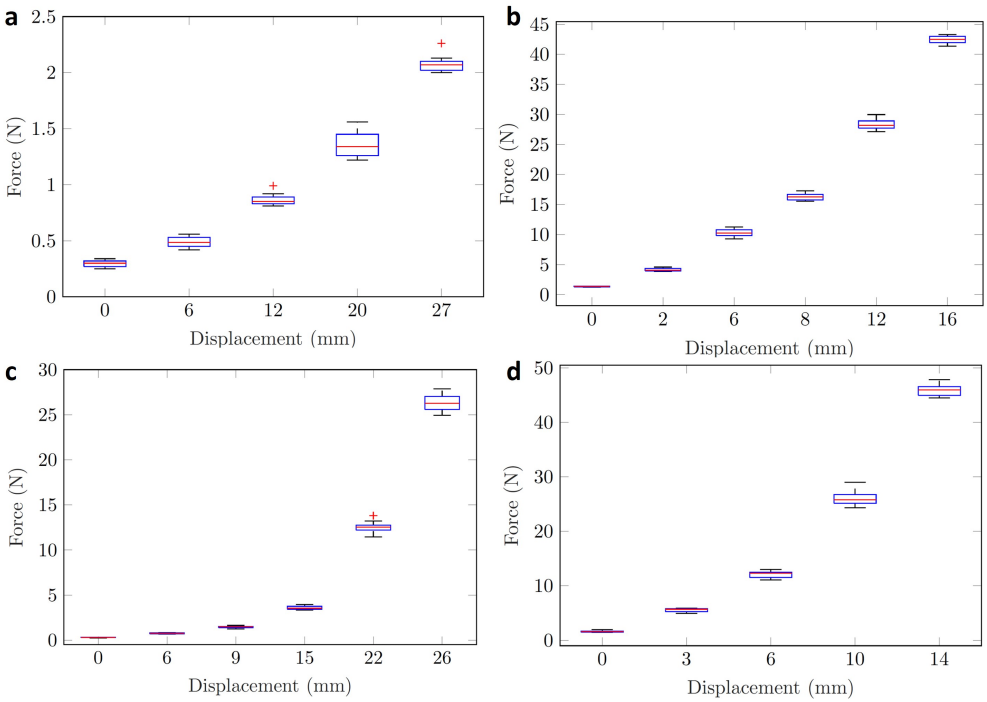

Figure 4.11: Box plots of force displacement relations for (a) pushing soft edge, (b) pushing hard edge, (c) pulling soft edge, and (d) pulling hard edge.

printed using a Nylon material (printed piece in Fig. 4.12d) and is used to link two solid triangles in each unit cell as a low-stiffness hinge. This hinge has two stable states, like the 3D-assembled bistable unit cell, with one state in topological polarized phase and the other one in non-polarized domain.

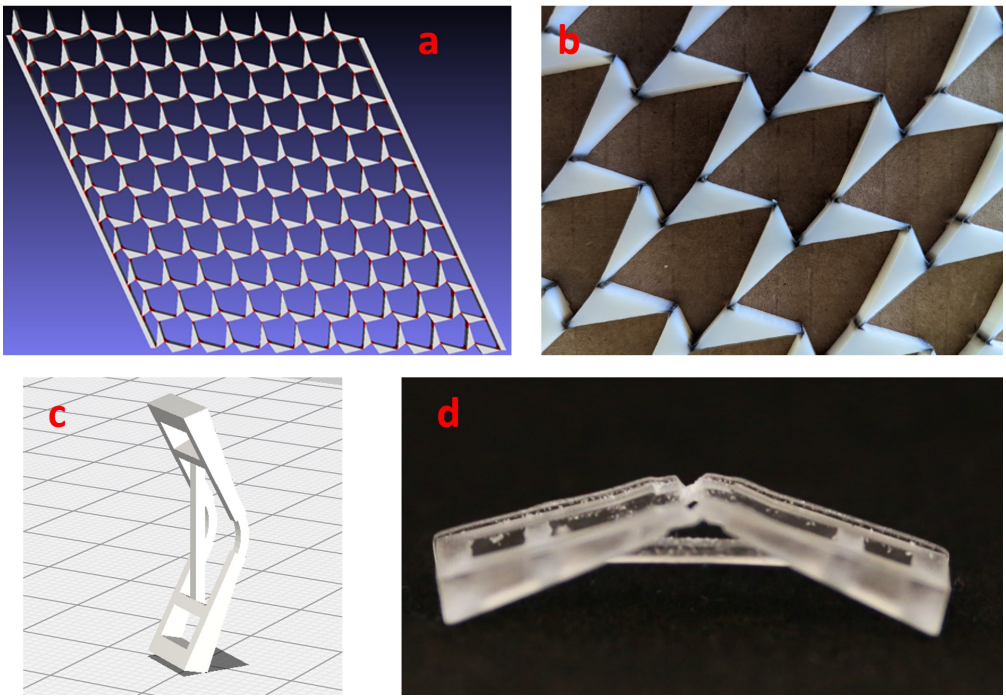

Figure 4.12: (a) 3-dimensional model of and (b) 3D printed multi-material bistable Maxwell lattice. (c) 3D modeled and (d) 3D printed bistable hinge.

CHAPTER 5

Quasi-static Nonlinear Wave-like Phenomena in a Topological Maxwell Lattice

This chapter summarizes the work *"Synthetically Non-Hermitian Nonlinear Wave-like Behavior in a Topological Mechanical Metamaterial"* co-authored by Haning Xiu, Ian Frankel, Harry Liu, Kai Qian, Siddhartha Sarkar, Brianna Macnider, Zi Chen1, Nicholas Boechler, and Xiaoming Mao under submission to PNAS, and posted as on arXiv as *arXiv:2207.09273*. The finalized version in the publication may appear with more contexts than this Chapter.

5.1 Introduction

The study of topological band theory in condensed matter physics has led to novel classes of materials termed topological insulators [123; 124] and topological superconductors [125], which support localized modes at the materials' edges that are highly robust to defects and perturbation [126]. The stability of these modes stems from topological protection conferred by the material's bulk properties. Topologically nontrivial materials have been shown to support unidirectional, backscattering-immune mode propagation, thus, facilitating the development of new superconducting devices [127] with applications in areas such as quantum computation [128; 129], as well as magnetoelectronic [130] and optoelectronic devices [131]. Recently, topological band theory has also been applied to the mechanical domain, which has enabled the creation of topological mechanical metamaterials (TMMs) that support phenomena such as energy localization and immunity to backscattering at finite frequencies, and a new ability to design and control quasi-static and spatiotemporally-varying stress and deformation fields in materials [132; 89; 86; 87; 94].

TMMs at the Maxwell point, referred to as Maxwell lattices, are a subclass of TMMs where the number of degrees of freedom (Degree of Freedom (DOF)s) balances with the number of constraints in the bulk (Fig. 5.1(a)); modes with zero energy arising in Maxwell lattices are referred to as "zero" or "floppy" modes [1; 53]. These ZMs have a topological nature described by a

polarization vector that is analogous to the topological invariant seen in the Su-Schrieffer-Heeger model [32] and they localize such that, in the linkage-limit, the edges the polarization vector points towards have zero stiffness and the opposite are rigid [1]. The direction of the polarization vector is controlled by the lattice's geometry and tunable [1; 53], arise. These ZMs have a topological nature described by a polarization vector that is analogous to the topological invariant seen in the Su-Schrieffer-Heeger model [32] and they localize such that, in the linkage-limit, the edges the polarization vector points towards have zero stiffness and the opposite are rigid [1]. The direction of the polarization vector is controlled by the lattice's geometry and tunable through a soft strain [16]. In the presence of interfaces or topological defects, this polarization can result in internal localized states of self-stress (SSSs) and ZMs [1; 14]. Further, due to the balanced numbers of DOFs and constraints in the bulk, such lattices are holographic and the state of the zero-energy configuration of a $d-$dimensional material can be fully prescribed from its $(d-1)$ dimensional boundary. In special cases such as twisted kagome lattices, the mechanisms can be written as conformal transformations [92; 30]. Such holography adds additional levels of deformation control since the bulk state can be controlled via the boundary. Due to their intrinsic scalability and high degree of control over deformation and stress fields through the tuning of the topological polarization vector, Maxwell lattices have been suggested for future use related to robotics, impact and energy absorption, tear resistance, nanoscale manufacturing via origami, and acoustic and phonon logic and computation devices (see, e.g., logic strategies via multistable metamaterials [133]) [23; 26; 25; 27; 134; 2].

Despite this revealed wealth of applications, the study of Maxwell lattices has been confined, by and large, to the linear, small deformation limit [53; 30; 1; 16; 22]. Intriguing nonlinear effects such as topological solitons have been revealed in one-dimensional (1D) Maxwell chains [93; 135]. In two-dimensional (2D) topological Maxwell lattices, the study of nonlinear effects have been so far limited to perturbation theories [23]. This is an important gap, as nonlinear systems do not obey superposition and, as such, support an ability to control the spatiotemporal allocation of energy in materials that vastly exceeds their linear counterparts [136; 137; 138] through phenomena such as self-localization [139; 140], frequency conversion and dynamic tunability [141; 142], and chaos [143], as well as rich interplay with finite-frequency topological states [23; 144; 124; 145; 146; 147; 148; 149]. Hence, we envision that combining nonlinear responses with the strong localization, non-reciprocity, and the robust nature of topological protection will lead to an important expansion of the ability to tailor spatiotemporal stress, deformation, and energy fields, with application areas demonstrated for nonlinear dynamical systems ranging from impact mitigation [150] to neuromorphic [151] and ultrafast mechanoacoustic computation [152; 153].

In this work, we show that ZMs of 2D topological Maxwell lattices map to waves in 1D non-

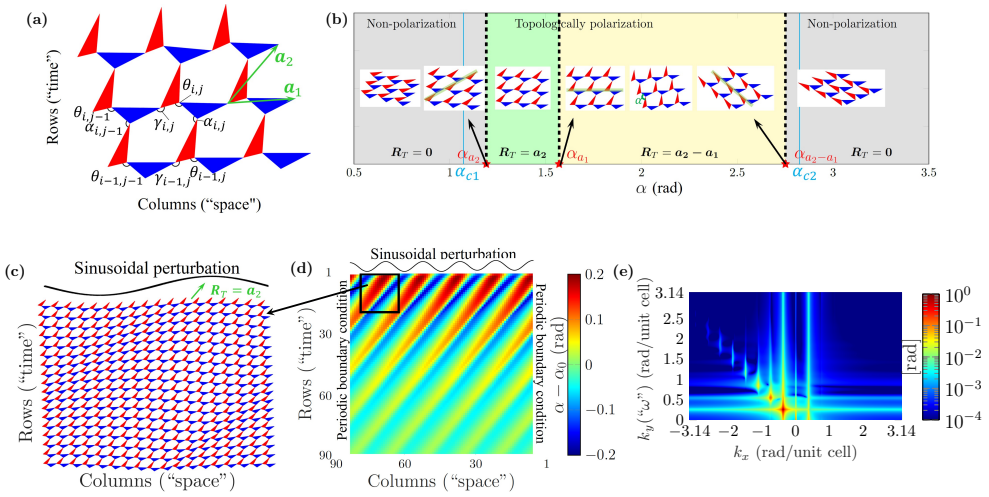

Figure 5.1: **Zero energy configuration, polarization diagram, and subsequent nonlinear wave-like behavior in the zero energy deformation field of a deformed kagome Maxwell lattice. The analogy between the 2D static deformation fields and a 1D, nonlinear, non-Hermitian wave equation is denoted in the axes labels**. (a) Geometry of the deformed kagome lattice we study here, where θ, α, and γ are internal angles between the red and blue triangles in the unit cells (with normalized dimensionless side lengths of (0.4, 0.8, 1) and (0.5, 0.7, 1) for red and blue triangles, respectively). (b) Topological transitions of the lattice shown in (a) by twisting α. The black arrows point to configurations at the boundary between polarization domains. The blue vertical lines denote angles between which $\det \epsilon_0 < 0$ and the linearized ZM deformation of the homogeneous lattice obeys hyperbolic PDEs, outside of which $\det \epsilon_0 > 0$ and the lattice obeys elliptic PDEs. (c) A zoomed-in view of a calculated section of an initially homogeneous lattice with $\mathbf{a_2}$ polarization, $\alpha_0 = 1.3344$, and periodic boundary conditions on left and right, perturbed by a sinusoidal static signal with $k_x = 0.349$ rad/unit cell and $\varepsilon = 20$ mrad. (d) The full lattice corresponding to the section shown in (c). (e) The 2D Fourier transform of the deformation field shown in (d), where the nonlinear phenomena of harmonic generation can be seen. Subscripts x and y denote the "columns" and "rows" axes, respectively.

Hermitian (active or damped [154; 155]) and non-reciprocal dynamical systems, and a rich set of nonlinear phenomena associated with dynamical systems arise in this static system, offering precise remote control of complex zero-energy spatial deformation patterns. It is important to highlight that there is a direct interplay between the topology of the lattice, which directly maps to the synthetic non-Hermiticity, and the observed nonlinear phenomena as a result of the induced amplification. In other fields, space-time mappings have historically brought critical insight in many fields in science, from polymer physics to quantum criticality, and time crystals [156; 157; 158; 159]. Using exact geometric calculations and subsequent experimental validation of nonlinear ZMs in deformed kagome TMMs, we observe spatial nonlinear wave-like phenomena including harmonic generation, localized topological domain switching, amplification enhanced frequency conversion, and solitary waves. The results presented here are scale-free, material independent, and add a new dimension to mechanical metamaterials engineering, wherein deformation fields can be predicted and intricately designed using insights derived from the analysis of nonlinear waves in non-Hermitian systems [154; 139; 136; 160; 161; 162; 163].

5.2 Results

5.2.1 Topological polarization and analogy to 1D dynamical systems

In Maxwell lattices, the number of DOFs and the number of constraints are identical in the bulk. By the Maxwell-Calladine index theorem [29; 1; 92; 53], this equality indicates that the difference between the number of ZMs and SSSs is proportional to the size of the open boundary. By manipulating the unit cell geometry, the ZMs can be localized at the boundaries of the lattice at which the topological polarization vector $\mathbf{R}_T$ points. Considering a finite 2D deformed kagome lattice consisting of N_x (number of columns) by N_y (number of rows) unit cells (with two triangles per unit cell), the total number of nodes and bonds (edges of triangles) under open boundary conditions are $N = 3N_xN_y + N_x + N_y$ and $N_b = 6N_xN_y$, respectively. Consequently, the number of ZMs N_0, is given by $N_0 = 2N - N_b + N_s = 2N_x + 2N_y + N_s$ where (N_s are the number of SSS in the system. $N_s = 0$ for a open boundary conditioned lattice). Removing the number of rigid body DOFs of the whole lattice, the remaining number of nontrivial ZMs is $2N_x + 2N_y - 3$. For our lattice, shown in Fig. 5.1(a), its configuration is described by a set of angles $\{\alpha_{i,j}, \theta_{i,j}, \gamma_{i,j}\}$ defined for each unit cell at i-th row and j-th column. For a homogeneous lattice, all $\{\alpha_{i,j}, \theta_{i,j}, \gamma_{i,j}\}$ are set to be the same in each unit cell, leaving only one free angle (i.e., the Guest-Hutchinson mode, labeled as α here) to determine the geometry of the homogeneous configuration as is shown in Fig. 5.1(b). This angle also determines the topological polarization $\mathbf{R}_T$ of the lattice [1], which is defined via the phase winding $\phi(k)$ of the determinant of the equilibrium matrix $\mathbf{Q}$ that maps tension on the bonds to the

total force on the sites in momentum space k, where $[\mathbf{Q}(\mathbf{k}) = |\mathbf{Q}(\mathbf{k})|^{\mathbf{i}\phi(\mathbf{k})}]$, and lattice vectors $\mathbf{a}_i$, such that $\mathbf{R}_T = \sum_i a_i \frac{1}{2\pi} \oint dk_i \cdot \nabla_{k_i} \phi(k)$. When $\mathbf{R}_T = 0$ (with a proper gauge), all edges of the lattice have ZMs, while when $\mathbf{R}_T \neq 0$, the polarization vector points towards the "soft" edges that the ZMs are localized to, such that the edges opposite to the direction of $\mathbf{R}_T$ becomes the "hard" edges. As shown in Fig. 5.1(b), the deformed kagome lattice experiences topological transitions at three critical angles $\alpha_{\mathbf{a_2}}$, $\alpha_{\mathbf{a_1}}$, and $\alpha_{\mathbf{a_2}-\mathbf{a_1}}$. When $\alpha < \alpha_{\mathbf{a_2}}$ or $\alpha > \alpha_{\mathbf{a_2}-\mathbf{a_1}}$, the lattice has $\mathbf{R}_T = 0$. Between these two critical angles, the lattice is topologically polarized, and $\mathbf{R}_T$ has two distinct directions, $\mathbf{a_2}$ or $\mathbf{a_2} - \mathbf{a_1}$, separated by α_{a_1}.

We first consider the deformation of our TMMs in the continuum limit, where ZMs are determined by partial differential equations (PDEs), such that to third derivatives at linear order of the x component of the displacement vector, u_x:

$$([\epsilon_{0yy}\partial_x^2 - 2\epsilon_{0xy}\partial_x\partial_y + \epsilon_{0xx}\partial_y^2] + [C_1\partial_x^3 + C_2\partial_x^2\partial_y + C_3\partial_x\partial_y^2])u_x = 0, \tag{5.1}$$

with ϵ_0 being the Guest-Hutchinson mode, a soft strain always present in Maxwell lattices [31] (see SI for the derivation of this PDE). As discussed in Ref. [16], this type of soft, spatially varying modes u generally arise in all materials in which a homogeneous strain ϵ_0 is soft. In Maxwell lattices, this soft strain ϵ_0 is guaranteed to exist and cost exactly zero energy [31], and the spatially varying soft modes u take the form of *exact zero energy* modes, protected by the Maxwell-Calladine index theorem [16; 30]. Such soft strain ϵ_0 can also accidentally arise due to geometric singularities in over-constrained lattices, such as planar quadrilateral kirigami, where these soft modes u cost a small amount of elastic energy even when the hinges are considered perfect [164; 165; 166; 167; 168]. Importantly, in Maxwell lattices, the fact that these ZMs are exact zero energy makes them scale free and materials independent.

Solutions to this PDE to the quadratic order (first square brackets) can be obtained by considering the case with prescribed k_x (wave number along x), where the ZM is given by $k_y = \frac{\epsilon_{0xy} \pm \sqrt{-\det \epsilon_0}}{\epsilon_{0xx}} k_x$. When $\det \epsilon_0 > 0$, corresponding to the Guest-Hutchinson mode being a dilation dominant (auxetic) mechanism and the PDE being elliptic, k_y is complex with an imaginary part $k_y'' \propto \pm k_x$, describing a pair of ZMs localized on the top and bottom edges, respectively. With proper coordinate transformations, these ZMs are mapped to conformal transformations [92; 16]. Adding terms with higher order derivatives only quantitatively changes these ZMs. In the opposite case, $\det \epsilon_0 < 0$, corresponding to the Guest-Hutchinson mode being a shear dominant (non-auxetic) mechanism and the PDE being hyperbolic, k_y is real, describing a pair of bulk ZMs. Unless fine-tuned, when terms of higher order derivatives (the second square brackets in Eq. (5.1)) are introduced, the solution of k_y becomes complex, with the imaginary part $k_y'' \propto k_x^2$ being higher order, indicating slower decay. Importantly, the sign of these decay rates is determined by the

topological polarization $\mathbf{R}_T$, in all cases. The same conclusion can be reached by starting with given k_y. We note that most known cases of topologically polarized 2D Maxwell lattices belong to the hyperbolic case ($\det \epsilon_0 < 0$) [16].

For the non-auxetic case, the mapping to a hyperbolic equation suggests that an analogy can be made between the *2D spatial* PDE of Eq. (5.1) and a *1D space-time* PDE. As shown in Fig. 5.1, the specific analogy between 2D spatial deformation and 1D spatiotemporal deformation we propose herein has progression across columns, or in the x direction, correlating with space, and progression across rows, or in the y direction, correlating with time evolution in the 1D analog dynamical system ($y \leftrightarrow t$). In Eq. 5.1, the 2nd order cross derivative term thus provides a conservative non-reciprocity along the x direction as the "waves" propagate in "time" (y). Interestingly, the 3rd order terms become *non-conservative* in the analog system, making the wave equation, "synthetically" non-Hermitian [155]. The y-component of the topological polarization in the 2D spatial lattice thus translates to a spatially uniform activity/damping in the 1D space-time lattice. Similarly, the $\partial_x \partial_y^2 u_x$ term provides a non-reciprocal activity in the effective 1D lattice.

Given aforementioned analogy to a 1D non-reciprocal, non-Hermitian, spatiotemporal system, we aim to study "wave propagation" in our 2D spatial TMM. With the expected polarization-dependent spatial amplification/decay, we expect large amplitude deformations outside the confines of a linear, small deformation approximation, leading to the proliferation of rich nonlinear phenomena. We note that while the spatiotemporal analogy is made using Eq. (5.1), which is linear, the full deformation field can be described by adding nonlinear terms, such that the mapping between the topological phase and the synthetic non-Hermiticity still applies in the nonlinear regime. To this end, we numerically calculate the exact nonlinear ZM configuration for chosen homogeneous configurations, with periodic boundary conditions on its left and right edges, and then an applied perturbation to the soft or hard edge of the lattice such that the θ angles $\theta_{1,j} = \theta_0 + f(j)$, where θ_0 is the initial homogeneous θ value. Given three angles and fixed edge lengths of the triangles, a hexagon is fully determined to within a choice of a single convex or concave angle (Fig. 5.1 and see the SI for details). We choose the convexity where the complementary angle (angle on the opposite side across the hinge) to θ is always less than π, which allows us to span the entire topological polarization range. By solving iteratively through each row starting with the edge where the perturbation is applied, the entire lattice can be determined geometrically, without approximation. Periodic boundary conditions are implemented by using Newton's method and numerically solving for a compatible periodic solution at each row. Within the context of our analogy to a 1D spatiotemporal system, this is as if we are applying an initial condition across the entire lattice, and then letting the system evolve in time.

5.2.2 Linear and weakly nonlinear response

We start by verifying wave characteristics of ZMs in 2D Maxwell lattices in the linear and weakly nonlinear regimes using our exact geometrical numerical method. Because the lattice satisfies the Maxwell criterion, this ZM configuration is exactly geometrically determined, independent of materials and length scales, in contrast to low energy modes studied in Refs. [164; 166; 167; 168]. We start with a homogeneous lattice deep in the $\mathbf{a_2}$ topologically polarized phase. The critical angles between which the lattice is hyperbolic, α_{c1}, α_{c2}, are shown in Fig. 5.1(b). We then apply a low-amplitude sinusoidal perturbation to the soft edge (the top row), such that $f(j) = \varepsilon \sin(k_x j)$. The resulting deformation field is shown in Fig. 5.2(a-c), and is described by a superposition of two ZMs that decay into the bulk that closely match expectations from the linear theory (further described in the SI). A 2D Fourier transform of the deformation field can be seen in Fig. 5.2(b), overlaid with two white lines denoting the real part of the wave number k_y of the two ZMs predicted by linear theory. Of the two ZMs, one has a shorter y-direction wavelength (higher "frequency" in the effective 1D spatiotemporal system) with faster decay, which is part of a highly dispersive branch, and the other a longer y-direction wavelength with slower decay, which is part of a weakly dispersive branch. The initial increase in amplitude of the deformation field with distance from the perturbation (decreasing row number) that can be seen in Fig. 5.2(a,c) is due to the input phase of the two ZMs and coherent interference. Fig. 5.2(d-f) details the same system shown in Fig. 5.2(a-c), but with a larger initial perturbation, inducing the nonlinear phenomena of harmonic generation [142], similar to Fig. 5.1.

5.2.3 Strongly nonlinear phenomena

We now proceed to explore more strongly nonlinear phenomena arising in these lattices. In particular, we show three examples, namely, automatic and localized topological polarization switching, amplification enhanced frequency conversion, and solitary wave formation. The first example, the switching of topological polarization as a result of nonlinear waves, occurs when the lattice is in the $\mathbf{a_2}$ phase close to the boundary with the $\mathbf{a_2} - \mathbf{a_1}$ phase. As shown in Fig. 5.3, for this case, a sinusoidal perturbation causes regions of deformation significant enough to cause local transitions to $\mathbf{a_2} - \mathbf{a_1}$ polarization. The boundaries between regions of different polarization are known to support internal SSSs [14], which has been shown to have implications for lattice fracture [54]. We highlight that this domain switching is a strictly nonlinear effect, as it requires finite deformation. Such finite deformation effects may lead to boundary-defined (holographic) programmable topological domain walls.

The second example, amplification enhanced frequency conversion, occurs when the lattice is excited from the hard edge of a polarized lattice, or either edge of a non-polarized lattice. In the

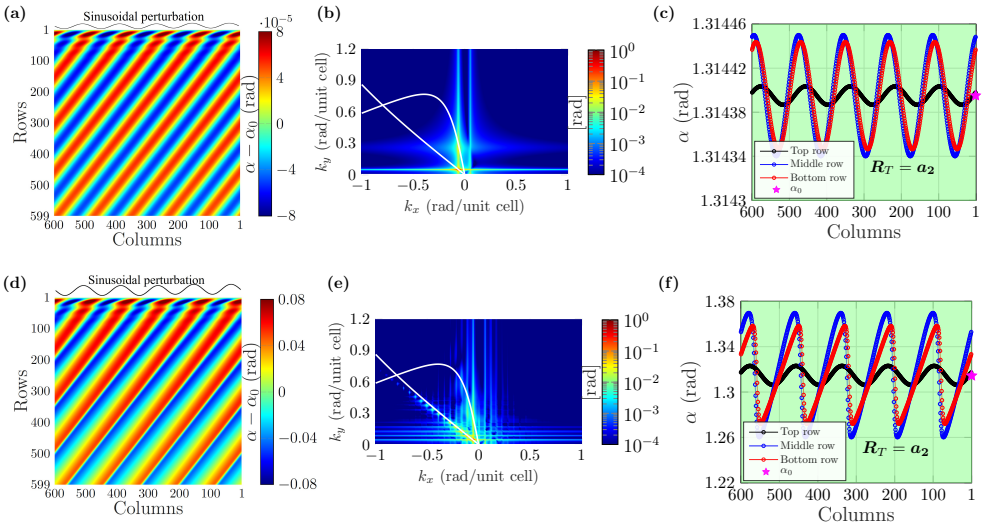

Figure 5.2: **Linear and weakly nonlinear response due to a sinusoidal perturbation applied to the soft (top) edge of a kagome Maxwell lattice deep in the $\mathbf{a_2}$ polarized region**. The lattice has $\alpha_0 = 1.3144$ rad and $k_x = 0.0524$ rad/unit cell. (a-c) Linear response at $\varepsilon = 1$ μrad. (d-f) Weakly nonlinear response and harmonic generation at $\varepsilon = 1$ mrad. (a,d) Deformation field. (b,e) 2D Fourier transform of (a,d). White lines denote the real part of the ZM modes predicted by linear theory. (c,f) Select rows of (a,d). The pink star in (c,f) denotes the initial homogeneous angle, and the background shading denotes the topological phase (always a_2 polarization in this case).

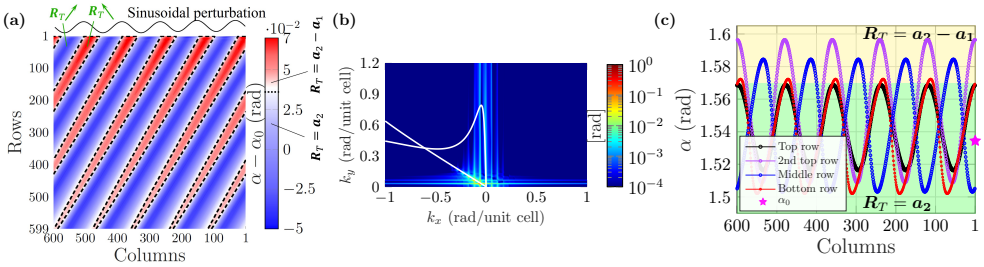

Figure 5.3: **Intrinsic localized topological polarization switching and domain formation due to a sinusoidal polarization applied to the soft edge (top) of the deformed kagome Maxwell lattice near the border of the $\mathbf{a_2}$ polarized phase**. The lattice has $\alpha_0 = 1.5344$ rad, $k_x = 0.0524$ rad/unit cell, and $\varepsilon = 1$ mrad. (a) Deformation field, (b) 2D Fourier transform of (a) with white lines representing the real part of the ZMs solved from the linear theory, and (c) Select rows of (a). The pink star in (c) denotes the initial homogeneous angle, and the background shading denotes the topological phases. The dashed black lines in (a) denote boundaries between regions of different polarizations.

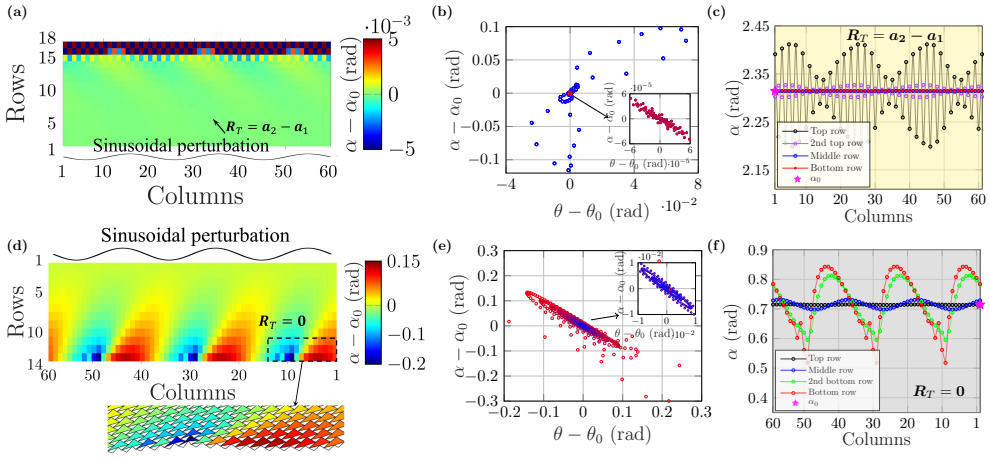

Figure 5.4: **Nonlinear wave amplification and frequency conversion in Maxwell lattices in response to sinusoidal perturbation**. (a-c) Hard edge perturbation (from the bottom) of an $\mathbf{a_2} - \mathbf{a_1}$ polarized lattice ($\alpha_0 = 2.3144$ rad), where $k_x = 0.314$ rad/unit cell and $\varepsilon = 1$ μrad. (d-f) Perturbation (from the top) of an unpolarized lattice with $\alpha_0 = 0.7144$ rad, with $k_x = 0.314$ rad/unit cell and $\varepsilon = 1$ mrad. (a,d) Deformation field. The configuration of the lattice in the dashed box is shown below the plot. (b,e) Phase space of (a,d), where blue to red color gradient denotes a progression from top to bottom rows, respectively. The insets provide a zoomed-in view near the perturbation. (c,f) Select rows of (a,d). The pink stars in (c,f) denote the initial homogeneous angles, and the background shadings denote the polarization regions.

case of perturbing from the hard edge, following the linear theory, we expect the perturbation to project to two ZMs which both grow exponentially into the bulk. In the context of our analogy with the 1D, non-reciprocal, non-Hermitian system, this would map to either an active system evolving forwards in time, or a damped system evolving backwards in time. In Fig. 5.4(a-c), we show the calculation for the sinusoidal perturbation of a lattice deep in the $\mathbf{a_2} - \mathbf{a_1}$ domain. As shown in Fig. 5.4(a), the deformation field amplifies into the bulk. We stop the calculation at 18 rows, after which a zero strain solution cannot be found, due to overlap or non-connection of the triangles, such that the lattice is "broken". To better illustrate the "time evolution" of the mode, we show the trajectory of the lattice in the phase space of the angles. In Fig. 5.4(a,c) the growth in amplitude can be seen to be accompanied by the generation of higher frequency wave components, which is connected to the blue loops in the angular phase space plot of Fig. 5.4(b).

The other case where the ZM amplifies is when an non-polarized lattice is perturbed from either edge. In this case, in the linear theory, one ZM grows and the other decays. A generic perturbation projects to both ZMs and the growing one is observed far from the edge. Here we study a sinusoidal perturbation on a lattice deep in the $\mathbf{R}_T = 0$ domain. As mentioned above, linear ZMs in this lattice are described by conformal transformations. In Fig. 5.4(d-f), using the same conventions as Fig. 5.4(a-c), we show the deformation of the perturbed lattice. In contrast to

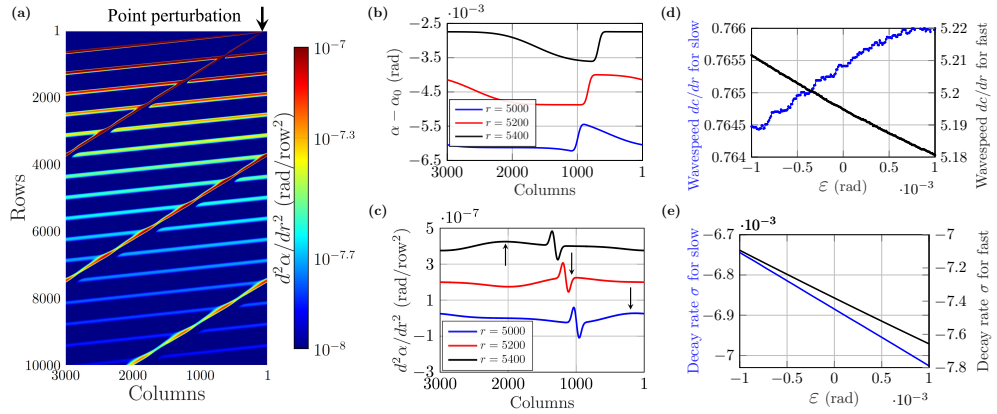

Figure 5.5: **Formation of two solitary waves resulting from a point perturbation at the edge of an a_2 polarized Maxwell lattice and their collisions**. The lattice has $\alpha_0 = 1.3144$ rad, and the point perturbation is applied to the top row at column 50. (a-c) Perturbation amplitude $\varepsilon = 0.23$ mrad. (a) $d^2\alpha/dr^2$ as a function of space. (b) $\alpha - \alpha_0$ and (c) $d^2\alpha/dr^2$ for rows 5000 (blue), 5200 (red), and 5400 (black). Rows 5200 and 5400 are sequentially offset by 1.25 mrad in (b) and 0.2 μrad/(unit cell)^2 for visualization purposes. The black arrows point to the fast moving, spatially wider, solitary wave. (d) "Speed" dc/dr of the solitary waves as a function of ε. (e) Decay rate of the peak-to-peak magnitude of $d^2\alpha/dr^2$ of the solitary waves σ, defined $\frac{d^2\alpha}{dr^2}_{max} - \frac{d^2\alpha}{dr^2}_{min} = Ae^{\sigma r}$.

the hyperbolic case of hard-edge perturbation, in Fig. 5.4(d,f), we see the formation of "kinks". At linear order, these kinks can be understood as a signature of conformal transformations, which have a one-to-one correspondence with complex analytic functions. All analytic functions periodic in x can be expanded in the basis of e^{ikz}, which features these kinks. Higher order terms, both in u and in derivatives, lead to further complex features of these kinks. Such kink formation may find future use in applications that can take advantage of deformation amplification or stress concentration. In the SI, we show further examples for sinusoidal perturbation of $\mathbf{R}_T = 0$ and $\mathbf{a_2} - \mathbf{a_1}$ lattices that are closer to the polarization boundaries, wherein domain switching can be observed.

The third—and perhaps the most intriguing—example, solitary waves, occur when the lattice is subject to localized perturbations. Typically described as localized waves that maintain their shape as they propagate with constant, often amplitude-dependent, speed and shape, solitary waves are one of the most canonical phenomena that emerge from nonlinear systems [139; 140; 138]. Herein, we distinguish solitary waves from the more restrictive localized type of wave referred to as "solitons", which "reappear virtually unaffected in size or shape" following collisions [169]. While solitary waves are most commonly considered in conservative systems, they have also been studied in a wide range of non-conservative (i.e. non-Hermitian) systems [154; 139; 136; 160; 138; 162; 163].

To explore the possibility of such localized traveling structures in our system, we induce a point perturbation at the top of a lattice with the same homogeneous configuration as studied in

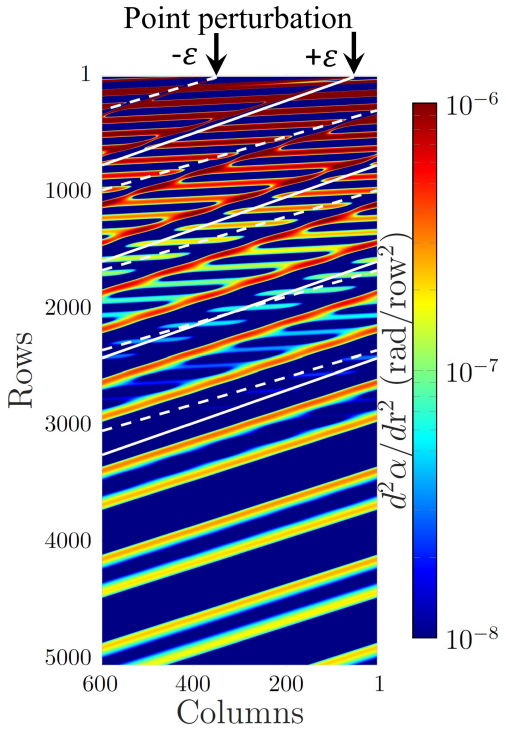

Figure 5.6: **Repulsion between two solitary waves, visualized via $\mathbf{d^2\alpha/dr^2}$, for two point perturbations applied to the soft edge (top) of a lattice with the same homogeneous angle as in Fig. 5.5**. Perturbations of $\pm\varepsilon = 0.6$ mrad are applied at columns 50 and 350, respectively. The solid and dashed lines demonstrate the predicted behavior of their perspective perturbations, respectively, based on the speeds calculated in the SI.

Fig. 5.2, and sweep a range of perturbation amplitudes, where $f(j) = \varepsilon\delta(j - j_p)$ and j_p is column to which the perturbation is applied. As can be seen in Fig. 5.5(a-c), using the language of the 1D spatiotemporal system analogy, we see two main solitary waves emerge with nearly constant speeds and interact with each other: one with a fast wave-speed and decay rate, and the other with a slow wave-speed and decay rate. In Fig. 5.5 and below, we use r and c to denote rows and columns, respectively, in the derivative terms. Figure 5.5(d,e) shows the dependence of speed and decay rate of the two solitary waves on perturbation amplitude. At first glance, it appears that there is a minimal interaction between the two solitary waves as they intersect. However, additional calculations for the same conditions as described in Fig. 5.5, but with five times fewer columns, and thus more collisions between the waves (see the SI), shows a significantly greater variation in the speeds and decay rates of the solitary waves. This suggests that the two solitary waves do interact upon their collisions. Additional data for the peak-to-peak decay rate in terms of α and the evolution of average α with increasing row number is included in the SI. Interestingly, both the narrow and wide lattices have perturbation amplitudes for which the decay rate of α is zero across the sampled rows (in contrast to $d^2\alpha/dr^2$), which is reminiscent of solitary waves in non-conservative systems, where nonlinearity, dispersion, and loss/gain balance to form a traveling wave packet of constant shape [154; 139; 138; 162; 163]. Such slow decay suggests that these waves can be considered analogs to weakly dissipative solitary waves [160; 163].

Augmenting the complexity of the two solitary waves generated from a single point perturbation in the examples of Fig. 5.6, we simulate the response of the TMM to two point perturbations of differing signs. As can be expected from the prior results, four solitary waves are generated, however, here we see the unexpected phenomenon that the two long-lived solitary waves appear to repel one another and propagate with similar speeds thereafter. This change of behavior can be seen by comparing to their predicted intersection is denoted by the white solid and dashed lines, which use the wave-speeds identified from the single perturbation case in the SI. Such repulsion has been seen for solitary waves in other nonlinear systems, for instance that of two kinks or two anti-kinks (topological solitons) in Sine-Gordon systems [140; 170] or optical spatial solitons [171].

5.2.4 Experimental validation

To validate the numerical simulation results, we built physical models composed of laser cut acrylic triangles pinned together such that they are free to rotate. Further details of the experimental setup are included in the SI. In summary, boundary conditions are set by pinning the edges to the prescribed periodic angles found from the simulation on the left and right, and to the top edge where the perturbation was initiated. The angles of each triangle in the resulting deformed configuration are then measured by using image processing to identify the position of each pinned

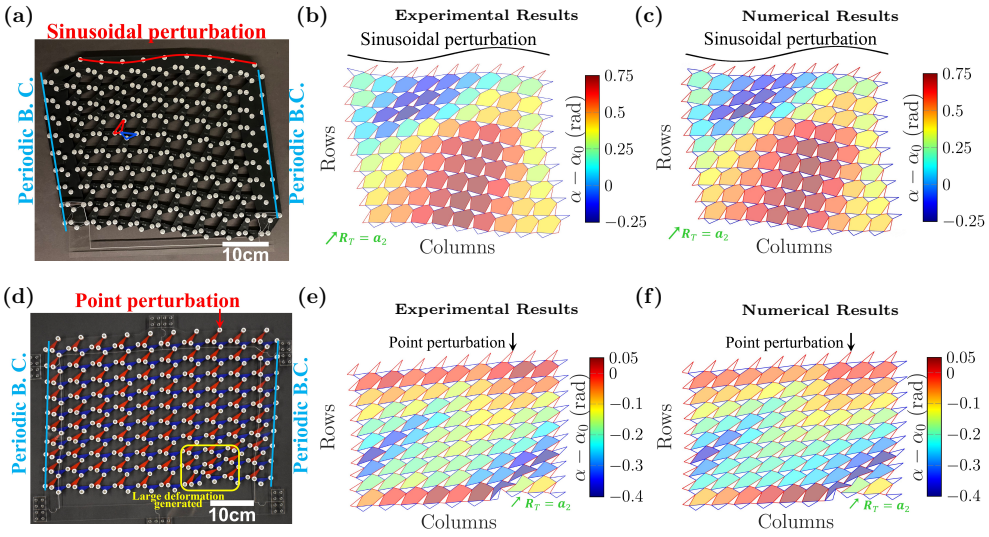

Figure 5.7: **Physical realization of $\mathbf{a_2}$ polarized Maxwell lattices with laser cut triangles, pinned hinges, and three prescribed boundaries, along with comparison to numerical predictions.** (a-c) Sinusoidal perturbation for $\alpha_0 = 1.3144$, $\varepsilon = 0.1$ rad, $k_x = 0.6283$ rad/unit cell. (d-f) Point perturbation for $\alpha_0 = 1.3144$ rad, $\varepsilon = 45$ mrad applied at column 3. (a,d) Photographs of the deformed lattice, where the left and right boundaries are prescribed to follow the computed periodic boundary configuration, (b,e) measured angles, and (c,f) simulated angles.

hinge. In Fig. 5.7, we show two lattice configurations with different sized unit cells under two different perturbations. The experimental lattices closely match the numerical predictions (exact error calculations given in the SI). We note that in our experimental realization for the configuration showing the solitary wave propagation Fig. 5.7(d-f), multiple unit cells with θ angles close to π with sufficient pressure can be forced to snap from concave to convex configurations with the given prescribed boundaries, as well as slight variability in the experimental configuration due to manufacturing tolerances of the hinges.

5.3 Discussion

The two central contributions of this work are: i) demonstrating, to the linear order, that the ZMs of 2D TMMs (Maxwell lattices) can be mapped to waves in 1D non-Hermitian, non-reciprocal, dynamical systems; and ii) extending the study of 2D TMMs to the nonlinear regime. Within that scope, we showed that an array of nonlinear wave-like phenomena exists, including harmonic generation, localized topological domain switching, amplification enhanced frequency conversion, and solitary wave generation. Each of these phenomena has its own unique implications for designing stress and deformation fields in materials that extends significantly past what has hitherto been achievable in linear regimes of TMMs, and, more broadly, via elasticity. Amongst these, localized

intrinsic domain formation has the potential to tailor regions of SSSs with implications to fracture mechanics [54], and solitary wave generation has implications for compact, amplitude-dependent spatially-addressable signal transmission [172] and remote-controlled localization of stress and deformation, both of which may find interesting use in the context of mechano-responsive metamaterials [173]. In the context of the analogy to the 1D spatiotemporal system, these 2D lattices offer a convenient emulator for nonlinear waves and shares similarities with the mapping between d-dimensional quantum systems with $(d+1)$-dimensional classical systems, which led to important advances in understanding quantum phase transitions [157]. Finally, we envision a potentially intriguing scenario stemming from this work, wherein elasticity and inertial effects are incorporated into the lattice, such that perturbations are restricted by the underlying topology of the lattice as shown herein, but evolve in time.

5.4 Materials and Methods

The fabricated lattice structures are created by laser cutting (using a Glowforge Basic 3D laser cutter) 1/8-inch-thick acrylic layers assembled with barrels (Fig. 5.7(a)) or dowel pins (Fig. 5.7(d)) and screws. For the experiment in Fig. 5.7(a), each of the barrels (6063 Aluminum Low-Profile Binding Barrels from McMaster-Carr) has a diameter of 13/64 inch and length of 1/4 inch (3/8 inch at the boundaries due to an extra layer of acrylic for prescribed periodic left-right boundary condition). For the experiment in Fig. 5.7(d), each of the dowel pins (Alloy Steel Pull-Out Dowel Pin from McMaster-Carr) has a diameter of 1/4 inch and a length of 1/2 inch. Geometries of triangle unit cells are shown in the SI. The lattices are assembled by pinning down the triangles in two layers and to the laser cut acrylic boundaries. Left and right boundaries are connected at the bottom without interfering with the bottom row of triangles mitigate bending of the boundary. Boundary pieces are connected using M3 screws and nuts.

5.5 Appendices

5.5.1 Note 1: Floppy Modes of Maxwell Lattice and Control Variables

For a general mechanical structural frame (a Maxwell lattice herein) in a d-dimensional domain that has point masses hinge-connected by central-force bonds, one can apply the Calladine index theorem [29; 1; 92; 53; 54] to count the number of zero energy lattice modes (ZMs). The ZMs are given by

$$dN - N_b = N_0 - N_s, \tag{5.2}$$

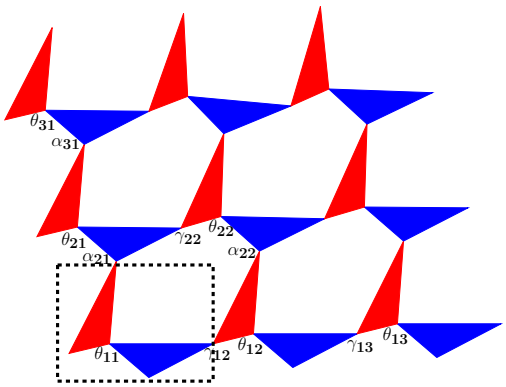

Figure 5.8: Schematic of a deformed kagome lattice with 3×3 unit cells. Each unit cell consists of a rigid red and blue triangle connected by hinges. The configuration of the lattice is represented by the angles between the triangles, θ, α, and γ.

where N_0 is the number of ZMs, N_s is the number of states of self-stress (SSSs), N is the number of nodes, and N_b is the number of bonds in the lattice. A periodic Maxwell lattice with no boundaries always yields $dN - N_b = 0$, resulting in no ZMs in the lattice unless pairs of SSS and ZM arise due to the geometric singularity, which is the case at topological transitions. However, the generation of ZMs can be achieved by selecting a finite piece from an infinite lattice. In that case, $dN - N_b > 0$, and the number of floppy modes are related to the length of the boundary. Considering a two-dimensional (2D) finite Maxwell lattice consisting of N_x columns by N_y rows of unit cells (the dashed box area in Fig. 5.8 represents a unit cell), the total number of nodes and bonds are $N = 3N_xN_y + N_x + N_y$ and $N_b = 6N_xN_y$, respectively, and consequently, the number of ZMs is $N_0 = 2N_x + 2N_y + N_s$. Removing the number of rigid body planar degrees of freedom (DOFs), the remaining floppy modes (FMs) of the finite lattice is $2N_x + 2N_y + N_s - 3$ (note in the main text FMs and ZMs are used almost interchangeable since for a large lattice they are approximately equal to each other and only differ by three rigid body rotations). In other words, by controlling these $2N_x + 2N_y - 3$ floppy modes (FMs) of a Maxwell lattice with $N_x \times N_y$ unit cells (here $N_s = 0$), the configuration of the lattice is fully determined.

A deformed kagome lattice (the type of Maxwell lattice considered herein) is configured by the internal angles of θ, α, and γ between triangles, each one of which is formed by three bonds. The angle, θ, is the one between the red and blue triangles in the unit cell. The notation of α represents the angle between triangles from different unit cells connected in adjacent rows, while γ shows the angle between triangles from different unit cells connected in adjacent columns. The Maxwell-Calladine counting rule, for a deformed kagome lattice with periodic left-right boundaries has $2(N_x + N_y) - 3$ floppy modes originally, then periodic boundary conditions give additional constraints on each row (except the bottom row) removing the $2N_y - 2$ modes. Additionally connecting the right-most node to the left-most node in the bottom row removes θ_{1,N_x} as a free variable leaving

$2N_x - 2$ floppy modes which can be fully defined by choosing θ, and γ angles along the bottom. Each $\alpha_{i,1} = \alpha_{i,N_x}$ angle is numerically determined such that periodicity is met (see Fig. 5.8). For example, a lattice consisting of 3×3 unit cells can be fully determined by 4 variables including θ_{11}, θ_{12}, γ_{12}, and γ_{13}. Here it is assumed $\theta_{13} = \theta_{11}$ from periodic boundary conditions. All other angles of $\theta_{i,j}$, $\alpha_{i,j}$, and $\gamma_{i,j}$ inside the lattice can be solved by these variables, and the remaining boundary variables θ_{21}, θ_{31}, α_{21} and α_{31} can be numerically solved using the periodic boundary conditions as constraints. The non-linear configuration of the Maxwell lattice in the following sections will be solved using these defined independent variables.

5.5.2 Note 2: Nonlinear Exact Solution of Zero Energy Configurations

The internal geometry formed by unit cells in the lattice is investigated and the corresponding structure of the lattice is then studied and presented. As can be seen in Fig. 5.8, a hexagon is generated by the adjacent four unit cells, including two entire unit cells of $\theta_{i,j}$ and $\theta_{i+1,j+1}$, a blue triangle from the unit cell of $\theta_{i+1,j}$, and a red triangle from the one of $\theta_{i,j+1}$, where the first subscript represents the row of the lattice while the second subscript denotes the column. The nonlinear configuration of the Maxwell lattice can be determined based on all angles in the lattice.

5.5.2.1 Geometry of a General Hexagon

Consider a hexagon defined in a Cartesian coordinate system (Fig. 5.9(a)) with the origin at site A, which is located at the angle of $\theta_{i,j}$. The x_{ij}-axis is aligned with side c_b of the blue triangle of the bottom row. Sites B to F correspond to the angles of $\gamma_{i,j+1}$, $\alpha_{i+1,j+1}$, $\theta_{i+1,j+1}$, $\gamma_{i+1,j+1}$, and $\alpha_{i+1,j}$, respectively. If initial conditions are given for the left and bottom edges of the lattice, all other angles can be obtained by solving hexagons from the bottom left corner to the top right corner in the lattice. Starting from a single hexagon, using known angles, $\theta_{i,j}$, $\gamma_{i,j+1}$ and $\alpha_{i+1,j}$, and related sides of triangles, the other unknown angles ($\theta_{i+1,j+1}$, $\gamma_{i+1,j+1}$ and $\alpha_{i+1,j+1}$) can be determined by calculating the intersection coordinate of site D. The coordinates of the remaining vertexes are given:

$$
\begin{aligned}
&x_A = 0, \quad y_A = 0, \quad x_B = c_b, \quad y_B = 0, \\
&x_C = c_b - c_r \cos(\gamma_{i,j+1} + \psi_{ab} + \psi_{br}), \quad y_C = -c_r \sin(\gamma_{i,j+1} + \psi_{ab} + \psi_{br}), \\
&x_F = b_r \cos(\theta_{ij} + \psi_{bb} + \psi_{cr}), \quad y_F = -b_r \sin(\theta_{ij} + \psi_{bb} + \psi_{cr}), \\
&x_E = b_r \cos(\theta_{ij} + \psi_{bb} + \psi_{cr}) - b_b \cos(\theta_{ij} + \alpha_{i+1,j} + \psi_{bb} + \psi_{cr} + \psi_{cb} + \psi_{ar}), \\
&y_E = -b_r \sin(\theta_{ij} + \psi_{bb} + \psi_{cr}) + b_b \sin(\theta_{ij} + \alpha_{i+1,j} + \psi_{bb} + \psi_{cr} + \psi_{cb} + \psi_{ar}),
\end{aligned}
\tag{5.3}
$$

where both the sides of the triangles c_b, b_b, c_r, and b_r, as well as the internal angles of the triangles ψ_{ab}, ψ_{bb}, ψ_{cb}, ψ_{ar}, ψ_{br} and ψ_{cr} are given in Fig. 5.9. Based on the geometry of the hexagon, the last site D should satisfy the following constraints:

$$\begin{cases} (x_D - x_E)^2 + (y_D - y_E)^2 = a_r^2, \\ (x_D - x_C)^2 + (y_D - y_C)^2 = a_b^2. \end{cases} \tag{5.4}$$

Equations (5.4) result in two solutions, one of which (x_{D_2}, y_{D_2}) forms $\theta_{i+1,j+1} > \pi$ (site D_2 in Fig. 5.9(a), which we call the concave solution), and the other of which (x_{D_1}, y_{D_1}) corresponds to $\theta_{i+1,j+1} \leqslant \pi$ (site D_1 in Fig. 5.9(a), which we call the convex solution). A hexagon is considered concave or convex based on the $\theta_{i+1,j+1}$ angle, or in coordinate basis the angle $E\bar{D}C$. There exists a particular situation where two solutions overlap and hence $\theta_{i+1,j+1} = \pi$. The concave solution D_1 is chosen if the previous $\theta_{i,j} < \pi$, and the convex solution is chosen if $\theta_{i,j} > \pi$.

The coordinate of site D can be presented in two ways using known angles defined above and written as

$$\begin{aligned} x_D = {} & b_r \cos(\theta_{i,j} + \psi_{bb} + \psi_{cr}) - b_b \cos(\theta_{i,j} + \alpha_{i+1,j} + \psi_{bb} + \psi_{cr} + \psi_{cb} + \psi_{ar}) \\ & + a_r \cos(\gamma_{i+1,j+1} - \theta_{i,j} - \alpha_{i+1,j} - \psi_{bb} - \psi_{cr} - \psi_{cb} - \psi_{ar}), \\ y_D = {} & -b_r \sin(\theta_{i,j} + \psi_{bb} + \psi_{cr}) + b_b \sin(\theta_{i,j} + \alpha_{i+1,j} + \psi_{bb} + \psi_{cr} + \psi_{cb} + \psi_{ar}) \\ & + a_r \sin(\gamma_{i+1,j+1} - \theta_{i,j} - \alpha_{i+1,j} - \psi_{bb} - \psi_{cr} - \psi_{cb} - \psi_{ar}). \end{aligned} \tag{5.5}$$

$$\begin{aligned} x_D &= c_b - c_r \cos(\gamma_{i,j+1} + \psi_{ab} + \psi_{br}) + a_b \cos(\gamma_{i,j+1} - \alpha_{i+1,j+1} + \psi_{ab} + \psi_{br}), \\ y_D &= -c_r \sin(\gamma_{i,j+1} + \psi_{ab} + \psi_{br}) + a_b \sin(\gamma_{i,j+1} - \alpha_{i+1,j+1} + \psi_{ab} + \psi_{br}). \end{aligned} \tag{5.6}$$

By solving Eqs. (5.5) and (5.6), angles of $\gamma_{i+1,j+1}$ and $\alpha_{i+1,j+1}$ can be achieved. The last angle $\theta_{i+1,j+1}$ is then obtained by the sum of the inner angles of the hexagon subtracting the other five angles. Figure 5.9(c) illustrates possible three known angles, which can generate hexagons using the configuration and parameters given from Fig. 5.9(b). Constraints, such as the strain free condition, are shown by blue, red, and green dots. The multicolored line (grey for $\mathbf{R}_T = 0$, light green for $\mathbf{R}_T = \mathbf{a_2}$, and light yellow for $\mathbf{R}_T = \mathbf{a_2} - \mathbf{a_1}$) represents the family of angles generating homogeneous Maxwell lattices. Processing along this line represents a uniform twisting synonymous with the Guest-Hutchinson modes in the system. The choice of solutions D_1 and D_2 to calculate the value of $\theta_{i+1,j+1}$ for the current hexagon is determined by the value of $\theta_{i,j}$. For the topological Maxwell lattice, we assume the more favorable solution for a lattice configuration is one with less discontinuous jumps in perturbation, thus we choose either the concave or convex $\theta_{i+1,j+1}$ based on the previous result $\theta_{i,j}$. If $\theta_{i,j} > \pi$, $\theta_{i+1,j+1}$ will still be greater than π, and vice versa. However, we note that the transition between different convexities does not happen for all cases shown.

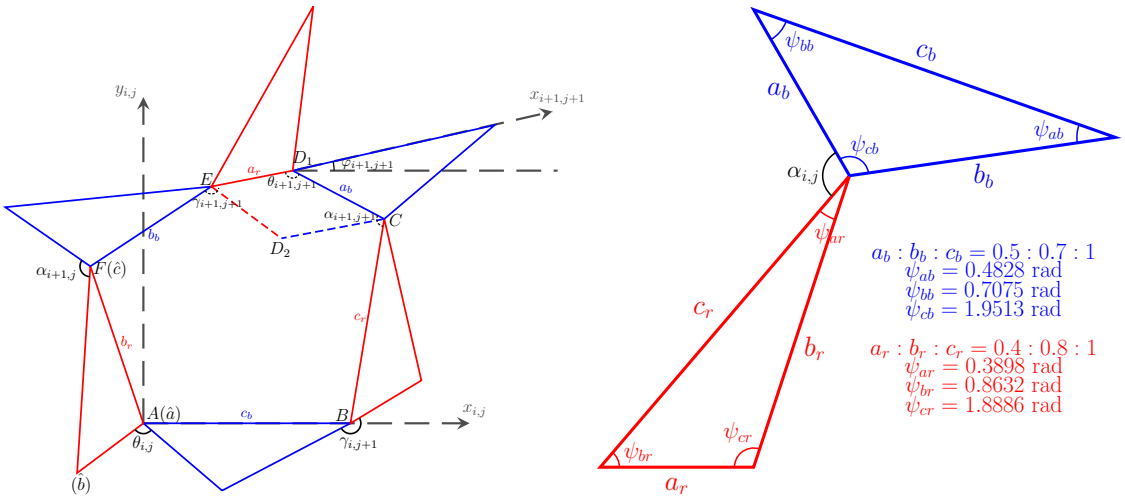

Figure 5.9: (a) Schematic of a general hexagon in the lattice. The hexagon is generated by sides from three red triangles and three blue triangles. Site A, B, and F correspond to three known angles, $\theta_{i,j}$, $\gamma_{i,j+1}$, and $\alpha_{i+1,j}$, respectively, while site C, D, and E are related to the other three angles ($\alpha_{i+1,j+1}$, $\theta_{i+1,j+1}$, and $\gamma_{i+1,j+1}$) to be solved. (b) Dimensions of a unit cell from (a). (c) Possible given angles that can generate hexagons shown in (a). Pink dots represent all possible given angles, which can form a hexagon without constraints (i.e. triangles can overlap indicating not a strain free condition or ZM), while blue, red, and green dots indicate all feasible angles under a strain free constraint. Blue and red dots show the convex (D_1) and concave (D_2) cases, respectively, and green dots imply that the given angles can create both convex and concave solutions.

Note that if a lattice is perturbed at the hard edge, we solve all unknown angles of hexagons ($\theta_{i+1,j+1}$, $\gamma_{i+1,j+1}$ and $\alpha_{i+1,j+1}$) using known angles of $\theta_{i,j}$, $\gamma_{i,j+1}$ and $\alpha_{i+1,j}$, shown in Fig. 5.9(a). If a lattice is perturbed at the soft edge, we start solving angles of $\bar{\theta}_{i,j}$, $\bar{\gamma}_{i,j+1}$, and $\bar{\alpha}_{i+1,j}$, which are complementary angles of $\theta_{i,j}$, $\gamma_{i,j+1}$, and $\alpha_{i+1,j}$ subtracting two neighboring inner angles of triangles, using $\bar{\theta}_{i+1,j+1}$, $\bar{\gamma}_{i+1,j+1}$, and $\bar{\alpha}_{i+1,j+1}$.

5.5.2.2 Transformation of Coordinates for Unit Cells

The positions of each unit cell can be solved once all necessary angles in the lattice are obtained. Here, local coordinate systems from each unit cell associated with $\theta_{i,j}$ must be rotated to align within a global coordinate system, set by the original unit cell and the value of θ_{11}.

To simplify the notations of the lattice, where all nodes except those on boundaries are shared with two surrounding unit cells, only three nodes are counted for one unit cell, noted by $\hat{a}$, $\hat{b}$, and $\hat{c}$ (symbols in the parentheses in Fig. 5.9(a) from red triangles). The coordinates of nodes $\hat{a}_{n,m}$, $\hat{b}_{n,m}$ and $\hat{c}_{n,m}$ in the unit cell at nth row and mth column (the lattice consists of $N_x \times N_y$ unit cells) are shown below:

Unit cell of $\theta_{n,m}$ $(n \leqslant m)$

$$
\begin{aligned}
\begin{pmatrix} x \\ y \end{pmatrix}_{\hat{a}_{n,m}} &= \sum_{p=1}^{m-n} \left(\prod_{i=1}^{p} \boldsymbol{R}(\varphi_{1i}) \begin{pmatrix} x_{\theta_{1,p}\to\theta_{1,p+1}} \\ y_{\theta_{1,p}\to\theta_{1,p+1}} \end{pmatrix} \right) + \\
&\quad \sum_{p=1}^{n-1} \left(\prod_{i=1}^{m-n} \boldsymbol{R}(\varphi_{1i}) \prod_{i=1}^{p} \boldsymbol{R}(\varphi_{i,i+m-n}) \begin{pmatrix} x_{\theta_{p,p+m-n}\to\theta_{p+1,p+m-n+1}} \\ y_{\theta_{p,p+m-n}\to\theta_{p+1,p+m-n+1}} \end{pmatrix} \right), \\
\begin{pmatrix} x \\ y \end{pmatrix}_{\hat{b}_{n,m}} &= \begin{pmatrix} x \\ y \end{pmatrix}_{\hat{a}_{n,m}} + \prod_{i=1}^{m-n} \boldsymbol{R}(\varphi_{1i}) \prod_{i=1}^{n} \boldsymbol{R}(\varphi_{i,i+m-n}) \begin{pmatrix} a_r \cos(\theta_{n,m} + \psi_{bb}) \\ -a_r \sin(\theta_{n,m} + \psi_{bb}) \end{pmatrix}, \\
\begin{pmatrix} x \\ y \end{pmatrix}_{\hat{c}_{n,m}} &= \begin{pmatrix} x \\ y \end{pmatrix}_{\hat{a}_{n,m}} + \prod_{i=1}^{m-n} \boldsymbol{R}(\varphi_{1i}) \prod_{i=1}^{n} \boldsymbol{R}(\varphi_{i,i+m-n}) \begin{pmatrix} b_r \cos(\theta_{n,m} + \psi_{bb} + \psi_{cr}) \\ -b_r \sin(\theta_{n,m} + \psi_{bb} + \psi_{cr}) \end{pmatrix},
\end{aligned}
\tag{5.7}
$$

Unit cell of $\theta_{n,m}$ $(n > m)$

$$
\begin{aligned}
\begin{pmatrix} x \\ y \end{pmatrix}_{\hat{a}_{n,m}} &= \sum_{p=1}^{n-m} \left(\prod_{i=1}^{p} \boldsymbol{R}(\varphi_{i1}) \begin{pmatrix} x_{\theta_{p,1}\to\theta_{p+1,1}} \\ y_{\theta_{p,1}\to\theta_{p+1,1}} \end{pmatrix} \right) + \\
&\quad \sum_{p=1}^{m-1} \left(\prod_{i=1}^{n-m} \boldsymbol{R}(\varphi_{i1}) \prod_{i=1}^{p} \boldsymbol{R}(\varphi_{i,i+n-m}) \begin{pmatrix} x_{\theta_{p,p+n-m}\to\theta_{p+1,p+n-m+1}} \\ y_{\theta_{p,p+n-m}\to\theta_{p+1,p+n-m+1}} \end{pmatrix} \right), \\
\begin{pmatrix} x \\ y \end{pmatrix}_{\hat{b}_{n,m}} &= \begin{pmatrix} x \\ y \end{pmatrix}_{\hat{a}_{n,m}} + \prod_{i=1}^{n-m} \boldsymbol{R}(\varphi_{i1}) \prod_{i=1}^{m} \boldsymbol{R}(\varphi_{i,i+n-m}) \begin{pmatrix} a_r \cos(\theta_{n,m} + \psi_{bb}) \\ -a_r \sin(\theta_{n,m} + \psi_{bb}) \end{pmatrix}, \\
\begin{pmatrix} x \\ y \end{pmatrix}_{\hat{c}_{n,m}} &= \begin{pmatrix} x \\ y \end{pmatrix}_{\hat{a}_{n,m}} + \prod_{i=1}^{n-m} \boldsymbol{R}(\varphi_{i1}) \prod_{i=1}^{m} \boldsymbol{R}(\varphi_{i,i+n-m}) \begin{pmatrix} b_r \cos(\theta_{n,m} + \psi_{bb} + \psi_{cr}) \\ -b_r \sin(\theta_{n,m} + \psi_{bb} + \psi_{cr}) \end{pmatrix},
\end{aligned}
\tag{5.8}
$$

where $\sum$ and $\prod$ are cumulative sum and product operators. The coordinate transformation matrix, $\boldsymbol{R}(\varphi_{i,j})$, is given by

$$
\boldsymbol{R}(\varphi_{i,j}) = \begin{bmatrix} \cos\varphi_{i,j} & -\sin\varphi_{i,j} \\ \sin\varphi_{i,j} & \cos\varphi_{i,j} \end{bmatrix}, \tag{5.9}
$$

where $\varphi_{i,j}$ is the deflection angle between $x_{i,j}$-axis and the previous x-axis ($\varphi_{11} = 0$), and:

$$
\begin{aligned}
&\varphi_{1,j} = \gamma_{1,j} + \theta_{1,j-1} + \psi_{ab} + \psi_{bb} - 2\pi, \\
&\varphi_{i,1} = 2\pi - \alpha_{i,1} - \theta_{i-1,1} - \psi_{ar} - \psi_{cr}, \\
&\varphi_{i,j} = \gamma_{i-1,j} - \alpha_{i,j} + \psi_{bb} + \psi_{ab} + \psi_{br} - \pi \quad (i,j > 1).
\end{aligned}
\tag{5.10}
$$

The cumulative coordinates with subscripts $\theta_{1,j} \to \theta_{1,j+1}$ (in Fig. 5.10(a)), $\theta_{i,1} \to \theta_{i+1,1}$ (in Fig. 5.10(b)), and $\theta_{i,j} \to \theta_{i+1,j+1}$ (in Fig. 5.9(a)) are those converted from $(1, j+1)^{\text{th}}$ to $(1, j)^{\text{th}}$ unit cell, from $(i+1, 1)^{\text{th}}$ to $(i, 1)^{\text{th}}$ unit cell and from $(i+1, j+1)^{\text{th}}$ to $(i, j)^{\text{th}}$ unit cell, respectively:

$$
\begin{aligned}
&x_{\theta_{1,j}\to\theta_{1,j+1}} = c_b - a_r \cos(\psi_{ab} + \gamma_{1,j+1}), \\
&y_{\theta_{1,j}\to\theta_{1,j+1}} = -a_r \sin(\psi_{ab} + \gamma_{1,j+1}), \\
&x_{\theta_{i,1}\to\theta_{i+1,1}} = b_r \cos(\theta_{i,1} + \psi_{bb} + \psi_{cr}) - a_b \cos(\alpha_{i+1,1} + \theta_{i,1} + \psi_{ar} + \psi_{cr} + \psi_{bb}), \\
&y_{\theta_{i,1}\to\theta_{i+1,1}} = -b_r \sin(\theta_{i,1} + \psi_{bb} + \psi_{cr}) + a_b \sin(\alpha_{i+1,1} + \theta_{i,1} + \psi_{ar} + \psi_{cr} + \psi_{bb})), \\
&x_{\theta_{i,j}\to\theta_{i+1,j+1}} = c_b - c_r \cos(\gamma_{i,j+1} + \psi_{ab} + \psi_{br}) + a_b \cos(\gamma_{i,j+1} - \alpha_{i+1,j+1} + \psi_{ab} + \psi_{br}), \\
&y_{\theta_{i,j}\to\theta_{i+1,j+1}} = -c_r \sin(\gamma_{i,j+1} + \psi_{ab} + \psi_{br}) + a_b \sin(\gamma_{i,j+1} - \alpha_{i+1,j+1} + \psi_{ab} + \psi_{br}).
\end{aligned}
\tag{5.11}
$$

Equations (5.7) and (5.8) solve for the number of nodes of $3N_xN_y$ related to all red triangles, while the remaining $(N_x + N_y)$ nodes come from the first row $\theta_{1,m}$ and last column θ_{n,N_x}, which

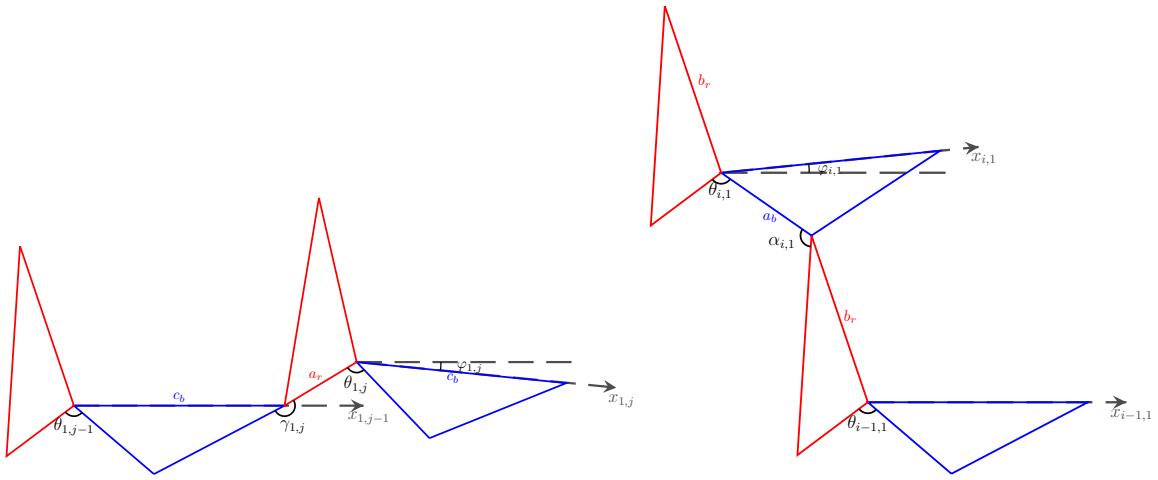

(a) (b)

Figure 5.10: Schematic of two unit cells from (a) the bottom edge and (b) the left edge of the lattice.

are respectively given by:

$$\begin{pmatrix} x \\ y \end{pmatrix}_{\hat{c}_{0,m}} = \begin{pmatrix} x \\ y \end{pmatrix}_{\hat{a}_{1,m}} + \prod_{i=1}^{m} \boldsymbol{R}(\varphi_{1i}) \begin{pmatrix} a_b \cos(\psi_{bb}) \\ -a_b \sin(\psi_{bb}) \end{pmatrix}. \tag{5.12}$$

$$\begin{aligned} \begin{pmatrix} x \\ y \end{pmatrix}_{\hat{b}_{n,N_x+1}} &= \begin{pmatrix} x \\ y \end{pmatrix}_{\hat{a}_{n,N_x}} + \prod_{i=1}^{N_x-n} \boldsymbol{R}(\varphi_{1i}) \prod_{i=1}^{n} \boldsymbol{R}(\varphi_{i,i+N_x-n}) \begin{pmatrix} c_b \\ 0 \end{pmatrix}, \ (n \leqslant N_x) \\ \begin{pmatrix} x \\ y \end{pmatrix}_{\hat{b}_{n,N_x+1}} &= \begin{pmatrix} x \\ y \end{pmatrix}_{\hat{a}_{n,N_x}} + \prod_{i=1}^{n-N_x} \boldsymbol{R}(\varphi_{i1}) \prod_{i=1}^{N_x} \boldsymbol{R}(\varphi_{i,i+n-N_x}) \begin{pmatrix} c_b \\ 0 \end{pmatrix}, \ (n > N_x). \end{aligned} \tag{5.13}$$

5.5.2.3 Periodic Boundary Conditions

Newton's method, an algorithm for finding roots of a function $f(x)$ such that $f(x) = 0$, is used in order to achieve periodic boundary conditions. Herein, the goal is to find periodic boundary conditions such that $f(x)$ is a function of α, and periodic boundary conditions are met when $f(\alpha_{i,1}) = \alpha_{i,n} - \alpha_{i,1} = 0$, for the i-th row of an $M \times N$ lattice. The general Newton's method algorithm is given below, where:

$$\alpha_{n+1} = \alpha_n - \frac{f(\alpha_n)}{f'(\alpha_n)}. \tag{5.14}$$

The input variable α_n is the initial guess for $\alpha_{i,1}$. The derivative $f'(\alpha_n)$ is calculated numerically using a central difference method, such that:

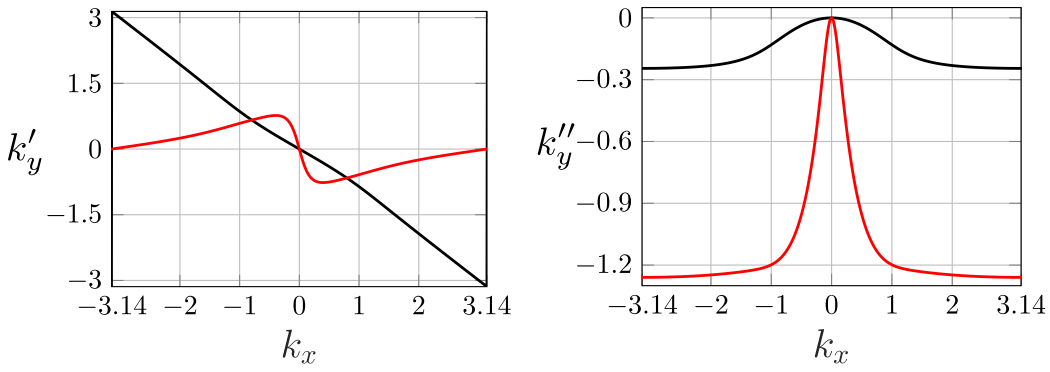

(a) (b)

Figure 5.11: "Dispersion relation." (a) Real component $k_y' = \mathrm{Re}(k_y)$ vs k_x in the first Brillouin Zone for an $\mathbf{a_2}$ polarized lattice. (b) Imaginary component $k_y'' = \mathrm{Im}(k_y)$ vs k_x for an $\mathbf{a_2}$ polarized lattice. The red branch has a much higher decay rate, and "velocity" at long wavelength (low k_x values).

$$f'(\alpha_n) = \frac{f(\alpha + h/2) - f(\alpha - h/2)}{h}, \tag{5.15}$$

where $h/2$ is an angular increment $\delta\alpha$ that is small in comparison to α. In this paper, a value of $\delta\alpha = 0.1$ μrad was used. For each value of $f(\alpha)$, $f(\alpha + \delta\alpha)$, and $f(\alpha - \delta\alpha)$, the corresponding configuration of the row must be calculated. The algorithm continues to update the initial guess of α, until the residual is less than a specified tolerance value. In this paper, we set the tolerance value as 0.01 μrad.

5.5.2.4 Linear Mode Analysis

In the small amplitude perturbation limit, where ε is small (on the order of 10^{-6} rad, for our simulations 10^{-3} rad was considered "large perturbations"), the numerically solved wave profile in the static limit can be approximated by a linear mode analysis. In our case, of a finite boundary in y and a periodic boundary in x, one can prescribe a real k_x and solve for a complex k_y that satisfies the condition $\det C(\vec{k}) = 0$ to find the ZMs [1]. The resulting complex $k_y = k_y'(k_x) + ik_y''(k_x)$ has $k_y' = \mathrm{Re}(k_y)$ being the real spatial wave profile in the lattice and $k_y'' = \mathrm{Im}(k_y)$ being the decay rate of the ZMs. The relation of k_x and k_y for the given homogeneous lattice ($\alpha_0 = 1.3144$ rad) is shown in Fig. 5.11 and Fig. 5.2 of the main text. The numerical results shown in Fig. 5.2(b) are in close agreement with the linear ZM analysis.

5.5.3 Note 3: Space-Time Mapping in Maxwell Lattices

In this section, we discuss the general elasticity theory of 2D materials with a soft strain (or "mechanism"), and how their static zero energy configurations map to 1D dynamical systems in linear and weakly nonlinear cases.

5.5.3.1 From soft strain to partial differential equations of ZMs in linear theory

We start by considering the general case of elasticity in 2D, where, to leading order in strain and spatial gradient of deformation, the elastic energy can be written as:

$$f_{el} = \frac{1}{2}\epsilon_a \mathbb{K}_{ab} \epsilon_b, \tag{5.16}$$

where $\epsilon = \{\epsilon_{xx}, \epsilon_{yy}, \epsilon_{xy}\}$ are the strains in Voigt notation, forming a 3-dimensional vector, and $\mathbb{K}$ is the (real symmetric) elastic constant matrix. This elastic energy can be generally applied to any 2D elastic structure. For lattices considered in this paper, this continuum elastic energy can be obtained by properly taking the long-wavelength limit from the lattice elastic energy [30; 73].

Now, let's consider the case when this material has a soft strain, which means the $\mathbb{K}$ matrix has an eigenvalue that is zero or much smaller than the other two eigenvalues. This can arise from microscopic mechanisms of the material, e.g. auxetic foams or pentamode metamaterials [174; 90]. In this paper, we are particularly interested in the case of Maxwell lattices, where this soft mode is *guaranteed to arise*, taking the form of Guest-Hutchinson modes [31; 30].

This soft strain has far-reaching effects on the elasticity of these lattices. To see this, we diagonalize the $\mathbb{K}$ matrix, $\mathbb{K} = V^T \Lambda V$, where V is a 3×3 orthogonal matrix, the row vectors of which formed by eigenvectors of $\mathbb{K}$, and Λ is a diagonal matrix with two positive eigenvalues:

$$V = \begin{pmatrix} \epsilon_1 \\ \epsilon_2 \\ \epsilon_0 \end{pmatrix}, \quad \Lambda = \begin{pmatrix} \lambda_1 & 0 & 0 \\ 0 & \lambda_2 & 0 \\ 0 & 0 & 0 \end{pmatrix}, \tag{5.17}$$

where the last strain vector ϵ_0 is the soft deformation, which comes with the zero eigenvalue in Λ.

To see the consequence of this elastic energy on spatially varying ZMs in the material, we rewrite Eq. (5.16) in terms of displacement field $u = \{u_x, u_y\}$:

$$f_{el} = \frac{1}{2}\epsilon_a \mathbb{K}_{ab} \epsilon_b = \frac{1}{2} u_i \overleftarrow{S^T_{ia}} \mathbb{K}_{ab} \overrightarrow{S_{bj}} u_j \equiv \frac{1}{2} u_i K_{ij} u_j, \tag{5.18}$$

where

$$\overrightarrow{S} \equiv i \begin{pmatrix} k_x & 0 \\ 0 & k_y \\ \frac{k_y}{2} & \frac{k_x}{2} \end{pmatrix}, \tag{5.19}$$

with k_x, k_y representing x and y directional wave vectors and the overhead arrow denoting that these wave vectors are differential operators (in real space) acting on the wave to the right. Similarly, the left overhead arrow on $\overleftarrow{S^T_{ia}}$ acts on u_i to its left.

With the diagonalization in Eq. (5.17), the stiffness matrix K is given by:

$$K = \overleftarrow{S^T} \mathbb{K} \overrightarrow{S} = \overleftarrow{S^T} V^T \Lambda V \overrightarrow{S}. \tag{5.20}$$

Because the last eigenvalue of Λ vanishes, we can define $\tilde{V}$ to be the 2×3 matrix with the last row removed from V, and $\tilde{\Lambda}$ to the 2×2 matrix with the last row removed in Λ. Thus, we have a 2×2 matrix C that maps displacement fields to the "nonsoft" strains:

$$\overrightarrow{C} = \tilde{V} \overrightarrow{S}, \tag{5.21}$$

and correspondingly

$$K = \overleftarrow{C^T} \tilde{\Lambda} \overrightarrow{C}. \tag{5.22}$$

Therefore, zero modes in this media are waves that satisfy:

$$\overrightarrow{C} u = 0. \tag{5.23}$$

We can eliminate u_y and write this as a differential equation of u_x only, which becomes:

$$\det \overrightarrow{C} u_x = 0. \tag{5.24}$$

This C matrix is the same as the final 2×2 matrix in the continuum theory (after integrating out high frequency modes and expanding to the linear order in wavenumbers k_x and k_y) for topological ZMs in Maxwell lattices [73].

Using the fact that $\{\epsilon_1, \epsilon_2, \epsilon_0\}$ form an orthogonal triplet, we have:

$$\det \overrightarrow{C} = -\frac{1}{2} \left(\epsilon_{02} k_x^2 - 2\epsilon_{03} k_x k_y + \epsilon_{01} k_y^2 \right). \tag{5.25}$$

It is perhaps more transparent if we turn q into differential operators, where Eq. (5.23) becomes:

$$\left(\epsilon_{02} \partial_x^2 - 2\epsilon_{03} \partial_x \partial_y + \epsilon_{01} \partial_y^2 \right) u_x = 0, \tag{5.26}$$

where $\{\epsilon_{01}, \epsilon_{02}, \epsilon_{03}\}$ are the 3 components of the soft strain ϵ_0 (using the Voigt notation). When $\det \epsilon_0 > 0$, the material is dilation dominated (auxetic), and this equation is elliptic; when $\det \epsilon_0 < 0$, the material is shear dominated (non-auxetic), and this equation is hyperbolic. The relationship between the real and imaginary components of the x and y component wavenumbers for the first Brillouin zone of an a_2 polarized lattice are shown in Fig. 5.11.

5.5.3.2 Interpreting Eq. (5.26) as a wave equation when $\det \epsilon_0 < 0$

Since for $\det \epsilon_0 < 0$, Eq. (5.26) is hyperbolic, it can be thought of as a wave equation in a 1D medium if we interpret spatial direction y as time t. With this interpretation, Eq. (5.26) can be rewritten as:

$$\left(\epsilon_{01}\partial_t^2 - 2\epsilon_{03}\partial_x\partial_t + \epsilon_{02}\partial_x^2\right) u_x = 0. \tag{5.27}$$

The presence of the second term means that the equation is not time reversal invariant since under the transformation $t \to -t$, $\partial_x\partial_t \to -\partial_x\partial_t$. This manifests itself in the nonsymmetric dispersion relation once we plug in the plane wave ansatz $u_x \sim e^{i(kx-\omega t)}$:

$$\omega = -\frac{\epsilon_{03}}{\epsilon_{01}}k \pm k\sqrt{\frac{\epsilon_{03}^2}{\epsilon_{01}^2} - \frac{\epsilon_{02}}{\epsilon_{01}}} = -\frac{\epsilon_{03}}{\epsilon_{01}}k \pm k\frac{\sqrt{-\det \epsilon_0}}{|\epsilon_{01}|}; \tag{5.28}$$

i.e., $\omega(k) \neq \omega(-k)$. Note that ω is real since $\det \epsilon_0 < 0$. And since the equations of motion is not time reversal symmetric, it is non-reciprocal.

Even though Eq. (5.27) is not time reversal symmetric, it is energy conserving. This can be seen from the following argument. This wave equation can be written as the Euler-Lagrange equation of the action:

$$S = \int dtdx\, \mathcal{L} = \int dtdx \left[\frac{1}{2}\epsilon_{01}(\partial_t u_x)^2 + \frac{1}{2}\epsilon_{02}(\partial_x u_x)^2 - \epsilon_{03}(\partial_t u_x)(\partial_x u_x)\right], \tag{5.29}$$

where $\mathcal{L}$ is the Lagrangian density. The Euler-Lagrange equation of this action is:

$$\partial_t \frac{\partial \mathcal{L}}{\partial(\partial_t u_x)} + \partial_x \frac{\partial \mathcal{L}}{\partial(\partial_x u_x)} = \frac{\partial \mathcal{L}}{\partial u_x} \Rightarrow \left(\epsilon_{01}\partial_t^2 - 2\epsilon_{03}\partial_x\partial_t + \epsilon_{02}\partial_x^2\right) u_x = 0, \tag{5.30}$$

which confirms the validity of the action. Since this Lagrangian is invariant under time translation $t \to t + t_0$, according to Noether's theorem, the energy E, defined below, is conserved:

$$E = \int dx \left[\frac{\partial \mathcal{L}}{\partial(\partial_t u_x)}\partial_t u_x - \mathcal{L}\right] = \int dx\, \frac{1}{2}\left[\epsilon_{01}(\partial_t u_x)^2 - \epsilon_{02}(\partial_x u_x)^2\right]. \tag{5.31}$$

The fact that energy E is conserved can be seen directly in the following way:

$$\begin{aligned}\frac{dE}{dt} &= \int dx\, \frac{1}{2}\partial_t \left[\epsilon_{01}(\partial_t u_x)^2 - \epsilon_{02}(\partial_x u_x)^2\right] \\ &= \int dx\, \left[\epsilon_{01}\partial_t u_x \partial_t^2 u_x - \epsilon_{02}\partial_x u_x \partial_t \partial_x u_x\right] \\ &= \int dx\, \left[\partial_t u_x (2\epsilon_{03}\partial_x \partial_t u_x - \epsilon_{02}\partial_x^2 u_x) - \epsilon_{02}\partial_x u_x \partial_t \partial_x u_x\right] \\ &= \int dx\, \partial_x \left[\epsilon_{03}(\partial_t u_x)^2 - \epsilon_{02}(\partial_x u_x)(\partial_t u_x)\right] \\ &= 0,\end{aligned} \tag{5.32}$$

where we used Eq. (5.27) from second to third equality. The last equality is due to periodic boundary conditions.

5.5.3.3 Higher order corrections to Eq. (5.23), topological polarization, and interpretation of the resulting equation as time evolution of non-Hermitian 1D system

So far we have kept to linear order terms in k_x and k_y in the effective 2×2 compatibility matrix $\overrightarrow{C}$, which corresponds to a classical elastic energy in terms of the strain tensor (without strain gradient terms). In this case, the ZMs are delocalized bulk modes. This can be seem from the fact that $\det \overrightarrow{C} = -\frac{1}{2}\left(\epsilon_{02}k_x^2 - 2\epsilon_{03}k_x k_y + \epsilon_{01}k_y^2\right) = 0$ results in $k_y = \frac{\epsilon_{03}}{\epsilon_{01}}k_x \pm k_x \frac{\sqrt{-\det \epsilon_0}}{|\epsilon_{01}|} \equiv k_\pm$, which are real—meaning that the ZMs are plane waves in the bulk.

The localization of the ZMs to edges are captured when terms up to the second order in k_x and k_y in the effective 2×2 compatibility matrix $\overrightarrow{C}$ are kept [30; 73]. To see this, we follow the steps from Eq. (5.23) to Eq. (5.25) keeping terms up to quadratic order in q in $\overrightarrow{C}$ to get:

$$\det \overrightarrow{C} = -\frac{1}{2}\left(\epsilon_{02}k_x^2 - 2\epsilon_{03}k_x k_y + \epsilon_{01}k_y^2\right) - \frac{i}{2}(C_1 k_x^3 + C_2 k_x^2 k_y + C_3 k_x k_y^2 + C_4 k_y^3) + \mathcal{O}(k^4), \tag{5.33}$$

where the parameters C_i, $i = 1, 2, 3, 4$ are real (this is due to time reversal symmetry of the Maxwell lattice) and are evaluated numerically using the scheme described in Ref. [73]. The cubic terms in k in $\det \overrightarrow{C}$ gives correction of order k_x^2 to solutions $k_y = k_\pm$ mentioned above. The real and imaginary components of k_x and k_y are shown in Fig. 5.11 for an $\mathbf{a_2}$ polarized hyperbolic PDE. To get the corrections, we plug in the ansatz $k_y = k_\pm + i\delta_\pm k_x^2$ in Eq. (5.33), and keep the

terms up to the cubic order in k_x to get:

$$\begin{aligned}
&(\epsilon_{02}k_x^2 - 2\epsilon_{03}k_x(k_\pm + i\delta_\pm k_x^2) + \epsilon_{01}(k_\pm + i\delta_\pm k_x^2)^2 + i(C_1k_x^3 + C_2k_x^2(k_\pm + i\delta_\pm k_x^2) + \\
&C_3k_x(k_\pm + i\delta_\pm k_x^2)^2 + C_4(k_\pm + i\delta_\pm k_x^2)^3) = 0, \\
&\Rightarrow i(2\epsilon_{01}k_\pm k_x^2 - 2\epsilon_{03}k_x^3)\delta_\pm + i(C_1k_x^3 + C_2k_x^2k_\pm + C_3k_xk_\pm^2 + C_4k_\pm^3) + \mathcal{O}(k_x^4) = 0 \\
&\Rightarrow \delta_\pm = \frac{C_1 + C_2\tilde{k}_\pm + C_3\tilde{k}_\pm^2 + C_4\tilde{k}_\pm^3}{2\epsilon_{03} - 2\epsilon_{01}\tilde{k}_\pm},
\end{aligned} \tag{5.34}$$

where we defined $\tilde{k}_\pm \equiv k_\pm/k_x = \frac{\epsilon_{03}}{\epsilon_{01}} \pm \frac{\sqrt{-\det\epsilon_0}}{|\epsilon_{01}|}$. Note that the solutions $k_y = \tilde{k}_\pm k_x + i\delta_\pm k_x^2$ to the order k_x^2 are complex numbers, meaning these zero modes are actually localized at the edges of the system. C_4 is numerically calculated to equal zero when the lattice vector $\mathbf{a_1}$ aligns with the x-axis, and in the case of topologically polarized Maxwell lattices, δ_+ and δ_- have the signs implying that both zero modes are at the same edge, hence the polarization. This is determined by the topological polarization.

Now, we can turn to the corresponding wave equation in a 1-dimensional dynamical system by replacing k_i with $(-i\partial_i)$ and interpreting direction y as time t:

$$\left[\left(\epsilon_{01}\partial_t^2 - 2\epsilon_{03}\partial_x\partial_t + \epsilon_{02}\partial_x^2\right) + (C_1\partial_x^3 + C_2\partial_x^2\partial_t + C_3\partial_x\partial_t^2 + C_4\partial_t^3)\right]u_x = 0. \tag{5.35}$$

We showed in the previous section that the terms with second order derivatives can be obtained from a time-invariant Lagrangian and hence energy conserving. However, the third order derivative terms cannot be obtained from a Lagrangian. The reason is the following. If there were a Lagrangian from which these terms with derivatives could be obtained, then that Lagragian would have to have three derivatives and have to be of the order u_x^2; hence the most generic form of the Lagrangian would be $u_x\partial_i\partial_j\partial_l u_x$ $(i,j,l \in \{x,t\})$. By taking variation of the action, we would obtain the following:

$$\begin{aligned}
\delta S = S[u_x + \delta u_x] - S[u_x] &= \int dtdx\,[(u_x + \delta u_x)\partial_i\partial_j\partial_l(u_x + \delta u_x) - u_x\partial_i\partial_j\partial_l u_x] \\
&= \int dtdx\,[u_x\partial_i\partial_j\partial_l\delta u_x + \delta u_x\partial_i\partial_j\partial_l u_x] \\
&= \int dtdx\,[\delta u_x\partial_i\partial_j\partial_l u_x - \delta u_x\partial_i\partial_j\partial_l u_x] \\
&= 0,
\end{aligned} \tag{5.36}$$

where we used integration by parts from the second to the third equality and assumed that the variations at the boundary of the integration domain are zero. This shows that the Euler-Lagrange equation of terms $u_x\partial_i\partial_j\partial_l u_x$ in the Lagrangian are zero; hence terms with third order derivatives

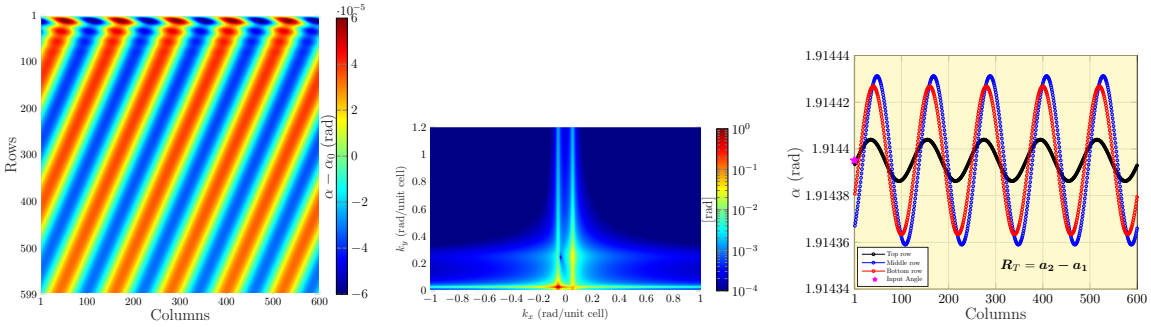

(a) (b) (c)

Figure 5.12: (a) Perturbation from homogeneous configuration $\alpha - \alpha_0$ for a 600×600 $\mathbf{a_2} - \mathbf{a_1}$ polarized lattice ($\alpha_0 = 1.9144$) with periodic boundary conditions given a sinusoidal wave perturbation on the top floppy edge with $k_x = 0.0523$ (rad/unit cell) and $\varepsilon = 1$ μrad. (b) 2D Fourier transform of (a). (c) Wave shapes of select rows (top, middle, and bottom) from the perturbed lattice for (a).

in an equation of motion cannot be obtained from a Lagrangian. As a result the argument of energy conservation in the previous subsection does not hold anymore as we include the terms with third order derivatives in the equation of motion. Furthermore, plugging the plane wave ansatz $u_x \sim e^{i(kx-\omega t)}$ along with $\omega = -\frac{\epsilon_{03}}{\epsilon_{01}}k \pm k\frac{\sqrt{-\det \epsilon_0}}{|\epsilon_{01}|} + i\delta_{\pm}k^2$ in Eq. (5.35), and carrying out a calculation similar to Eq. (5.34), we would get complex ω. Depending on the sign of the imaginary part of ω, the wave would grow/decay exponentially with time. Hence, we can interpret the system as active/dissipative. Interestingly, the distinction between active and dissipative in this 1D problem is determined by the topological polarization of the 2D lattice.

5.5.4 Note 4: Simulated Soft Edge Sinusoidal Perturbation of an $\mathbf{a_2} - \mathbf{a_1}$ Polarized Lattice

In addition to the simulations of the soft edge sinusoidal perturbation of $\mathbf{a_2}$ lattices in the main text (Figs. 5.2), here we show simulations with similar perturbation, but of $\mathbf{a_2} - \mathbf{a_1}$ polarized lattices. Figure 5.12 and Fig. 5.13 shows the simulated deformation field for the $\mathbf{a_2} - \mathbf{a_1}$ polarized lattices at low and high perturbation magnitudes, respectively. The key difference that can be observed between cases shown here and the $\mathbf{a_2}$ polarized lattices shown in the main text, is that the two excited modes propagate in opposite directions, rather than the same direction, as was the case for the $\mathbf{a_2}$ polarized lattices.

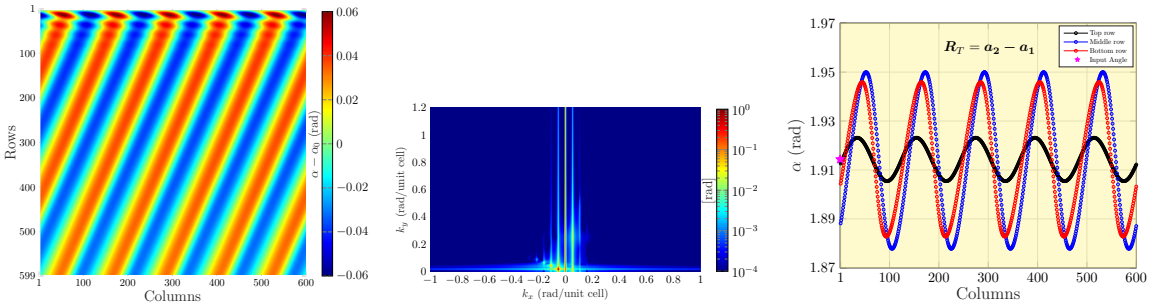

(a) (b) (c)

Figure 5.13: (a) Perturbation from homogeneous configuration $\alpha - \alpha_0$ for a 600×600 $\mathbf{a_2} - \mathbf{a_1}$ polarized lattice ($\alpha_0 = 1.9144$) with periodic boundary conditions given a sinusoidal wave perturbation on the top floppy edge with $k_x = 0.0523$ (rad/unit cell) and $\varepsilon = 1$ mrad. (b) 2D Fourier transform of (a). (c) Wave shapes of select rows (top, middle, and bottom) from the perturbed lattice for (a).

5.5.5 Note 5: Additional Wave Amplification Simulations

In Fig. 5.14, we show additional computational examples of wave amplification for 60-column-wide lattices with periodic boundary conditions over an array of α_0 values. We observe polarization domain switching in Fig. 5.14(a,b,d,e,f) and high frequencies generation (compared to the input wavelength) in Fig. 5.14(e,f).

5.5.6 Note 6: Solitary-Wave-Like Behavior of the Deformed Kagome Lattice

In addition to the example of the 10000×3000 $\mathbf{a_2}$ polarized lattice in the main text, here we show a 10000×600 $\mathbf{a_2}$ polarized lattice with a point perturbation applied at the top (floppy) edge. The computational results are shown in Figs. 5.15 and 5.16.

In Fig. 5.17, we further analyze the simulated results from Fig. 5.15. Fig. 5.17(a) [(b)] is obtained by tracking the peak magnitude of $d^2\alpha/dr^2$ (where derivatives with respect to r are found via a finite difference formulation subtracting over columns) in each row for slower [faster] moving solitary wave using the *findpeaks* command in MATLAB. Figure 5.17(c) shows the rate of change of average α, where α_{avg} is the mean value in each row given by $\alpha_{avg} = \sum \alpha/c = \alpha/600$, with respect to rows, as a function of point perturbation value ε. This is tracked by taking α_{avg} at each row and performing a linear fitting $\alpha_{avg} = mr + b$ ranging the entire lattice (rows $1-10000$), using the *polyfit* command in MATLAB. $d\alpha_{avg}/dr$ is thus given by the fitting parameter m.

Figure 5.17(d) shows the fitted decay rate s of the slower moving solitary wave, as a function of point perturbation value ε, obtained by finding α_{max} and α_{min} using the *max* and *min* commands in MATLAB, and then calculating the peak-to-peak amplitude $\alpha_{max} - \alpha_{min}$ at each row. The

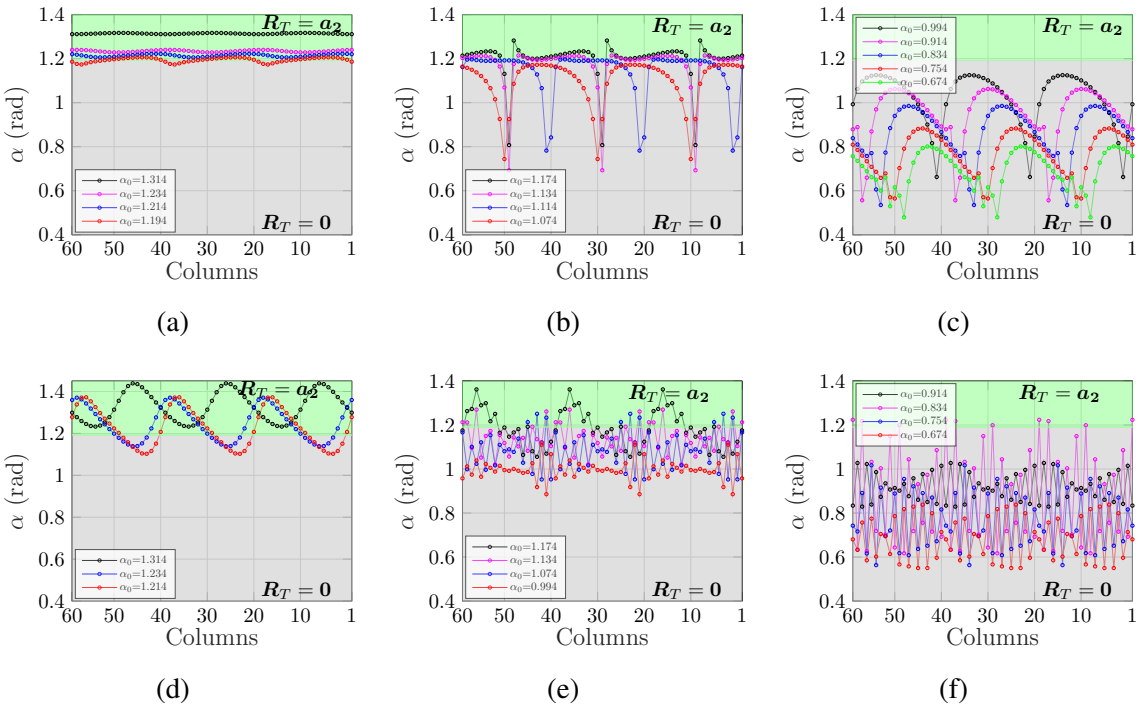

Figure 5.14: Computational results (α) of wave amplification in 60-column-wide lattices with periodic boundary conditions due to sinusoidal perturbation ($k_x = 0.314$) for an array of α_0 values. (a,d) α_0 originally in $\mathbf{a_2}$ polarization, near the boundary with $\mathbf{R}_T = 0$. (b,e) α_0 in $\mathbf{R_T = 0}$ polarization near the boundary with $\mathbf{a_2}$. (c,f) α_0 further in $\mathbf{R}_T = 0$ than before. (a-c) Perturbation amplitude $\varepsilon = 1$ mrad. (a) Bottom edges after perturbing at the top (soft) edges. (b,c) Bottom edges after perturbing at the top edge of the unpolarized lattices. (d-f) Perturbation amplitude $\varepsilon = 1$ μrad. (d) Top edges after perturbing at the bottom (hard) edges. (e,f) Top edges after perturbing the bottom of the unpolarized lattices. In (a), 60 rows is chosen; In (b-f), the displayed row is the last row before the lattice breaks.

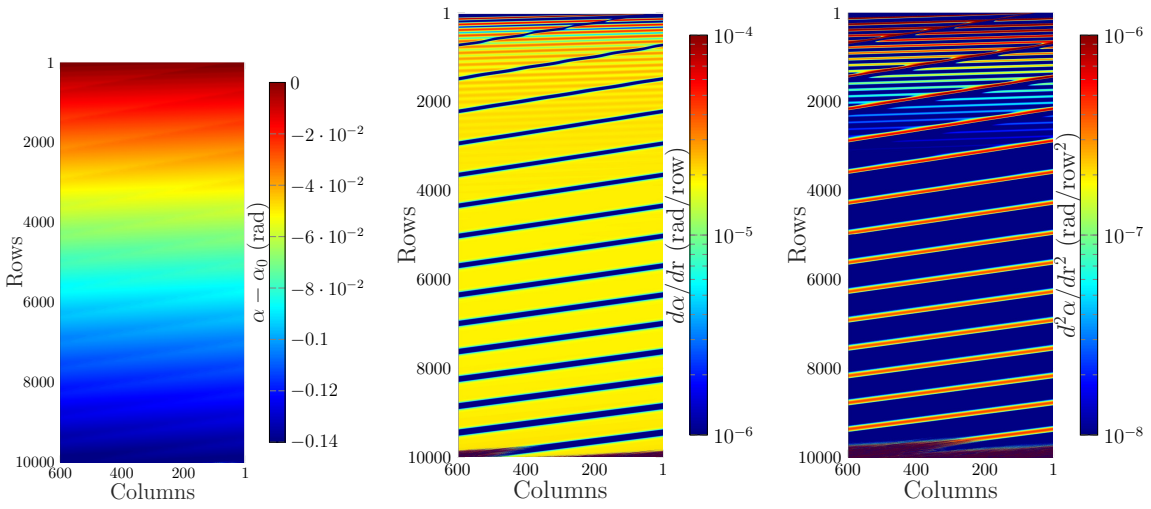

Figure 5.15: Computational results of a 10000×600 $\mathbf{a_2}$ polarized lattice with periodic left-right boundary conditions. The lattice has $\alpha_0 = 1.3144$ rad, and the point perturbation is applied on the top row at column 50. (a) $\alpha - \alpha_0$, (b) $d\alpha/dr$, and (c) $d^2\alpha/dr^2$. Logarithmic scale is used in the colorbars of (b) and (c). Note, (b) [(c)], $d\alpha/dr$ [$d^2\alpha/dr^2$] is saturated at the lower limit of 10^{-6} rad [10^{-8} rad].

behavior of the peak to peak amplitude is oscillatory and decaying, in order to fit the decay rate, we first find the peak values of $\alpha_{max} - \alpha_{min}$ in the plot of $\alpha_{max} - \alpha_{min}$ versus r using the *findpeak* command in MATLAB, then fit these peak values to an exponential function Ae^{sr}. Figure 5.17(e) shows the fitted decay rate σ for both slower and faster moving solitary waves, as a function of point perturbation value ε, based on ${d^2\alpha/dr^2}_{max} - {d^2\alpha/dr^2}_{min}$ at each row, instead of $\alpha_{max} - \alpha_{min}$. Here, for each solitary wave, ${d^2\alpha/dr^2}_{max}$ and ${d^2\alpha/dr^2}_{min}$ represent the local maximum and minimum of $d^2\alpha/dr^2$ at each row. For the results shown in Fig. 5.17(e), rows $50 - 300$ are the chosen range for fitting ${d^2\alpha/dr^2}_{max} - {d^2\alpha/dr^2}_{min} = Ae^{\sigma r}$ since the solitary waves separate from each other and have not collided again.

The "speed" of the solitary waves for the 600 column wide lattice is shown in Fig. 5.17(f). Differing algorithms were used to find the speed for the 3000 (main text) and 600 (here) column wide lattices, since the higher number of interactions in the 600 column wide lattice makes it difficult to locate the individual solitary wave peaks in each row. For the 3000-column-wide lattice shown in the main text, the speed $d(col)/d(row) \rightarrow dc/dr$ is obtained by tracking the location of peaks for $d^2\alpha/dr^2$ at each row, which can correspond with slower (bigger peak) and faster solitary waves (smaller peak). Again, the *findpeaks* command in MATLAB is used here. During collision no data is collected. Once peaks of $d^2\alpha/dr^2$ are found at each row, a linear fitting is performed on rows $50 - 400$. The row range is chosen for the same reason as the previous fitting in Fig. 5.17(e).

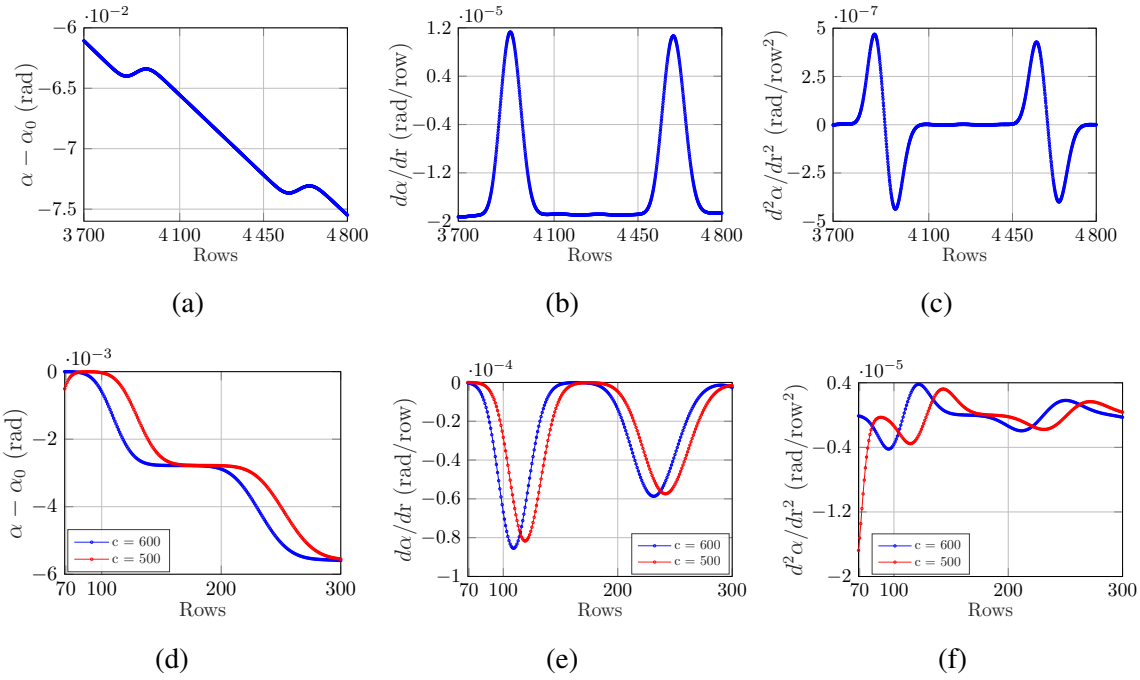

Figure 5.16: Selected computational results for the two solitary waves observed in the lattice in Fig. 5.15. (a-c) Slower moving solitary wave: (a) $\alpha - \alpha_0$, (b) $d\alpha/dr$, and (c) $d^2\alpha/dr^2$ at column 300 (middle column). Rows $3700 - 4800$ are chosen to minimize the interaction with the faster moving solitary wave. (d-f) Faster moving solitary wave: (d) $\alpha - \alpha_0$, (e) $d\alpha/dr$, and (f) $d^2\alpha/dr^2$ at columns 500 (red) and 600 (blue), respectively. Rows $70 - 300$ are chosen to avoid the effect of substantial amplitude decay. Note that we avoid very early rows $1 - 70$ to give the solitary waves adequate time to separate.

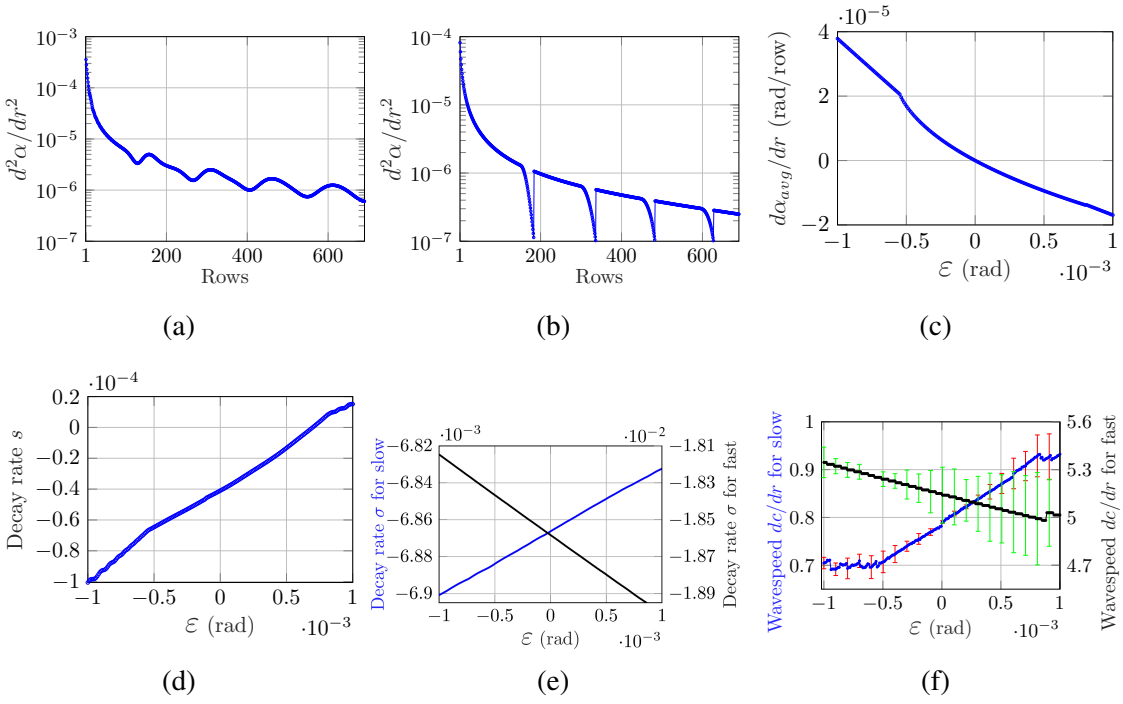

Figure 5.17: (a,b) Peak magnitude of $d^2\alpha/dr^2$ as a function of rows for (a) slower and (b) faster moving solitary waves. The fluctuation of magnitude is due to the interaction of two solitary waves. As a function of point perturbation magnitude ϵ the: (c) rate of change of α_{avg} with respect to rows, (d) decay rate s based on the amplitude $\alpha_{max} - \alpha_{min}$ at each row of the slower moving solitary wave, (e) decay rate σ based on the peak-to-peak magnitude of $d^2\alpha/dr^2$ at each row for both solitary waves, and (f) wave-speeds of slower and faster moving solitary waves versus the point perturbation value ϵ.

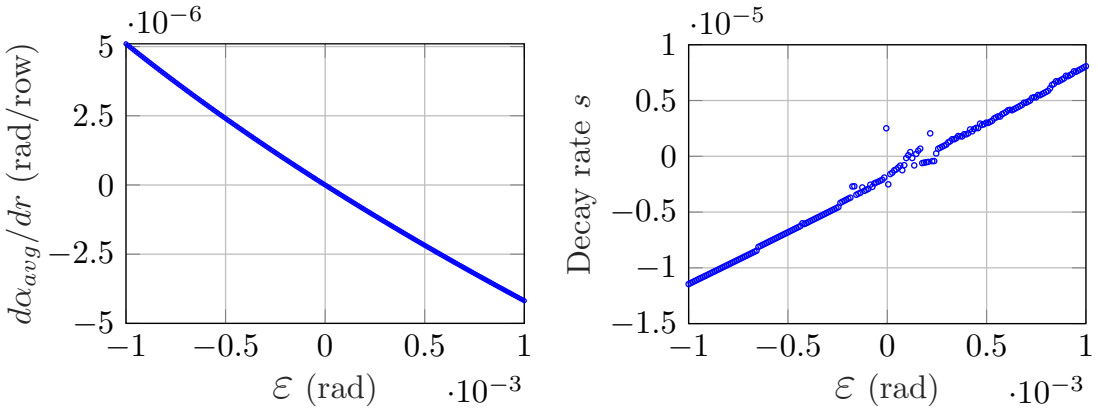

(a) (b)

Figure 5.18: Additional computational results of a 10000×3000 $\mathbf{a_2}$ polarized lattice ($\alpha_0 = 1.3144$ rad) with periodic left-right boundary conditions and the point perturbation applied on the top row at column 50. As a function of point perturbation magnitude ϵ, the: (a) rate of change of α_{avg} with respect to rows, and (b) decay rate s based on the amplitude $\alpha_{max} - \alpha_{min}$ at each row of the slower moving solitary wave.

For each solitary wave, columns can be related to rows in the linear form $r = m'c + b'$ the slope m' gives wave-speed dc/dr. For the 600 column wide lattice, the local maximum is found using the same peak detection algorithm, however this time, the data analyzed comes from one column for a prescribed set of rows, such as in Fig 5.16(c). The peaks denote when the solitary wave passes the column of interest, the distance between peaks Δr is calculated. The columns traversed is the width of the lattice, thus the velocity is given by $dc/dr = \Delta c/\Delta r = 600/\Delta r$. In order to avoid the interaction between the two solitary waves at the beginning rows of the lattice, the slower moving solitary wave is investigated in the range of $r/3 - 4r/5$. The final speed in main text Fig. 5 is calculated as the average of $600/\Delta r$ for all Δr in the specified range. The error bars are calculated by taking the maximum and minimum solitary wave velocities for a particular ε value. The amplitude of the faster moving solitary wave is found by looking at the far right column (column 600) and the first 500 rows of the acceleration term $d^2\alpha/dr^2$. The peaks and their corresponding row locations of the fast solitary wave are obtained using the *findpeaks* command, which gives Δr, the faster solitary wave's velocity is then found in the same manner as before $dc/dr = 600/(\Delta r)$. The error is found similar to the slower solitary wave case by taking the difference between the maximum and the minimum velocities.

Additional computational results of a 10000×3000 $\mathbf{a_2}$ polarized lattice are shown in Fig. 5.18.

5.5.7 Note 7: Experimental Setup and Image Processing

Photographs of the assembled lattices were taken and MATLAB was used to post process the images. The hinge points were found using the *imfindcircles* function, which allows the lattice to be reconstructed and analyzed. The lattices composed of laser cut black [red and blue] acrylic triangles in both the SI and the main text are shown in Fig. 5.19 [Fig. 5.20], respectively. Figure 5.21 shows the error between the measured and simulated lattices shown in Fig. 5.7.

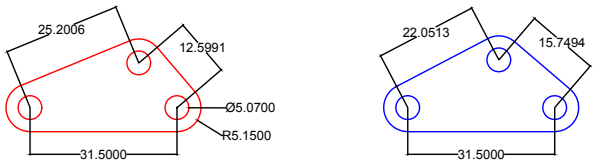

Figure 5.19: Dimensions (in the unit of mm) of laser cut acrylic triangles in the unit cell used in Fig. 5.7(a) of the main text.

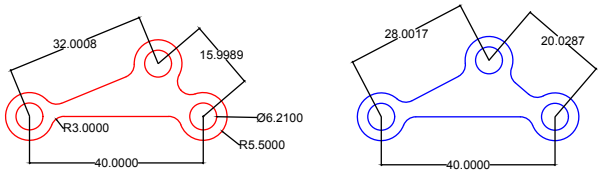

Figure 5.20: Dimensions (in the unit of mm) of laser cut acrylic triangles in the unit cell used in Fig. 5.7(d) of the main text.

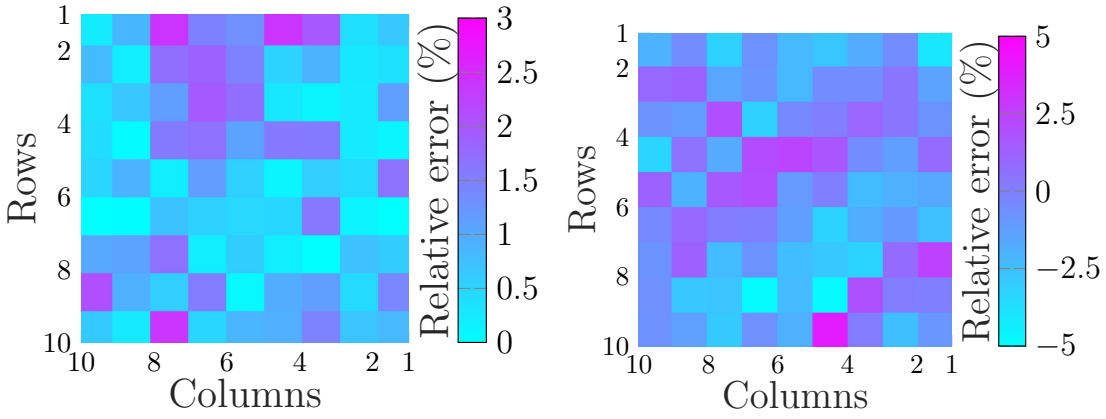

(a) (b)

Figure 5.21: Difference between measured and simulated angles normalized by homogeneous angle $\alpha_0 = 1.3144$ for the two examples shown in Fig. 5.7. (a) Sinusoidal perturbation for $\varepsilon = 0.1$ rad, $k_x = 0.6283$ rad/unit cell. (b) Point perturbation for $\varepsilon = 45$ mrad applied at column 3.

CHAPTER 6

Summary and Outlooks

6.1 Conclusions

In this thesis, I have explored the Maxwell mechanical frames in the scope of both non-ideal springs and non-linear deformations. In Chapter II, I examined the *Vertex Model* (VM) and *Active Tension Network* (ATN) models for the epithelial tissue, in which the springs are on the faces of the polygons which represent the cells, rather than the regular springs which have only site-to-site interactions. Under such a model, the Maxwell-Calladine index theorem still applies, and the isostaticity of the system still holds, thus it was possible for me to find a topologically polarized *floppy modes* (FM) in this model, which perhaps indicates how the boundary phenomena in tissue morphogenesis are controlled by geometry. In Chapter III, the effect of bending stiffness is taken into consideration, and it was discovered that the increase in bending stiffness would have a masking effect on the stress-focusing effect at a topological domain wall. Not only such an effect is observed, but by tuning the geometry of the Maxwell lattice, such masking can be reduced. Furthermore, by tuning the geometry of the Maxwell lattice, the response to different strains such as shear can be engineered. The inclusion of bending stiffness, even through simple models, was able to facilitate our understanding of how the theoretically predicted topological phenomena appear in real materials. In Chapter IV, a Maxwell lattice with bi-stable unit cells is engineered to give multi-stability to the whole lattice. In this lattice, the incorporation of bi-stable units accomplished convenient and robust transformations between topologically distinguished states, and the quasi-static analysis on the interface between the two states shows the possible pathway of the transformation under the multi-stability. Through the observation of the transformation pathway, one can observe a hint of how topologically polarized Maxwell lattices respond to impact, which is an important step to utilize the asymmetric boundary stiffness of the topologically polarized Maxwell lattices to achieve the design of a metamaterial for mechanical cloaking. In Chapter V, a study on the Maxwell lattice under both topologically polarized and non-polarized regimes is performed after giving a sinusoidal perturbation at one of the boundaries of the lattice to a non-linear level.

Under such a condition, the non-linear zero energy deformations are examined, in which not only the regular phenomena in non-linear systems were revealed, but a solitary wave is also observed. The formation of the solitary wave suggests a compact, amplitude-dependent spatially-addressable signal transmission and remote-controlled localization of stress and deformation, which leads to opportunities for application in mechano-responsive metamaterials.

Using theoretical modeling, numerical simulation, and experimental demonstration, the works demonstrated in this thesis extend the analysis of topological states in Maxwell lattices to a level when non-ideal springs and large deformations are considered. The interesting phenomena caused by the non-ideal springs and non-linearity revealed its potential for many future physics problems and engineering considerations. Thus, I'll introduce some of the potential future perspectives in both physical and engineering aspects.

6.2 Outlook

On the results shown in Chapter II, although the epithelial tissue demonstrates polarized topological states, it happens under a very strict situation that the cells must have a concave shape. Though it is uncommon to observe such a phenomenon in biology, it is possible to appear in future experiments. Besides, one can speculate an experimental design that has elastic constraints on polygonal faces that restricts the perimeter and area of the polygon to observe the topologically polarized states. On the theoretical side, one can imagine an inclusion of the active elements of biology so that the expansion and contraction of cells on the epithelial tissue have an asymmetry that breaks the energy conservation of the system. Under such a consideration, the dynamical matrix of the system becomes non-Hermitian, and interesting physics may appear as other non-Hermiticity physical systems that have been extensively considered [154; 175; 23; 149; 161].

Chapter III has demonstrated the effect of bending stiffness on the topological states of Maxwell lattices, and showed the possibility of achieving the ability of stress control, but the story is far from complete. The simple *angular spring* (AS) and *next nearest neighbor* (NNN) model offered us insight into the bending strength at the hinges, but the hinge is treated as unbreakable. And as it was observed in both experiments and simulation that fracturing happens more often at the hinges instead of the bonds, it would be a natural extension to assign fracturing thresholds to the AS and NNN springs to study hinge fracturing. Another important extension would be to use the model on 2D systems with Weyl points to examine the effect finite bending stiffness has on the Weyl points. Or even modify the model to a 3D Maxwell system such as the Pyrochlore lattice, which has been observed with the presence of Weyl lines [18], to investigate the effect of bending stiffness on topological modes in 3D structures, as well as the modes on the Weyl line.

The multi-stable Maxwell lattice introduced in Chapter IV promised many potential applica-

tions that it can be applied to, such as mechanical shock absorbers, mechanical computing logic systems, etc., which are all great natural future directions to work towards in the engineering perspective. Moreover, it is natural to extend the 2D system to a 3D lattice, while making the unit cells multi-stable. This would offer a tremendously large configuration space for the Maxwell lattice, and it would be a step closer to the mechanical shock absorber mentioned above. Another aspect of this work that requires further attention is the study of the interface between two distinct topological states. It has an important relation with impact mitigation as the interface would form when the lattice goes through the transformation from the topologically polarized state to the non-polarized state. Thus, it is important to follow up with the dynamics and the impact loading on the Maxwell lattice.

The work presented in Chapter V utilized a quasi-static method to solve for the exact geometry of the Maxwell lattice following the zero energy deformations under a prescribed boundary. The observation of non-linear wave formation already gives us insights into the dynamics of a 2D Maxwell lattice, but it would be great to extend it to include the time domain dynamics. With the time domain inclusion, the mapping demonstrated in this work from space to time is no longer needed to verify the non-Hermiticity of the 2D Maxwell lattice.

BIBLIOGRAPHY

[1] C. L. Kane and T. C. Lubensky, "Topological boundary modes in isostatic lattices," *Nature Physics*, vol. 10, pp. 39–45, dec 2013.

[2] O. R. Bilal, R. Süsstrunk, C. Daraio, and S. D. Huber, "Intrinsically Polar Elastic Metamaterials," *Advanced Materials*, vol. 29, p. 1700540, jul 2017.

[3] M. Pishvar and R. L. Harne, "Soft Topological Metamaterials with Pronounced Polar Elasticity in Mechanical and Dynamic Behaviors," *Physical Review Applied*, vol. 14, p. 044034, oct 2020.

[4] H. Xiu, H. Liu, A. Poli, G. Wan, E. M. Arruda, X. Mao, and Z. Chen, "Multistable Topological Mechanical Metamaterials," jul 2022.

[5] J. C. Jolly, B. Jin, L. Jin, Y. Lee, T. Xie, S. Gonella, K. Sun, X. Mao, and S. Yang, "Soft mechanical metamaterials with transformable topology protected by stress caching," aug 2022.

[6] J. C. Maxwell, "L. On the calculation of the equilibrium and stiffness of frames," *The London, Edinburgh, and Dublin Philosophical Magazine and Journal of Science*, vol. 27, pp. 294–299, apr 1864.

[7] A. J. Liu and S. R. Nagel, "Jamming is not just cool any more," *Nature*, vol. 396, pp. 21–22, nov 1998.

[8] C. P. Broedersz, X. Mao, T. C. Lubensky, and F. C. Mackintosh, "Criticality and isostaticity in fibre networks," *Nature Physics*, vol. 7, pp. 983–988, oct 2011.

[9] H. Honda, "Geometrical Models for Cells in Tissues," *International Review of Cytology*, vol. 81, pp. 191–248, jan 1983.

[10] D. Bi, J. H. Lopez, J. M. Schwarz, and M. L. Manning, "A density-independent rigidity transition in biological tissues," *Nature Physics*, vol. 11, pp. 1074–1079, sep 2015.

[11] D. Bi, X. Yang, M. C. Marchetti, and M. L. Manning, "Motility-driven glass and jamming transitions in biological tissues," *Physical Review X*, vol. 6, p. 021011, apr 2016.

[12] L. Yan and D. Bi, "Multicellular Rosettes Drive Fluid-solid Transition in Epithelial Tissues," *Physical Review X*, vol. 9, p. 011029, feb 2019.

[13] D. B. Staple, R. Farhadifar, J. C. Röper, B. Aigouy, S. Eaton, and F. Jülicher, "Mechanics and remodelling of cell packings in epithelia," *European Physical Journal E*, vol. 33, pp. 117–127, nov 2010.

[14] J. Paulose, B. G. G. Chen, and V. Vitelli, "Topological modes bound to dislocations in mechanical metamaterials," *Nature Physics*, vol. 11, pp. 153–156, jan 2015.

[15] J. Paulose, A. S. Meeussen, and V. Vitelli, "Selective buckling via states of self-stress in topological metamaterials," *Proceedings of the National Academy of Sciences of the United States of America*, vol. 112, pp. 7639–7644, jun 2015.

[16] D. Z. Rocklin, S. Zhou, K. Sun, and X. Mao, "Transformable topological mechanical metamaterials," *Nature Communications*, vol. 8, pp. 1–9, jan 2017.

[17] D. Z. Rocklin, B. G. G. Chen, M. Falk, V. Vitelli, and T. C. Lubensky, "Mechanical Weyl Modes in Topological Maxwell Lattices," *Physical Review Letters*, vol. 116, p. 135503, apr 2016.

[18] O. Stenull, C. L. Kane, and T. C. Lubensky, "Topological Phonons and Weyl Lines in Three Dimensions," *Physical Review Letters*, vol. 117, p. 068001, aug 2016.

[19] D. Zhou, L. Zhang, and X. Mao, "Topological Edge Floppy Modes in Disordered Fiber Networks," *Physical Review Letters*, vol. 120, p. 068003, feb 2018.

[20] D. Zhou, L. Zhang, and X. Mao, "Topological Boundary Floppy Modes in Quasicrystals," *Physical Review X*, vol. 9, p. 021054, jun 2019.

[21] B. G. G. Chen, B. Liu, A. A. Evans, J. Paulose, I. Cohen, V. Vitelli, and C. D. Santangelo, "Topological Mechanics of Origami and Kirigami," *Physical Review Letters*, vol. 116, p. 135501, mar 2016.

[22] D. Z. Rocklin, "Directional mechanical response in the bulk of topological metamaterials," *New Journal of Physics*, vol. 19, jun 2017.

[23] D. Zhou, J. Ma, K. Sun, S. Gonella, and X. Mao, "Switchable phonon diodes using nonlinear topological Maxwell lattices," *Physical Review B*, vol. 101, p. 104106, mar 2020.

[24] L. M. Nash, D. Kleckner, A. Read, V. Vitelli, A. M. Turner, and W. T. Irvine, "Topological mechanics of gyroscopic metamaterials," *Proceedings of the National Academy of Sciences of the United States of America*, vol. 112, pp. 14495–14500, nov 2015.

[25] W. Zunker and S. Gonella, "Soft topological lattice wheels," *Extreme Mechanics Letters*, vol. 46, p. 101344, jul 2021.

[26] J. L. Silverberg, J. H. Na, A. A. Evans, B. Liu, T. C. Hull, C. D. Santangelo, R. J. Lang, R. C. Hayward, and I. Cohen, "Origami structures with a critical transition to bistability arising from hidden degrees of freedom," *Nature Materials*, vol. 14, pp. 389–393, mar 2015.

[27] J. McInerney, B. G. G. Chen, L. Theran, C. D. Santangelo, and D. Zeb Rocklin, "Hidden symmetries generate rigid folding mechanisms in periodic origami," *Proceedings of the National Academy of Sciences of the United States of America*, vol. 117, pp. 30252–30259, dec 2020.

[28] X. F. Guo and L. Ma, "Periodic topological lattice with different indentation hardness on opposite surfaces," *Materials and Design*, vol. 180, p. 107953, oct 2019.

[29] C. R. Calladine, "Buckminster Fuller's "Tensegrity" structures and Clerk Maxwell's rules for the construction of stiff frames," *International Journal of Solids and Structures*, vol. 14, pp. 161–172, jan 1978.

[30] T. C. Lubensky, C. L. Kane, X. Mao, A. Souslov, and K. Sun, "Phonons and elasticity in critically coordinated lattices," *Reports on Progress in Physics*, vol. 78, p. 073901, jun 2015.

[31] S. D. Guest and J. W. Hutchinson, "On the determinacy of repetitive structures," *Journal of the Mechanics and Physics of Solids*, vol. 51, pp. 383–391, mar 2003.

[32] W. P. Su, J. R. Schrieffer, and A. J. Heeger, "Solitons in polyacetylene," *Physical Review Letters*, vol. 42, pp. 1698–1701, jun 1979.

[33] A. J. Niemi and G. W. Semenoff, "Index theorems on open infinite manifolds," *Nuclear Physics, Section B*, vol. 269, pp. 131–169, may 1986.

[34] A. Bergne, G. Baardink, E. G. Loukaides, and A. Souslov, "Scalable 3D printing for topological mechanical metamaterials," jun 2022.

[35] L. D. Landau and E. M. Lifshitz, "Theory of Elasticity," 1986.

[36] D. H. Arnold, "The mécanique physique of Siméon Denis Poisson: The evolution and isolation in France of his approach to physical theory (1800-1840) - II. The laplacian program," *Archive for History of Exact Sciences*, vol. 28, no. 3, pp. 267–287, 1983.

[37] A. Maradudin, E. Montroll, G. Weiss, and I. Ipatova, *Theory of lattice dynamics in the harmonic approximation*. 1963.

[38] H. Liu, D. Zhou, L. Zhang, D. K. Lubensky, and X. Mao, "Topological floppy modes in models of epithelial tissues," *Soft Matter*, vol. 17, pp. 8624–8641, oct 2021.

[39] H. Xiu, I. Frankel, H. Liu, K. Qian, S. Sarkar, B. C. Macnider, Z. Chen, N. Boechler, and X. Mao, "Synthetically Non-Hermitian Nonlinear Wave-like Behavior in a Topological Mechanical Metamaterial," jul 2022.

[40] F. Schöck and N. Perrimon, "Molecular mechanisms of epithelial morphogenesis," *Annual Review of Cell and Developmental Biology*, vol. 18, pp. 463–493, nov 2002.

[41] L. Solnica-Krezel and D. S. Sepich, "Gastrulation: Making and shaping germ layers," *Annual Review of Cell and Developmental Biology*, vol. 28, pp. 687–717, oct 2012.

[42] D. Fristrom, "The cellular basis of epithelial morphogenesis. A review," *Tissue and Cell*, vol. 20, pp. 645–690, jan 1988.

[43] M. Leptin, "Gastrulation movements: The logic and the nuts and bolts," *Developmental Cell*, vol. 8, pp. 305–320, mar 2005.

[44] J. F. Colas and G. C. Schoenwolf, "Towards a cellular and molecular understanding of neurulation," *Developmental Dynamics*, vol. 221, pp. 117–145, jun 2001.

[45] G. Trichas, A. M. Smith, N. White, V. Wilkins, T. Watanabe, A. Moore, B. Joyce, J. Sugnaseelan, T. A. Rodriguez, D. Kay, R. E. Baker, P. K. Maini, and S. Srinivas, "Multi-cellular rosettes in the mouse visceral endoderm facilitate the ordered migration of anterior visceral endoderm cells," *PLoS Biology*, vol. 10, p. e1001256, feb 2012.

[46] S. C. Cowin and S. B. Doty, *Tissue mechanics*. 2007.

[47] C. Guillot and T. Lecuit, "Mechanics of epithelial tissue homeostasis and morphogenesis," 2013.

[48] E. Heller and E. Fuchs, "Tissue patterning and cellular mechanics," *Journal of Cell Biology*, vol. 211, pp. 219–231, oct 2015.

[49] J. R. Lange and B. Fabry, "Cell and tissue mechanics in cell migration," *Experimental Cell Research*, vol. 319, pp. 2418–2423, oct 2013.

[50] K. P. Landsberg, R. Farhadifar, J. Ranft, D. Umetsu, T. J. Widmann, T. Bittig, A. Said, F. Jülicher, and C. Dahmann, "Increased Cell Bond Tension Governs Cell Sorting at the Drosophila Anteroposterior Compartment Boundary," *Current Biology*, vol. 19, pp. 1950–1955, dec 2009.

[51] M. Aliee, J. C. Röper, K. P. Landsberg, C. Pentzold, T. J. Widmann, F. Jülicher, and C. Dahmann, "Physical mechanisms shaping the Drosophila dorsoventral compartment boundary," *Current Biology*, vol. 22, pp. 967–976, jun 2012.

[52] D. Umetsu, B. Aigouy, M. Aliee, L. Sui, S. Eaton, F. Jülicher, and C. Dahmann, "Local increases in mechanical tension shape compartment boundaries by biasing cell intercalations," *Current Biology*, vol. 24, pp. 1798–1805, aug 2014.

[53] X. Mao and T. C. Lubensky, "Maxwell Lattices and Topological Mechanics," *Annual Review of Condensed Matter Physics*, vol. 9, pp. 413–433, mar 2018.

[54] L. Zhang and X. Mao, "Fracturing of topological Maxwell lattices," *New Journal of Physics*, vol. 20, p. 063034, jun 2018.

[55] K. K. Chiou, L. Hufnagel, and B. I. Shraiman, "Mechanical stress inference for two dimensional cell arrays," *PLoS Computational Biology*, vol. 8, p. e1002512, may 2012.

[56] N. Noll, M. Mani, I. Heemskerk, S. J. Streichan, and B. I. Shraiman, "Active tension network model suggests an exotic mechanical state realized in epithelial tissues," *Nature Physics*, vol. 13, pp. 1221–1226, aug 2017.

[57] P. Hayes and J. Solon, "Drosophila dorsal closure: An orchestra of forces to zip shut the embryo," *Mechanisms of Development*, vol. 144, pp. 2–10, apr 2017.

[58] D. P. Kiehart, J. M. Crawford, A. Aristotelous, S. Venakides, and G. S. Edwards, "Cell sheet morphogenesis: Dorsal closure in drosophila melanogaster as a model system," *Annual Review of Cell and Developmental Biology*, vol. 33, pp. 169–202, oct 2017.

[59] N. Ninov, D. A. Chiarelli, and E. Martín-Blanco, "Extrinsic and intrinsic mechanisms directing epithelial cell sheet replacement during Drosophila metamorphosis," *Development*, vol. 134, pp. 367–379, jan 2007.

[60] A. Ainslie, J. R. Davis, J. Williamson, A. Ferreira, A. Torres-Sanchez, A. Hoppe, F. Mangione, M. Smith, E. Martin-Blanco, G. Salbreux, and N. Tapon, "ECM remodelling and spatial cell cycle coordination determine tissue growth kinetics," *bioRxiv*, vol. 10.1101/20, pp. 1–19, nov 2020.

[61] A. E. Bruce and C. P. Heisenberg, "Mechanisms of zebrafish epiboly: A current view," *Current Topics in Developmental Biology*, vol. 136, pp. 319–341, jan 2020.

[62] S. Begnaud, T. Chen, D. Delacour, R. M. Mège, and B. Ladoux, "Mechanics of epithelial tissues during gap closure," *Current Opinion in Cell Biology*, vol. 42, pp. 52–62, oct 2016.

[63] V. Hakim and P. Silberzan, "Collective cell migration: A physics perspective," *Reports on Progress in Physics*, vol. 80, p. 076601, apr 2017.

[64] R. Farhadifar, J. C. Röper, B. Aigouy, S. Eaton, and F. Jülicher, "The Influence of Cell Mechanics, Cell-Cell Interactions, and Proliferation on Epithelial Packing," *Current Biology*, vol. 17, pp. 2095–2104, dec 2007.

[65] A. G. Fletcher, M. Osterfield, R. E. Baker, and S. Y. Shvartsman, "Vertex models of epithelial morphogenesis," *Biophysical Journal*, vol. 106, pp. 2291–2304, jun 2014.

[66] X. Yang, D. Bi, M. Czajkowski, M. Merkel, M. L. Manning, and M. C. Marchetti, "Correlating cell shape and cellular stress in motile confluent tissues," *Proceedings of the National Academy of Sciences of the United States of America*, vol. 114, pp. 12663–12668, nov 2017.

[67] M. Merkel and M. L. Manning, "A geometrically controlled rigidity transition in a model for confluent 3D tissues," *New Journal of Physics*, vol. 20, feb 2018.

[68] L. Hufnagel, A. A. Teleman, H. Rouault, S. M. Cohen, and B. I. Shraiman, "On the mechanism of wing size determination in fly development," *Proceedings of the National Academy of Sciences of the United States of America*, vol. 104, pp. 3835–3840, mar 2007.

[69] G. Salbreux, L. K. Barthel, P. A. Raymond, and D. K. Lubensky, "Coupling Mechanical Deformations and Planar Cell Polarity to Create Regular Patterns in the Zebrafish Retina," *PLoS Computational Biology*, vol. 8, aug 2012.

[70] M. A. Spencer, Z. Jabeen, and D. K. Lubensky, "Vertex stability and topological transitions in vertex models of foams and epithelia," *European Physical Journal E*, vol. 40, jan 2017.

[71] L. Euler, "Elementa doctrinae solidorum," *Novi Commentarii academiae scientiarum Petropolitanae*, vol. 4, pp. 109–140, jan 1758.

[72] O. Stenull and T. C. Lubensky, "Signatures of Topological Phonons in Superisostatic Lattices," *Physical Review Letters*, vol. 122, jun 2019.

[73] K. Sun and X. Mao, "Continuum Theory for Topological Edge Soft Modes," *Physical Review Letters*, vol. 124, p. 207601, may 2020.

[74] A. Saremi and Z. Rocklin, "Topological Elasticity of Flexible Structures," *Physical Review X*, vol. 10, p. 011052, mar 2020.

[75] M. Nagashima, J. Hadidjojo, L. K. Barthel, D. K. Lubensky, and P. A. Raymond, "Anisotropic Müller glial scaffolding supports a multiplex lattice mosaic of photoreceptors in zebrafish retina," *Neural Development*, vol. 12, pp. 1–20, nov 2017.

[76] N. S. Houssin, J. B. Martin, V. Coppola, S. O. Yoon, and T. F. Plageman, "Formation and contraction of multicellular actomyosin cables facilitate lens placode invagination," *Developmental Biology*, vol. 462, pp. 36–49, jun 2020.

[77] J. M. López-Gay, H. Nunley, M. Spencer, F. di Pietro, B. Guirao, F. Bosveld, O. Markova, I. Gaugue, S. Pelletier, D. K. Lubensky, and Y. Bellaïche, "Apical stress fibers enable a scaling between cell mechanical response and area in epithelial tissue," *Science*, vol. 370, oct 2020.

[78] P. A. Raymond, S. M. Colvin, Z. Jabeen, M. Nagashima, L. K. Barthel, J. Hadidjojo, L. Popova, V. R. Pejaver, and D. K. Lubensky, "Patterning the cone mosaic array in zebrafish retina requires specification of ultraviolet-sensitive cones," *PLoS ONE*, vol. 9, jan 2014.

[79] N. A. Kaplan and N. S. Tolwinski, "Spatially defined Dsh-Lgl interaction contributes to directional tissue morphogenesis," *Journal of Cell Science*, vol. 123, pp. 3157–3165, sep 2010.

[80] R. P. Simone and S. DiNardo, "Actomyosin contractility and discs large contribute to junctional conversion in guiding cell alignment within the Drosophila embryonic epithelium," *Development*, vol. 137, pp. 1385–1394, apr 2010.

[81] L. LeGoff, H. Rouault, and T. Lecuit, "A global pattern of mechanical stress polarizes cell divisions and cell shape in the growing Drosophila wing disc," *Development (Cambridge)*, vol. 140, pp. 4051–4059, oct 2013.

[82] K. Dierkes, A. Sumi, J. Solon, and G. Salbreux, "Spontaneous oscillations of elastic contractile materials with turnover," *Physical Review Letters*, vol. 113, p. 148102, oct 2014.

[83] J. Sedzinski, M. Biro, A. Oswald, J. Y. Tinevez, G. Salbreux, and E. Paluch, "Polar actomyosin contractility destabilizes the position of the cytokinetic furrow," *Nature*, vol. 476, pp. 462–468, aug 2011.

[84] M. L. Manning, R. A. Foty, M. S. Steinberg, and E. M. Schoetz, "Coaction of intercellular adhesion and cortical tension specifies tissue surface tension," *Proceedings of the National Academy of Sciences of the United States of America*, vol. 107, pp. 12517–12522, jul 2010.

[85] J. B. Pendry, "Negative Refraction Makes a Perfect Lens," *Physical Review Letters*, vol. 85, p. 3966, oct 2000.

[86] S. D. Huber, "Topological mechanics," *Nature Physics*, vol. 12, pp. 621–623, jun 2016.

[87] K. Bertoldi, V. Vitelli, J. Christensen, and M. Van Hecke, "Flexible mechanical metamaterials," *Nature Reviews Materials*, vol. 2, pp. 1–11, oct 2017.

[88] X. Yu, J. Zhou, H. Liang, Z. Jiang, and L. Wu, "Mechanical metamaterials associated with stiffness, rigidity and compressibility: A brief review," *Progress in Materials Science*, vol. 94, pp. 114–173, may 2018.

[89] L. Xin, Y. Siyuan, L. Harry, L. Minghui, and C. Yanfeng, "Topological mechanical metamaterials: A brief review," *Current Opinion in Solid State and Materials Science*, vol. 24, p. 100853, oct 2020.

[90] R. S. Lakes, "Negative-Poisson's-Ratio Materials: Auxetic Solids," *Annual Review of Materials Research*, vol. 47, pp. 63–81, jul 2017.

[91] Z. G. Nicolaou and A. E. Motter, "Mechanical metamaterials with negative compressibility transitions," *Nature Materials*, vol. 11, pp. 608–613, may 2012.

[92] K. Sun, A. Souslov, X. Mao, and T. C. Lubensky, "Surface phonons, elastic response, and conformal invariance in twisted kagome lattices," *Proceedings of the National Academy of Sciences of the United States of America*, vol. 109, pp. 12369–12374, jul 2012.

[93] B. G. G. Chen, N. Upadhyaya, and V. Vitelli, "Nonlinear conduction via solitons in a topological mechanical insulator," *Proceedings of the National Academy of Sciences of the United States of America*, vol. 111, pp. 13004–13009, sep 2014.

[94] N. Singh and M. Van Hecke, "Design of Pseudo-Mechanisms and Multistable Units for Mechanical Metamaterials," *Physical Review Letters*, vol. 126, p. 248002, jun 2021.

[95] J. Ma, D. Zhou, K. Sun, X. Mao, and S. Gonella, "Edge Modes and Asymmetric Wave Transport in Topological Lattices: Experimental Characterization at Finite Frequencies," *Physical Review Letters*, vol. 121, p. 094301, aug 2018.

[96] A. Altland and M. R. Zirnbauer, "Nonstandard symmetry classes in mesoscopic normal-superconducting hybrid structures," *Phys. Rev. B*, vol. 55, pp. 1142–1161, Jan 1997.

[97] C.-K. Chiu, J. C. Y. Teo, A. P. Schnyder, and S. Ryu, "Classification of topological quantum matter with symmetries," *Rev. Mod. Phys.*, vol. 88, p. 035005, Aug 2016.

[98] B. Florijn, C. Coulais, and M. Van Hecke, "Programmable mechanical metamaterials," *Physical Review Letters*, vol. 113, p. 175503, oct 2014.

[99] A. S. Meeussen, J. Paulose, and V. Vitelli, "Geared topological metamaterials with tunable mechanical stability," *Physical Review X*, vol. 6, p. 041029, nov 2016.

[100] M. Boguslawski, P. Rose, and C. Denz, "Nondiffracting kagome lattice," *Applied Physics Letters*, vol. 98, p. 061111, feb 2011.

[101] Q. Chen, S. C. Bae, and S. Granick, "Directed self-assembly of a colloidal kagome lattice," *Nature*, vol. 469, pp. 381–384, jan 2011.

[102] A. Bolens and N. Nagaosa, "Topological states on the breathing kagome lattice," *Physical Review B*, vol. 99, p. 165141, apr 2019.

[103] H. M. Guo and M. Franz, "Topological insulator on the kagome lattice," *Physical Review B - Condensed Matter and Materials Physics*, vol. 80, p. 113102, sep 2009.

[104] T. Mei, Z. Meng, K. Zhao, and C. Q. Chen, "A mechanical metamaterial with reprogrammable logical functions," *Nature Communications*, vol. 12, pp. 1–11, dec 2021.

[105] U. Waheed, C. W. Myant, and S. N. Dobson, "Boolean AND/OR mechanical logic using multi-plane mechanical metamaterials," *Extreme Mechanics Letters*, vol. 40, p. 100865, oct 2020.

[106] C. El Helou, P. R. Buskohl, C. E. Tabor, and R. L. Harne, "Digital logic gates in soft, conductive mechanical metamaterials," *Nature Communications*, vol. 12, pp. 1–8, mar 2021.

[107] B. Khoda, A. M. Ahsan, A. N. Shovon, and A. I. Alam, "3D metal lattice structure manufacturing with continuous rods," *Scientific Reports 2021 11:1*, vol. 11, pp. 1–17, jan 2021.

[108] R. Tao, L. Xi, W. Wu, Y. Li, B. Liao, L. Liu, J. Leng, and D. Fang, "4D printed multi-stable metamaterials with mechanically tunable performance," *Composite Structures*, vol. 252, p. 112663, nov 2020.

[109] D. Sharma and S. S. Hiremath, "Bio-inspired repeatable lattice structures for energy absorption: Experimental and finite element study," *Composite Structures*, vol. 283, p. 115102, mar 2022.

[110] R. Levien, "The elastica: a mathematical history," ... *Engineering and Computer Sciences University of* ..., no. UCB/EECS-2008-103, pp. 1–25, 2008.

[111] E. H. Mansfield, *The bending and stretching of plates.* Pergamon Press; [distributed in the Western Hemisphere by Macmillan, New York], 1964.

[112] Q. Guo, Y. Pan, J. Lin, G. Wan, B. Xu, N. Hua, C. Zheng, Y. Huang, Y. Mei, W. Chen, and Z. Chen, "Programmable 3D Self-Folding Structures with Strain Engineering," *Advanced Intelligent Systems*, vol. 2, p. 2000101, dec 2020.

[113] S. Armon, E. Efrati, R. Kupferman, and E. Sharon, "Geometry and mechanics in the opening of chiral seed pods," *Science*, vol. 333, pp. 1726–1729, oct 2011.

[114] Z. Chen, Q. Guo, C. Majidi, W. Chen, D. J. Srolovitz, and M. P. Haataja, "Nonlinear geometric effects in mechanical bistable morphing structures," *Physical Review Letters*, vol. 109, p. 114302, sep 2012.

[115] X. Yu, L. Zhang, N. Hu, H. Grover, S. Huang, D. Wang, and Z. Chen, "Shape formation of helical ribbons induced by material anisotropy," *Applied Physics Letters*, vol. 110, p. 091901, feb 2017.

[116] Z. L. Wu, M. Moshe, J. Greener, H. Therien-Aubin, Z. Nie, E. Sharon, and E. Kumacheva, "Three-dimensional shape transformations of hydrogel sheets induced by small-scale modulation of internal stresses," *Nature Communications*, vol. 4, pp. 1–7, mar 2013.

[117] Z. D. Jastrzebski, *The nature and properties of engineering materials*. Wiley, 1977.

[118] L. Euler, *The rational mechanics of flexible or elastic bodies : 1638-1788 : introduction to Leonhardi Euleri Opera Omnia / vol. 10. et 11., seriei secundae.* Auctoritate et impensis Societatis scientiarum naturalium Helveticae, 1980.

[119] J. O. Smith, *Physical Audio Signal Processing, December 2008 Edition*, vol. 10. W3K Publishing, 2008.

[120] Y. Zhao, Y. Chen, and Y. Zhou, "Novel mechanical models of tensile strength and elastic property of FDM AM PLA materials: Experimental and theoretical analyses," *Materials & Design*, vol. 181, p. 108089, nov 2019.

[121] H. Gonabadi, A. Yadav, and S. J. Bull, "The effect of processing parameters on the mechanical characteristics of PLA produced by a 3D FFF printer," *International Journal of Advanced Manufacturing Technology*, vol. 111, pp. 695–709, nov 2020.

[122] C. Abeykoon, P. Sri-Amphorn, and A. Fernando, "Optimization of fused deposition modeling parameters for improved PLA and ABS 3D printed structures," *International Journal of Lightweight Materials and Manufacture*, vol. 3, pp. 284–297, sep 2020.

[123] M. Z. Hasan and C. L. Kane, "Colloquium: Topological insulators," *Reviews of Modern Physics*, vol. 82, pp. 3045–3067, nov 2010.

[124] F. Zangeneh-Nejad, A. Alù, and R. Fleury, "Topological wave insulators: A review," *Comptes Rendus Physique*, vol. 21, no. 4, pp. 467–499, 2021.

[125] X. L. Qi and S. C. Zhang, "Topological insulators and superconductors," *Reviews of Modern Physics*, vol. 83, p. 1057, oct 2011.

[126] J. K. Asbóth, L. Oroszlány, and A. Pályi, "A Short Course on Topological Insulators: Band-structure topology and edge states in one and two dimensions," sep 2015.

[127] C. Beenakker and L. Kouwenhoven, "A road to reality with topological superconductors," *Nature Physics*, vol. 12, pp. 618–621, jun 2016.

[128] D. Aasen, M. Hell, R. V. Mishmash, A. Higginbotham, J. Danon, M. Leijnse, T. S. Jespersen, J. A. Folk, C. M. Marcus, K. Flensberg, and J. Alicea, "Milestones toward Majorana-based quantum computing," *Physical Review X*, vol. 6, p. 031016, aug 2016.

[129] C. Tutschku, R. W. Reinthaler, C. Lei, A. H. Macdonald, and E. M. Hankiewicz, "Majorana-based quantum computing in nanowire devices," *Physical Review B*, vol. 102, p. 125407, sep 2020.

[130] M. J. Gilbert, "Topological electronics," *Communications Physics*, vol. 4, pp. 1–12, apr 2021.

[131] H. Chorsi, B. Cheng, B. Zhao, J. Toudert, V. Asadchy, O. F. Shoron, S. Fan, and R. Matsunaga, "Topological Materials for Functional Optoelectronic Devices," *Advanced Functional Materials*, vol. 32, p. 2110655, may 2022.

[132] Z. Yang, F. Gao, X. Shi, X. Lin, Z. Gao, Y. Chong, and B. Zhang, "Topological Acoustics," *Physical Review Letters*, vol. 114, p. 114301, mar 2015.

[133] H. Zhang, J. Wu, D. Fang, and Y. Zhang, "Hierarchical mechanical metamaterials built with scalable tristable elements for ternary logic operation and amplitude modulation," *Science Advances*, vol. 7, feb 2021.

[134] A. Bossart, D. M. Dykstra, J. van der Laan, and C. Coulais, "Oligomodal metamaterials with multifunctional mechanics," *Proceedings of the National Academy of Sciences of the United States of America*, vol. 118, p. e2018610118, may 2021.

[135] P. W. Lo, C. D. Santangelo, B. G. G. Chen, C. M. Jian, K. Roychowdhury, and M. J. Lawler, "Topology in Nonlinear Mechanical Systems," *Physical Review Letters*, vol. 127, p. 076802, aug 2021.

[136] G. U. Patil and K. H. Matlack, "Review of exploiting nonlinearity in phononic materials to enable nonlinear wave responses," *Acta Mechanica*, vol. 233, pp. 1–46, nov 2022.

[137] M. Lapine, I. V. Shadrivov, and Y. S. Kivshar, "Colloquium: Nonlinear metamaterials," *Reviews of Modern Physics*, vol. 86, p. 1093, sep 2014.

[138] A. Scott, *Encyclopedia of nonlinear science*, vol. 42. Routledge, 2005.

[139] Z. Chen, M. Segev, and D. N. Christodoulides, "Optical spatial solitons: Historical overview and recent advances," *Reports on Progress in Physics*, vol. 75, p. 086401, jul 2012.

[140] T. Dauxois and M. Peyrard, *Physics of solitons*. Cambridge University Press, 2006.

[141] R. W. Boyd, *Nonlinear Optics*. Elsevier Inc., 2008.

[142] A. H. Nayfeh and D. T. Mook, *Nonlinear Oscillations*. Wiley, may 1995.

[143] S. Strogatz, *Nonlinear dynamics and chaos : with applications to physics, biology, chemistry, and engineering*. Westview Press, 2000.

[144] B. Many Manda, R. Chaunsali, G. Theocharis, and C. Skokos, "Nonlinear topological edge states: From dynamic delocalization to thermalization," *Physical Review B*, vol. 105, p. 104308, mar 2022.

[145] D. Smirnova, D. Leykam, Y. Chong, and Y. Kivshar, "Nonlinear topological photonics," *Applied Physics Reviews*, vol. 7, p. 021306, jun 2020.

[146] R. Chaunsali, H. Xu, J. Yang, P. G. Kevrekidis, and G. Theocharis, "Stability of topological edge states under strong nonlinear effects," *Physical Review B*, vol. 103, p. 024106, jan 2021.

[147] J. R. Tempelman, K. H. Matlack, and A. F. Vakakis, "Topological protection in a strongly nonlinear interface lattice," *Physical Review B*, vol. 104, p. 174306, nov 2021.

[148] N. Pernet, P. St-Jean, D. D. Solnyshkov, G. Malpuech, N. Carlon Zambon, Q. Fontaine, B. Real, O. Jamadi, A. Lemaître, M. Morassi, L. Le Gratiet, T. Baptiste, A. Harouri, I. Sagnes, A. Amo, S. Ravets, and J. Bloch, "Gap solitons in a one-dimensional driven-dissipative topological lattice," *Nature Physics*, vol. 18, pp. 678–684, may 2022.

[149] D. Zhou, D. Z. Rocklin, M. Leamy, and Y. Yao, "Topological invariant and anomalous edge modes of strongly nonlinear systems," *Nature Communications 2022 13:1*, vol. 13, pp. 1–9, jun 2022.

[150] V. F. Nesterenko, *Dynamics of Heterogeneous Materials*. Springer New York, 2001.

[151] D. Marković, A. Mizrahi, D. Querlioz, and J. Grollier, "Physics for neuromorphic computing," *Nature Reviews Physics*, vol. 2, pp. 499–510, jul 2020.

[152] A. S. Raja, S. Lange, M. Karpov, K. Shi, X. Fu, R. Behrendt, D. Cletheroe, A. Lukashchuk, I. Haller, F. Karinou, B. Thomsen, K. Jozwik, J. Liu, P. Costa, T. J. Kippenberg, and H. Ballani, "Ultrafast optical circuit switching for data centers using integrated soliton microcombs," *Nature Communications*, vol. 12, pp. 1–7, oct 2021.

[153] T. J. Kippenberg, A. L. Gaeta, M. Lipson, and M. L. Gorodetsky, "Dissipative Kerr solitons in optical microresonators," *Science*, vol. 361, aug 2018.

[154] R. El-Ganainy, K. G. Makris, M. Khajavikhan, Z. H. Musslimani, S. Rotter, and D. N. Christodoulides, "Non-Hermitian physics and PT symmetry," *Nature Physics*, vol. 14, pp. 11–19, jan 2018.

[155] Y. Ashida, Z. Gong, and M. Ueda, "Non-Hermitian physics," *Advances in Physics*, vol. 69, no. 3, pp. 249–435, 2020.

[156] P. G. De Gennes, "Soluble model for fibrous structures with steric constraints," *The Journal of Chemical Physics*, vol. 48, pp. 2257–2259, sep 1968.

[157] S. L. Sondhi, S. M. Girvin, J. P. Carini, and D. Shahar, "Continuous quantum phase transitions," *Reviews of Modern Physics*, vol. 69, pp. 315–333, jan 1997.

[158] B. H. Kolner, "Space-Time Duality and the Theory of Temporal Imaging," *IEEE Journal of Quantum Electronics*, vol. 30, no. 8, pp. 1951–1963, 1994.

[159] F. Wilczek, "Quantum time crystals," *Physical Review Letters*, vol. 109, p. 160401, oct 2012.

[160] C. Chong and P. G. Kevrekidis, *Coherent Structures in Granular Crystals: From Experiment and Modelling to Computation and Mathematical Analysis*. Springer, 2018.

[161] S. Xia, D. Kaltsas, D. Song, I. Komis, J. Xu, A. Szameit, H. Buljan, K. G. Makris, and Z. Chen, "Nonlinear tuning of PT symmetry and non-Hermitian topological states," *Science*, vol. 372, pp. 72–76, apr 2021.

[162] M. C. Cross and P. C. Hohenberg, "Pattern formation outside of equilibrium," *Reviews of Modern Physics*, vol. 65, pp. 851–1112, jul 1993.

[163] A. Ankiewicz and N. Akhmediev, *Dissipative Solitons: From Optics to Biology and Medicine*, vol. 751 of *Lecture Notes in Physics*. Berlin, Heidelberg: Springer Berlin Heidelberg, 2008.

[164] Y. Zheng, I. Niloy, P. Celli, I. Tobasco, and P. Plucinsky, "Continuum Field Theory for the Deformations of Planar Kirigami," *Physical Review Letters*, vol. 128, p. 208003, may 2022.

[165] M. Moshe, E. Esposito, S. Shankar, B. Bircan, I. Cohen, D. R. Nelson, and M. J. Bowick, "Nonlinear mechanics of thin frames," *Physical Review E*, vol. 99, p. 013002, jan 2019.

[166] M. Czajkowski, C. Coulais, M. van Hecke, and D. Z. Rocklin, "Conformal elasticity of mechanism-based metamaterials," *Nature Communications*, vol. 13, pp. 1–9, jan 2022.

[167] Y. Zheng, I. Tobasco, P. Celli, and P. Plucinsky, "Modeling planar kirigami metamaterials as generalized elastic continua," may 2022.

[168] M. Czajkowski and D. Z. Rocklin, "Duality and Sheared Analytic Response in Mechanism-Based Metamaterials," pp. 1–15, may 2022.

[169] N. J. Zabusky and M. D. Kruskal, "Interaction of "solitons" in a collisionless plasma and the recurrence of initial states," *Physical Review Letters*, vol. 15, pp. 240–243, aug 1965.

[170] N. Gao and K. Lu, "An underwater metamaterial for broadband acoustic absorption at low frequency," *Applied Acoustics*, vol. 169, p. 107500, dec 2020.

[171] G. I. Stegeman and M. Segev, "Optical spatial solitons and their interactions: Universality and diversity," *Science*, vol. 286, pp. 1518–1523, nov 1999.

[172] B. Garbin, J. Javaloyes, G. Tissoni, and S. Barland, "Topological solitons as addressable phase bits in a driven laser," *Nature Communications*, vol. 6, pp. 1–7, jan 2015.

[173] M. A. Ghanem, A. Basu, R. Behrou, N. Boechler, A. J. Boydston, S. L. Craig, Y. Lin, B. E. Lynde, A. Nelson, H. Shen, and D. W. Storti, "The role of polymer mechanochemistry in responsive materials and additive manufacturing," *Nature Reviews Materials*, vol. 6, pp. 84–98, oct 2021.

[174] G. W. Milton and A. V. Cherkaev, "Which elasticity tensors are realizable?," *Journal of Engineering Materials and Technology, Transactions of the ASME*, vol. 117, no. 4, pp. 483–493, 1995.

[175] C. Scheibner, A. Souslov, D. Banerjee, P. Surówka, W. T. Irvine, and V. Vitelli, "Odd elasticity," *Nature Physics*, vol. 16, pp. 475–480, mar 2020.